

**Computational investigations to understand the coking  
thermodynamics and intrinsic chemistry of methane  
steam reforming on Ni**

by

Sai Sharath Yadavalli

In partial fulfillment of the requirements for the degree of

Doctor of Philosophy

at

University College London

Supervised by

Prof. Michail Stamatakis & Dr. Glenn Jones

Department of Chemical Engineering

UCL

I, Sai Sharath Yadavalli confirm that the work presented in this thesis is my own. Where information has been derived from other sources, I confirm that this has been indicated in the thesis.....

*I dedicate this thesis to my mother Mythili.*

## Abstract

Efficient production of hydrogen is of paramount importance to meet the global energy demands of the 21<sup>st</sup> century. Methane Steam Reforming (MSR) is a major contributor to hydrogen production at the industrial scale. In chemical industries, Ni is the preferred choice as a catalyst for the MSR reaction due to its high activity and low price. However, it is highly susceptible to coking at steam reforming conditions. Ni catalyst deactivation (due to “coking”) in MSR is a critical industrial challenge that requires imminent solutions. In this contribution, we have employed Density Functional Theory (DFT) calculations, microkinetic (MK) models, and Kinetic Monte Carlo (KMC) simulations to gain a fundamental understanding of the coking thermodynamics and intrinsic chemistry of MSR. At first, we performed a detailed screening study to identify a suitable DFT functional for the MSR-graphene system (“graphene” is a model for coke at the molecular level). The DFT predictions were systematically compared to experimental binding energies of MSR species and graphene (obtained from the literature). Subsequently, we developed a first-principles-based KMC model for the methane cracking reaction on Ni(111) to understand the coke morphology and identify conditions of coking. The thermodynamic stabilities of large-body carbon-based configurations were captured under the cluster expansion (CE) framework of KMC. Upon completion of the aforementioned study, we performed CE-based KMC simulations to elucidate the role of potassium in MSR. The MSR reaction was modelled on the clean Ni(111) and potassium-doped (with different loadings) Ni(111) surfaces. The effect of potassium on MSR kinetics was thoroughly investigated. Finally, we formulated an *ab-initio* MK model for the methane cracking and C-C coupling reactions to understand the coking mechanism on Ni(111). The MK model identifies favourable coking pathways and rate-limiting/inhibiting events. These investigations pave the way for identifying next-generation Ni-based catalysts that are resistant to poisoning.

## Impact Statement

There is tremendous interest in the scientific community to use hydrogen as an alternative clean energy source in fuel cells to effectively tackle impending threats to humanity such as climate change/global warming. MSR contributes substantially to the commercial output of hydrogen worldwide. In the United States, MSR is responsible for around 95% of the yearly hydrogen production. The Ni catalyst used in the MSR process is prone to deactivation predominantly due to coking. Chemical industries spend billions of dollars annually to replace/regenerate deactivated Ni catalysts. In this regard, the thesis attempts to shed light on the fundamental aspects of the coking problem at the molecular level. In this thesis, we have performed a systematic DFT functional screening study to quantify the computational error/uncertainty in the first-principles-based design of coke-resistant Ni catalysts. The results of the screening study act as a valuable guide for the academic/catalysis community to swiftly select the suitable DFT functional for investigating the coking mechanism in MSR reaction. Furthermore, the screening study also opens up avenues for DFT method development. In subsequent parts of the thesis, we studied the coking thermodynamics using CE-based KMC simulations. These KMC models shed light on the coke morphology and identify the conditions where Ni is susceptible to coking. These computations establish the superiority of the KMC simulation over traditional mean-field MK models that fail to capture adsorbate correlation effects accurately. The KMC model predictions can potentially aid/motivate future experimental studies and collaborations to identify design strategies that reduce the coking propensity of Ni at steam reforming conditions. Although potassium (alkali-based promoter) is used to alleviate coking at the industrial scale, its promotional effect is not well understood. In this contribution, we developed a CE-based KMC model to rationalise the role of potassium in the MSR reaction. We clearly identify the mechanisms/pathways that potassium promotes during the MSR reaction. These results are of high importance from an industrial standpoint, providing a deeper understanding on the existing solutions to coking at the commercial level. The KMC findings can be further validated by performing suitable experimental works. Furthermore, the KMC computations also provide a framework to identify novel Ni-based alloys and promoters that are highly resistant to coking. In the final parts of the thesis (chapter 6), we also delved into the coking mechanism. We developed a simple MK model to predict the favourable pathways and rate-limiting/inhibiting steps of the coking process. These preliminary investigations are important as industrialists are keen on gaining a thorough insight into the growth mechanism of carbon whiskers (coke). Overall, the outcomes of this thesis have profound implications for both academia and industry.

## List of Publications

**Yadavalli, S. S.**, Jones, G. and Stamatakis, M. (2021). "DFT Benchmark Studies on representative species and poisons of methane steam reforming on Ni(111)". *Physical Chemistry Chemical Physics*, 23(29), pp.15601-15612.

**Yadavalli, S. S.**, Benson, R., Jones, G. and Stamatakis, M. (2023). "Assessing the impact of Adlayer Description Fidelity on Theoretical Predictions of Coking on Ni(111) at Steam Reforming conditions". *The Journal of Physical Chemistry C*, 127(18), pp.8591-8606. *Featured on the cover of The Journal of Physical Chemistry C.*

## **Acknowledgements**

I express my sincere gratitude to Prof. Michail Stamatakis and Dr. Glenn Jones for their guidance and support throughout my PhD. I would like to thank the Stamatakis group researchers for all the fruitful discussions. I am grateful to the journal reviewers/editors for providing constructive feedback on my work. During my PhD, I had the opportunity to meet scholars from different disciplines who kept inspiring and pushing me to produce high-quality work. I thank these people – Kostas G. Papanikolaou, Giannis Savva, Hector Pratz, Sushila Marlow and Julia Schumann – from the bottom of my heart. I am indebted to my uncle Bhaskar Nelapatla and aunt Priya Vempati for supporting me in my academic endeavours. Finally, I would like to thank my family and friends for their constant encouragement.

## Table of Contents

<b>1. Thesis background</b>	12
1.1 Methane steam reforming	12
1.2 Ni catalyst deactivation	15
1.3 Relevance of KMC simulations	17
1.4 Research gaps and thesis objectives	18
<b>2. Methodology</b>	22
2.1 Principles of quantum mechanics	22
2.1.1 Variational principle	23
2.2 DFT method	23
2.2.1 Exchange-correlation approximations	25
2.2.2 Dispersion inclusive DFT functionals	27
2.3 Practical aspects of DFT calculations	27
2.3.1 Bloch's theorem	27
2.3.2 Brillouin zone integration	28
2.3.3 Plane-wave energy cut-off	28
2.3.4 Pseudopotentials	29
2.3.5 Transition state search algorithms	29
2.4 Transition state theory	31
2.5 Master equation	34
2.6 KMC simulations	35
2.7 MK models	39
<b>3. DFT benchmark studies on representative species and poisons of methane steam reforming on Ni(111)</b>	43
3.1 Introduction	43
3.2 Computational details	45
3.3 Results and discussion	47
3.3.1 DFT benchmarks of graphene-Ni(111)	47
3.3.2 DFT benchmarks of MSR species	53



3.4 Conclusions .....	61
<b>4. Assessing the impact of adlayer description fidelity on theoretical predictions of coking on Ni(111) at steam reforming conditions .....</b>	<b>64</b>
4.1 Introduction.....	64
4.2 Computational details .....	66
4.2.1 DFT calculations .....	66
4.2.2 Mean-field MK model .....	67
4.2.3 KMC simulations .....	67
4.2.4 Establishment of equivalence between MK and KMC models .....	71
4.2.5 Estimation of pre-exponentials and activation energy parametrization .....	71
4.3 Results and discussion .....	72
4.3.1 DFT results .....	73
4.3.2 Methane cracking reaction – MK/KMC predictions .....	77
4.3.3 Changes to the KMC adlayer with varying levels of interactions.....	82
4.3.4 Effect of Temperature on the KMC adlayer.....	88
4.4 Conclusions.....	88
<b>5. Elucidating the role of potassium in methane steam reforming using first-principles-based Kinetic Monte Carlo Simulations .....</b>	<b>92</b>
5.1 Introduction.....	92
5.2 Computational details .....	93
5.2.1 DFT calculations .....	93
5.2.2 KMC simulations .....	95
5.2.3 Estimation of turnover rates and reaction flux in KMC .....	95
5.3 Results and discussions .....	96
5.3.1 DFT results .....	96
5.3.2 KMC predictions at different operating conditions.....	100
5.3.3 KMC process statistics .....	103
5.3.4 KMC flux analysis.....	108
5.3.5 KMC lattice snapshots of K-Ni(111) .....	110
5.4 Conclusions.....	112

<b>6. DFT and microkinetic studies of C-C coupling reactions on the Ni(111) surface ...</b>	<b>116</b>
6.1 Introduction.....	116
6.2 Computational details .....	117
6.2.1 DFT calculations .....	117
6.2.2 MK model.....	118
6.3 Results and discussions .....	118
6.3.1 DFT results .....	119
6.3.2 MK studies .....	122
6.4 Conclusions .....	126
<b>7. Concluding remarks and future work .....</b>	<b>129</b>
7.1 Contributions of this Thesis.....	129
7.2 Opportunities for future research .....	132
<b>Appendix I .....</b>	<b>134</b>
<b>Appendix II .....</b>	<b>147</b>
<b>Appendix III .....</b>	<b>161</b>
<b>Appendix 1V .....</b>	<b>188</b>
<b>References .....</b>	<b>196</b>

# Chapter 1

## 1. Thesis background

In this thesis, we have primarily focussed on understanding the coking thermodynamics and intrinsic kinetics of Methane Steam Reforming (MSR) on Ni(111) using first-principles-based Kinetic Monte Carlo (KMC) simulations. In this chapter, we provide a brief overview about MSR and the coking problem of Ni catalysts. Furthermore, we identify the research gaps and clearly state the objectives of our study.

### 1.1 Methane steam reforming

Since the inception of industrial revolution in the late 18<sup>th</sup> century, hydrogen has been an indispensable part of several chemical processes. In the petrochemical industry, hydrogen is widely used in a variety of operations such as removal of sulphur/nitrogen containing compounds from crude oil, hydrogenation of unsaturated hydrocarbons and methanol production. Hydrogen plays a critical role in the manufacture of ammonia (an important raw material for producing fertilizers). In recent years, several investigations have been conducted to use hydrogen as an alternative fuel in automobiles.<sup>1,2</sup> With the burgeoning growth of technological prowess in the 21<sup>st</sup> century, there is tremendous interest to tap into the potential of hydrogen energy.<sup>3</sup> The scale of hydrogen production in chemical industries is important for meeting the energy demands of the future. Generally, hydrogen is produced in the chemical industries using processes such as MSR, partial oxidation of methane and dry reforming of methane.<sup>4,5</sup> Among the aforementioned processes, MSR is an important contributor to the production of hydrogen. In the United States, around 95% of hydrogen is produced from the MSR process.<sup>6</sup> Currently, MSR is reported to be the most efficient and economically cheap industrial method available for hydrogen production.<sup>7</sup>

MSR involves the formation of syngas (H<sub>2</sub> and CO) from methane and steam. It is a highly endothermic process with a standard reaction enthalpy of 206 kJ/mol.<sup>8,9</sup> The temperature and pressure of MSR range from 600-900 °C and 10-30 bar, respectively.<sup>10</sup> The steam-to-methane ratio is maintained in the range of 2-4.<sup>8</sup> The main reforming reaction is stated below. The water-gas shift reaction is an important side reaction at steam reforming conditions.<sup>6,11</sup>



The MSR process consists of a primary reformer, which has long tubes (typically 10 m in length) loaded with catalyst pellets. Several studies have shown that metals such as Pt, Pd, Ir, Ni, Ru and Rh are suitable catalysts for the MSR reaction. Among these metals, Ni is commonly the preferred choice as a catalyst for MSR due to its cheap price and high activity. As with any reaction taking place on the surface of a heterogeneous catalyst, MSR comprises the following steps: Firstly, it involves the diffusion of species between the gas phase and the

catalyst surface. Secondly, there is an internal diffusion of species within the catalyst. Finally, a number of intermediate reactions occur in series/parallel to form products ( $H_2$ , CO and  $CO_2$ ). The detailed reaction pathways of MSR are very well established in the literature.<sup>9,10,12</sup> As shown in Figure 1, the MSR reaction network can be primarily classified into four parts: 1) Methane cracking – it involves the dissociation of  $CH_4(g)$  on Ni(111) to form  $CH_x$  (x ranging from 1-3) and C species, 2) Water adsorption/dissociation – this includes adsorption and dissociation of  $H_2O(g)$  to form OH/O species, 3) Reforming pathways – the CH/C species react with OH/O to form carbon monoxide (via several pathways) and 4) syngas formation – the hydrogen species associatively desorbs to form  $H_2(g)$  and CO desorbs from the catalyst surface to  $CO(g)$  (which are end products of MSR).<sup>6</sup> In Figure 1, the important reforming pathways have only been depicted. There are several other possible pathways to form CO (via  $CH_2O$ ,  $CH_3O$  intermediates). However, Density Functional Theory (DFT) calculations and microkinetic (MK) studies have shown that these auxiliary pathways have little to no contribution to the  $CO(g)$  production rate.<sup>6,10</sup> Therefore, in this work, we have solely focussed on the MSR pathways shown in Figure 1.

Methane cracking	
$CH_4(g) + 2^* \rightleftharpoons CH_3^* + H^*$	
$CH_3^* + ^* \rightleftharpoons CH_2^* + H^*$	
$CH_2^* + ^* \rightleftharpoons CH^* + H^*$	
$CH^* + ^* \rightleftharpoons C^* + H^*$	
Water adsorption/dissociation	
$H_2O(g) + ^* \rightleftharpoons H_2O^*$	
$H_2O^* + ^* \rightleftharpoons OH^* + H^*$	
$OH^* + ^* \rightleftharpoons O^* + H^*$	
Final products	
$CO^* \rightleftharpoons CO(g) + ^*$	
$2H^* \rightleftharpoons H_2(g) + 2^*$	

Reforming pathways	
CHOH pathway	
$CH^* + OH^* \rightleftharpoons CHOH^* + ^*$	
$CHOH^* \rightleftharpoons CHO^* + H^*$	
$CHOH^* \rightleftharpoons COH^* + H^*$	
CHO pathway	
$CH^* + O^* \rightleftharpoons CHO^*$	
COH pathway	
$C^* + OH^* \rightleftharpoons COH^* + ^*$	
CO formation	
$C^* + O^* \rightleftharpoons CO^* + ^*$	
$CHO^* + ^* \rightleftharpoons CO^* + H^*$	
$COH^* + ^* \rightleftharpoons CO^* + H^*$	

Figure 1: The important elementary events of MSR reaction network.

In the past few decades, several experimental studies have been conducted to gain a detailed understanding of the MSR kinetics. Some of the earliest experimental studies developed macroscopic/non-elementary rate equations to predict MSR rates. These studies provide little to no detail about the intermediate steps involved in the MSR reaction. Thus motivated, Xu and Froment<sup>13</sup> conducted extensive laboratory-scale studies to delineate the kinetics of MSR.

The authors derived the reaction mechanism for MSR on Ni/MgAl<sub>2</sub>O<sub>4</sub> catalyst using thermodynamic analysis and model discrimination/parameter estimation techniques. Initially, extensive sets of reaction pathways were considered. Most of these reaction sets were systematically eliminated by comparing to the experimental MSR reaction energy. The retained kinetic models were fitted to experimental rates using parameter estimation. The final kinetic model was thermodynamically consistent, and its kinetic parameters were statistically significant. Another important experimental work (with regards to the MSR reaction) was carried out by Wei and Iglesia.<sup>14</sup> The authors found the reaction rates of MSR had a linear dependence on the partial pressure of methane. Furthermore, a rigorous kinetic/isotopic analysis was also performed which confirmed that the methane activation step is kinetically relevant and has a significant impact on the MSR rates. On the other hand, MSR rates were reported to be independent of the partial pressure of water. Aparicio<sup>15</sup> developed a MK model to understand the MSR kinetics. The kinetic parameters of the MK model were obtained by combining experimental adsorption/desorption energies and isotopic analysis data with estimates of pre-exponential factors/activation energies. Similarly, Chen et al.<sup>16</sup> also developed a MK model for dry reforming of methane on the Ni catalyst. An important shortcoming of this approach is that the experimental determination of kinetic parameters/constants of MSR elementary events/steps is an extremely challenging task (mainly due to the short lifetimes of several intermediates and extreme operating conditions of MSR).<sup>6</sup>

With significant advancements made in computational power, DFT has been widely employed to estimate the activation barriers of MSR elementary events. Bengaard et al.<sup>17</sup> constructed the potential energy surface (PES) diagram for the MSR reaction on Ni(111) and Ni(211) facets using DFT. The authors found the steps to be more active than the terrace sites. Furthermore, they reported that atomic carbon was more stable on the Ni(211) facet compared to Ni(111). Although useful information is obtained about the reaction chemistry of MSR from the aforementioned DFT study, the authors have not accounted for thermal/entropic effects (which are important as MSR reaction occurs at high temperature and pressure). Jones et al.<sup>18</sup> performed DFT calculations to develop the free energy profiles of MSR reaction on several transition metals. The free energies were computed on Ni(111) by using the concepts/formulae of statistical thermodynamics. The authors report that the methane activation and CO formation steps can be rate-limiting at MSR conditions. At lower temperatures (around 600 - 800 K), it was found that the free energy barrier of CO formation is greater than CH<sub>4</sub> activation, whereas at higher temperatures (900 - 1100 K), the free energy barrier of methane activation was greater than CO formation. The authors conclude that the rate-controlling step of MSR might have a dependency on the operating conditions. In recent years, several studies have

developed first-principles-based MK models to study the detailed kinetics of MSR on the Ni catalyst. Blaylock et al.<sup>6</sup> developed a mean-field MK model of MSR on Ni(111) at industrial conditions. The study provides useful mechanistic information about the MSR reaction. The reforming pathway involving the CHO intermediate was found to be the most dominant at steam reforming conditions. The CHOH pathway was reported to be the second most dominant pathway on the Ni(111) facet. Sensitivity analysis revealed that CH<sub>4</sub> adsorption, CHO pathway and CHOH pathway have a significant influence on the net rate of MSR (refer to Figure 1 for the reaction steps of the aforementioned reforming pathways). In a subsequent study, Blaylock et al.<sup>10</sup> formulated a MK model for the MSR reaction on a multi-faceted Ni catalyst. The study shows that the MSR reaction is more active on the steps compared to open/terrace facets. The authors report that the COH and CHO pathways are dominant at low temperatures, whereas at high temperatures CO pathway (via direct oxidation of C and O) had a significant contribution to the overall rate compared to other pathways. The MSR overall rate was found to be sensitive to CH<sub>4</sub> dissociation step and CH/C oxidation pathways. These studies are important contributions on the MSR kinetics (available in the open literature). Furthermore, many MK studies have also been carried out to investigate the dry reforming of methane on Ni surfaces.<sup>16,19,20</sup> Nevertheless, MK models use mean-field approximations to account for surface coverage effects between MSR species. It is very well established that MF approximations fail to capture lateral interactions/correlation effects in a systematic way.<sup>21-24</sup> These effects can significantly influence the chemistry/kinetics of MSR reaction.

## 1.2 Ni catalyst deactivation

The deactivation of Ni catalyst is a major impediment to the productivity of the MSR process. The presence of hydrocarbons and extreme operating conditions (high temperatures and pressures) of MSR make Ni susceptible to deactivation. During the steam reforming reaction, the Ni catalyst undergoes deactivation via the following processes: carbon poisoning, sulphur poisoning and Ni particle sintering.<sup>25</sup> Carbon poisoning mainly occurs due to the deposition of carbon-based intermediates on the Ni surface. These carbonaceous species can potentially block the active sites of the catalyst and increase the pressure drop of the reformer. The presence of sulphur containing compounds in the MSR input feed (in ppb level) could lead to sulphur deposition on the Ni surface. Sulphur is a common poison (similar to carbon-based intermediates). Sintering is a phenomenon in which the particle size of Ni increases due to agglomeration. This reduces the active surface area of the Ni catalyst and thereby reducing its activity. Concerted efforts are necessary to address the aforementioned challenges of the MSR reaction.

Among the catalyst deactivation processes, carbon poisoning has been reported to severely affect the performance of MSR. The carbon poisoning process is commonly referred to as

“coking”.<sup>26-28</sup> The coking process mainly involves deposition of carbonaceous species, which have been found to exist in the form of pyrolytic carbon, encapsulating carbon (gums) and carbon whiskers. The pyrolytic carbon is formed on the tubular walls of the reformer upon exposure of heavier hydrocarbons to high temperatures. Encapsulating carbon involves the deposition of  $\text{CH}_x$ -type film on the Ni catalyst surface – this mainly occurs when the feed contains high amounts of aromatic carbon. Whisker carbon (also known as “Filamentous carbon”) is the most destructive form of coke. The carbon formed in MSR binds to the step sites of the Ni catalyst initially and then migrates to the support side and agglomerates in the form of graphitic layers (carbon whiskers). Whisker carbon formation leads to significant reduction of Ni catalyst activity, increase in pressure drop and reactor blockage.<sup>29-31</sup>

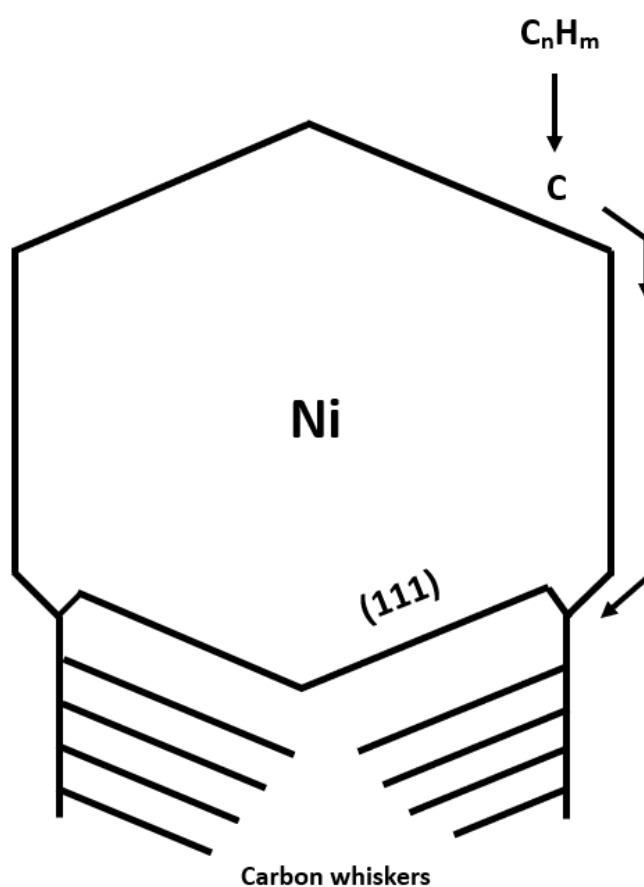


Figure 2: Pictorial representation of whisker carbon growth process on the Ni particle. Adapted from the work of Sehested (permissions obtained from the publisher).<sup>25</sup>

In the last few decades, several experimental studies have been carried out to gain a comprehensive understanding of the whisker carbon formation process.<sup>32-35</sup> It is generally accepted that the methane cracking ( $\text{CH}_4(\text{g}) \rightarrow \text{C} + 2\text{H}_2(\text{g})$ ) and Boudouard ( $2\text{CO} \rightarrow \text{C} + \text{CO}_2(\text{g})$ ) reactions are primarily responsible for the growth of whisker carbon on the Ni catalyst surface at MSR conditions.<sup>30,36,37</sup> Snoeck et al.<sup>30</sup> performed extensive experiments to derive



a kinetic model that accounts for the growth of carbon whiskers in the methane cracking reaction. Apart from the surface reactions of methane cracking, the authors included three additional elementary steps to describe the whisker carbon growth of methane cracking: 1) the dissolution/segregation of carbon from the Ni surface (steps) into Ni bulk, 2) the diffusion of carbon through Ni bulk to the support side, 3) the precipitation of carbon in the form of whiskers on the support side (refer to Figure 2). It was hypothesised that at the coking threshold, the rate of whisker carbon formation is determined by the concentration difference between carbon gas and carbon bulk, while the diffusion of carbon from the bulk phase to the support side is fast. The authors also assumed that there is a uniform concentration of carbon at the Ni bulk and support side. Under these assumptions, a kinetic model was derived for the methane cracking reaction. The rate parameters of the model were determined by fitting to experimental data using parameter estimation techniques. Other studies have also used a similar approach to determine the coking propensity of Ni in the methane cracking reaction at steam reforming conditions.<sup>38-40</sup> Although these studies provide useful insight into the whisker carbon formation on Ni, the coking process is far more complex. Despite these efforts, the morphology of coke (make up of “Whisker Carbon”) and its detailed kinetics on Ni remain elusive. First-principles based kinetic models of methane cracking can shed light on thermodynamic stabilities of carbon whiskers ( $C_xH_y$  species) at steam reforming conditions. These models can provide clues about the conditions at which Ni is most susceptible to coking and what type/shape of carbon-based clusters encapsulate the Ni surface at poisoning conditions. Furthermore, the basic build-up mechanism of carbon (via C-C coupling events), which leads to carbon whiskers on the Ni catalyst, can be potentially derived. These investigations are important for the design of poison resistant Ni based catalysts.

### 1.3 Relevance of KMC simulations

Traditionally, mean-field-based MK models are employed to study the kinetics of industrial reactions such as MSR, Water gas shift (WGS) and Fischer-Tropsch synthesis.<sup>6,41,42</sup> Although mean-field MK models provide important information about the dominant pathways and sensitive elementary steps of a reaction network, the lateral interactions between adsorbates are not taken into account in a systematic way. As discussed previously, these effects can substantially alter the kinetics of reactions. In recent years, KMC simulations have gained significant prominence, as a viable alternative to mean-field MK models, for studying catalytic reactions under high species coverage regimes.<sup>43</sup> In the KMC model, the lateral interactions are captured by using cluster expansion (CE) Hamiltonians<sup>44-46</sup> (detailed information about CE methodology is provided in the subsequent section of the thesis). The KMC simulations have been employed to compute turnover rates and rate orders of ethylene hydrogenation on Pd(100) by including detailed adlayer energetics.<sup>47</sup> Piccinin and Stamatakis<sup>48</sup> conducted CE-

based KMC simulations for the CO oxidation reaction on Pd(111). The authors were able to explain the apparent change in reaction order of CO oxidation at different reaction conditions (observed experimentally) by systematically accounting for lateral interactions between O and CO adspecies. Liu et al.<sup>49</sup> used first-principles-based KMC simulations to model NO-CO reactions on Rh(100) and Rh(111) by including the lateral interactions. They computed turnover rates and identified sensitive elementary events of the reaction network. Chen et al.<sup>50</sup> performed KMC simulations for the formic decomposition reaction on Au<sub>18</sub> nanoclusters. By including the adsorbate-adsorbate interactions in the KMC model, the study rationalises the experimentally observed highly selective nature of Au in producing HD from singly deuterated FA isotopomers. Wu et al.<sup>44</sup> carried out Grand Canonical Monte Carlo (GCMC) simulations of NO oxidation on Pt(111). The adlayer energetics (comprising of oxygen species) were accurately captured by CE Hamiltonians. The parameters of the CE model were trained on an extensive set of DFT configurations of oxygen at varying coverages. The GCMC simulations predicted apparent activation barriers/rate orders, which were in excellent agreement with experimental results. Furthermore, KMC models have been used to understand the kinetics of CO oxidation on RuO<sub>2</sub>(111) and WGS reaction on Pt metal surfaces.<sup>51,52</sup> These studies highlight the significance of using KMC as an important computational tool to capture adsorbate lateral interactions (in great detail) and intrinsic kinetics of catalytic reactions.

#### 1.4 Research gaps and thesis objectives

The commercial catalyst employed for the MSR reaction is Ni/ $\alpha$ -Al<sub>2</sub>O<sub>3</sub>.<sup>53</sup> Although it is important to capture metal support interactions to gain a thorough understanding of the MSR kinetics and coke formation, in this study, we have solely focussed on developing kinetic models for the Ni(111) facet.<sup>54</sup> Wei and Iglesia<sup>14</sup> conducted experiments for the MSR reaction using Ni catalyst particles of approximately 7 nm in size. For an average Ni particle size of 7 nm, Ni(111) is considered to be active and most abundant/stable facet (based on the truncated octahedron model).<sup>10</sup> A recent study has shown that the methane dissociation (rate-controlling event of MSR) predominantly occurs on the Ni(111) surface at high carbon coverages (as the step sites are poisoned).<sup>6,55</sup> As discussed in section 1.2, it is believed that the Ni nanoparticle is completely deactivated (detaches from the support) by the encapsulation of the Ni terrace sites by coke.<sup>25</sup> Therefore, as a first approximation, we have modelled the MSR/coking chemistries on Ni(111) to gain fundamental insights.

Even though extensive DFT studies have been carried out for the MSR reaction (in recent years), there is no systematic assessment of the error in the DFT predictions. It is well established in the literature that the choice of exchange-correlation functional is a major challenge in Kohn-Sham DFT. The exact form of exchange-correlation functional is unknown,<sup>56,57</sup> and several approximations have been developed for the exchange-correlation

energy. Based on the choice of the exchange-correlation functional, the DFT prediction of adsorbate binding energies and activation barriers can vary substantially.<sup>56</sup> There is a need for systematic benchmarking of DFT functionals with available experimental data - this mainly includes binding energies of MSR species and graphene (model for coke) on Ni(111). In this thesis (chapter 3), we have rigorously benchmarked several important DFT functionals for the MSR-graphene system. These computations are important to ensure that an appropriate choice is made for the DFT functional, and thereby, reduce the error in DFT-based design of poison-resistant Ni catalysts.

As discussed earlier (in section 1.2), the formation of carbon whiskers (coking) on Ni is a major industrial challenge for the MSR reaction. In the past few years, there has been tremendous interest in the catalysis community to address the coking problem of Ni.<sup>31,37,58</sup> Nevertheless, there are little to no literature studies that provide a detailed understanding of the coke morphology at MSR conditions. Furthermore, there is limited theoretical understanding on the conditions at which Ni is susceptible to coking. In Chapter 4 of the thesis, we developed a CE-based KMC model for the methane cracking reaction on Ni(111). The KMC model accounts for the kinetics of C-H activation steps, while coke formation is treated at the level of thermodynamics. The CE parameters have been extensively trained on 173 DFT configurations of  $C_xH_y$  species (which exist in the form of rings, branches and chains) on Ni(111). The KMC model sheds light on the following at MSR conditions: 1) The influence of C-CH cluster interactions on the coke morphology, 2) Type/shape of  $C_xH_y$  cluster that is thermodynamically stable on the Ni(111) surface and 3) Conditions at which Ni is susceptible to coking. These simulations can potentially aid experimentalists in designing the next-generation Ni-based catalysts that are more resistant to coking.

In recent years, several solutions have been proposed to tackle the coking issue of the MSR reaction. A few MK/experimental studies have reported that alloying the Ni catalyst with noble metals such as Pt, Au and Ag can improve its stability.<sup>4,59,60</sup> However, these Ni-based alloys are not very effective in reducing coke formation at the commercial scale. In chemical industries, doping Ni with potassium (alkali-based promoter) is a common practice to alleviate coke formation and improve MSR productivity.<sup>61</sup> Despite numerous computational/experimental studies, a detailed understanding on the role of potassium in MSR reaction remains elusive. It is paramount to develop computational models that can clearly demonstrate the promotional effect of potassium on MSR kinetics. Thus motivated, we have performed KMC simulations for the MSR reaction on the pure and potassium-doped Ni(111) surfaces (refer to Chapter 5). The MSR coverages and turnover rates were estimated for different loadings of potassium on Ni(111). The KMC process statistics was thoroughly examined to identify the MSR elementary steps/events promoted by potassium. The flux

analysis was carried out to determine the dominant reforming pathways of MSR in the presence of potassium. These investigations provide a comprehensive insight into the potassium effect at steam reforming conditions.

Although several attempts have been made in the past, our understanding on the kinetics of coking is limited.<sup>25,62</sup> In order to design coke-resistant Ni catalysts, it is critical to gain a thorough insight into the coking mechanism at MSR conditions. Therefore, in chapter 6 of this thesis, we have developed a first-principles-based MK model of methane cracking and C-C coupling reactions to delineate the coking kinetics on Ni(111). We report the coverage profiles of dominant species as a function of temperature. The dominant pathway of coke formation is predicted. Furthermore, we also perform sensitivity analysis to identify the rate-inhibiting/limiting events. These preliminary computations lay the foundation for more elaborate models on the whisker carbon growth at steam reforming conditions.

# Chapter 2

## 2. Methodology

In this chapter, we have provided a broad outline on the underpinning concepts of DFT. The practical considerations made in DFT calculations of periodic systems have been explained. We discuss the basic idea/assumptions of transition state theory in the context of kinetic modelling. We also provide a thorough discussion on the working principles of KMC and MK models. Furthermore, the key advantages and limitations of MK and KMC models are highlighted.

### 2.1 Principles of quantum mechanics

Quantum theory has played a pivotal role in our understanding of the electronic structure of matter. The current theoretical methods use the fundamental equations of quantum mechanics to predict the properties of materials. Any material is primarily a collection of electrons and nuclei. The energy of an interacting system of electrons and nuclei can be described using the time-independent, non-relativistic Schrödinger equation:

$$\hat{H}\Psi = E\Psi \quad \text{eq. 3}$$

In eq. 3,  $\hat{H}$  is the Hamiltonian operator,  $\Psi$  is the wave function and  $E$  is the total energy of the system.<sup>63</sup> The wave function  $\Psi$  does not have any physical meaning. However, the squared modulus of the wavefunction ( $|\Psi^2|$ ) gives the probability density of finding a particle at any point in space.<sup>64</sup> The Hamiltonian operator  $\hat{H}$  for a system of  $n$  electrons and  $T$  nuclei is defined below (in terms of atomic units).

$$\hat{H} = \sum_{i=1}^n \frac{-\nabla_i^2}{2} + \sum_{k=1}^T \sum_{i=1}^n \frac{Z_k}{|r_i - R_k|} + \sum_{i=1}^n \sum_{j>i}^n \frac{1}{|r_i - r_j|} - \sum_{k=1}^T \frac{\nabla_k^2}{2M_k} + \sum_{k=1}^T \sum_{l>k}^T \frac{Z_k Z_l}{|R_k - R_l|} \quad \text{eq. 4}$$

The symbols used in the above equation have the following meaning:  $Z$  is the atomic number, the position of the electron is represented by vector  $r$ ,  $M$  is the ratio of mass of nucleus to mass of electron,  $T$  indicates the number of nuclei and  $n$  represent the number of electrons and  $R$  is a vector that gives the position of the nucleus in the system.

An important principle of quantum mechanics is the Born-Oppenheimer approximation, according to which, the value of nuclei kinetic energy is much lower in comparison to the kinetic energy of electrons. This assumption allows us to propose a Hamiltonian which accounts for the motion of electrons for a fixed position of nuclei.<sup>63</sup> The simplified expression of the Hamiltonian is as follows:<sup>65</sup>

$$\hat{H} = \sum_{i=1}^n \frac{-\nabla_i^2}{2} + \sum_{k=1}^T \sum_{i=1}^n \frac{Z_k}{|r_i - R_k|} + \sum_{i=1}^n \sum_{j>i}^n \frac{1}{|r_i - r_j|} + \sum_{k=1}^T \sum_{l>k}^T \frac{Z_k Z_l}{|R_k - R_l|} \quad \text{eq. 5}$$

The Hamiltonian for an n-electron system (where  $n > 1$ ) has several electron pair interactions, and it is mathematically intractable to find an analytical solution for the Schrödinger equation. In the last 50 years, several mathematical approaches and algorithms have been developed to provide a reasonable approximate solution for the Schrödinger equation.<sup>63</sup>

### 2.1.1 Variational principle

To date, most of the algorithms use the variational principle to solve the Schrödinger equation. The variational principle of quantum mechanics makes an important generalisation about the ground state energy of the wave function. It states that the expectation value of the Hamiltonian obtained by using any normalised wave function is always greater than or equal to the actual ground state energy of the system.<sup>66</sup> For a system of  $n$  electrons, the solution of the Schrödinger equation yields a set of eigenfunctions  $|\Psi_i\rangle$  with corresponding eigenvalues  $E_i$  (refer to eq. 6):

$$\hat{H}|\Psi_i\rangle = E_i|\Psi_i\rangle, \text{ where } i = 0, 1, 2 \dots n \quad \text{eq. 6}$$

$E_0$  is the ground state energy of the system. According to the variational principle, if we choose any random wave function  $|\varphi\rangle$  which is normalized (eq. 7), then the value of the total energy obtained using the wave function  $|\varphi\rangle$  will always be greater than or equal to the ground state energy  $E_0$  (as shown in eq. 8).

$$\langle \varphi | \varphi \rangle = \int_{-\infty}^{\infty} \varphi^* \varphi \, dv = 1 \quad \text{eq. 7}$$

$$\langle \varphi | \hat{H} | \varphi \rangle = \int_{-\infty}^{\infty} \varphi^* \hat{H} \varphi \, dv \geq E_0 \quad \text{eq. 8}$$

The variational principle allows us to define an initial trial wave function (the function has a dependency on a set number of parameters) for estimating the ground state energy. The parameters of the trial wave function can be altered until a minimum is found for the total energy value. This minimum is referred to as the variational prediction of the ground state energy of the system.<sup>67</sup>

### 2.2 DFT method

The DFT methodology is widely accepted to be reasonably accurate and computationally efficient theoretical method available for modelling the electronic structure of materials. There are two fundamental theorems of DFT, which were developed by Hohenberg and Kohn.<sup>65</sup> The first theorem of DFT states that the total energy of an n-electron interacting system can be expressed as a distinct functional of the ground-state electron density. The ground-state electron density contains all the information necessary to estimate the properties of the

system.<sup>68</sup> If the Schrödinger equation can be expressed in terms of electron density, then the N-electron problem is reduced from 3N dimensions to three dimensions. However, the first DFT theorem does not provide any information about the properties of the functional. The second theorem of DFT states the following: the electron density that minimises the value of the energy functional is the actual ground-state electron density of the system. This principle tells us that the ground-state electron density can be obtained by using the variational approach.<sup>66,68</sup>

According to the aforementioned theorems of DFT, the total energy of an n-electron interacting system can be formulated as a functional of the electron density  $\eta(r)$  (eq. 9).

$$E[\eta] = R[\eta] + E_{ne}[\eta] + E_{ee}[\eta] \quad \text{eq. 9}$$

In the above equation,  $R[\eta]$  is the total kinetic energy,  $E_{ne}[\eta]$  indicates the nucleus-electron interaction energy and  $E_{ee}[\eta]$  is the electron-electron interaction energy.<sup>66,68</sup>

An important caveat in this approach is that the functional form of the energy is not known. To address this problem, Kohn-Sham replaced the n-electron system with a hypothetical model of non-interacting electrons, which has the same density  $\eta(r)$ . The non-interacting system comprises of single electron spin orbitals  $\varphi_i^\sigma(r)$  (where  $r$  is the space coordinate and  $\sigma$  represents the spin). The density of the non-interacting system is evaluated as a sum of squares of the probability amplitude of  $\varphi_i^\sigma(r)$  (eq. 10). Similarly, the kinetic energy of the non-interacting system is defined using the single electron spin orbitals (eq. 11). The Hartree energy ( $E_{Hartree}[\eta]$ ) accounts for the electron-electron repulsions in terms of electron density. It also includes electron self-interaction terms (eq. 12):

$$\eta(r) = \sum_{\sigma} \sum_i^{n^{\sigma}} |\varphi_i^{\sigma}(r)|^2 \quad \text{eq. 10}$$

$$R_{KS}[\eta] = \sum_{\sigma} \sum_i^{n^{\sigma}} \int \varphi_i^{\sigma}(r)^* \frac{-\nabla_i^2}{2} \varphi_i^{\sigma}(r) d^3r \quad \text{eq. 11}$$

$$E_{Hartree}[\eta] = \frac{1}{2} \int d^3r d^3r' \frac{\eta(r) \eta(r')}{|r - r'|} \quad \text{eq. 12}$$

In the Kohn-Sham model, the total energy of the system is given by the following equation:

$$E[\eta] = R_{KS}[\eta] + E_{ne}[\eta] + E_{Hartree}[\eta] + E_{xc}[\eta] \quad \text{eq. 13}$$

$$E_{xc}[\eta] = R[\eta] + E_{ee}[\eta] - (R_{KS}[\eta] + E_{Hartree}[\eta]) \quad \text{eq. 14}$$

The last term of eq. 13 ( $E_{xc}[\eta]$ ) is referred to as the exchange-correlation energy. It accounts for the difference in kinetic energy and electron-electron repulsion energy, between the original system and the Kohn-Sham model, as shown in eq. 14.<sup>68</sup> Solving the Kohn Sham equations



will give us the same energy as the original system. The variational method is used to minimise the total energy of the Kohn-Sham system; the single electron wave functions are varied subject to the constraint that they remain orthonormal (eq. 15).<sup>66</sup>

$$\langle \varphi_i^\sigma | \varphi_j^{\sigma'} \rangle = \delta_{i,j} \delta_{\sigma,\sigma'} \quad \text{eq. 15}$$

The minimisation of the Kohn-Sham total energy yields a set of equations (as represented in eq. 16), which are solved using the self-consistent field (SCF) approach.

$$(H_{KS}^\sigma - \varepsilon_i^\sigma) \varphi_i^\sigma(r) = 0 \quad \text{eq. 16}$$

$$H_{KS}^\sigma = -\frac{\nabla^2}{2} + V_{KS}^\sigma(r) \quad \text{eq. 17}$$

$$V_{KS}^\sigma(r) = V_{ext}(r) + V_{Hartree}(r) + V_{xc}^\sigma(r) \quad \text{eq. 18}$$

In eq. 17, the term  $V_{KS}^\sigma(r)$  is the Kohn-Sham potential. It comprises the nuclei-electron interaction  $V_{ext}(r)$ , the Hartree interactions  $V_{Hartree}(r)$  and the exchange-correlation term  $V_{xc}^\sigma(r)$ <sup>68</sup> (as shown in eq. 18). Figure 3 depicts the fundamental working principle of solving the Kohn-Sham equations in the form of a flow sheet.

### 2.2.1 Exchange-correlation approximations

As discussed previously, the Kohn-Sham model introduces an exchange-correlation term, which includes the corrections for the kinetic energy and the self-interaction error generated due to the Hartree energy. The exact functional relationship between electron density and exchange-correlation energy is unknown. In the past few decades, several approximations have been suggested for the exchange-correlation term. One of the earliest proposals includes the Local Spin Density Approximation (LSDA). The exchange and correlation interactions are considered as short-range effects in LSDA calculations. At any given point  $r$ , the energy density of exchange-correlation is calculated by assuming a homogeneous electron gas system with the same density, as shown in eq. 19:

$$E_{xc}^{LSDA}[\eta^\uparrow, \eta^\downarrow] = \int \eta(r) \varepsilon_{xc}^{hom}(\eta^\uparrow(r), \eta^\downarrow(r)) d^3r \quad \text{eq. 19}$$

The LSDA calculations were found to over predict the binding energy of most molecules. To improve the performance of LSDA, a few studies have incorporated the gradient of the density as a functional of exchange-correlation energy; this approach is known as the Generalized Gradient Approximation (GGA). The generic mathematical representation of GGA is given below:<sup>68</sup>

$$E_{xc}^{GGA}[\eta^\uparrow, \eta^\downarrow] = \int \eta(r) \varepsilon_x^{hom}(\eta) F_{xc}(\eta^\uparrow, \eta^\downarrow, |\nabla \eta^\uparrow|, |\nabla \eta^\downarrow|) d^3r \quad \text{eq. 20}$$

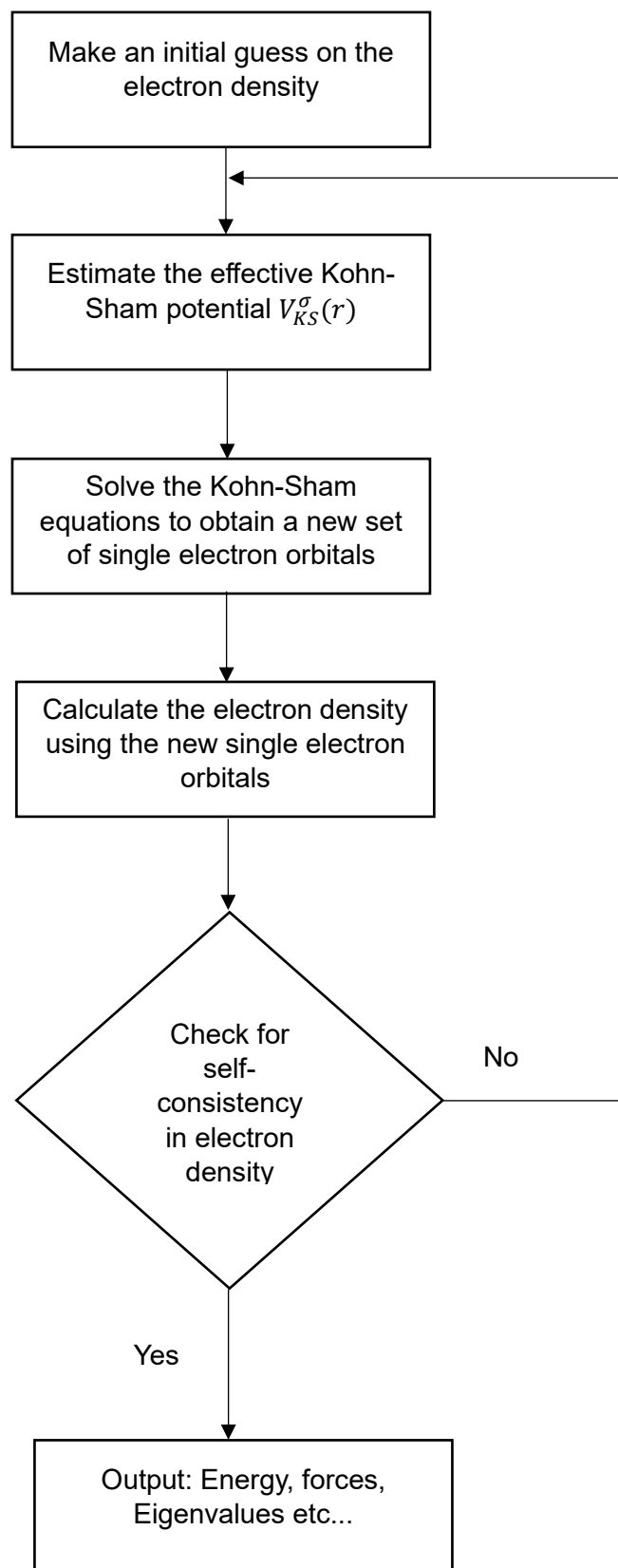


Figure 3: A schematic representation of the solution of Kohn-Sham equation using the SCF procedure.<sup>68</sup>

In eq. 20,  $\varepsilon_x^{hom}(\eta)$  is the exchange energy of the homogenous electron gas and  $F_{xc}$  is a dimensionless enhancement factor. The value of  $F_{xc}$  depends upon the gradient of the density. GGA functionals are widely used by computational chemists to perform DFT calculations. Some important examples of GGA functionals include Becke (B88), Perdew and Wang (PW91), and Perdew, Burke, and Enzerhof (PBE).<sup>68</sup>

### 2.2.2 Dispersion inclusive DFT functionals

Dispersion effects (colloquially called as van der Waals forces) are long-range attractive interactions, which typically originate due to dipole-dipole forces present between electrons separated at a finite distance. The van der Waals forces play an important role in determining the binding strength of several materials such as biomolecules, adsorbates and graphene-metal interfaces. The exchange-correlation approximations described in the previous sections - LDA and GGA functionals - do not capture the van der Waals forces.<sup>69</sup> Other higher-order approximations such as meta-GGA and hybrid functionals also fail to incorporate van der Waals forces.<sup>70</sup> The description of van der Waals interactions is a major challenge of modern DFT. In recent years, several types of functionals have been developed to explicitly account for the van der Waals forces between atoms/molecules. DFT-D and van der Waals density functionals (vdW-DF) are two classes of functionals that have been reported to be successful in describing van der Waals forces for many cases.<sup>69</sup>

### 2.3 Practical aspects of DFT calculations

At the atomistic level, most metallic systems are known to exist in the form of periodic crystals. The crystal lattice structure consists of a unit cell, which is translated across space. The translation vector in three dimensions ( $Q(n)$ ) is represented using a set of primitive lattice vectors  $a_1$ ,  $a_2$  and  $a_3$ .

$$Q(n) = n_1 a_1 + n_2 a_2 + n_3 a_3 \quad (n_1, n_2 \text{ and } n_3 \text{ are integers}) \quad \text{eq. 21}$$

The symmetry and periodic properties of crystals, such as Ni, are exploited to reduce the computational time of DFT calculations.<sup>71</sup> Some of the important working principles of periodic DFT calculations are discussed in the following subsections.

#### 2.3.1 Bloch's theorem

Any periodic function  $f(r)$  can be represented using a Fourier series in  $k$  space ( $r$  and  $k$  are vectors in real and reciprocal space, respectively). In a crystal, the relationship between the vectors  $k$  and  $r$  can be deduced by using Born-Von Karmen periodic boundary conditions.<sup>71</sup> For a given real space lattice vectors  $a_1$ ,  $a_2$  and  $a_3$ , the  $k$  vectors are defined by reciprocal components  $b_1$ ,  $b_2$  and  $b_3$ , which satisfy the condition stated below:

$$a_i \cdot b_i = 2\pi \quad (\text{where } i \text{ can take values } 1, 2 \text{ and } 3) \quad \text{eq. 22}$$

$$\psi_k(r) = e^{ik \cdot r} u_k(r) \quad \text{eq. 23}$$

According to Bloch's theorem, if the Hamiltonian of the Schrödinger equation is a periodic operator, then each of the eigenfunctions can be defined as a product of a phase factor ( $e^{ik \cdot r}$ ) and a periodic function  $u_k(r)$ , which has the same periodicity as the crystal. This wave function of a periodic potential (eq. 23) allows us to compute properties such as total energies and electron density by integrating over  $k$  in the reciprocal space.<sup>71</sup>

### 2.3.2 Brillouin zone integration

The Brillouin zone is a specific region in the reciprocal lattice. The first Brillouin zone is defined by the intersection of planes, which are perpendicular bisectors of the vectors joining the origin to its nearest lattice points. Any wave vector in the reciprocal space can be translated to the first Brillouin zone. Thus, all the essential properties of a periodic crystal can be estimated by integrating over the volume of the first Brillouin zone. In the equation below,  $g_i(k)$  is any function in  $k$  space,  $V_{BZ}$  is the volume of the first Brillouin zone and  $\bar{g}_i$  is the mean value of the function.

$$\bar{g}_i = \frac{1}{V_{BZ}} \oint g_i(k) dk \quad \text{eq. 24}$$

In DFT calculations, the above integral is expressed as a weighted sum of a set of discrete points (which are called as  $k$ -points, refer to eq. 25).

$$\bar{g}_i = \frac{1}{V_{BZ}} \sum_k w_k g_i(k) \quad \text{eq. 25}$$

In the equation above,  $w_k$  indicates the weight. The number of  $k$ -points is usually selected by performing a systematic convergence test. The Brillouin zone summation significantly reduces the computational cost of periodic DFT calculations.<sup>63,71</sup>

### 2.3.3 Plane-wave energy cut-off

As discussed previously, in a periodic system, the eigenfunction of the Schrödinger equation is written as a product of a phase factor and a periodic function (eq. 23). The function  $u_k(r)$  can be represented using a basis set of plane waves (eq. 26).

$$u_k(r) = \sum_G C_G \exp(iG \cdot r) \quad \text{eq. 26}$$

$$G = m_1 b_1 + m_2 b_2 + m_3 b_3 \quad (m_1, m_2 \text{ and } m_3 \text{ are integers}) \quad \text{eq. 27}$$

$G$  is a vector expressed using the reciprocal lattice components  $b_1$ ,  $b_2$  and  $b_3$ . Using eq. 23 and eq. 26, the following relation can be derived for the wavefunction (refer to eq. 28):

$$\Psi_k(r) = \sum_G C_{k+G} \exp(i(k+G) \cdot r) \quad \text{eq. 28}$$

$$E_{cut} = \frac{\hbar^2}{2m} |k+G|^2 = \frac{\hbar^2}{2m} G_{cut}^2 \quad \text{eq. 29}$$

The vector  $G$  can take infinite number of values. It is impractical to include all the values of  $G$  in a DFT calculation, and thus, a cut-off energy  $E_{cut}$  is defined to truncate the infinite series of plane waves. Any vector  $G$ , which has an energy value greater than  $E_{cut}$  (eq. 29), is not included in the plane-wave basis set. Usually, the value of  $E_{cut}$  is selected for an electronic system by performing a convergence study.<sup>63</sup>

#### 2.3.4 Pseudopotentials

The core electrons of an atom do not directly participate in bond formation and cleavage. The computational cost of DFT calculations can be significantly decreased by approximating the influence of core electrons. Pseudopotentials substitute the electron density of core electrons with a fictitious potential that has similar mathematical and physical features; this approach is called the frozen core approximation. The use of pseudopotentials substantially reduces the size of the plane-wave basis set. Some of the important types of frozen core approximations include hard pseudopotentials, ultrasoft pseudopotentials (USPPs) and projector augmented waves (PAW). The PAW method is widely accepted as a suitable approach for DFT calculations.<sup>63</sup>

#### 2.3.5 Transition state search algorithms

A Transition state (TS) is a first-order saddle point in the potential energy surface (PES) region. If a good initial guess of the TS configuration is available, the Quasi-Newton optimisation algorithm can be used to locate first-order saddles. However, in most cases, it is difficult to predict the TS geometry with the Quasi-Newton method. To overcome this problem, several TS search methods such as dimer<sup>72</sup> and Nudged Elastic Band (NEB)<sup>73,74</sup> have been developed. In the dimer method, two images of the system are used. These two images are created by slightly perturbing the system by a finite distance ( $\Delta R$ ) in the opposite directions using a displacement unit vector  $\hat{N}$  (a random vector, which provides the orientation to the dimer) (refer to eq. 30 and eq. 31).

$$R_1 = R + \Delta R \hat{N} \quad \text{eq. 30}$$

$$R_2 = R - \Delta R \hat{N} \quad \text{eq. 31}$$

The dimer algorithm evaluates the forces and energies of the two images (at every step) to translate the system towards the transition state (first-order saddle). Furthermore, at each step, the two-image system is also rotated in an attempt to align it to the Minimum energy path

(MEP). The dimer algorithm does not require any information regarding the product configuration (final state) of the system. However, it is necessary to provide a good initial guess of the vector  $\hat{N}$ . If the initial displacement is not a good guess, then the dimer algorithm might converge to an undesired transition state.<sup>72</sup>

In the NEB approach, a trial MEP is defined, which connects the reactant and product states by using a set of images. Each image has a unique configuration. These images are located at positions  $r_1, r_2, r_3 \dots r_{n-1}$  of the PES region. The forces between the images are defined by harmonic equations (spring forces). The typical NEB calculation is a constrained optimisation. The force update for any  $i^{\text{th}}$  image is calculated by summing up the parallel component of the spring force and perpendicular component of the DFT force (along the local tangent) (as shown in the equations below):<sup>74</sup>

$$F_{i,\text{spring}}^{\text{par}} = k(|r_{i+1} - r_i| - |r_i - r_{i-1}|) \cdot \hat{a} \quad \text{eq. 32}$$

$$F_{i,\text{DFT}}^{\text{per}} = F_{i,\text{DFT}} - (F_{i,\text{DFT}} \cdot \hat{a}) \quad \text{eq. 33}$$

$$F_{i,\text{update}} = F_{i,\text{spring}}^{\text{par}} + F_{i,\text{DFT}}^{\text{per}} \quad \text{eq. 34}$$

In eq. 32, eq. 33 and eq. 34,  $F_{i,\text{spring}}^{\text{par}}$  is the parallel component (along the local tangent) of the spring force of image  $i$ ,  $k$  indicates the spring constant,  $r_i$  is the position of the image  $i$ ,  $\hat{a}$  is a unit vector in the direction of the local tangent,  $F_{i,\text{DFT}}^{\text{per}}$  represents the perpendicular component (along the local tangent) of the DFT computed force on the  $i^{\text{th}}$  image and  $F_{i,\text{update}}$  indicates the force update of image  $i$ . The NEB algorithm attempts to push the images to the MEP. In most NEB calculations, the images converge on the MEP. However, the highest energy image is not exactly at the saddle point. Usually, force and energy based cubic polynomial interpolation of adjacent images (closer to the saddle point) is carried out to estimate the activation barrier. Alternately, a climbing image (CI) algorithm has been implemented in NEB to accelerate the TS search. In the CI method, the energy of the highest image is maximised along the bands and minimised in other directions by inverting the perpendicular component of the DFT force (along the tangent). The highest image does not experience the spring forces in the CI algorithm.<sup>74</sup> Usually, the typical NEB calculation is carried out first to ensure the system is along the MEP and the highest image is closer to the saddle point. Then the CI method is invoked to drive the highest image to the first-order saddle. In recent years, Machine learning (ML) based NEB method has been developed to accelerate the convergence rate/speed of the TS state search calculation.<sup>75</sup> In chapters 4,5 and 6, we have employed dimer and different NEB calculations (conventional type, CI method and ML based) to identify the transition states of coking/MSR reaction events.

## 2.4 Transition state theory

Typically, the reaction rate of an event can be computed by employing classical molecular dynamics, in which numerical integration of Newtonian equations is carried out to evaluate the trajectory of the system. However, this approach is computationally expensive as the system spends significant periods of time in the reactant state (mainly undergoing random vibrations) before transitioning to the product state. Thus, it becomes increasingly tedious to compute rates of rare events such as catalytic reactions using the aforementioned approach. Among the many theories developed to calculate reaction rates, the transition state theory (TST), also known as the theory of absolute reaction rates, has been found to provide a simple solution to circumvent this problem. Transition state theory divides the PES into three regions: 1) Initial state – the most stable configuration of the reactant region. 2) Final state – the most stable configuration of the product region. 3) Transition state – it is a dividing hypersurface between the reactant and product region. As mentioned previously (in section 2.3.5), the lowest energy configuration of the Transition state is a first-order saddle point.

There are several important assumptions made to derive the expression of the rate constant under TST. The energy of the initial state is assumed to follow the Maxwell-Boltzmann distribution. In the development of TST, the Born-Oppenheimer approximation is invoked - which assumes the nuclei movement to be negligible in comparison to the motion of electrons. The quantum tunnelling effects (particles cross/bypass barriers without reaching the transition state) are assumed to be insignificant. Furthermore, if the system reaches the transition state with a certain velocity, it is assumed to react and form the final state configuration. The recrossing of the system back to the reactant region is not allowed.<sup>76,77</sup> According to TST, the propensity of a reaction (rate constant) is essentially a product of the probability of the system reaching the transition state and rate of crossing the transition state in direction of the product region. The probability of finding the system in the transition state configuration is estimated as a ratio of the partition functions (dimensionless quantities which have information on the statistical properties of the system) of transition and initial states, respectively (refer to eq. 35 and eq. 36).

$$P_{TS \pm \frac{\delta x}{2}} = \frac{Q^{TS \pm \frac{\delta x}{2}}}{Q^R} \quad \text{eq. 35}$$

$$k_{TST} = r_C P_{TS \pm \frac{\delta x}{2}} \quad \text{eq. 36}$$

In the above equations,  $Q^{TS \pm \frac{\delta x}{2}}$  represents the partition function within the thickness  $\delta x$  of the transition state configuration space,  $Q^R$  indicates the partition function of reactant (initial) state,  $r_C$  is the rate at which the system is traversing to reach the product region and  $P_{TS \pm \frac{\delta x}{2}}$  is the

probability of the system to reach the transition state. Under the limit of  $\delta x$  moving to zero, the mathematical form of the wave function is assumed to be a plane wave. The energy of the system is quantized based on the solutions of “particle in a box”. Using the aforementioned approach, the rate constant is evaluated to have the following form (as shown in eq. 37, refer to chapter 4 of the book “Fundamental concepts in Heterogeneous catalysis”<sup>77</sup> for a detailed derivation of the result below):

$$k_{TST} = \frac{k_B T}{h} \frac{Q^{TS}}{Q^R} \exp\left(-\frac{E^{act}}{k_B T}\right) \quad \text{eq. 37}$$

In eq. 37,  $Q^{TS}$  represents the partition function of the system at the transition state,  $k_B$  is the Boltzmann constant,  $h$  is the Planck’s constant,  $T$  is the temperature of the system and  $E^{act}$  is the activation energy at 0 K. The pre-factor term  $\left(\frac{k_B T}{h} \frac{Q^{TS}}{Q^R}\right)$  contains the thermal and entropic contributions of the system. In heterogenous catalytic systems, the elementary events mainly include adsorption, desorption, diffusion and surface reactions. The partition functions of the transition/initial states are estimated by splitting the energy of the system into translational, rotational and vibrational contributions. The translational partition function for gas-phase molecules in a container is estimated using the equation below (where  $V$  is the volume of the container and  $m$  is mass of the molecule):<sup>78</sup>

$$Q^{Trans,3D} = \frac{V (2m\pi k_B T)^{\frac{3}{2}}}{h^3} \quad \text{eq. 38}$$

On the catalytic surface, the gaseous species are assumed to be a 2D gas. The z component of the  $Q^{Trans,3D}$  partition function is decoupled as follows ( $L_z$  is the length of the gas-phase in the z-direction):

$$Q_{gas}^{Trans,3D} = Q_{gas}^{Trans,2D} L_z \frac{\sqrt{2m\pi k_B T}}{h} \quad \text{eq. 39}$$

The translation of the gas-phase species is restricted to the area around the active site of the catalyst. Thus, the 2D translation partition function ( $Q^{Trans,2D}$ ) is estimated using eq. 40 ( $A_{st}$  is the effective area of the active site/sites where the reaction occurs).<sup>78</sup> The rotational partition function is evaluated based on the geometry of the molecule. For linear molecules, the rotational component of the partition function is calculated using eq. 41. In eq. 41, the symbols  $I$  and  $\sigma$  indicate the moment of inertia and symmetry factor of the gas molecule, respectively. In the case of non-linear molecules, the rotational partition function is estimated using eq. 42.<sup>78,79</sup>



$$Q_{gas}^{Trans,2D} = A_{st} \frac{2 \pi m k_B T}{h^2} \quad \text{eq. 40}$$

$$Q_{gas}^{rot,linear} = \frac{8 \pi^2 I k_B T}{\sigma h^2} \quad \text{eq. 41}$$

$$Q_{gas}^{rot,non-linear} = \frac{(\pi I_a I_b I_c)^{1/2}}{\sigma} \left( \frac{8 \pi^2 k_B T}{h^2} \right)^{\frac{3}{2}} \quad \text{eq. 42}$$

The partition function for the vibrational modes of the molecule is estimated by assuming the energies are distributed based on the harmonic oscillator model. As shown in eq. 43, the overall vibrational partition function of the molecule is calculated as a product of the contributions from each vibrational mode. The symbol  $\nu_k$  is the vibrational frequency of the  $k^{\text{th}}$  vibrational mode.<sup>78,79</sup>

$$Q^{vib} = \prod_k \frac{\exp(-\frac{h \nu_k}{2 k_B T})}{1 - \exp(-\frac{h \nu_k}{k_B T})} \quad \text{eq. 43}$$

For a species adsorbed on the catalyst surface, it can undergo several types of motion – these include bond stretching between atoms, frustrated translations and frustrated rotations. In the current study, the partition functions (entropic contributions) of frustrated translations/rotations of the adsorbed species have been calculated using the harmonic oscillator model (eq. 43). The harmonic approximation gives a reasonable/acceptable estimate of the entropy for the frustrated translations/rotations of chemisorbed (tightly bound) species on the catalytic surface.<sup>80</sup> However, in the case of physisorbed (weakly bound) species, the harmonic approximation underestimates the entropic contributions of frustrated translations/rotations. Alternatively, employing free translator/rigid rotor models (such as eq. 39, eq. 41 and eq. 42) for weakly bound species (such as CH<sub>4</sub>) is not the correct approach. These models significantly overestimate the entropic contributions of weakly bound species. In recent years, more sophisticated methods such as the hindered translator/rotor models have been developed to accurately account for the entropic contributions of frustrated translations/rotations of weakly bound species.<sup>81</sup> Nonetheless, employing these methods requires the estimation of translation/rotational activation barriers. It is beyond the scope of this work to perform such calculations. Furthermore, most of the adsorbates studied in this work bind tightly to the Ni(111) surface. Thus, we have considered the harmonic approximation for estimating the entropy of frustrated translation/rotational motions of adsorbates.

According to TST, the propensity of a reaction (rate constant) can also be expressed in the following manner (as the energies of the reactant state and transition state are in equilibrium):<sup>77</sup>

$$k_{TST} = \frac{k_B T}{h} e^{\frac{-\Delta G_{TS}}{k_B T}} \quad \text{eq. 44}$$

In eq. 44,  $\Delta G_{TS}$  represents the Gibbs free energy change (between transition state and initial state),  $T$  is the temperature,  $k_B$  indicates the Boltzmann constant and  $h$  is the Planck's constant. The free energy ( $\Delta G_{TS}$ ) term encompasses the thermal and entropic contributions. The above equation can be further written in the following way (refer to eq. 45):<sup>77</sup>

$$k_{TST} = \frac{k_B T}{h} e^{\frac{\Delta S_{TS}}{k_B}} e^{\frac{-\Delta H_{TS}}{k_B T}} \quad \text{eq. 45}$$

The terms  $\Delta H_{TS}$  and  $\Delta S_{TS}$  are changes in enthalpy and entropy (between transition state and initial state), respectively. For surface reactions in catalytic systems, the pre-factor term ( $\frac{k_B T}{h} e^{\frac{\Delta S_{TS}}{k_B}}$ ) of eq. 45 is often approximated to  $\frac{k_B T}{h}$ . This assumption is valid in cases where there is a minimal change in entropy when the system moves from the initial state to the transition state on the catalytic surface. Entropic effects become more pronounced when there is a transition of the system from surface to gas-phase or vice versa (as molecules have large translational/rotational degrees of freedom in the gas-phase).

## 2.5 Master equation

As discussed previously, the TST gives us a simplified solution to calculate the rate constant (propensity) of an elementary event by coarse-graining the trajectory of the system into systematic state-to-state hops. The “state” refers to the stable geometry of an adsorbate on the lattice. The time evolution of the system undergoing such discrete hops/jumps is governed by the Markovian master equation (generally called as the master equation).<sup>82</sup> The master equation is a set of coupled differential equations which provides the probabilistic rate (with respect to time) for the system to jump from state  $\alpha$  to state  $\beta$  (refer to eq. 46).<sup>46,79</sup>

$$\frac{dP_\alpha(t)}{dt} = - \sum_{\alpha \neq \beta} k_{\alpha\beta} P_\alpha(t) + \sum_{\alpha \neq \beta} k_{\beta\alpha} P_\beta(t) \quad \text{eq. 46}$$

In eq. 46,  $k_{\alpha\beta}$  refers to the transition probability for the system to move from state  $\alpha$  to state  $\beta$ ,  $P_\alpha(t)$  is the probability of finding the system in state  $\alpha$ ,  $k_{\beta\alpha}$  indicates the transition probability for the system to move from state  $\beta$  to  $\alpha$ ,  $P_\beta(t)$  is the probability of finding the system in state  $\beta$ . The eq. 46 is essentially a loss-gain equation; the first term on the right-hand side is the total rate at which the system leaves the state  $\alpha$  (the loss) and the second term is the total rate at which the system enters the state  $\alpha$  (the gain). At steady-state conditions, an important constraint of the master equation is that the sum of the rates of all transitions from states  $\alpha$  to  $\beta$  must be equal to the sum of the rates of all transitions from states  $\beta$  to  $\alpha$  (as shown in eq. 47). Furthermore, at thermodynamic equilibrium, a stricter constraint is imposed on the master

equation, which is referred to as the principle of detailed balance. For any reaction network, the principle of detailed balance states that the difference in forward and reverse rates of each elementary event/step must be zero at thermodynamic equilibrium (refer to eq. 48) <sup>46,83</sup>

$$\frac{dP_{\alpha}(t)}{dt} = - \sum_{\alpha \neq \beta} k_{\alpha\beta} P_{\alpha}(t) + \sum_{\alpha \neq \beta} k_{\beta\alpha} P_{\beta}(t) = 0 \quad \text{eq. 47}$$

$$k_{\alpha\beta} P_{\alpha}(t) - k_{\beta\alpha} P_{\beta}(t) = 0 \quad \text{eq. 48}$$

The master equation is seminal to the development of kinetic models that help us understand the kinetics of chemical reactions on the catalytic surface.<sup>79</sup> The analytical solution of the master equation is mathematically intractable even for a very small system. For instance, consider a system with 100 sites in which we are simulating only adsorption and desorption events for a single adsorbate species. The total number of possible states for such a system is  $2^{100}$ , which is quite an extensive/large set for the master equation to be solved analytically. Thus, numerical solutions have been developed to solve the master equations for catalytic systems.<sup>46</sup>

## 2.6 KMC simulations

In the Monte Carlo methodology, the master equation is not solved explicitly, instead a stochastic simulation algorithm (first developed by Gillespie<sup>84</sup>) is used to propagate the system from state-to-state whose statistics satisfy the master equation. Time-averaging of the stochastic trajectories (upon reaching the steady state) allows us to estimate the observables of interest.<sup>83,85</sup> The KMC approach uses the aforementioned procedure to determine the kinetics of a catalytic reaction. At each step of the KMC simulation, the event to be executed and its time of occurrence must be determined. Consider a system that is in state  $i$  in the KMC simulation, and it can propagate to  $j$  states. The escape probability for the system is the same at every short time interval (or instance) it spends in state  $i$  since there is a loss of memory in the system. This leads to exponentially decaying survival statistics.<sup>46</sup> Thus, the cumulative probability for a system to escape from state  $i$  to any of the  $j$  states (for any time  $\tau$ ) is given by the following relationship:

$$P(\tau) = 1 - \exp(-k_{tot}\tau) \quad \text{eq. 49}$$

$$k_{tot} = \sum_k^j k_{ik} \quad \text{eq. 50}$$

The derivative of  $P(\tau)$  gives us the escape probability of the system from state  $i$  to any of the  $j$  states (probability density function, which has an exponential distribution, refer to eq. 51).

The time of occurrence of an event or the escape time (for a system with such a distribution) is given by eq. 52 (where  $r_1$  is a random number between 0 and 1).

$$p(\tau) = k_{tot} \exp(-k_{tot}\tau) \quad \text{eq. 51}$$

$$t_{escape} = -\frac{\ln(r_1)}{k_{tot}} \quad \text{eq. 52}$$

The direct method (also called as the variable step size method<sup>86</sup>) and the first reaction method<sup>87</sup> are widely employed to propagate the system from state-to-state in the KMC simulations (refer to refs. 79, 83 and 84 for more information about the mathematical formulation of these methods).

Having discussed the fundamental concept behind state propagation in KMC, we proceed to give a thorough understanding on the working principle of the KMC algorithm: 1) The required simulation parameters such as rate constants of events, adlayer energetics, reaction conditions and type/number of lattice sites must be specified to initialise the KMC simulation. 2) The KMC lattice configuration must be specified – this can be an empty lattice or a pre-defined lattice in which adsorbates/species are placed on specific sites. 3) The KMC algorithm scans the entire lattice to construct a list of all plausible events and creates a process queue. 4) The KMC algorithm determines the time of occurrence and the event to be executed using Direct/First reaction method. 5) Upon executing the selected event, the KMC algorithm updates the lattice configuration and the process queue. For instance, consider a CO adsorption event executed on site numbered as 2 of the KMC lattice. The KMC algorithm updates lattice state of site 2 as occupied by CO adsorbate and the concomitant processes that need to be included/removed (due to this change) are updated in the process queue. At every time step of the KMC simulation, this procedure is repeated until the simulation reaches the steady state.<sup>43</sup> The working principle of the KMC algorithm is also shown in the form of a flow sheet in Figure 4.

Unlike other kinetic approaches (such as Langmuir-Hinshelwood models and mean-field MK models), the KMC methodology allows us to capture adsorbate-adsorbate interactions with high fidelity.<sup>43</sup> In catalytic systems, especially at high coverage regimes, the adsorbate stability is significantly influenced by its interaction with neighbouring adsorbates. These interactions mainly include: 1) Overlap of adsorbate electronic states (which is attractive by nature, also called as direct interactions), 2) indirect interactions – the presence of an adsorbate alters the electronic structure of the catalytic surface, which in turn affects the binding affinity of another adsorbate, 3) elastic interactions – in some cases, the surface of the catalyst is distorted (at a local level) due to adsorption, this distortion is experienced as a repulsion by other adsorbates.

4) Dipole-dipole interactions – a prime example of this type of interaction is hydrogen bonding.<sup>88</sup>

In KMC simulations, the CE Hamiltonian provides the framework to capture local interactions with high accuracy.<sup>89-91</sup> In the last few decades, the CE methodology has been employed widely to predict the thermodynamic stabilities of adlayer structures.<sup>92-94</sup> According to CE formalism, the energetics of any n-body configuration can be written as a sum of individual interaction energies of 1-body, 2-body, 3-body ... n-body figures/parameters.<sup>95</sup> In the lattice-gas model with  $N_L$  sites, the CE Hamiltonian of any state ( $H(\sigma)$ , where  $\sigma = \{\sigma_1, \sigma_2, \sigma_3 \dots \sigma_{N_L}\}$ ) is expressed using a site occupation variable  $\sigma_i$ . If site  $i$  is empty, then  $\sigma_i$  takes the value 0. Whereas if site  $i$  is occupied by an adsorbate, then  $\sigma_i$  is given a value of 1. The CE formulation is shown in the equation below:<sup>96</sup>

$$H(\sigma) = h_0 + h_1 \sum_{i=1}^{N_L} \sigma_i + \frac{1}{2!} \sum_i^{N_L} \sum_{j,j \neq i}^{N_L} J_{ij} \sigma_i \sigma_j + \dots \quad \text{eq. 53}$$

In eq. 53,  $h_0$  is the formation energy of the surface,  $h_1$  represents the formation energy of a single adsorbate,  $J_{ij}$  is the pairwise interaction term between adsorbates. Nielsen et al.<sup>89</sup> implemented the CE method in graph-theoretical KMC (Zacros<sup>78</sup>). The figures of the CE model are represented as graph patterns in Zacros. These graph patterns are detected on the KMC lattice by solving the sub-graph isomorphism problems.<sup>89</sup> The occupation variable  $\sigma_i$  (where  $i \in \{1, 2, 3 \dots N_L\}$ ) is a three dimensional vector in graph-theoretical KMC (as represented in the eq. 54):

$$\sigma_i \in \{1, 2, 3, \dots, N_L\} \times \{0, 1, 2, \dots, N_s\} \times \{1, 2, \dots, \text{maxdent}\} \quad \text{eq. 54}$$

In eq. 54,  $N_L$  represents the number of lattice sites,  $N_s$  is the number of species and *maxdent* indicates the maximum value of the set -  $\{S_1, S_2, \dots, S_j, \dots, S_{N_s}\}$ , where  $S_j$  represents the number of sites occupied by species  $j$  on the KMC lattice. The CE in graph-theoretical KMC is formulated as follows:<sup>48</sup>

$$H(\sigma) = \sum_{k=1}^{N_c} \frac{ECI_k}{GM_k} NCE_k(\sigma) \quad \text{eq. 55}$$

In eq. 55,  $NCE_k(\sigma)$  indicates the number of times cluster  $k$  is detected by the pattern detection algorithm of graph-theoretical KMC,  $ECI_k$  is the effective cluster interaction energy of cluster  $k$ ,  $GM_k$  represents the graph multiplicity factor of cluster  $k$  (correction factor to avoid double counting of symmetrical patterns) and  $N_c$  denotes the total number of clusters/graph patterns.

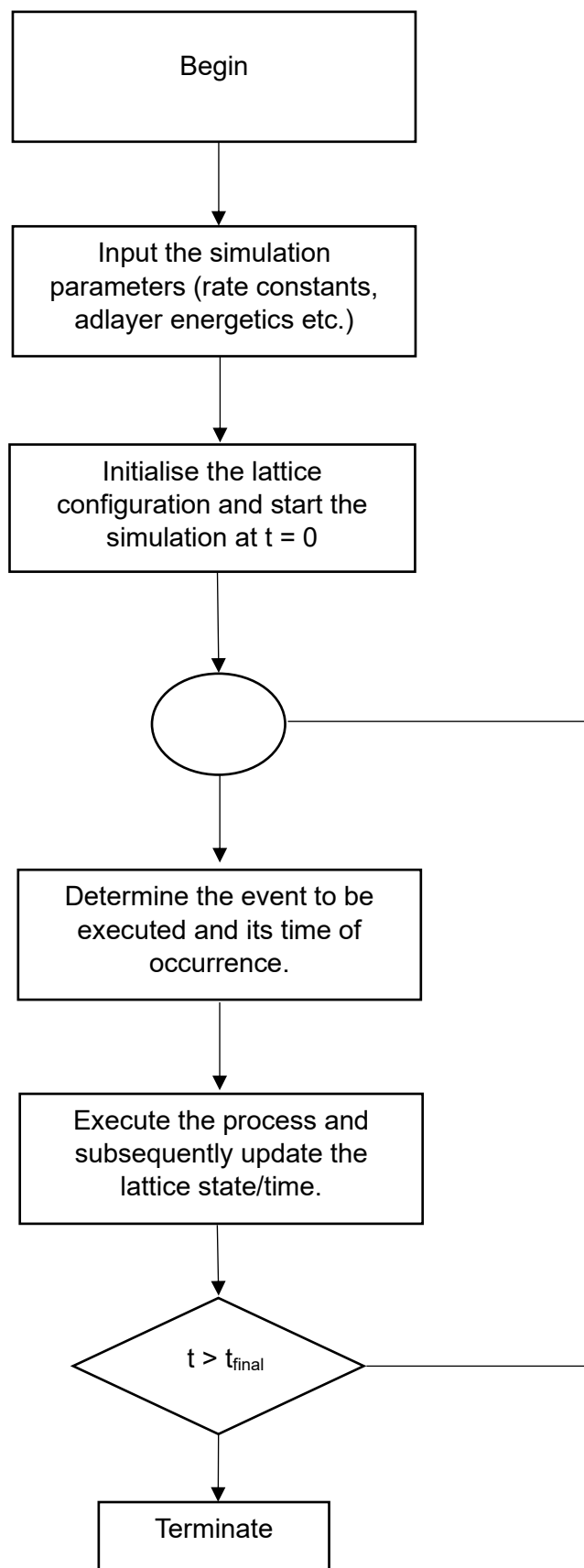


Figure 4: A flow sheet representing the working principle of the KMC algorithm.<sup>43</sup>

In theory, one can include all the plausible clusters in the CE Hamiltonian. However, it is computationally expensive to include larger body CE clusters in the KMC simulation. This problem can be circumvented by truncating the terms of the CE model through a least-squares-fitting exercise. The CE fitting is a trial-and-error method in which a finite set of clusters are identified/trained to capture the energetics of a large dataset of DFT configurations. It is a practical challenge to identify the optimal set of clusters in the CE fitting exercise. Including fewer clusters could give us poor predictive accuracy, however, a CE model with too many clusters can lead to overfitting issues as we start capturing the DFT error. Usually, a hierarchical approach is followed in identifying the clusters.<sup>90,97</sup> The quality of the CE fit is assessed by using metrics such as root-mean-square error, mean absolute deviation, leave-one-out cross-validation score and Cook's distances. The readers can go through refs. 98 and 99 to understand the methodology of LOOCV and Cook's distances, respectively. As discussed previously (in subsection 1.3 of the "Thesis Background" chapter), recent studies have established the importance of using CE-based KMC simulations to rationally explain experimental observations (that hitherto remained elusive), and also, capture complex chemistries/reactions on the catalyst surface.

## 2.7 MK models

MK models play an important role in the identification and development of catalytic materials with improved performance and selectivity. For any catalytic reaction, the MK models provide a theoretical framework to predict the species coverages, turnover rates, rate-controlling steps and dominant reaction pathways.<sup>100,101</sup> The formulation of MK models is essentially derived by reducing the Markovian master equation into a system of ODEs at the thermodynamic limit of very large lattices and infinitely fast diffusions.<sup>22</sup> The spatial information about the species location and site connectivity is lost within the MK framework.<sup>102,103</sup> The species count on the lattice is averaged out over the total number of sites. The MK model equations for any reaction network are given as follows:

$$r_{fwd,j} = GM_{fac} k_{fwd,j} \prod_{i \in R_j^{surf}} (\theta_i)^{v_{ij}} \quad \text{eq. 56}$$

$$r_{rev,j} = GM_{fac} k_{rev,j} \prod_{i \in P_j^{surf}} (\theta_i)^{v_{ij}} \quad \text{eq. 57}$$

$$r_j = r_{fwd,j} - r_{rev,j} \quad \text{eq. 58}$$

$$\frac{d\theta_i}{dt} = \sum_{j=1}^{Nr} v_{ij} r_j \quad \text{eq. 59}$$

$$\sum_{i=1}^{Ns} N_i^{occup-sites} \theta_i + \theta_{vacant} = 1 \quad \text{eq. 60}$$

In eq. 56, eq. 57 and eq. 58,  $k$  refers to the rate constant,  $R_j^{surf}$  is the set of reactant species of the reaction,  $P_j^{surf}$  is the set of product species of the reaction,  $\theta$  represents the surface coverage (normalised with respect to the total number of sites),  $GM_{fac}$  is the geometry factor (accounting for site connectivity),  $v_{ij}$  is the stoichiometric coefficient of species  $i$  in reactant/product set  $j$  and  $r_j$  represents the overall rate of reaction  $j$ . The system of ODEs is represented using eq. 59 (where  $Nr$  is the number of reactions). The equality constraint that must be satisfied between species coverages is shown in eq. 60, where  $Ns$  represents the total number of species,  $N_i^{occup-sites}$  is the number of sites occupied by species  $i$  on the catalytic surface and  $\theta_{vacant}$  is the fractional coverage of vacant sites.

Unlike KMC models, the correlation effects between adsorbates are neglected in the MK formulation. Generally, mean-field approximations are applied in MK models to capture coverage effects.<sup>87,104</sup> In the mean-field approximation (also called as the Bragg-Williams approximation), the adsorbate interaction is estimated by taking into account site connectivity, interaction parameter and adsorbate fractional coverage (as shown in eq. 61).<sup>105</sup>

$$E_i^{FE-cov} = E_i^{FE} + GM_{fac1} \sum_{j=1}^m E_{ij}^{1NN} \theta_j + GM_{fac2} \sum_{j=1}^m E_{ij}^{2NN} \theta_j + \dots \quad \text{eq. 61}$$

In eq. 61,  $E_i^{FE}$  indicates the formation energy,  $E_i^{FE-cov}$  is the coverage-dependent formation energy,  $m$  represents the number of species,  $E_{ij}^{1NN}$  and  $E_{ij}^{2NN}$  are the first nearest neighbour and second nearest neighbour interaction parameters, respectively. In recent years, several higher-order approximations have been developed in the MK framework to capture lateral interactions.<sup>21,22,106</sup> Nevertheless, these approximations have been formulated/tested only for simple systems. Further work is necessary to extend these higher-order approximations to complex reaction networks. So far, we have discussed about the formulations used in MK/KMC models to account for the change in formation energy of the species due to adsorbate-adsorbate interactions. These local interactions also influence the activation energy barriers of elementary events. The forward/reverse coverage-dependent activation barriers for any reaction are estimated using the Brønsted-Evans-Polanyi (BEP) relations (as shown in eq. 62 and eq. 63 below) in MK/KMC models.<sup>107,108</sup>

$$E_{Actfwd}^{finite-coverage} = \max(0, \Delta E_{rxn}, E_{Actfwd}^{zero-coverage} + w_{fwd} (\Delta E_{rxn} - \Delta E_{rxn}^0)) \quad \text{eq. 62}$$



$$E_{Actrev}^{finite-coverage} = \max (0, -\Delta E_{rxn}, E_{Actrev}^{zero-coverage} - (1 - w_{fwd})(\Delta E_{rxn} - \Delta E_{rxn}^0)) \quad \text{eq. 63}$$

In eq. 62 and eq. 63,  $\Delta E_{rxn}$  is the coverage-dependent reaction energy,  $\Delta E_{rxn}^0$  is the zero-coverage reaction energy,  $w$  is the proximity factor and  $E_{Act}^{zero-coverage}$  is the zero-coverage activation barrier.

In some cases, the mean-field MK models capture the coverage dependence of binding energies of species reasonably well. However, they fail to account for several important local effects on the catalytic surface such as adsorbate lateral interactions, adsorbate ordering/island formation and lattice inhomogeneities. As discussed previously, the CE-based KMC models capture the aforementioned effects with high fidelity. Furthermore, the diffusions are assumed to be fast (quasi-equilibrated) events in the MK methodology. It is well known that diffusion events are fast on transition metals – the diffusion activation barrier for any adsorbate is usually around 12% of its adsorption energy.<sup>109</sup> Nevertheless, this might not be true on metal oxide/stepped surfaces.<sup>103</sup> Slow diffusion of species can significantly alter the catalytic rate. In KMC simulations, the diffusion events can be modelled explicitly, and the effect of slow diffusions can be captured reliably. In terms of computational cost, the KMC simulations are more expensive than MK models. In recent times, significant efforts have been undertaken to reduce the computational cost of KMC simulations.<sup>78,110,111</sup> Overall, kinetic models such as mean-field MK models and KMC simulations will play a crucial role in accelerating the identification of next-generation catalysts.<sup>112</sup>

# Chapter 3

### 3. DFT benchmark studies on representative species and poisons of methane steam reforming on Ni(111)

The whisker carbon poisoning of MSR primarily involves the formation of graphene islands on the support side of the Ni catalyst (at the molecular scale). First-principles-based approaches, such as DFT calculations, can provide valuable insight into the stability of graphene (carbon poison in the MSR reaction) and binding propensity of MSR species on Ni(111). It is critical that a DFT functional can adequately describe the long-range interactions (weak van der Waals forces) of graphene-Ni(111), as well as the short-range interactions between MSR species (which are chemisorbed) and Ni(111). In this chapter, a systematic benchmark study has been carried out to identify a suitable DFT functional for the MSR-graphene system. The binding energies of graphene and important MSR species, as well as the reaction energies of methane dissociation and carbon oxidation, were computed on Ni(111) using GGA functionals, DFT-D and vdW-DF. *The contents of this chapter have been published in Physical Chemistry Chemical Physics, 23(29), pp. 15601-15612.*

#### 3.1 Introduction

The graphene-Ni(111) system requires a thorough description of local interactions as well as van der Waals forces (non-local correlations).<sup>113</sup> The incorporation of van der Waals forces in the exchange-correlation is a major challenge of Kohn-Sham DFT. Some of the standard exchange-correlation functionals, such as those based on the local density approximation (LDA), the generalised gradient approximation (GGA) and hybrid functionals do not account for the description of van der Waals forces.<sup>69</sup> Several studies attempted to address this issue by developing dispersion-inclusive DFT functionals such as DFT-D and vdW-DF. The DFT-D approach involves the inclusion of a correction term to the Kohn-Sham DFT energy, which captures the asymptotic behaviour of long-range interactions.<sup>69</sup> Some notable DFT-D correction schemes have been developed by Grimme,<sup>114</sup> Tkatchenko-Scheffler,<sup>115</sup> Steinmann,<sup>116,117</sup> and Ortmann<sup>118</sup>. In the vdW-DF formalism, on the other hand, the non-local correlations are expressed as a functional of electron density; there is no dependence on additional input parameters.<sup>69</sup> The first general such functional (vdW-DF) was developed by Dion et al.<sup>119</sup>. Modified versions of vdW-DF have subsequently been developed, such as the optB86b-vdW, optB88-vdW and optPBE-vdW functionals<sup>120,121</sup> as well as the Bayesian error estimation functional (BEEF-vdW<sup>122</sup>).

Recent studies have extensively tested the applicability of DFT-D3 functionals and vdW-DF for accurately describing the graphene-Ni(111) interactions. Li et al.<sup>123</sup> studied the graphene-Ni(111) system using DFT functionals - PBE, PBE-D3 and optB86b-vdW; the authors report that the optB86b-vdW functional gives a reasonable estimate of the graphene-Ni distance and the graphene binding energy. Mittendorfer et al.<sup>113</sup> compared the graphene-Ni(111) binding

energy predictions of several vdW-DF. In that study, the optB88-vdW functional was found to accurately predict the binding energy of graphene on Ni(111). Furthermore, Janthou et al.<sup>124</sup> and Muñoz-Galán et al.<sup>125</sup> have carried out comprehensive benchmark studies of graphene-Ni(111) using vdW-DF and DFT-D functionals; these works mainly conclude that the PBE-D3 (Grimme correction) functional has excellent predictive accuracy and the vdW-DF such as optB86b-vdW and optB88-vdW are also promising. In summary, the benchmark studies have successfully identified a few suitable DFT functionals - PBE-D3, optB86b-vdW and optB88-vdW – for capturing the chemical interactions between graphene and Ni(111).

The aforementioned DFT benchmark studies have solely focussed on the graphene-Ni(111) system. However, the MSR reaction network involves several intermediates that bind on Ni(111) mainly via short-range interactions (unlike graphene). In order to develop a reliable DFT model for graphene formation in MSR, it is equally important to capture the chemistry of such intermediates. DFT benchmarks of chemisorbed species/intermediates (bonding mainly via short-range interactions in most cases) are not uncommon in the literature. In this context, Zhu et al.<sup>126</sup> used several GGA functionals and DFT-D3 functionals to compute the binding energies of H and H<sub>2</sub>O on the Ni(111) surface. PBE was able to estimate the binding energy of hydrogen with acceptable accuracy; however, it significantly under-predicts the water binding energy. On the other hand, DFT-D3 functionals (such as PBE-D3 and RPBE-D3) predict the binding energy of water with excellent accuracy but overestimate the hydrogen binding energy. Göttl et al.<sup>127</sup> benchmarked the performance of important GGA functionals, DFT-D functionals and vdW-DF for predicting the heat of molecular/dissociative adsorptions of CH<sub>4</sub>, CH<sub>3</sub>I, CH<sub>3</sub>, I and H on Ni(111). The authors conclude that no individual DFT functional has high accuracy for all the species. For instance, the PBE-D3 functional was found to exhibit high predictive accuracy for species such as CH<sub>4</sub>, CH<sub>3</sub> and CH<sub>3</sub>I, whereas the BEEF-vdW functional gave the best estimate for the binding energies of H and I. Gautier et al.<sup>70</sup> computed the binding energies of carbon monoxide, oxygen, hydrogen and several hydrocarbons on Pt(111) using DFT functionals such as PBE, PBE-dDsC and few other vdW-DF. The authors compared the predictions of these functionals with micro-calorimetry data obtained from the literature. In addition, Wellendorff et al.<sup>128</sup> carried out a benchmark study for the DFT functionals using experimental data of ten different transition metals. There are other DFT benchmark studies that have tested the applicability of DFT-D functionals and vdW-DF for various systems.<sup>97,129</sup> Nevertheless, to the best of our knowledge, a thorough investigation on the performance of GGA functionals, DFT-D functionals and vdW-DF in predicting the binding energies of key intermediates of MSR and graphene on Ni(111) is not available in the literature.

The main objective of this work is to do a systematic comparative study on the predictive accuracy of relevant GGA functionals, DFT-D functionals and vdW-DF for graphene and a few

representative MSR elementary reactions. To achieve this goal, the binding energies of graphene and MSR species (CO, C, CH<sub>3</sub>, H<sub>2</sub>O, H, O and OH), and the reaction energies of methane dissociation (considered to be the rate-determining step of MSR) and carbon oxidation were computed on the Ni(111) surface. The DFT functionals include PBE<sup>130</sup>, RPBE<sup>131</sup>, and revPBE<sup>132</sup> (GGA functionals), PBE-D3, RPBE-D3, revPBE-D3<sup>114</sup>, PBE-dDsC and PBE-TS<sup>116,117</sup>, optB86b-vdW, optB88-vdW, optPBE-vdW<sup>120</sup>, and BEEF-vdW<sup>122</sup> (vdW-DF). The predictions of the aforementioned DFT functionals have been benchmarked against experimental and computational data (from higher-level theory) available in the literature.

The rest of this chapter is organised as follows: The “Computational details” section includes information about the computational setup of the DFT calculations and the relevant formulae used to estimate the DFT binding energy, the zero-point energy (ZPE) correction, the thermal energy contributions and the root-mean-square deviation (RMSD). Subsequently, the “Results and Discussion” section presents the comparison of DFT predictions of graphene and MSR species to relevant literature data and puts the key findings in the context of practical catalysis. Finally, in the “Conclusions” section, a broad perspective on the performance of GGA functionals, DFT-D functionals and vdW-DF is provided along with some needs and potential opportunities for DFT method development are also discussed.

### 3.2 Computational details

Spin-polarised DFT calculations have been performed using the Vienna *ab-initio* Simulation Package (VASP). The projector augmented wave (PAW) method was used to model the interactions between core and valence electrons. A plane-wave basis set was employed, and the kinetic energy cut-off was set to 400 eV (refer to Figure A1(b) and Figure A2(b) of Appendix I for the plane-wave cut-off convergence plots). The Ni bulk calculations were carried out using a 19×19×19 k-point grid. In the Ni bulk system, the electron smearing is performed using the tetrahedron method with Blöchl corrections and the smearing width was set to 0.05 eV. The Ni(111) surface was modelled with a six-layer p(4×4) slab, where the Ni atoms of the three bottom-most layers were fixed at the optimised lattice constant and others were allowed to fully relax. The periodic images along the z-direction were separated by a vacuum of 12 Å. The first Brillouin zone of Ni(111) was sampled with a 5×5×1 Monkhorst-Pack k-point grid. The k-point mesh was chosen by performing convergence tests on carbon-Ni(111) and graphene-Ni(111), respectively (refer to Figure A1(a) and Figure A2(a) of Appendix I). The electronic self-consistency tolerance was set to 10<sup>-7</sup> eV, and the geometry optimisation terminated when the Hellmann-Feynman forces acting on the atoms that are allowed to relax reached a value less than 0.01 eV/Å. The smearing of electrons was carried out using the Methfessel-Paxton method and the smearing width was set to 0.1 eV. In the vibrational calculations, the Hessian

matrix was computed using the central finite-difference method. The step size of the displacement was set to 0.02 Å.

The binding energy of the adsorbate has been computed using eq. 64, where  $E_{tot}^{slab}$  is the DFT-computed total energy of the clean Ni(111) slab,  $E_{tot}^{A(g)}$  indicates the gas-phase DFT total energy of the adsorbate,  $E_{tot}^{A+slab}$  represents the DFT total energy of the adsorbate-Ni(111) system, and  $E_{bind}^{DFT}$  is the DFT-predicted binding energy of the adsorbate on Ni(111). If the adsorbate undergoes dissociative adsorption, eq. 65 is used to estimate the binding energy of the adsorbate, where  $E_{tot}^{A_2(g)}$  is the gas-phase DFT total energy of the adsorbate molecule. In an effort to make a reliable comparison to experimental data, the ZPE and thermal energy corrections have been calculated, making it possible to report the internal energy of binding. The ZPE contributions (within the harmonic approximation) for the species in the gas phase and the bound state are estimated using eq. 66 and eq. 67, respectively.<sup>133,134</sup> In these equations,  $N$  denotes the total number of atoms of the molecule,  $N_{trans}$  indicates the number of translational modes,  $N_{rot}$  is the number of rotational modes,  $v_i$  represents the frequency of the  $i^{th}$  vibrational mode and  $h$  is the Planck's constant.

$$E_{bind}^{DFT} = E_{tot}^{slab} + E_{tot}^{A(g)} - E_{tot}^{A+slab} \quad \text{eq. 64}$$

$$E_{bind}^{DFT} = E_{tot}^{slab} + \frac{E_{tot}^{A_2(g)}}{2} - E_{tot}^{A+slab} \quad \text{eq. 65}$$

$$E_{gas\ phase}^{ZPE} = \sum_{i=1}^{3N-N_{trans}-N_{rot}} \frac{hv_i}{2} \quad \text{eq. 66}$$

$$E_{bound\ state}^{ZPE} = \sum_{i=1}^{3N} \frac{hv_i}{2} \quad \text{eq. 67}$$

When an adsorbate binds to the Ni(111) surface, the translational and rotational motions are reduced to vibrational modes. The thermal energy contribution of the bound state has been computed by using the harmonic approximation.<sup>133,134</sup> According to Réocreux et al.<sup>135</sup>, the thermal corrections of chemisorbed species obtained under the harmonic approximation have acceptable accuracy (even for low-frequency modes). The bound state vibrational calculation is performed by fixing the positions of the Ni surface atoms (vibrational modes of the Ni surface atoms, commonly referred to as phonons, are assumed to have an insignificant contribution to energies of adsorption or reaction). The thermal energy contribution for species in gas phase and bound state are calculated using eq. 68 and eq. 69. In eq. 70, the ZPE and thermal corrections are added to the DFT predicted binding energy.

$$U_{gas\ phase}^{TC} = \frac{N_{trans}}{2} k_B T + \frac{N_{rot}}{2} k_B T + \sum_i^{3N-N_{trans}-N_{rot}} \frac{h\nu_i e^{\frac{-h\nu_i}{k_B T}}}{1 - e^{\frac{-h\nu_i}{k_B T}}} \quad \text{eq. 68}$$

$$U_{bound\ state}^{TC} = \sum_i^{3N} \frac{h\nu_i e^{\frac{-h\nu_i}{k_B T}}}{1 - e^{\frac{-h\nu_i}{k_B T}}} \quad \text{eq. 69}$$

$$U_{bind}^{theory} = E_{bind}^{DFT} + E_{gas\ phase}^{ZPE} + U_{gas\ phase}^{TC} - E_{bound\ state}^{ZPE} - U_{bound\ state}^{TC} \quad \text{eq. 70}$$

$$RMSD = \sqrt{\frac{\sum_i (U_{bind,i}^{theory} - U_{bind,i}^{exp})^2}{N}} \quad \text{eq. 71}$$

The term  $U_{bind}^{theory}$  from eq. 70 is used to make comparisons with experimental data and the RMSD defined by eq. 71 is adopted to obtain a quantitative measure on the overall performance of the DFT functional (in subsection 3.3.2). In eq. 71,  $U_{bind,i}^{theory}$  indicates the DFT predicted binding energy of the  $i^{th}$  species,  $N$  is the number of observables and  $U_{bind,i}^{exp}$  represents the experimental binding energy of the  $i^{th}$  species.

### 3.3 Results and discussion

Our systematic benchmark study aims at identifying an appropriate DFT functional for the MSR reaction species including graphene. To this end, we employ the computational setup discussed in the “Computational Details” section to calculate the binding energies of these species on Ni(111) using a range of functionals (GGA, DFT-D, vdW-DF) and assess the performance thereof by comparing the predictions with theoretical and experimental data available in the literature. In the following, we discuss our results in detail, starting with the DFT benchmarks of graphene-Ni(111), subsequently, the graphene-Ni(111) potential energy profiles are presented (subsection 3.3.1), and finally, the DFT benchmarks of MSR species are provided (subsection 3.3.2). Additionally, we tested the predictive accuracy of DFT functionals in reproducing the energies of gas-phase reactions relevant to MSR, as well as graphite formation (refer to Table A2 of Appendix I).

#### 3.3.1 DFT benchmarks of graphene-Ni(111)

For all of our calculations of pure graphene and Ni(111), we have used the DFT-predicted lattice constants which are provided in Appendix I for each functional (refer to Table A1). For the calculations of graphene bound to Ni(111), the Ni lattice constant was adopted. It is known that the LDA, GGA and hybrid functionals fail to capture the van der Waals interactions between graphene and Ni(111)<sup>69</sup>, and thus, in this benchmark study, the performance of DFT-D and vdW-DF has been tested.

The DFT predictions must be compared to reliable experimental or theoretical values; however, there is limited experimental data on the binding energy of graphene on Ni(111). Shelton et al.<sup>136</sup> have studied the segregation behaviour of carbon on Ni(111) and concluded that the binding energy of graphene on Ni(111) is around 50 meV greater than the graphite exfoliation energy. Recent experimental works have reported the exfoliation energy of graphite to be in the range of 24.87–66.33 meV/C atom.<sup>124,137,138</sup> Based on the findings of Shelton et al.<sup>136</sup>, the graphene binding energy on Ni(111) can be deduced to be in the range of 74.62–116.08 meV/C atom.<sup>124</sup>

As the graphene binding energy estimate is derived using the findings of only a single experimental study (Shelton et al.<sup>136</sup>), a certain level of caution must be exercised while comparing this value to the DFT predictions. Thus, we also compare our calculated values to theoretical ones, obtained with higher level *ab-initio* methods. A few studies have reported that the random-phase approximation (RPA) method accurately captures the van der Waals interactions.<sup>113,139</sup> The RPA prediction of graphene binding energy will therefore be used in assessing the performance of DFT functionals. The RPA predicts two minima for graphene on Ni(111), located at graphene-Ni distances of 2.17 Å and 3.25 Å, respectively.<sup>113,140,141</sup> The RPA prediction at the former minimum (referred to as “the first minimum” henceforth) is of importance as it is in close agreement with the experimental graphene-Ni distance of  $2.11 \pm 0.07$  Å.<sup>142</sup> Figure 5 compares the DFT-predicted binding energies, RPA prediction<sup>113</sup> and experimental value<sup>124,136</sup> at the first minimum of graphene-Ni(111). The DFT calculations of graphene-Ni(111) are performed using the top-fcc configuration, which is the most stable configuration (refer to Figure A3 of Appendix I for the different types of graphene-Ni(111) configurations).<sup>143,144</sup> In Table 1, the DFT binding energy predictions of this work are compared to the values reported by other theoretical studies available in the literature. The graphene-Ni distance predictions of the DFT functionals are also recorded in Table 1.



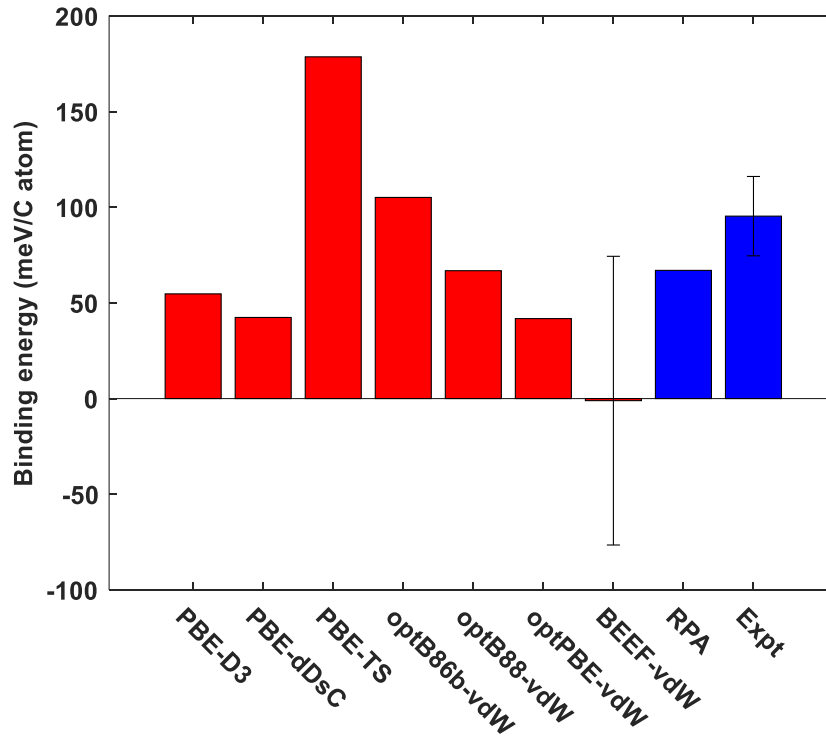


Figure 5: Comparison of the binding energy predictions of the DFT functionals used in this study with the RPA<sup>113</sup>/experimental value<sup>124,136</sup> at the first minimum of graphene-Ni(111).

Among the DFT functionals which use the vdW-DF formalism, the binding energy prediction of the optB88-vdW functional is in excellent agreement with the RPA value. The optB88-vdW prediction also agrees closely with the lower bound of the experimental result (refer to Figure 5). Furthermore, Mittendorfer et al.<sup>113</sup> have shown that the optB88-vdW functional predicts the binding energy of graphene with high accuracy. As illustrated in Figure 5, the optB86b-vdW functional slightly overpredicts the binding energy of graphene with respect to the RPA value, though the predicted value is within the experimental range. Shepard and Smeu<sup>140</sup> and Li et al.<sup>123</sup> have reported similar binding energy values for graphene using the optB86b-vdW functional. On the contrary, the calculations performed by Janthon et al.<sup>124</sup> show that there is close agreement between the optB86b-vdW prediction and the RPA value (refer to Table 1 for the optB86b-vdW predictions obtained from the literature).

**Table 1. Comparative study of DFT predictions of the first minimum of graphene-Ni(111)**

Functional	Binding energy (meV/C atom)	Graphene-Ni distance (Å)	Binding energy predictions from literature (meV/C atom)
PBE-D3	54.72	2.23	79.80 (ref. 125), 86.02 (ref. 124), 53 (ref. 140)
PBE-dDsC	42.39	2.12	No values reported
PBE-TS	178.61	2.15	51.82 (ref. 124), 128.52 (ref. 125)
RPBE-D3	[No binding]	-	No values reported
revPBE-D3	[No binding]	-	No values reported
optB86b-vdW	105.12	2.15	68.40 (ref. 124), 102 (ref. 140), 112 (ref. 123)
optB88-vdW	66.82	2.22	40.42 (ref. 124), 67 (ref. 113)
optPBE-vdW	41.79	2.22	9.33 (ref. 124)
BEEF-vdW	-1.09 ( $\pm$ 75.45)	2.18	around -8 (ref. 122), 10 (ref. 140)

Ref. 113 uses a five-layer Ni(111) supercell, a  $19 \times 19 \times 1$  k-point mesh and a kinetic energy cut-off value of 400 eV. Ref. 122 uses a five-layer  $p(1 \times 1)$  Ni(111) slab (two bottom layers fixed) and a  $20 \times 20 \times 1$  k-point mesh. In ref. 123 a four-layer  $p(1 \times 1)$  Ni(111) supercell (two bottom layers are fixed), a  $20 \times 20 \times 1$  k-point mesh and a plane-wave cut-off energy value of 500 eV was used. Ref. 124 and ref. 125 use a six-layer  $p(1 \times 1)$  Ni(111) supercell (three bottom layers fixed), a  $7 \times 7 \times 1$  k-point grid and a kinetic energy cut-off value of 415 eV. Ref. 140 uses a six-layer  $p(1 \times 1)$  Ni(111) supercell (three bottom layers are fixed), a k-point mesh of size  $25 \times 25 \times 1$  and a plane-wave cut-off energy value of 500 eV. a) For the graphene-Ni(111) calculation with the PBE-TS functional, we have used the PBE-D3 optimised Ni lattice constant. On the other hand, if the PBE-TS optimised Ni lattice constant is used for this calculation, the latter does not converge to the first minimum. Further details are provided in Appendix I (refer to Table A16 and Figure A7).

As shown in Table 1, the optPBE-vdW functional estimates a binding energy value of 41.79 meV/C atom for graphene-Ni(111), which is in reasonable agreement with the RPA value. Janthon et al.<sup>124</sup> report that the optPBE-vdW functional predicts a much weaker adsorption energy for graphene-Ni(111) (9.33 meV/C atom). The authors use a different computational setup compared to our study; this could be the reason for such a substantial difference in the reported optPBE-vdW predictions (key information on the computational setup of the literature studies is provided in the footnote of Table 1). The BEEF-vdW functional was found to predict a weak repulsive interaction between graphene and Ni(111), as also pointed out by Wellendorff et al.<sup>122</sup> The computational error estimate of BEEF-vdW (it is the standard deviation of an ensemble of predictions obtained by randomly sampling from the probability distribution of BEEF-vdW model parameter fluctuations<sup>122</sup>) is large. Certain caution needs to be exercised while using the BEEF-vdW error estimate which results in a graphene binding energy range

from -76.54 meV/C (negative values are qualitatively incorrect with respect to the RPA prediction) to 74.36 meV/C (substantially strong binding affinity between graphene and Ni(111); which closely matches the RPA value). This wide variation also underscores the importance of using the appropriate exchange-correlation approximation to obtain accurate results.

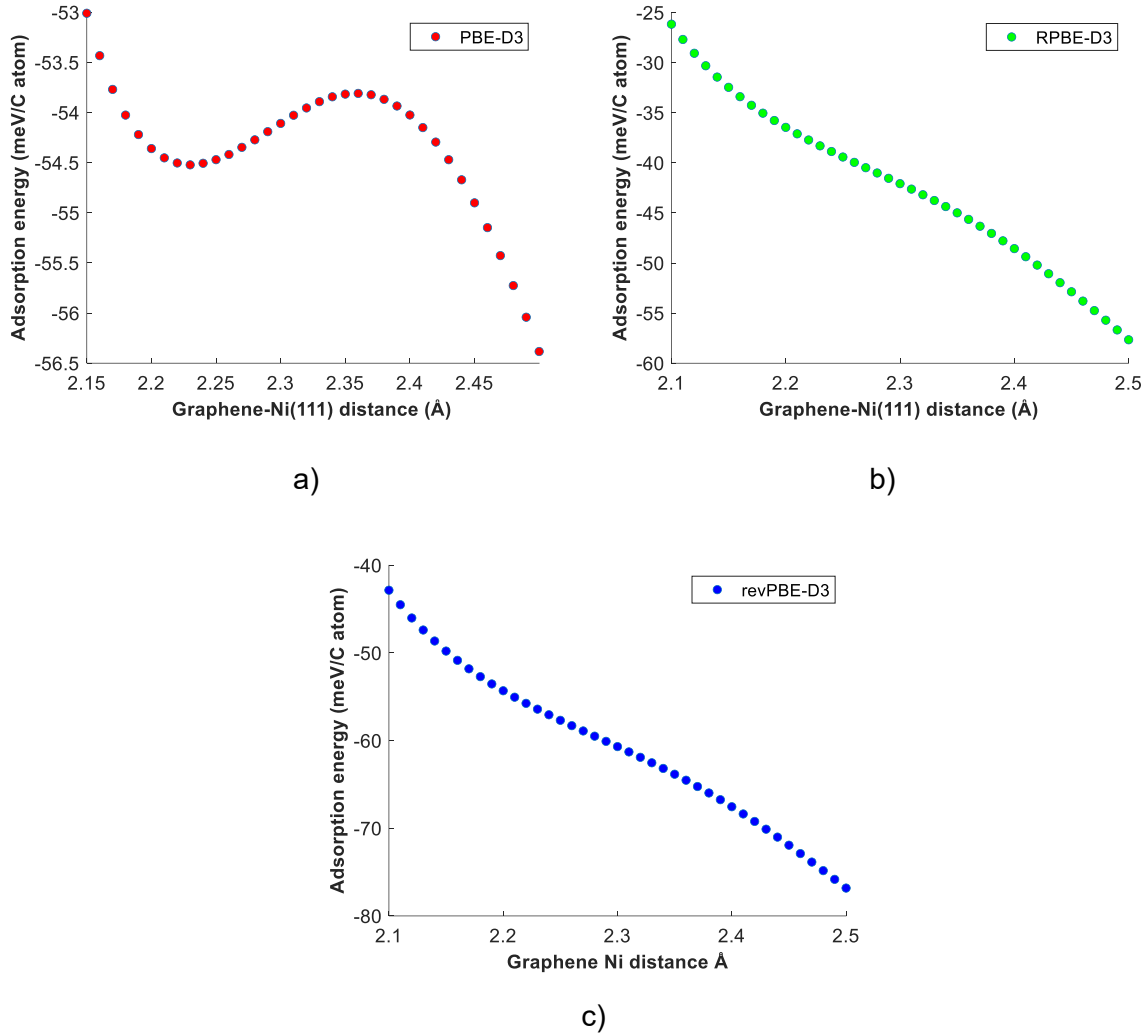


Figure 6: Potential energy profiles of graphene-Ni(111): (a) PBE-D3 functional, (b) RPBE-D3 functional and (c) revPBE-D3 functional. The adsorption energy is equivalent to  $-E_{\text{bind}}^{\text{DFT}}$  (obtained using eq. 64). The complete graphene-Ni(111) potential energy scans (up to the second minimum) of DFT-D3 functionals are provided in the SI (refer to Figure A6).

As shown in Figure 5, the PBE-TS functional significantly overestimates the graphene binding propensity on the Ni(111) crystal. The PBE-D3 and PBE-dDsC functionals predict the binding energy of graphene in reasonable agreement with RPA. However, the predictions of both functionals are substantially lower than the experimental value, though there is quite some uncertainty in the latter, as discussed earlier. The benchmark studies of Muñoz-Galán et al.<sup>125</sup>

and Janthon et al.<sup>124</sup> also conclude that the PBE-D3 functional is an appropriate choice to describe the graphene-Ni(111) interactions. On the other hand, the DFT calculations of RPBE-D3 and revPBE-D3 functionals do not converge to the first minimum of graphene-Ni(111). These functionals show a qualitative disagreement with the RPA prediction at the first minimum of graphene-Ni(111). In an effort to further substantiate these results, the potential energy profiles of graphene-Ni(111) were generated for the DFT-D3 functionals. It is evident from Figure 6(a) that a shallow minimum at a graphene-Ni distance of 2.23 Å is obtained using the PBE-D3 functional. In contrast, the potential energy profiles of RPBE-D3 and revPBE-D3 functionals predict no such minimum at a graphene-Ni distance range of 2.10–2.50 Å, and thus, both functionals do not give an accurate description of graphene-Ni(111) interactions at the first minimum (refer to Figure 6(b) and Figure 6(c)).

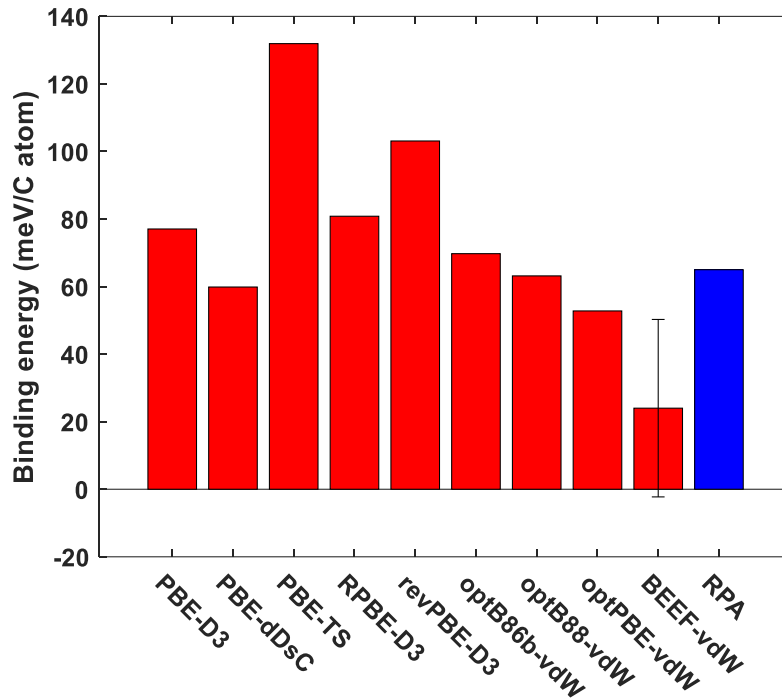


Figure 7: Comparison of the binding energy predictions of the DFT functionals used in this study with the RPA value<sup>140,141</sup> at the second minimum of graphene-Ni(111).

At the second minimum of graphene-Ni(111) i.e. the one predicted by RPA (at a graphene-Ni distance of 3.25 Å), the hcp-fcc geometry is reported to be the most stable binding configuration.<sup>124</sup> Even though this binding configuration of graphene may be of limited interest, as there is no experimental evidence for it yet, it is instructive to compare the pertinent DFT predictions with the RPA value.<sup>140,141</sup> Thus, Figure 7 shows that the PBE-D3, PBE-dDsC, RPBE-D3, optB86b-dW, optB88-vdW and optPBE-vdW functionals predict the binding energy of the second minimum of graphene in fair agreement with the RPA value. Taken together, the

results of our benchmark studies show that the graphene-Ni(111) interactions are best represented by the optB88-vdW functional. The optB86b-vdW, PBE-D3, PBE-dDsC, and optPBE-vdW functionals also perform reasonably well.

### 3.3.2 DFT benchmarks of MSR species

In a second set of benchmark calculations, the DFT functionals were used to estimate the reaction energies of methane dissociative adsorption, carbon oxidation, and the binding energies of representative species of the MSR reaction, in particular: CO, C, CH<sub>3</sub>, H<sub>2</sub>O, H, O and OH on Ni(111). The predictions of these functionals have been systematically compared against experimental data, the sources of which are compiled in Table 2. The binding sites of the MSR species are provided in Appendix I (refer to Figure A4). For each MSR species under study, Table 2 reports the pertinent adsorption reaction, the details of the experiment that we compare against, the simulation setup of the corresponding DFT calculation (this information is provided as a footnote in Table 2), and finally, the value of the experimental binding energy. In Table 2, ML is defined to be the ratio of number of adsorbate atoms/molecules to the number of Ni atoms on the Ni(111) surface. An important caveat to be noted is that the experimental surface coverage of carbon is not clearly known (refer to the last row of Table 2 for more details), therefore, certain caution is exercised while comparing DFT predictions to the experimental binding energy of carbon.

In Table 3, the experimental values and the DFT predictions of MSR species are systematically recorded. The colour code in Table 3 gives an indication on the extent of deviation of the DFT prediction from the corresponding experimental value (the convention of the colour code is stated as a footnote in Table 3). As shown in Figure 8, the deviations of the DFT predictions from the experimental values have been presented using radar plots. Furthermore, the RMSD values have been computed to make a quantitative assessment on the overall performance of the DFT functionals (refer to Figure 9).

**Table 2. The experimental binding/reaction energies of MSR species obtained from the literature**

System	Experimental method	$U_{bind}^{exp}$ (eV)
$\text{CO(g)} + * \rightleftharpoons \text{CO}^*$	The differential heat of adsorption of CO on Ni(111) is recorded at the limit of zero-coverage using calorimetry. The temperature is maintained at 300 K.	1.32 <sup>a,b</sup> ( $\pm 0.03$ ) (ref. 145)
$\text{D}_2\text{O(g)} + * \rightleftharpoons \text{D}_2\text{O}^*$	The single-crystal adsorption calorimetry (SCAC) method is employed to study the molecular adsorption of D <sub>2</sub> O on Ni(111). The differential heat of D <sub>2</sub> O adsorption has been reported at 100 K and zero-coverage limit.	0.55 <sup>a,b,e</sup> (ref. 146)
$\text{H}_2\text{(g)} + 2* \rightleftharpoons 2\text{H}^*$	The associative desorption of hydrogen is studied using flash desorption spectroscopy. The desorption of H/Ni(111) has been observed to follow second-order kinetics at low coverages. The Arrhenius activation barrier of associative desorption of hydrogen has been estimated.	0.98 <sup>a,c</sup> ( $\pm 0.04$ ) (ref. 147)
$\text{O}_2\text{(g)} + 2* \rightleftharpoons 2\text{O}^*$	The dissociative adsorption of O <sub>2</sub> on Ni(111) is studied using SCAC at 300 K. The heat of adsorption of oxygen is reported at the zero-coverage limit.	4.53 <sup>a,b</sup> ( $\pm 0.2$ ) (ref. 148)
$\text{OD(g)} + * \rightleftharpoons \text{OD}^*$	The SCAC method is used to study oxygen assisted D <sub>2</sub> O dissociation on Ni(111). The heat of adsorption of OD-Ni(111) is derived using thermodynamic cycles (at 0.5 ML coverage).	3.26 <sup>b,d,e</sup> (ref. 146)
$\text{CH}_3\text{(g)} + * \rightleftharpoons \text{CH}_3^*$	The dissociative adsorption of methyl iodide is studied using SCAC at 160 K. The heat of methyl adsorption is obtained via thermodynamic cycles.	2.25 <sup>a,b</sup> ( $\pm 0.14$ ) (ref. 149)
$\text{CH}_4\text{(g)} + 2* \rightleftharpoons \text{CH}_3^* + \text{H}^*$	Carey et al. <sup>149</sup> estimated the enthalpy of methane dissociation at 160 K by using the experimental heats of adsorption of CH <sub>3</sub> and H on Ni(111) (obtained from calorimetric studies), and the heat of formation of CH <sub>4</sub> (g).	0.43 <sup>a,b,f</sup> (ref. 149)
$\text{C(g)} + * \rightleftharpoons \text{C}^*$	The isosteric heat of formation of carbon (at 600 K) is derived from the Boudouard equilibrium. The study is conducted using alumina-supported polycrystalline Ni. The carbon coverage is defined to be half of the saturation coverage of CO at 195 K. According to Netzer and Madey <sup>150</sup> , the CO adsorbate has a saturation coverage of around 0.57 ML on Ni(111) (at temperatures 220-240 K). Using this information, the carbon coverage might be around 0.29 ML.	6.84 <sup>a,b</sup> (ref. 151)
$\text{C}^* + (\frac{1}{2})\text{O}_2\text{(g)} \rightleftharpoons \text{CO(g)}$	The reaction energy of “carbon oxidation” (to form carbon on Ni(111) and O <sub>2</sub> (g)) is derived using the experimental carbon adsorption energy (with respect to C(g)) and the CO gas-phase formation energy (obtained from the atomisation energies dataset of CCSD(T) <sup>152</sup> ). The value is reported at 0 K (the ZPE/thermal contributions of “carbon adsorption” reaction is removed using the PBE functional prediction).	1.71 <sup>a,f</sup> (refs. 151,152)

- a) The DFT simulation setup as stated in the “Methods” section is used for estimating the binding energy of the adsorbate. The coverage of the adsorbate on the Ni(111) supercell is 0.0625 ML.
- b) The experimental internal energy of adsorption is reported (the heat of adsorption obtained from the experiment is reduced by  $k_B T$ ).<sup>153</sup> This value is compared to the DFT prediction  $U_{bind}^{theory}$ .
- c) The Arrhenius activation barrier obtained from flash desorption studies of hydrogen was compared to the ZPE-corrected DFT energy prediction (no thermal corrections were included, only eq. 65, eq. 66 and eq. 67 of section 3.2 were used in this case).
- d) Since the experimental surface coverage is 0.5 ML, a p(2×2) Ni(111) supercell (constituting two OH atoms adsorbed on the three-fold hollow sites) has been used and the Brillouin zone integration was done with a 10×10×1 k-point grid.
- e) The kinetic isotope effects are assumed to be negligible.
- f) By convention, a positive value indicates exothermic reaction, in which case the dissociative adsorption is favourable. A negative value indicates endothermic dissociative adsorption (not favoured).

The oxygen binding energy predictions (reported in Table 3) have been computed with reference to O<sub>2</sub> gas-phase DFT energy. It is known that the triplet (ground) state of O<sub>2</sub> is poorly captured by DFT calculations; hence, the O<sub>2</sub> gas-phase energy obtained may exhibit low accuracy. Alternatively, the O<sub>2</sub> gas-phase energy can be estimated from H<sub>2</sub>O gas-phase formation energy (obtained from the literature),<sup>128</sup> H<sub>2</sub> gas-phase energy and H<sub>2</sub>O gas-phase energy (both these energies are calculated using DFT). However, this alternative approach was found to further deteriorate the performance of most of the DFT functionals. The results of oxygen binding energies obtained using aforementioned approaches are provided in Appendix I (refer to Table A3). Similarly, the O<sub>2</sub>(g) DFT energy has been used to calculate the reaction energy of carbon oxidation ( $C^* + (\frac{1}{2})O_2(g) \rightleftharpoons CO(g)$ ).

The PBE functional predicts the reaction energy of methane dissociation with reasonable accuracy (the deviation is -0.23 eV). It performs appreciably well for MSR species such as hydrogen, oxygen and hydroxyl. The PBE functional overpredicts the binding energy of carbon monoxide by more than 0.5 eV (as depicted in Figure 8(a)). In the literature, it is well established that the PBE exchange-correlation approximation fails to accurately predict the binding energy of carbon monoxide.<sup>128</sup> The PBE functional underpredicts the binding energy of H<sub>2</sub>O, as it does not include the dispersive interactions between H<sub>2</sub>O and Ni(111). Zhu et al.<sup>126</sup> also report the same behaviour for the PBE functional. As shown in Table 3 and Figure 8(a), the PBE functional accurately estimates the carbon binding energy and the reaction energy of carbon oxidation (however, we note again that the experimental value of carbon might be subject to finite coverage effects).

The RPBE and revPBE functionals give a better estimate of CO binding energy than the other DFT functionals tested in this study (as shown in Figure 8(a) and Table 3). However, the predictions of these functionals deviate significantly from the experimental binding energies of CH<sub>3</sub>, O, OH, H<sub>2</sub>O and C. Furthermore, both functionals predict that the methane dissociation reaction on Ni(111) is an endothermic elementary event (this is qualitatively incorrect as methane dissociates exothermically on Ni(111); refer to Table 3). As shown in Figure 9, the PBE functional has better overall performance than other GGA functionals. Nonetheless, the GGA functionals do not account for the dispersive interactions of graphene-Ni(111) (as stated in section 3.3.1), and therefore, they are not suitable to investigate the carbon poisoning mechanism of Ni in the MSR reaction.

**Table 3. Comparisons of DFT predictions with experimental values of MSR species**

Method	Binding/reaction energy (eV)								
	CO	H <sub>2</sub> O	2×H	2×O	OH	C	CH <sub>3</sub>	CH <sub>4</sub> -diss	C-oxid
Expt.	1.32 (±0.03)	0.55	0.98 (±0.04)	4.53 (±0.2)	3.26	6.84	2.25 (±0.14)	0.43	1.71
PBE	1.88	0.25	1.04	4.68	3.15	6.83	1.88	0.20	1.69
RPBE	1.48	0.05	0.71	4.13	2.78	6.37	1.43	-0.29	1.94
revPBE	1.54	0.05	0.76	4.20	2.82 <sup>a</sup>	6.43	1.49	-0.22	1.90
PBE-D3	2.06	0.48	1.24	4.75	3.29 <sup>a</sup>	6.91	2.25	0.68	1.61
RPBE-D3	1.79	0.40	1.00	4.27	3.02	6.52	1.99	0.40	1.78
revPBE-D3	1.86	0.46	1.09	4.34	3.06 <sup>a</sup>	6.59	2.15	0.60	1.73
PBE-dDsC	2.03	0.41	1.13	4.79	3.52 <sup>g,h</sup>	6.95	2.12	0.49	1.58
PBE-TS	2.20	0.59	1.21	4.63	3.46	6.93	2.38	0.78	1.59
optB86b-vdW	2.11	0.48	1.07	5.25	3.41 <sup>a</sup>	6.98	2.31	0.60	1.57
optB88-vdW	1.95 <sup>b</sup>	0.44 <sup>c</sup>	0.94	5.28 <sup>d</sup>	3.37 <sup>e</sup>	6.85	2.11 <sup>f</sup>	0.39	1.74
optPBE-vdW	1.82	0.39	0.84	5.06	3.24	6.69	1.97	0.24	1.82
BEEF-vdW	1.55 (±0.18)	0.23 (±0.17)	0.61 (±0.20)	4.44 (±0.46)	2.98 <sup>a</sup> (±0.21)	6.34 (±0.26)	1.62 (±0.26)	-0.13 (±0.30)	2.05 (±0.27)

Deviation = |DFT predicted value – Experimental value|. The colour code has the following convention: **green**: Deviation < 0.1 eV, **yellow**: 0.1 eV ≤ Deviation ≤ 0.3 eV, **red**: Deviation > 0.3 eV. The following modifications were introduced to alleviate the convergence issues of a few calculations: a) The vibrational calculations of OH in the gas phase was performed for the DFT functionals revPBE, PBE-D3, revPBE-D3, optB86b-vdW and BEEF-vdW using electronic minimisation tolerance values of 5×10<sup>-5</sup> eV, 1×10<sup>-5</sup> eV, 1×10<sup>-6</sup> eV, 3×10<sup>-5</sup> eV and 1×10<sup>-5</sup> eV, respectively. b) The geometric optimisation and vibrational analysis of CO in the gas phase were performed by setting the electronic minimisation tolerance value to 5×10<sup>-6</sup> eV. c) The vibrational calculation of H<sub>2</sub>O in the gas phase was carried out with an electronic minimisation tolerance value of 10<sup>-6</sup> eV. d) The geometric optimisation and vibrational analysis of O<sub>2</sub> in the gas phase were performed by setting the electronic minimisation tolerance value to 10<sup>-6</sup> eV. e) The geometric optimisation and vibrational calculations of OH in the gas phase were carried out using electronic minimisation tolerance values of 10<sup>-6</sup> eV and 10<sup>-5</sup> eV, respectively. f) The geometric optimisation and vibrational analysis of CH<sub>3</sub>(g) were performed with an electronic minimisation tolerance value of 10<sup>-6</sup> eV. g) The OH-Ni(111) DFT calculation was executed with a geometric optimisation tolerance value of 0.02 eV/Å. h) The vibrational analysis of OH gas-phase was performed with an electronic minimisation tolerance value of 10<sup>-6</sup> eV.

It can be inferred from Table 3 and Figure 8(b) that the performance of functionals within the vdW-DF class is unsatisfactory. Although optB86b-vdW and optB88-vdW functionals predict the reaction energies of methane dissociation and carbon oxidation, and the binding energies of CH<sub>3</sub>, H<sub>2</sub>O, H and C with acceptable accuracy, both functionals perform poorly for species such as CO and O (as depicted in Figure 8(b)). In agreement with the findings of our study,



Hensley et al.<sup>154</sup> also report that the optB86b-vdW and optB88-vdW functionals do not predict the binding energies of CO with acceptable accuracy. The RMSD values of optB86b-vdW and optB88-vdW functionals are 0.37 eV and 0.33 eV, respectively, which is much higher than most of the other dispersion-inclusive DFT functionals (refer to Figure 9). Thus, neither of these functionals appear promising for studying graphene formation in the MSR reaction.

The BEEF-vdW functional provides a better prediction of the CO binding energy than other vdW-DF (the deviation from experimental value is 0.23 eV; Wellendorf et al.<sup>128</sup> report a similar result for this functional). Nonetheless, the BEEF-vdW functional exhibits large deviations in estimating the reaction energy of carbon oxidation and the binding energies of MSR species such as H<sub>2</sub>O, H, C and CH<sub>3</sub> (as illustrated in Figure 8(b)). It predicts the dissociative adsorption of methane on Ni(111) to be an endothermic step (this result is not in qualitative agreement with the experimental value; refer to Table 3). The computational error predictions of the BEEF-vdW functional range from 0.17 to 0.3 eV in most cases, except for O<sub>2</sub> dissociative adsorption (at infinite separation), for which the BEEF-vdW gives a computational error of 0.46 eV (as shown in Table 3). The BEEF-vdW functional has the highest RMSD score among all the dispersion-inclusive DFT functionals benchmarked in this study (refer to Figure 9); which makes it unsuitable for the graphene-MSR system. The optPBE-vdW functional predicts the binding energy of OH with high accuracy. For species such as H<sub>2</sub>O, H and C, the optPBE-vdW functional produces deviations within an acceptable range (0.14–0.16 eV). It estimates the reaction energy of methane dissociation with reasonable accuracy (the deviation is 0.19 eV). The optPBE-vdW deviations for carbon oxidation reaction energy and CH<sub>3</sub> binding energy are 0.11 eV and -0.27 eV, respectively. In the case of species such as CO and O, the predictions of optPBE-vdW are in poor agreement with experimental data (refer to Table 3 and Figure 8(b)). Nevertheless, the optPBE-vdW functional has a much better overall performance. The RMSD score of optPBE-vdW functional is 0.28 eV, which is substantially lower than the other vdW-DF (as shown in Figure 9). Furthermore, as discussed in section 3.1, the optPBE-vdW functional predicts the first minimum of graphene with reasonable accuracy. Therefore, among the vdW-DF, the optPBE-vdW functional can be considered to study the chemistry of carbon poisoning on Ni(111) (with appropriate corrections to CO and O binding energy values).

In contrast to vdW-DF, the DFT-D functionals perform reasonably well for this system. The deviations of DFT-D functionals are less than or equal to 0.35 eV for all MSR species except CO (refer to Figure 8(c)). As depicted in Figure 9, the RMSD values of RPBE-D3 and revPBE-D3 functionals are lower than the other dispersion-inclusive functionals tested in this study. These two functionals predict with acceptable accuracy the reaction energies of methane dissociation and carbon oxidation, and the binding energies of MSR species (H, H<sub>2</sub>O, CH<sub>3</sub>, OH), though, in the case of CO, they exhibit significant deviations from the experimental data

(refer to Table 3 and Figure 8(c)). However, these two functionals do not capture the first minimum of graphene on Ni(111) (as discussed in subsection 3.3.1).

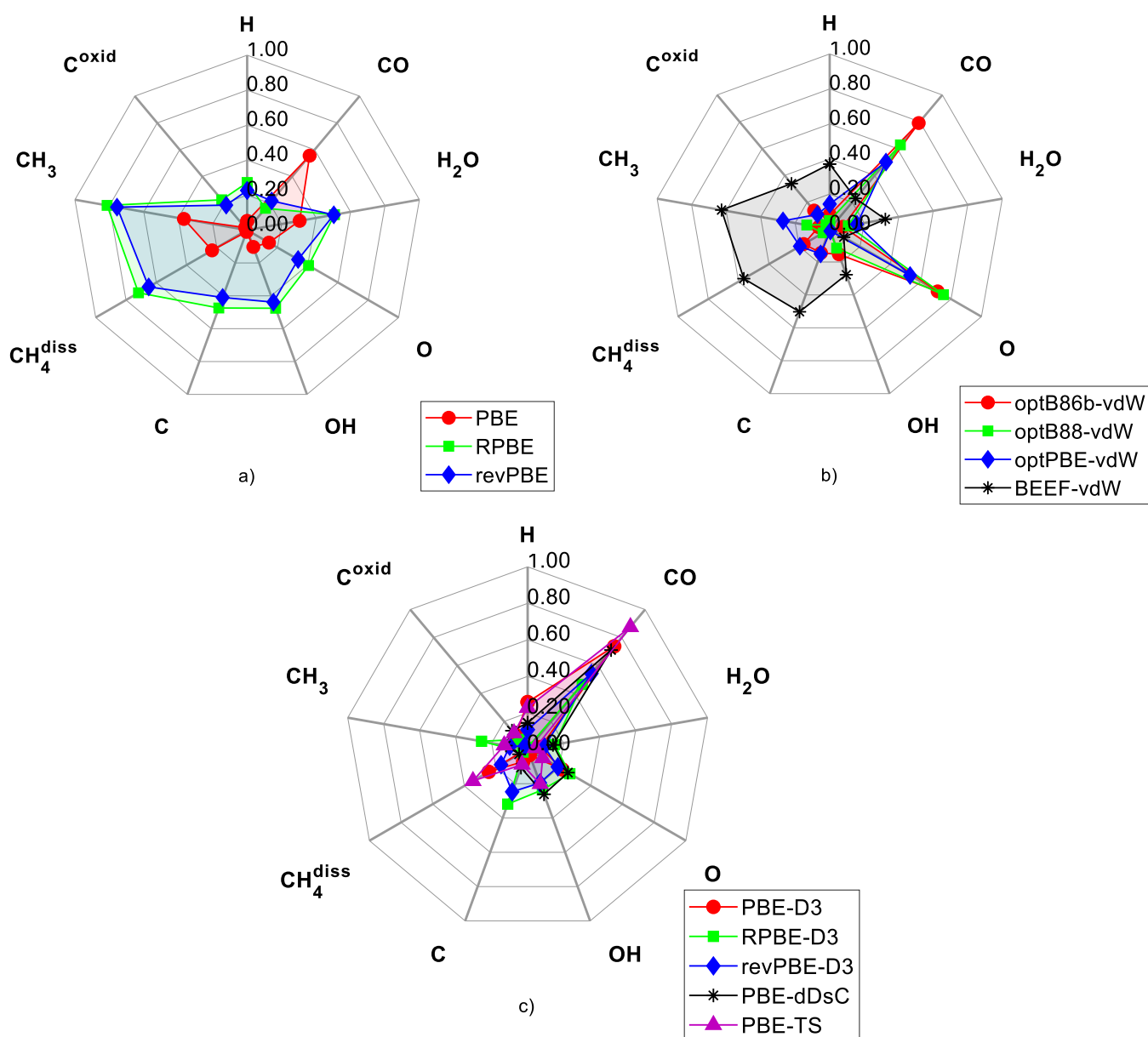


Figure 8: Performance of the DFT functionals in capturing MSR species binding energies, depicted using radar plots of Deviation = |DFT predicted value – Experimental value| (in units of eV). (a) GGA functionals, (b) vdW-DF functionals and (c) DFT-D functionals.

The dispersion-corrected flavours of PBE; namely, PBE-TS, PBE-D3 and PBE-dDsC functionals produce interesting results. It is important to note that the aforementioned functionals significantly overestimate the CO binding energy. This behaviour is expected as the PBE approximation yields a poor description of CO adsorption (the deviation is 0.56 eV), and upon inclusion of dispersion corrections, the deviation from the CO experimental binding

energy value is further exacerbated. The PBE-TS functional has high predictive accuracy for species such as H<sub>2</sub>O, O and C (as illustrated in Figure 8(c), with deviations that are less than 0.1 eV). It predicts the binding energies of CH<sub>3</sub>, H and OH with deviations 0.13 eV, 0.23 eV and 0.20 eV, respectively (these deviations are within the acceptable range). Göttl et al.<sup>127</sup> have also obtained similar results for CH<sub>3</sub> and H using the PBE-TS functional. In the case of CH<sub>4</sub> dissociative adsorption, the PBE-TS functional overestimates the reaction energy by 0.35 eV. The inaccurate prediction of CO adsorption and CH<sub>4</sub> dissociative adsorption mainly contribute to the high RMSD value of PBE-TS functional. Furthermore, the PBE-TS functional significantly overpredicts the graphene binding energy on Ni(111) (as discussed in subsection 3.3.1). Thus, the PBE-TS functional is not an appropriate choice.

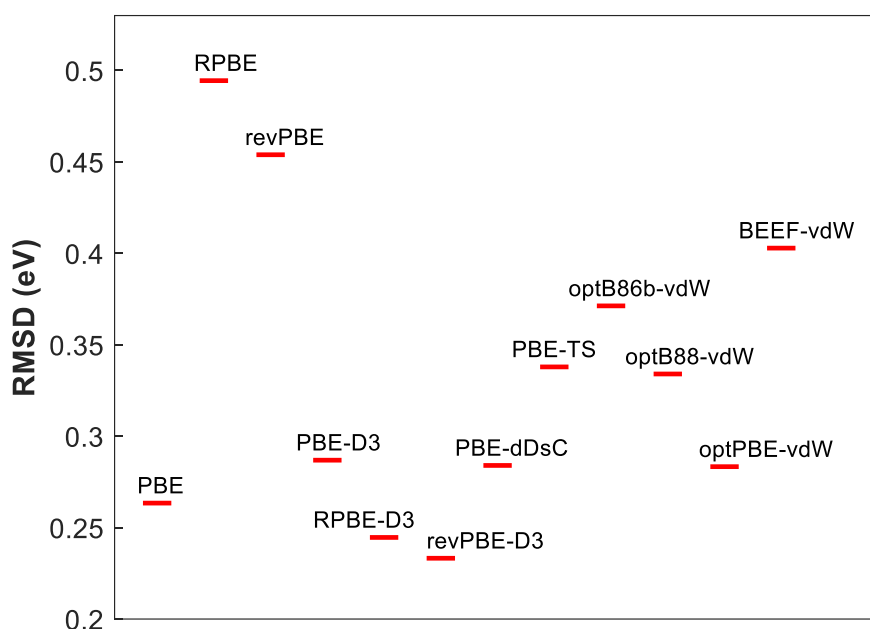


Figure 9: RMSD values (obtained using eq. 71) of the DFT functionals considered in this study.

The PBE-D3 functional predicts the binding energies of OH and C with appreciable accuracy. It provides a good description of the H<sub>2</sub>O-Ni(111) interactions, whereas, the hydrogen binding energy is substantially overestimated; Zhu et al.<sup>126</sup> have also made similar observations. According to Table 3, PBE-D3 predicts the CH<sub>3</sub> binding energy to be 2.25 eV, which agrees closely with the experimental result. Furthermore, it has been found to predict with reasonable accuracy the reaction energies of methane dissociation and carbon oxidation, as well as the oxygen binding energy (the deviations are less than 0.25 eV; refer to Figure 8(c)). In a recent study, Göttl et al.<sup>127</sup> have reported that the PBE-D3 functional provides accurate estimates of the CH<sub>3</sub> binding energy and the reaction energy of CH<sub>4</sub> dissociation. The PBE-dDsC functional

exhibits excellent predictive accuracy in estimating the reaction energy of methane dissociation. It predicts the reaction energy of carbon oxidation and the binding energies of H, H<sub>2</sub>O, C and CH<sub>3</sub> within a deviation range of 0.10-0.15 eV. In the case of O and OH, the PBE-dDsC predictions deviate from the experimental data by around 0.25 eV (as shown in Figure 8(c) and Table 3).

The predictions of PBE-D3 and PBE-dDsC functionals agree well with most MSR species (all the deviations lie well within 0.3 eV excluding CO). Both functionals have similar overall predictive capability for MSR intermediates – the RMSD values of these functionals are around 0.30 eV (as shown in Figure 9). They also account for the graphene-Ni(111) interactions with acceptable accuracy (refer to Table 1 of subsection 3.3.1). In summary, the PBE-D3 and PBE-dDsC functionals perform better than the other DFT functionals tested in this work, and thus, make suitable choices for understanding the chemistry of graphene formation in the MSR reaction.

Overall, the benchmark studies of graphene and MSR species give us some useful insights into the predictive accuracy of DFT-D and vdW-DF functionals. Comparisons with RPA calculations (which accurately capture the van der Waals interactions) reveal that the optB88-vdW functional predicts the binding energy of graphene with excellent accuracy. The PBE-D3, PBE-dDsC and optPBE-vdW functionals also show reasonable agreement with the RPA prediction of graphene-Ni(111). On the other hand, the BEEF-vdW functional was found to produce a weak repulsive interaction between graphene and Ni(111). Moreover, the RPBE-D3 and revPBE-D3 functionals do not generate the first minimum of the graphene-Ni(111) system. The DFT benchmarks of the MSR species reveal that the vdW-DF exhibit large deviations for species such as CO and O. Among the vdW-DF, the optPBE-vdW functional has the best overall performance; it can be considered for studying graphene-MSR chemistry on Ni(111) (appropriate corrections need to be made for CO and O intermediates). In the case of DFT-D functionals, the PBE-D3 and PBE-dDsC functionals predict with acceptable accuracy the binding energies of most MSR species (except CO), as well as the reaction energies of dissociative adsorption of methane (an important elementary step of MSR) and carbon oxidation. These functionals also provide a good description of the van der Waals interactions of graphene-Ni(111). Overall, the PBE-D3 and PBE-dDsC functionals are promising for more detailed studies to understand the carbon poisoning chemistry of Ni(111) in the MSR reaction (suitable corrections are required for the CO binding energy predictions of these functionals).

### 3.4 Conclusions

Detailed DFT studies of the MSR reaction on Ni can provide valuable mechanistic insight on catalyst poisoning and deactivation phenomena, which have a severe impact on industrial operations. At the molecular scale, the poisoning mechanism primarily involves the formation of graphene islands; thus, the accurate description of graphene-Ni(111) interactions is paramount to develop a reliable carbon poisoning model for MSR. Graphene binds in a commensurate manner to the Ni(111) surface and its accurate description necessitates taking into account local as well as non-local interactions (van der Waals forces) using appropriate DFT functionals. In addition, to ensure an accurate description of the MSR chemistry, including the pathways that lead to poisoning precursors, these functionals should be able to faithfully reproduce the binding of key intermediates within these pathways. GGA functionals fail to capture the dispersion interactions of graphene-Ni(111), however, dispersion-inclusive functionals, such as DFT-D and vdW-DF could be effectively used to this end. Indeed, several studies have shown that some of the DFT-D functionals and vdW-DF are promising for the graphene-Ni(111) system. However, there is little evidence on the accuracy of these functionals in predicting binding energies of important MSR intermediates.

In this chapter, a systematic benchmark analysis has been carried out to assess the performance of DFT-D functionals and vdW-DF in predicting the binding energies of graphene and MSR species, and the reaction energies of methane dissociation and carbon oxidation on Ni(111). The optB88-vdW, optB86b-vdW, optPBE-vdW, PBE-D3 and PBE-dDsC functionals have been found to yield promising results for graphene-Ni(111). The DFT predictions for the binding energies of key MSR species have been compared to experimental data from calorimetric and flash desorption studies available in the literature. The vdW-DF exhibit large RMSD values with respect to experimental data of MSR species. Nonetheless, among the vdW-DF, the optPBE-vdW functional is an appropriate choice for the graphene-MSR system. The DFT-D functionals exhibit a much better performance than the vdW-DF in predicting the binding energies of MSR species. In the case of DFT-D functionals, PBE-D3 and PBE-dDSC functionals appear to be suitable choices for investigations of carbon poisoning of Ni(111) in the MSR reaction.

Our analysis shows that none of the DFT functionals considered were found to predict the binding energies of all the key MSR species with equally high accuracy. The RMSD values of DFT functionals fall in the range of 0.2-0.5 eV, which indicates that there is scope for further improving the predictive accuracy of DFT. Although optB88-vdW accurately accounts for the van der Waals interactions of graphene-Ni(111), it significantly overestimates the binding energies of important MSR intermediates such as O and CO. Moreover, the RPBE-D3 and revPBE-D3 functionals do not reproduce the experimentally observed binding configuration of

graphene on Ni(111), the “first minimum” at a distance of  $2.11 \pm 0.07$  Å, despite having dispersion correction terms in their formulations. Furthermore, our analysis can guide the catalysis community in the selection of appropriate DFT functionals for future MSR studies.

Overall, we recognise that the performance of the DFT functionals is far from perfect. Nevertheless, our work and literature studies show that the PBE-D3 functional captures the graphene-Ni(111) interactions with acceptable accuracy.<sup>124,125</sup> The graphene binding energy prediction of PBE-D3 is reasonably close to RPA value (which is the “gold standard” method for systems with vdW interactions).<sup>124</sup> Among the DFT functionals that are applicable for the graphene-Ni(111) (tested in this study), the PBE-D3, PBE-dDsC and optPBE-vdW have the best overall predictive accuracy in capturing the binding energies of important MSR adsorbates (refer to Figure 9). In comparison to PBE-dDsC and optPBE-vdW, the PBE-D3 functional is computationally less expensive and has little to no convergence issues. Therefore, based on the benchmark analysis of current state-of-the-art DFT functionals and computational resource availability, we decided to proceed with the PBE-D3 functional to carry out the kinetic studies of coking and MSR reaction.

# Chapter 4

#### 4. Assessing the impact of adlayer description fidelity on theoretical predictions of coking on Ni(111) at steam reforming conditions

Coking is the accumulation of a stable poison over time, occurring at high temperatures; thus, to a first approximation, it can be treated as a thermodynamic problem. In this chapter, we developed an *ab-initio* KMC model for methane cracking on Ni(111) at steam reforming conditions. The model captures C-H activation kinetics in detail, while graphene sheet formation is described at the level of thermodynamics, to obtain insight into the “terminal (poisoned) state” of graphene/coke within reasonable computational times. We used CEs of progressively higher fidelity (in the KMC model) to systematically assess the influence of effective cluster interactions between adsorbed or covalently bonded C and CH species on “terminal state” morphology. We compared the predictions of KMC models incorporating these CEs to mean-field MK models in a consistent manner. Furthermore, we identify the conditions where Ni is susceptible to poisoning. *The contents of this chapter have been published in The Journal of Physical Chemistry C, 127(18), pp. 8591-8606.*

##### 4.1 Introduction

In recent times, a few DFT studies have attempted to elucidate the thermodynamic stability of long-range carbon configurations such as chains, branches and rings on Ni(111).<sup>155-157</sup> Wang et al.<sup>155</sup> calculated the binding energies of atomic carbon, carbon clusters (C<sub>2</sub>-C<sub>4</sub>) and graphene on Ni(111), and reported that graphene is thermodynamically the most stable configuration on Ni(111). Li et al.<sup>157</sup> used DFT to find the optimised structures/energetics of carbon clusters such as chains, rings and branches (containing up to six carbon atoms) on Ni(111), and concluded that carbon chains have better stability than rings/branches. The aforementioned DFT studies do not account for thermal, entropic and coverage effects, which are important to thoroughly understand the coke formation due to the methane cracking reaction at MSR conditions.<sup>9,54</sup> Recently, Li et al.<sup>158</sup> developed a first-principles-based KMC model for methane cracking on Ni(111), in the context of exploring the growth of carbon nanotubes (CNTs) on Ni. While the model shed light on the key role of surface species diffusion on CNT growth, effective cluster interactions between carbon-based intermediates were neglected.

Typically, DFT-parameterised MK models are employed to study the reaction kinetics of catalytic systems.<sup>45,105</sup> MK models predict important macroscopic observables of interest, such as turnover rates and species coverages at any given reaction condition. In the MK model formulation, mean-field approximations are typically used to account for adsorbate-adsorbate interactions.<sup>159</sup> Several studies in the past have used mean-field MK models to capture the intrinsic kinetics and carbon poisoning chemistry under reforming conditions.<sup>6,10,16,19</sup>



Although mean-field approximations, within the MK framework, adequately take into account adsorbate interactions in some catalytic systems, they usually fail to capture short/long-range correlations, clustering of adsorbates, lattice inhomogeneities and island formation.<sup>50,159,160</sup> In the methane cracking reaction, these effects might play a vital role in the accumulation of coke on Ni. Indeed, the need to systematically capture adsorbate correlation effects of carbon-based species has previously been highlighted in the context of gaining a detailed understanding of the catalyst poisoning at reforming conditions.<sup>10,54</sup>

As discussed previously (in the “Thesis Background” section), KMC simulations have gained significant prominence, as a viable alternative to mean-field MK models, for studying catalytic reactions that involve high species coverages or occur under poisoning conditions. The CE methodology implemented in KMC provides a highly accurate description of adsorbate correlation effects, thereby allowing us to capture in detail the chemistry of complex catalytic reactions.<sup>45,50</sup> Coking is by definition the accumulation of a very stable poison over time, and for the MSR reaction, it happens in the context of a high-temperature process. Thus, to an acceptable first approximation, we are dealing with a thermodynamic problem, not a kinetic one. At long time scales, the most thermodynamically stable species will cover the Ni(111) surface, and thus, under the CE framework, we can capture the detailed energetics of such species to understand the formation of carbon-rich adlayers and identify the conditions where the emergence of coke is favourable. In this work, we developed an *ab-initio* KMC model for the methane cracking reaction on Ni(111), the primary reaction responsible for coke formation (as discussed previously). The model captures in detail the kinetics of the C-H activation steps, while graphene sheet formation is described at the level of thermodynamics, so as to obtain insight into the “terminal state” resulting in catalytic surface poisoning within reasonable computational times. We systematically explored the implications of including effective cluster interaction effects in the methane cracking reaction to understand the terminal state of coke on Ni(111). In the KMC model, we have not considered the diffusion of carbon into the bulk and subsequent precipitation to form Ni carbide. Previous experimental works have argued that the growth of graphene/coke mainly occurs by carbon surface diffusion/agglomeration on the Ni support side<sup>58,161,162</sup> and DFT calculations have also shown that the diffusion barriers to Ni subsurface (around 1.34 eV) and Ni bulk (1.6–1.8 eV) are high.<sup>158</sup> The rest of the chapter is organised as follows. In section 4.2 – Computational details, we provide a thorough discussion about the methods employed in this study, and in section 4.3 – Results and Discussion, the results of the DFT calculations and kinetic simulations (using the MK and KMC approaches) are presented in a systematic way. Finally, in section 4.4 – Conclusions, we provide a detailed discussion on the conclusions/implications of this study and the potential opportunities for future work.

## 4.2 Computational details

### 4.2.1 DFT calculations

We performed spin-polarised plane-wave DFT calculations using VASP 5.4.1. The tolerance value for the electronic (self-consistency) convergence was set to  $10^{-7}$  eV. Our detailed DFT functional screening work (Chapter 3) has shown that PBE-D3 is suitable for the MSR-graphene system. Thus, the PBE-D3 functional has been employed to capture the exchange-correlation effects in this study. The plane wave energy cut-off value was set to 400 eV and the interactions between core and valence electrons were modelled using the projector augmented wave (PAW) potentials.

For the Ni lattice constant optimisation calculations, the tetrahedron method with Blöchl corrections was employed to perform the electron smearing (the smearing width was set to 0.05 eV) and the Brillouin zone was sampled with a  $19 \times 19 \times 1$  k-point mesh. The optimised Ni lattice constant was thus found to be 3.481 Å (which is in reasonable agreement with the experimental Ni lattice constant – 3.524 Å).<sup>127</sup> The Ni(111) surface has been modelled using a six-layer  $p(4 \times 4)$  slab (which has a vacuum height of 12 Å). The Ni atoms of the three bottom-most layers were fixed to their respective bulk positions and the rest were fully relaxed until the Hellmann-Feynman forces reached a value of less than  $10^{-2}$  eV/Å. In the Ni slab calculations, the electrons were smeared by employing the Methfessel-Paxton method (with a smearing width value of 0.1 eV) and the Brillouin zone sampling was performed using a  $5 \times 5 \times 1$  Monkhorst-Pack k-point grid. The geometric optimisation of the adsorbates was conducted by employing the conjugate gradient search algorithm. The transition states (TS) were located by using the dimer<sup>72</sup> and quasi-newton methods. The coordinates of the converged TS structures reported by Blaylock et al.<sup>6</sup> were used as an initial guess (the coordinates of atoms were rescaled to account for the slightly different lattice constants between the two calculation setups). The vibrational frequencies of the converged structures were obtained by evaluating the Hessian matrix with the central finite difference method and a step size for the displacement of 0.02 Å. As shown in Table A18 of Appendix II, all the TS structures have a single imaginary mode, which indicates that these are first-order saddle points on the potential energy surface.

The formation energies of the adsorbates are computed using Ni(111) clean slab, CH<sub>4</sub>(g) and H<sub>2</sub>(g) as reference (refer to eq. 72 below).

$$E_{FE}^A = E_{tot}^{A+slab} - E_{tot}^{Ni(111)} - (mE_{tot}^{CH_4(g)} + nE_{tot}^{H_2(g)}) \quad \text{eq. 72}$$

$$E_{IE}^{AB} = E_{FE}^{AB} - E_{FE}^A - E_{FE}^B \quad \text{eq. 73}$$

In eq. 72,  $E_{tot}^{Ni(111)}$  refers to the DFT total energy of the Ni(111) slab,  $E_{tot}^{A+slab}$  is the DFT total energy of the adsorbate-Ni(111) system,  $E_{tot}^{CH_4(g)}$  represents the gas-phase DFT total energy of methane,  $E_{tot}^{H_2(g)}$  indicates the gas-phase DFT total energy of hydrogen,  $E_{FE}^A$  is the formation energy of the adsorbate. The stoichiometry between the adsorbate and the gas-phase reference species (that is the number of C/H atoms) is balanced out using the real numbers  $m$  and  $n$ . For instance, the formation energy calculation of CH adsorbate would have  $m$  and  $n$  values as 1 and -1.5, respectively. As shown in eq. 73, the interaction energy for any co-adsorbed pair of species A and B ( $E_{IE}^{AB}$ ) is obtained by subtracting the formation energies at infinite separation (the terms  $E_{FE}^A$  and  $E_{FE}^B$ ) from the co-adsorbed state formation energy ( $E_{FE}^{AB}$ ).

#### 4.2.2 Mean-field MK model

As discussed previously (in chapter 2), the MK methodology is derived by reducing the master equation into a system of ordinary differential equations (ODEs) under the assumption of infinitely fast adsorbate diffusions and large lattice size, whereby the correlation effects between adsorbates are neglected. Thus, the information about the spatial distribution of adsorbates on the lattice is lost within the MK framework.<sup>22,102,103</sup> The methane cracking reaction involves 5 elementary reaction events (as shown in Table 5). All reactions are assumed to be reversible. The rate equations for each of these elementary reactions have been written in accordance with the formulation provided in the “Methodology” chapter (refer to all the equations between eq. 56 and eq. 60). The lateral interactions between adsorbates are captured using the Bragg-Williams approximation (refer to eq. 61 of chapter 2). The MK model equations have been solved numerically using the ODE15s solver in MATLAB 2019b.

#### 4.2.3 KMC simulations

The KMC approach does not deliver an explicit solution of the Markovian master equation; rather, it employs a stochastic simulation algorithm to generate trajectories whose statistics follow this equation (as discussed in Chapter 2). The observables of interest can be obtained by time-averaging these stochastic realisations (trajectories) upon reaching steady-state conditions.<sup>22,163</sup> In this work, the KMC simulations have been carried out by using the graph-theoretical KMC software Zacros 3.01.<sup>164</sup>

The preferred binding sites of methane cracking adsorbates are recorded in Table A17 of Appendix II. We have chosen a KMC lattice which comprises top and three-fold hollow sites (where fcc and hcp sites are considered identical). In Figure A9 of Appendix II, the KMC lattice is depicted. The circles and triangles (which are coloured in blue for vacant sites) represent the top and hollow sites, respectively. A lattice of size 10×10 has been used to run the KMC simulations (lattice convergence results are shown in Table A24). In order to reduce the computational cost of KMC simulations, the pre-exponentials of quasi-equilibrated (fast)

events are downscaled systematically by carefully analysing the event occurrence statistics plot throughout the run time of the KMC simulation (the frequency of events is checked for a sliding interval of  $5 \times 10^{-1}$  KMC time units).

The interactions between adsorbates or covalently bonded species have been captured by employing the CE methodology implemented in the graph-theoretical KMC framework by Nielsen et al.<sup>89</sup>. The CE formalism has been discussed in great detail in chapter 2 (refer to section 2.6 of the “Methodology” chapter). The formation energy of any type of C-CH configuration can be accurately represented by using CEs in the KMC simulation. The mathematical formula of the CE framework has been provided in the “Methodology” chapter (refer to eq. 53 and eq. 55).

**Table 4. The CE optimisation metrics for the CH/C DFT configurations**

Metrics	Value
Number of DFT configurations	173
Number of parameters/figures	23
RMSE (meV/site)	52.65
LOOCV score (meV/site)	8.87

In principle, we can include all the possible 1-body, 2-body .... n-body clusters/figures in the CE model to have an exact representation of energy in the KMC simulation. However, this procedure becomes increasingly tedious and computationally expensive for a large dataset of DFT configurations.<sup>96</sup> This problem can be addressed by truncating the CE model using a finite set of optimal clusters/figures, which are obtained by performing CE-based least-squares fitting. The identification and parameterisation of clusters in the CE fitting exercise is a non-trivial task.<sup>97</sup> It involves trial and error, and the decision on when the CE is accurate enough involves the use of metrics such as root-mean-square error (RMSE) and leave-one-out cross-validation (LOOCV) score (this provides a statistical measure of the CE model predictive accuracy).<sup>97,165</sup>

$$RMSE^2 = \frac{1}{N_{conf}} \sum_{i=1}^{N_{conf}} (FE_i^{CE} - FE_i^{DFT})^2 \quad \text{eq. 74}$$

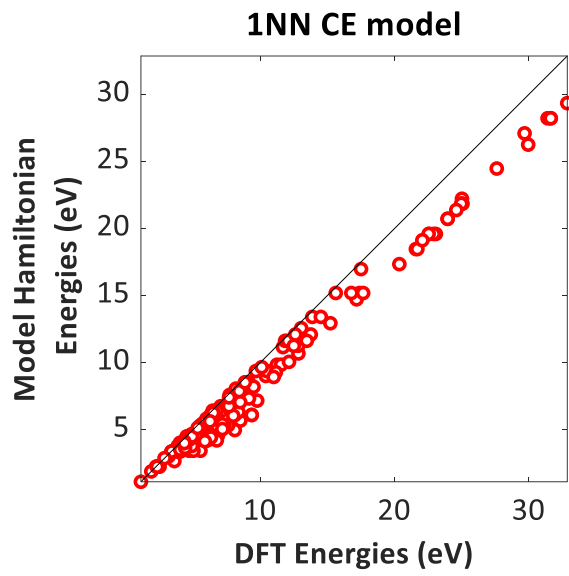
$$CV^2 = \frac{1}{N_{conf}} \sum_{i=1}^{N_{conf}} (FE_{i(i)}^{CE} - FE_i^{DFT})^2 \quad \text{eq. 75}$$

In eq. 74, the formula for obtaining RMSE is shown.  $FE_i^{CE}$  denotes the formation energy of the  $i^{\text{th}}$  configuration, as predicted by the CE (using the entire dataset of  $N_{conf}$  configurations) and  $FE_i^{DFT}$  is the formation energy calculated from DFT. The LOOCV score ( $CV$ ) is computed using

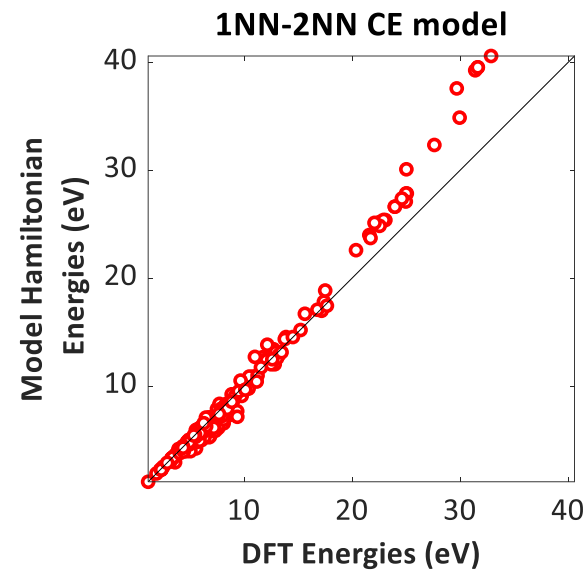
eq. 75, with  $FE_{i(i)}^{CE}$  denoting the formation energy of configuration  $i$ , when configuration  $i$  is omitted from the dataset used for the CE fitting. For more details, we refer the reader to the work by Miller and Kitchen<sup>98</sup>, which includes a discussion and an application of the LOOCV methodology in the context of CE fitting. Briefly, a low LOOCV score ensures high-quality fit of CE parameters.<sup>165</sup> In some cases, the CE model's predictive capability is also benchmarked against experimental data (if available). Furthermore, it is crucial to identify the appropriate number of clusters, as the use of too many clusters in the CE model can lead to overfitting issues.<sup>98</sup> The pairwise effective cluster interaction parameters, as estimated using eq. 73, are recorded in Table A22 of Appendix II. In Figure A9, a schematic for each type of pairwise interaction pattern is provided. We also performed a CE optimisation for a dataset of 173 unique DFT configurations on 4×4 supercells. The dataset mainly comprises rings, branches, and chain type configurations of CH/C species (more details are provided in the “Results and Discussion” section). The statistical metrics of the CE fit are provided in Table 4 – these values are similar to other literature studies where CEs have been employed to capture adlayer energetics.<sup>96,98,165</sup> In Figure A10, Figure A11 and Figure A12 of Appendix II, the schematics of the parameters/figures used for fitting the CE model are illustrated. Furthermore, Cook's distances<sup>99</sup> were estimated for each configuration of the CE dataset (refer to Figure A13 of Appendix II), in order to detect configurations that potentially exert a strong influence on the ECI values obtained from the regression. The Cook's distance for the  $i^{\text{th}}$  configuration has been calculated using the following equation:

$$D_i = \frac{1}{p \text{ MSE}} \sum_{j=1}^{N_{conf}} (FE_j^{CE} - FE_{j(i)}^{CE})^2 \quad \text{eq. 76}$$

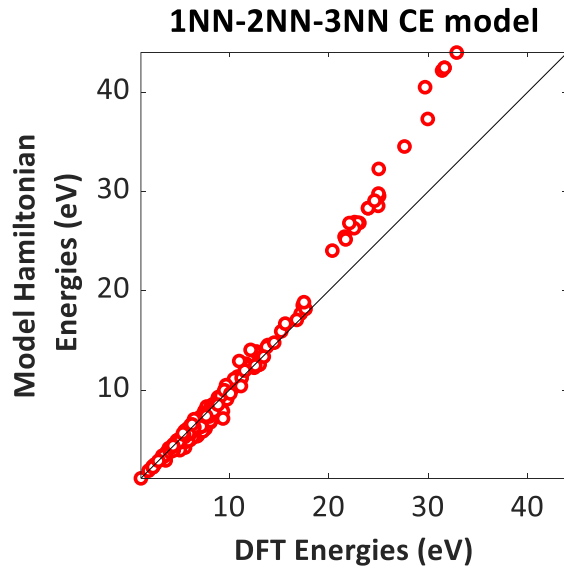
Where  $p$  is the number of parameters/figures of the CE model, MSE represents the mean squared error and  $FE_{j(i)}^{CE}$  is the formation energy of configuration  $j$  obtained after omitting configuration  $i$  in the dataset of CE fitting. The 173 configurations used to fit the CE were constructed in a systematic manner. We started off with one-body, two-body and three-body configurations of C and CH species and fitted the CE with simple parameters/figures. Then, we gradually expanded the dataset to higher-body configurations and used a trial-and-error approach to identify the suitable parameters/figures for our CE model. We consistently used the metrics such as RMSE, LOOCV score and Cook's distances to check the quality of the fit. If any of the metrics were unsatisfactory, we refitted the CE model by removing/including figures. Furthermore, whenever a highly influential configuration was found (as quantified by its Cook's distance), we enriched the dataset with configurations that contained similar motifs, thereby better sampling that region of the configuration space. The DFT dataset includes configurations which have coverage ranging from 0-1 ML.



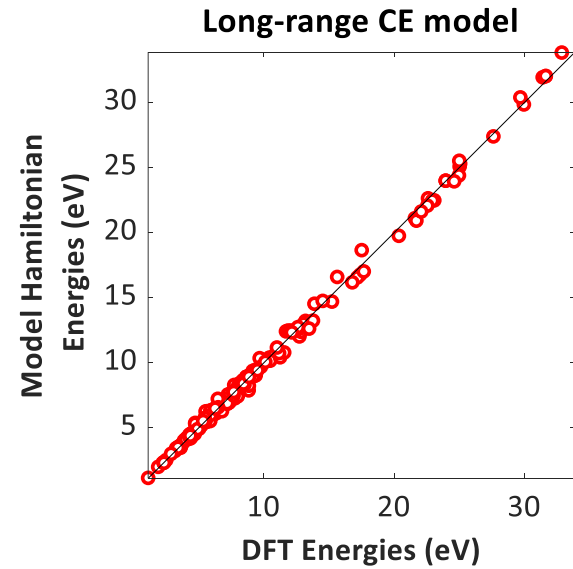
a)



b)



c)



d)

Figure 10: Parity plots of the CEs of KMC models: a) KMC-1NN, b) KMC-1NN-2NN, c) KMC-1NN-2NN-3NN and d) KMC-long-range.

The parity plots of the CEs of all the KMC models (developed in this study) are illustrated in Figure 10. The RMSE values of KMC-1NN, KMC-1NN-2NN, KMC-1NN-2NN-3NN and KMC-long-range CE models are 234.2 meV/site, 252.5 meV/site, 354.4 meV/site and 52.65 meV/site, respectively. It is important to note that the CE parameters/figures of KMC-1NN, KMC-1NN-2NN, KMC-1NN-2NN-3NN models have not been fitted against the DFT dataset (which constitutes the 173 configurations). We remind the readers that the ECI values of CEs of these models are obtained using eq. 73. The parity plots/RMSE values of the four KMC models have been shown/calculated for the purpose of comparing their corresponding predictive accuracies. We can clearly infer from the parity plots (Figure 10) and RMSE values that the KMC-long-range model captures the adlayer energetics with higher accuracy than other KMC models.

#### 4.2.4 Establishment of equivalence between MK and KMC models

In order to make a systematic comparison between MK and KMC models, it is imperative to first obtain equivalent results. The equivalence condition for MK and KMC models is as follows: at the limit of fast diffusions and large system size, without interactions, both MK and KMC models give identical results.<sup>112</sup> There are some “technicalities” involved in establishing equivalence between MK and KMC models; in particular, appropriate geometry factors ( $GM_{fac}$ ) must be included in the MK model equations (as shown in eq. 56 and eq. 57 of the “Methodology” chapter) to account for site connectivity of the lattice. For events in which the reactant patterns are symmetric, the pattern detection algorithm of Zacros double counts the number of instances thereof on the lattice. Thus, the kinetic constants of such events must be corrected by dividing them with the “event-multiplicity” factor. The geometry and event-multiplicity factors for each reaction step of the methane cracking reaction network are provided in Table A21. As stated above, it is critical to ensure that the diffusion events are quasi-equilibrated (fast) to achieve equivalence between MK and KMC models. However, in certain scenarios (especially under high species coverage regimes), it might be necessary to include adsorbate swap diffusions in the KMC simulation to establish equivalence with MK predictions. These are concerted diffusion events which may not necessarily be physically realistic; their role is to ensure better homogenisation of the KMC lattice under “crowded” (high species coverage) conditions.<sup>112</sup> In our study, we have been able to obtain quantitatively similar results for the methane cracking reaction using MK and KMC models at the equivalence condition (more details are provided in section 4.3).

#### 4.2.5 Estimation of pre-exponentials and activation energy parametrization

The first reaction step in the methane cracking reaction involves dissociative adsorption of methane to form methyl and hydrogen on the Ni(111) surface (as shown in Table 5). For an activated dissociative adsorption event, we calculate the forward/reverse rate constants using

eq. 77 and eq. 78 (as defined below). In these equations,  $m_{CH_4}$  is the mass of the methane molecule,  $P_{CH_4}$  represents the pressure of methane gas,  $A_{st}$  is the contact surface area of the Ni atom,  $T$  is the temperature,  $k_B$  is the Boltzmann constant,  $E_{Actfwd}^{finite-coverage}$  represents the coverage-dependent forward activation energy,  $E_{Actrev}^{finite-coverage}$  is coverage-dependent reverse activation energy,  $Q_{trans-2D}$  is the translational partition function of a 2D gas,  $Q_{rot}$  and  $Q_{vib}$  are the rotational and vibrational partition functions, respectively. The formulas of the partition functions are provided in chapter 2 (refer to section 2.4).

$$k_{diss-ads}^{fwd} = \frac{Q_{vib}^{TS}}{Q_{trans-2D}^{IS} Q_{rot}^{IS} Q_{vib}^{IS}} \frac{P_{CH_4} A_{st}}{\sqrt{2 \pi m_{CH_4} k_B T}} \exp\left(-\frac{E_{Actfwd}^{finite-coverage}}{k_B T}\right) \quad \text{eq. 77}$$

$$k_{diss-ads}^{rev} = \frac{k_B T}{h} \frac{Q_{vib}^{TS}}{Q_{vib}^{FS}} \exp\left(-\frac{E_{Actrev}^{finite-coverage}}{k_B T}\right) \quad \text{eq. 78}$$

$$k_{diss-surf}^{fwd} = \frac{k_B T}{h} \frac{Q_{vib}^{TS}}{\prod_{i \in R^{surf}} Q_{vib}^i} \exp\left(-\frac{E_{Actfwd}^{finite-coverage}}{k_B T}\right) \quad \text{eq. 79}$$

$$k_{diss-surf}^{rev} = \frac{k_B T}{h} \frac{Q_{vib}^{TS}}{\prod_{i \in P^{surf}} Q_{vib}^i} \exp\left(-\frac{E_{Actrev}^{finite-coverage}}{k_B T}\right) \quad \text{eq. 80}$$

In the case of surface reactions, the frustrated translations and rotations of chemisorbed species are considered as vibrations. The vibrational partition function is estimated by using the harmonic approximation (refer to eq. 43 in Chapter 2). The forward/reverse rate constants of surface reactions are estimated using eq. 79 and eq. 80 (as shown above). The forward/reverse coverage-dependent activation barriers for any reaction are calculated using the BEP relations (as shown in eq. 62 and eq. 63 of Chapter 2) in MK and KMC models.

#### 4.3 Results and discussion

In this study, we attempted to elucidate the formation of carbon-based poisoning species on the Ni support surface by systematically accounting for effective cluster interactions in the methane cracking reaction (as discussed previously in section 4.1). The methane cracking reaction is a highly correlated system. Thus, the inclusion of interactions between adsorbates or covalently bonded species in the methane cracking reaction can potentially provide us with useful information about the morphology of coke/graphene on the Ni support surface. Moreover, it could lay the groundwork for more complicated models that capture in detail the growth kinetics of the various  $C_xH_y$  coke precursors. With these points in mind, the “Results and discussion” section is structured as follows: we first discuss in detail the nature/magnitude of interactions between carbonaceous species (at 1NN, 2NN and 3NN distances) and present



the DFT dataset of C/CH long-range configurations in section 4.3.1. Next, we compare systematically the MK and KMC predictions of methane cracking and draw conclusions about the influence of interactions on the thermodynamic stability and macroscopic coverages of methane cracking species in section 4.3.2. We subsequently demonstrate lattice configurations obtained from KMC simulations with varying levels of detail in the description of adlayer energetics and develop an understanding of the dependence of the terminal state (the structure of the adlayer at the poisoned state) on effective cluster interactions in section 4.3.3. Finally, we illustrate, in section 4.3.4, the effect of temperature on the KMC adlayer.

#### 4.3.1 DFT results

The adsorbate binding energies and activation barriers of methane cracking reaction are reported in Appendix II. We have systematically compared the binding energy/activation barrier predictions of our study with literature values (refer to Table A17 and Table A19 of Appendix II). As mentioned previously (in section 4.2), Table A22 provides the interaction energy values at 1NN, 2NN and 3NN distances for all the possible pairs of methane cracking adsorbates. It can be inferred from Table A22 that there is substantial variation in the type of interaction, attractive or repulsive, between 1NN and 2NN pairs of adsorbate or covalently bonded species encountered in methane cracking. At the 1NN distance, most co-adsorbed configurations of methane cracking species are unstable (due to the presence of strong repulsive interactions) – for such adsorbate-pairs a penalty is introduced in the MK/KMC model by fixing the value of ECI to 5 eV (as shown in Table A22), to prevent such configurations from appearing during the course of the simulation. In the case of C and CH species, we observe that the interaction is strongly attractive at the 1NN level.

Thus, as shown in Figure 11, the ECI values of the C-C, CH-C and CH-CH 1NN pairs are -0.471 eV, -0.494 eV and -0.355 eV, respectively, which indicates that these pairs are highly stable on the Ni(111) surface. A few studies have also made similar observations about the C-C interactions.<sup>156,157</sup> Li et al.<sup>157</sup> have performed projected density of states (PDOS) analysis of C-C species on Ni(111) and reported that there is an overlap of 2s and 2p orbitals of both carbon atoms, which is indicative of a strong C-C bond. The C/CH adsorbate-1NN pairs could be potential precursors to coke formation at steam reforming conditions.

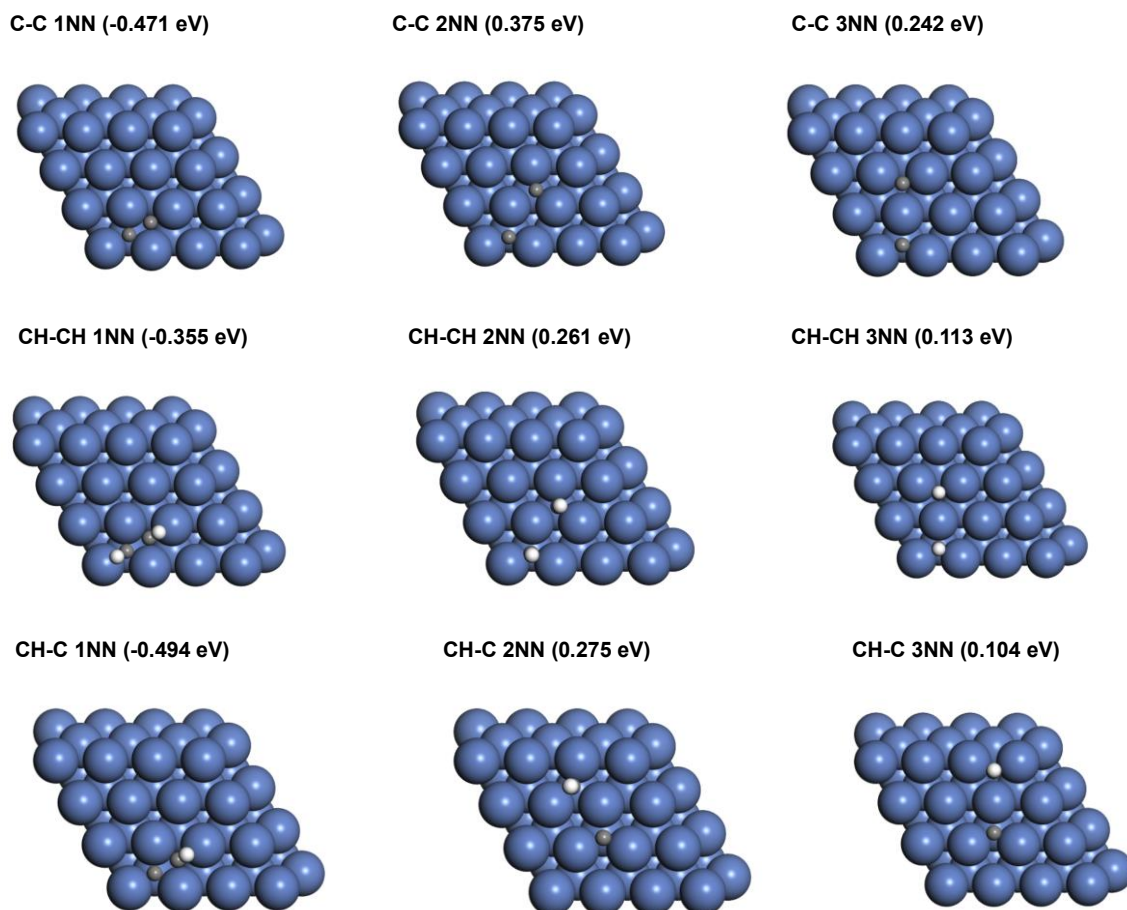


Figure 11: The top-view of the DFT configurations for the C/CH pairwise co-adsorbed states at 1NN, 2NN and 3NN distances. The numbers in the parentheses are the ECI values of the corresponding patterns.

In contrast to the attractive 1NN interactions of C/CH species, all the methane cracking species experience substantial repulsive interactions at the 2NN level (refer to Table A22). The C-C, CH-CH and CH-C 2NN-adsorbate pairs have positive ECI values (refer to Figure 11). As shown in Table A22, most methane cracking 3NN-adsorbate pairs have a weaker repulsive interaction (the ECI values are converging to zero in some cases). At the 3NN distance, the interactions become less pronounced as the adsorbates are placed further apart from each other. It can be inferred from Figure 11 that the formation of long-range carbonaceous species on Ni(111) primarily involves an interplay of attractive (C-C, CH-CH and CH-C bond formation at the 1NN level) and repulsive interactions (C-C, CH-CH and CH-C repulsions at the 2NN/3NN level).

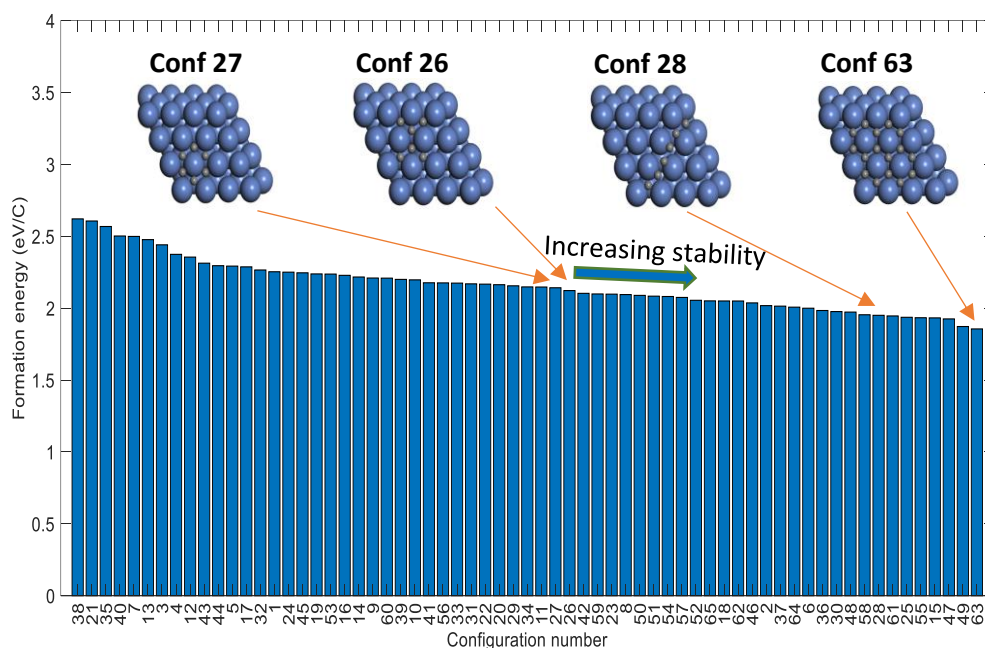


Figure 12: The formation energies (eV/C) of carbon configurations (reported in increasing order of stability - from left to right), which are part of the DFT dataset used for CE training.

We further explored the stability of long-range chains, branches and rings (composed of C/CH species) on the Ni(111) surface. We performed DFT calculations to compute the formation energies of 173 different carbon, CH and CH-C configurations on Ni(111) as mentioned earlier in section 4.2. The dataset has been developed in a systematic way; it includes a range of configurations at varying C/CH coverages (0–1 ML). The formation energies of carbon, CH, C-CH configurations are depicted in Figure 12, Figure 13 and Figure 14, respectively.

It can be observed from Figure 12 that the formation energies of carbon configurations are in the range of 1.86–2.62 eV/C. As shown in Figure 12, among the six body configurations, the carbon chain has a formation energy of 1.95 eV/C (configuration 28), whereas the carbon branch and carbon ring configuration have a formation energy of 2.12 eV/C (configuration 26) and 2.14 eV/C (configuration 27), respectively. Li et al.<sup>157</sup> and Cheng et al.<sup>156</sup> have also reported that the six-body chain type carbon configurations have better stability than six-body rings/branches. Nevertheless, as depicted in Figure 12, the C<sub>16</sub> ring-based (configuration 63) has the highest stability among the carbon configurations computed in this study, which indicates that the terminal state of coke could be composed of higher-body ring-based carbon structures.

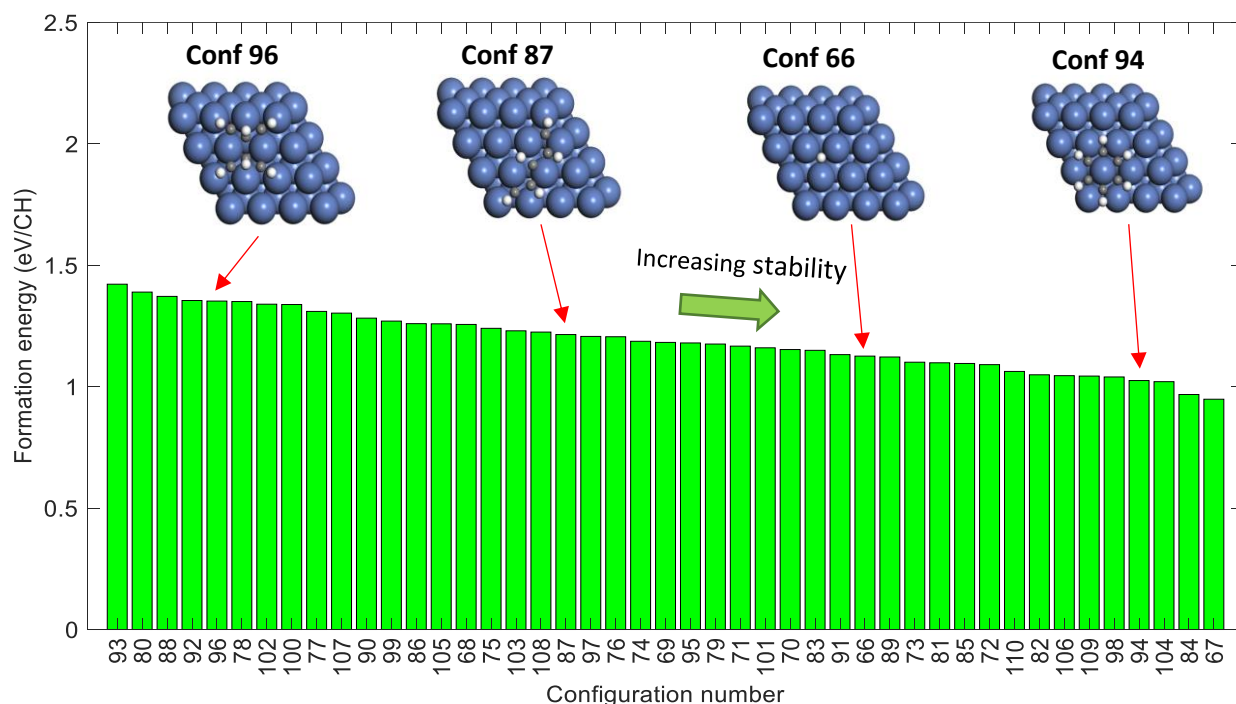


Figure 13: The formation energies (eV/CH) of CH configurations (reported in increasing order of stability - from left to right), which are part of the DFT dataset used for CE training.

The formation energies of CH configurations lie in the range of 0.95–1.42 eV/CH (refer to Figure 13). The six-body CH ring, which is benzene (configuration 94), has far greater stability than most of the other CH configurations – this is mainly due to the  $\pi$ - $\pi$  conjugation between carbon atoms in the benzene ring (the formation energy of benzene on Ni(111) is 1.03 eV/CH). As shown in Figure 13, the five-body chain (configuration 87) has higher stability than the six-body branch type CH configuration (configuration 96).

The C-CH configurations (Figure 14) have formation energies in the range of 1.10–2.11 eV/adsorbate (this is within the formation energy ranges of carbon and CH configurations). As illustrated in Figure 14, naphthalene (configuration 173) is very stable on the Ni(111) surface. The formation energies of configurations 127 (partially hydrogenated carbon-based ring) and 143 (partially hydrogenated carbon-based chain) are 1.52 eV/adsorbate and 1.42 eV/adsorbate, respectively (these lie in the moderate range in terms of stability in the DFT dataset). On the other hand, the C-CH branch-based structure (configuration 133) is less stable in comparison to other configurations (the formation energy value is 1.80 eV/adsorbate). Some of the CE training schematics of C-CH configurations are shown in Figure A14 and Figure A15 of Appendix II. The complete dataset of DFT configurations has been made available in the NOMAD repository.<sup>166</sup>

These calculations clearly indicate that C/CH correlation effects play a critical role in the formation of long-range carbonaceous species (which ultimately poison the Ni surface). Thus, it is important to systematically account for interactions between adsorbates or covalently bonded species to understand the coke morphology/terminal state of carbon-based species at steam reforming conditions.

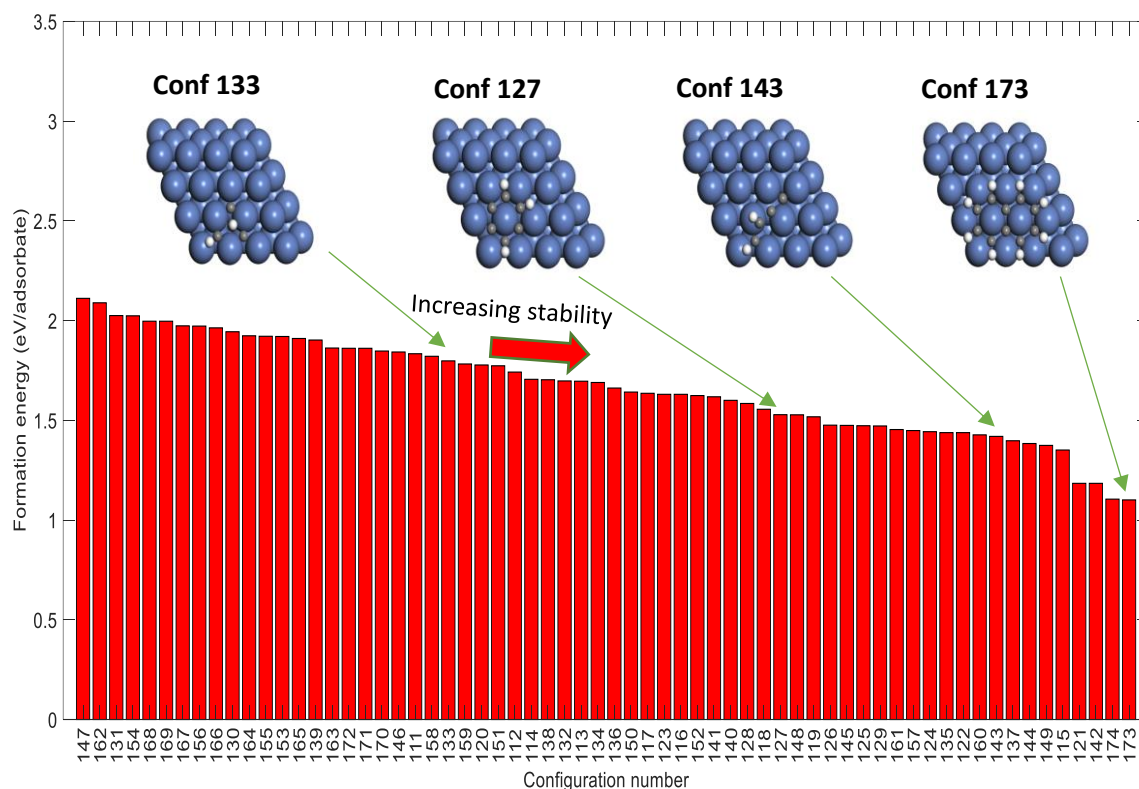


Figure 14: The formation energies (eV/adsorbate) of CH-C configurations, which are part of the DFT dataset used for CE training.

#### 4.3.2 Methane cracking reaction – MK/KMC predictions

In an attempt to clearly understand the implications of interactions, we followed a systematic approach in developing MK and KMC models for the methane cracking reaction. In Table 5, the list of elementary reactions of methane cracking along with their corresponding activation barriers, reaction energies and pre-exponentials are provided. In the first instance, we attempted to obtain equivalence between MK and KMC models in the absence of interactions, and thus appropriate geometry and event-multiplicity factors were included as discussed previously in section 4.2.4. Upon achieving this equivalence, we systematically started incorporating effective cluster interaction parameters in both models.

**Table 5. The list of elementary events, activation barriers/reaction energies and pre-exponents of the Methane cracking KMC model at 1000 K and 10.01 bar.**

Event ID: Reaction	$E_{Actfwd(rev)}^{zero-coverage}$ (eV)	$\Delta E_{rxn}^0$ (eV)	Pre-exp fwd (rev) (s <sup>-1</sup> )
R <sub>1</sub> : CH <sub>4</sub> (g) + *(fcc) + *(top) + *(fcc) $\leftrightarrow$ CH <sub>3</sub> *(fcc) + *(top) + H*(fcc)	0.41 (0.94)	-0.53	7.47×10 <sup>8</sup> (3.70×10 <sup>14</sup> )
R <sub>2</sub> : CH <sub>3</sub> *(fcc) + *(top) + *(fcc) $\leftrightarrow$ CH <sub>2</sub> *(fcc) + *(top) + H*(fcc)	0.66 (0.64)	0.02	1.09×10 <sup>14</sup> (4.63×10 <sup>13</sup> )
R <sub>3</sub> : CH <sub>2</sub> *(fcc) + *(fcc) $\leftrightarrow$ CH*(fcc) + H*(fcc)	0.26 (0.63)	-0.36	3.21×10 <sup>13</sup> (4.16×10 <sup>13</sup> )
R <sub>4</sub> : CH*(fcc) + *(top) + *(fcc) $\leftrightarrow$ C*(fcc) + *(top) + H*(fcc)	1.31 (0.84)	0.46	1.92×10 <sup>14</sup> (1.14×10 <sup>14</sup> )
R <sub>5</sub> : H*(fcc) + *(top) + H*(fcc) $\leftrightarrow$ H <sub>2</sub> (g) + *(fcc) + *(top) + *(fcc)	1.33 (0.00)	1.33	9.80×10 <sup>6</sup> (6.25×10 <sup>15</sup> )

Note: The activation barriers and reaction energies reported in this table do not include ZPE corrections. The reverse activation barriers/pre-exponentials of the corresponding reactions are shown in parentheses. The TS configurations of steps R<sub>1</sub>, R<sub>2</sub>, R<sub>4</sub> and R<sub>5</sub> involve top sites of Ni(111), and thus, the KMC event definitions for these reactions include top sites. Please refer to Figure A8 (in Appendix II) for the TS geometries of these reactions.

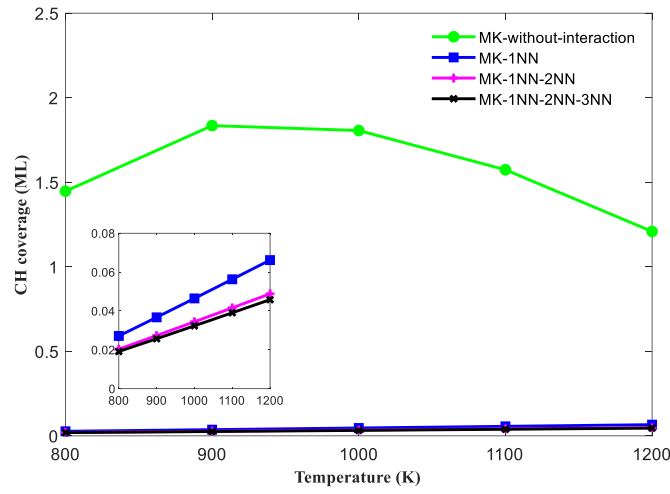
The BW approximation (eq. 61) was used to account for pairwise interactions up to 3NN level in the MK model. Three MK models were thus developed, namely, MK-1NN, which includes 1NN interactions, MK-1NN-2NN, which incorporates 1NN and 2NN interactions, and MK-1NN-2NN-3NN, which includes 1NN, 2NN and 3NN interactions. Whereas in the KMC model, the CE methodology (eq. 55) was used to account for interactions between adsorbates or covalently bonded species. We developed four different KMC models with increasing levels of complexity: the first three, KMC-1NN, KMC-1NN-2NN, and KMC-1NN-2NN-3NN, include the interactions noted, as per the naming convention of the MK models just discussed (refer to Table A22 of Appendix II for ECI values). The fourth model, KMC-long-range, includes the pairwise interactions up to 3NN level, as well as the higher-level interactions, which are parameterised by fitting against the DFT dataset that includes long-range carbon-based species (refer to Table A23 of Appendix II for ECI values).

The MK/KMC predictions were obtained at temperature ranges of 800–1200 K. The methane partial pressure and H<sub>2</sub> partial pressure were maintained at 10.00 bar and 0.01 bar, respectively (in the gas phase). These are the typical industrial operating conditions of steam reforming<sup>6,18,167</sup> and Snoeck et al.<sup>30</sup> have also conducted experiments on the methane cracking

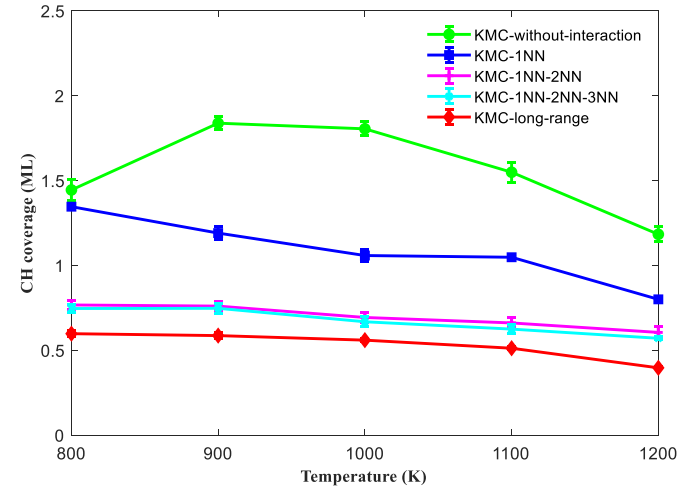
reaction at similar conditions to investigate the carbon whisker growth. Figure 15(a) and Figure 15(b) show the CH coverage predictions of the MK and KMC models, respectively (at varying temperatures), while the carbon coverage predictions are depicted in Figure 15(c) and Figure 15(d), respectively. The error bars in Figure 15 indicate the sample standard deviation of the KMC simulation. We also computed the population standard deviation (also called as the “standard error”) of the KMC predictions – these results are presented in Table A30 and Table A31 of Appendix II.

In the absence of interactions, the MK and KMC models predict quantitatively identical coverage trends (refer to the “MK-without-interaction” and “KMC-without-interaction” model predictions in Figure 15). Without the inclusion of interactions in the MK/KMC models, the CH species is found to have high coverages on Ni(111) at steam reforming conditions (refer to Figure 15(a) and Figure 15(b)). The surface dissociation steps following methane activation, i.e., the cleavage of CH<sub>3</sub> and CH<sub>2</sub> species, have high propensities, and thus, the CH<sub>3</sub> and CH<sub>2</sub> intermediates are short-lived on the Ni(111) surface. On the other hand, the CH dissociation step has a high free-energy barrier and CH is thermodynamically the most stable species on the Ni(111) surface (refer to Table A25, Table A26, Table A27, Table A28 and Table A29 of Appendix II for the free-energy/kinetic data), which justifies the high coverage prediction of CH species at steam reforming conditions.

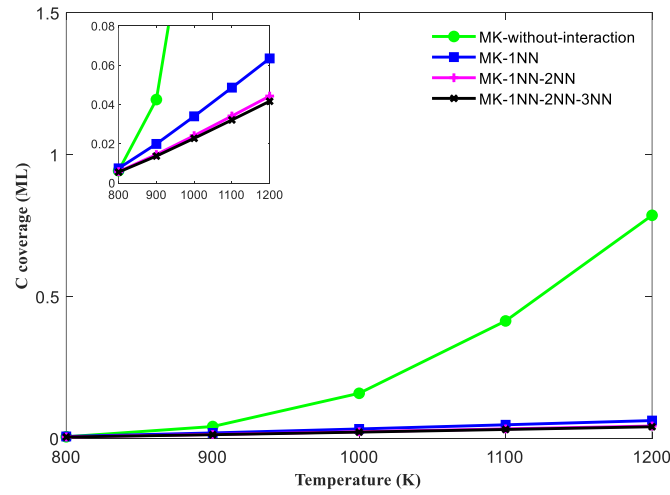
As shown in Figure 15(c) and Figure 15(d), the MK-without-interaction and KMC-without-interaction models show an increasing trend of carbon coverage with respect to temperature. Although the CH dissociation event is endothermic, at higher temperatures, the formation of carbon is favoured as kinetic effects become more pronounced (refer to Table A25, Table A26, Table A27, Table A28 and Table A29 for the free energy/kinetic data). The inclusion of interactions between adsorbates or covalently bonded species in the MK and KMC model can substantially alter the thermodynamic stabilities of carbon intermediates of methane cracking reaction (under the BEP relation) – this will be discussed in further detail below.



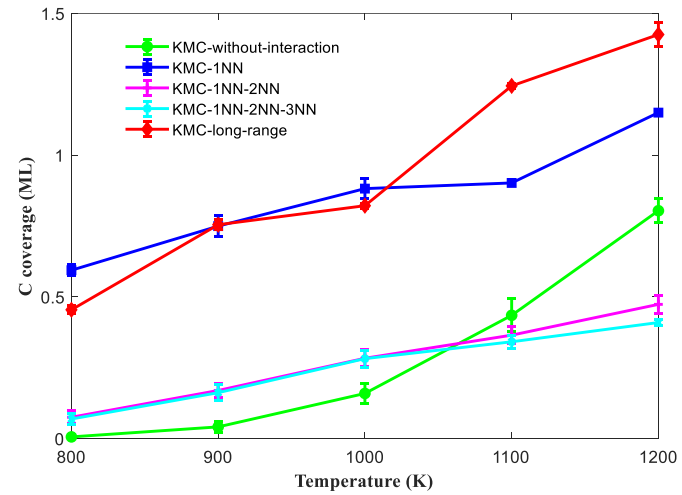
a)



b)



c)



d)

Figure 15: The coverage (ML) profiles with respect to temperature: a) MK results of CH coverages, b) KMC results of CH coverages, c) MK results of carbon coverages and d) KMC results of carbon coverages. The methane and hydrogen pressure were maintained at 10.00 bar and 0.01 bar, respectively. The coverage is normalised with respect to number of surface Ni atoms, and thus the maximum coverage is 2, when all hollow sites are covered.



It is evident from Figure 15(a) and Figure 15(c) that the MK models fail to capture the effect of interactions in a systematic fashion. The MK-1NN, MK-1NN-2NN and MK-1NN-2NN-3NN models predict very low coverages of CH and C despite the inclusion of attractive interactions (CH-CH-1NN, CH-C-1NN and C-C-1NN). The MK models tend to show small variation in CH and C coverages with respect to temperature. There is a significant difference between the predictions of MK and KMC models at all operating conditions (as shown in Figure 15 the difference lies in the range of 0.4–1 ML). Under the BW approximation, the likelihood of the occurrence of an adsorbate pair is determined by the geometry factor (accounting for site connectivity), the corresponding ECI value and the averaged coverage. Since the spatial information of adsorbates is represented using averaged coverage in the BW methodology, the MK models provide an inaccurate estimate of the “average” number of CH/C interactions at any time step of the simulation. Thus, the mean-field MK models may not be reliable in capturing the thermodynamic stabilities of carbonaceous species at steam reforming conditions.

The KMC-1NN model predicts high CH and carbon coverages at all reaction conditions (800–1200 K). As discussed previously, the CH-CH, CH-C and C-C interactions are attractive at the 1NN-level due to bond formation between C/CH species (refer to Table A22 of Appendix II for the ECI values). At steam reforming conditions, these attractive interactions increase the stability of CH/C species on Ni(111). We observe that the KMC-1NN model predicts far higher carbon coverages on Ni(111) in comparison to the “KMC-without-interaction” model (refer to Figure 15(d)). The coverage-dependent reaction energy term ( $\Delta E_{rxn}$ ) of the CH dissociation event is lowered due to the inclusion of these attractive C-C and CH-C 1NN interactions, which in turn reduces the coverage-dependent forward activation barrier of the CH dissociation event as per the BEP relation (refer to eq. 62). The improved thermodynamic stability of carbon species and reduction in coverage-dependent forward CH dissociation barrier favours the formation of carbon on the Ni(111) surface.

Upon inclusion of both 1NN, 2NN interactions, the KMC simulation predicts substantial CH (0.60-0.77 ML) and carbon coverages (0.07–0.47 ML) on Ni(111) at steam reforming conditions. However, the KMC-1NN-2NN CH/C coverage predictions are significantly lower than those of the KMC-1NN model (as shown in Figure 15(b) and Figure 15(d)). As discussed previously, at the 2NN level, the carbon-based species experience substantial repulsive interactions (refer to Table A22 for ECI values at the 2NN level). These repulsive interactions decrease the overall thermodynamic stability of the CH/C adsorbates, which results in lower CH/C coverages on Ni(111).

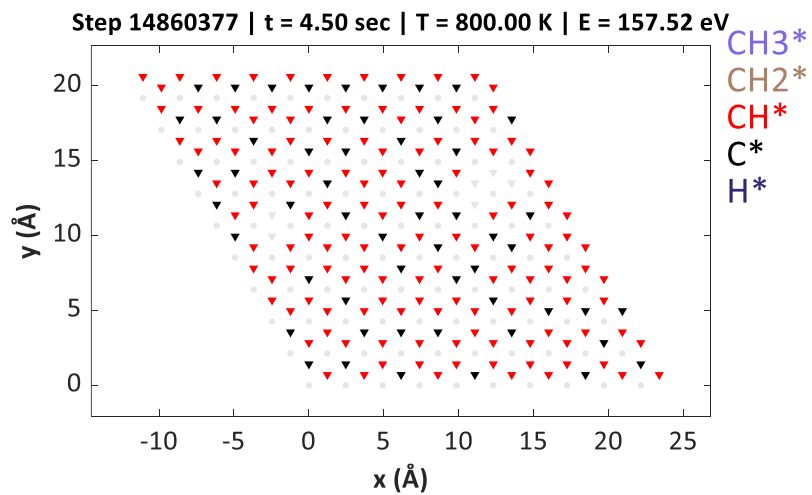
Furthermore, as depicted in Figure 15(b) and Figure 15(d), the KMC-1NN-2NN-3NN model predicts C/CH coverages similar to those of the KMC-1NN-2NN model. At the 3NN level, the repulsions between adsorbates are weaker than at 2NN distance as the adsorbates are further apart (refer to Table A22 for 3NN ECI values). Thus, the coverages of C/CH species are not significantly different than those of the KMC-1NN-2NN model.

Interestingly, upon capturing the detailed energetics of large-body configurations (chains, branches and rings) in the KMC simulation, we observe that carbon species tend to dominate over CH at higher temperatures (900 K and above). For instance, at 1200 K, the KMC-long-range model predicts the CH and carbon coverages to be 0.40 ML and 1.43 ML, respectively (refer to Figure 15(b) and Figure 15(d)). This is at variance to the free energy/kinetic data in the absence of interactions (refer to Table A25, Table A26, Table A27, Table A28 and Table A29 of Appendix II), according to which the CH species are more thermodynamically stable than carbon at steam reforming conditions. However, in the presence of long-range CH-CH, CH-C and C-C interactions, the stability of carbon species improves dramatically as demonstrated by the predictions of the KMC-long-range model.

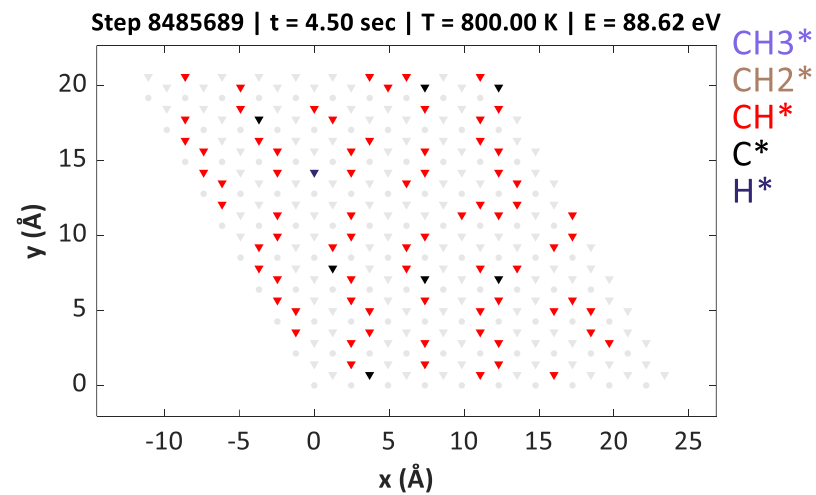
Overall, the KMC models (with varying degrees of accuracy in capturing adlayer energetics) have shown that effective cluster interactions play a critical role in determining the overall thermodynamic stability and macroscopic coverages of the methane cracking species. These results give rise to several important questions: 1) Does the surface morphology of Ni(111) change due to interactions? 2) What is the type/shape of carbon-based cluster that is thermodynamically stable on the Ni(111) surface? 3) At what operating conditions is Ni more susceptible to coking/poisoning? In the subsequent sections, we will address these questions in detail.

#### 4.3.3 Changes to the KMC adlayer with varying levels of interactions

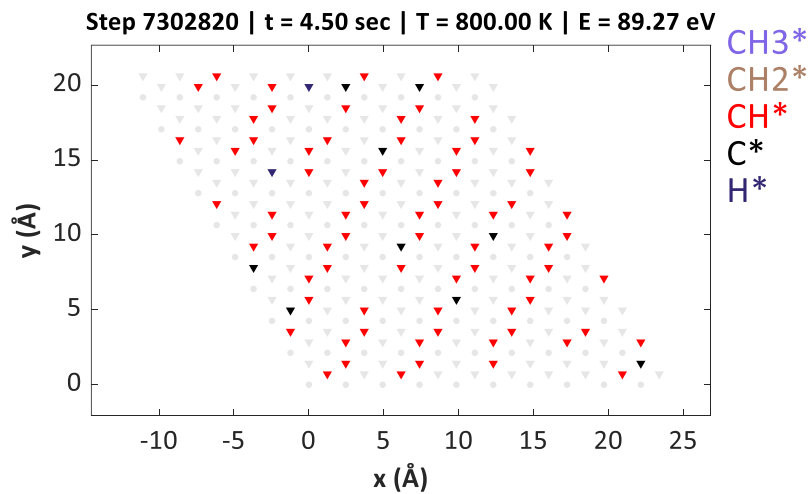
In the previous discussion, we have observed that the reaction thermodynamics and macroscopic coverages of carbon-based species are significantly altered upon gradually refining the effective cluster interactions model in the KMC simulations of methane cracking. Interactions between adsorbates or covalently bonded species, as captured via the CE methodology, give a better representation of the local environment at poisoning conditions, thereby allowing us to examine in detail the predictions of different CE-based models regarding the terminal state of coke on Ni(111). Thus motivated, Figure 16 provides the final lattice snapshots, for which the net rate of CH<sub>4</sub> consumption/coking is close to zero (poisoned state), for the four KMC models. We assume the system has reached the poisoned/terminal state when the species coverage fluctuations are within 0.02 ML.



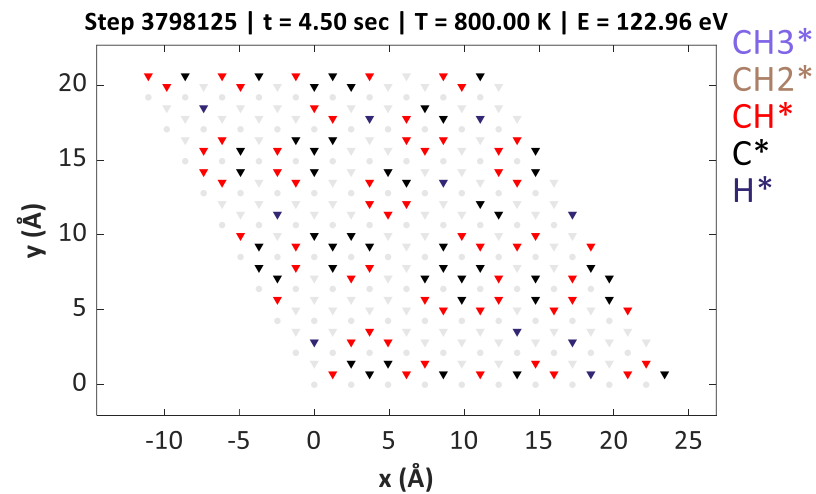
a)



b)



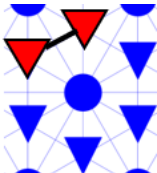
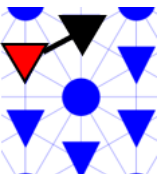
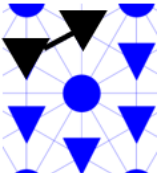
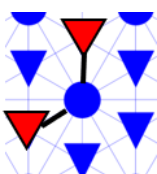
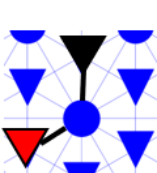
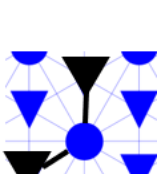
c)



d)

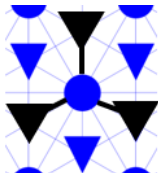
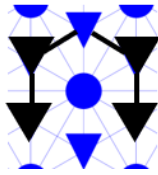
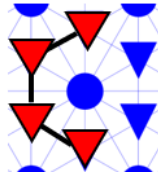
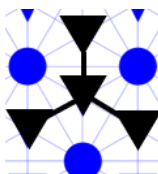
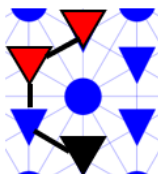
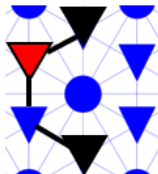
Figure 16: KMC lattice snapshots upon reaching the steady state (poisoned condition) at 800 K. The CH<sub>4</sub> and H<sub>2</sub> pressures were maintained at 10.00 bar and 0.01 bar, respectively. a) KMC-1NN, b) KMC-1NN-2NN, c) KMC-1NN-2NN-3NN and d) KMC-long-range.

**Table 6: The ECI values of important 1NN and 2NN figures/patterns**

Figure/pattern name	Figure/pattern schematic	ECI value (eV)
CH-CH-1NN		-0.36
CH-C-1NN		-0.49
C-C-1NN		-0.47
CH-CH-2NN		0.26
CH-C-2NN		0.28
C-C-2NN		0.38

Note: The schematics of the Table 6 have the following colour code: 1) Blue triangles indicate the Ni fcc sites, 2) Blue circles are the Ni top sites, 3) Red triangles represent the CH species and 4) Black triangles are the carbon species.

**Table 7. The ECI values of important many-body figures/patterns of the CE fit model**

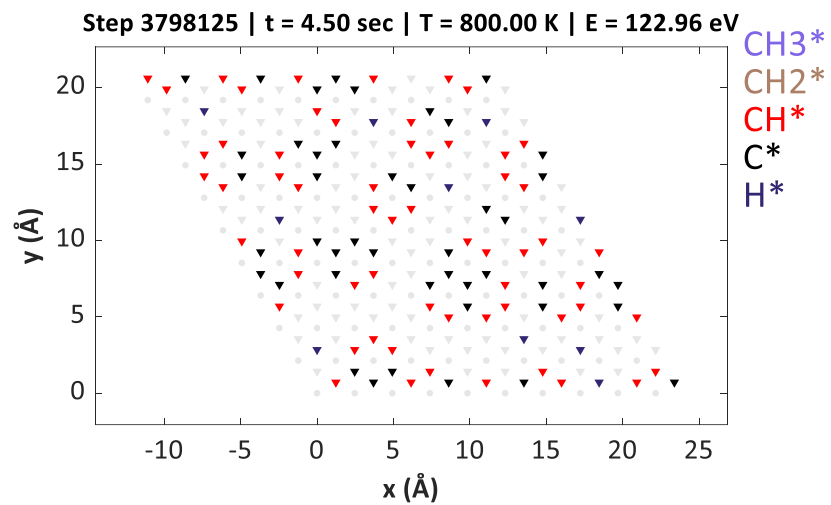
Figure/pattern name	Figure/pattern schematic	ECI value (eV)
Carbon-three-body-ring		-0.31
Carbon-four-body-square		-0.45
Four-CH-semi-ring		-0.46
Four-C-branch		-0.61
TwoCH-oneC-ring1		-0.41
TwoC-oneCH-ring2		-0.20

Note: The schematics of the Table 7 have the following colour code: 1) Blue triangles indicate the Ni fcc sites, 2) Blue circles are the Ni top sites, 3) Red triangles represent the CH species and 4) Black triangles are the carbon species.

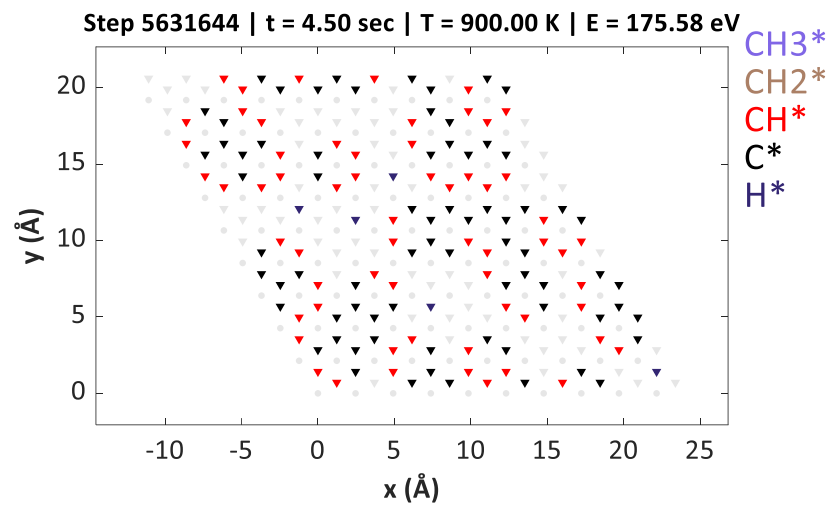
The final lattice state of the KMC-1NN model is completely covered with CH/C species. Although there is no visible ordering of CH/C species into specific configurations, we do observe small clusters of carbon surrounded by three CH species throughout the KMC-1NN lattice (for instance at  $x = 20$ ,  $y = 20$  in Figure 16(a)). The observed “clustering” can be explained by the nature of interactions of CH/C species at the 1NN level. As shown in Table 6, the two-body figures such as CH-CH-1NN, CH-C-1NN and C-C-1NN have ECIs -0.36 eV, -0.49 eV and -0.47 eV, respectively. This is indicative that these figures are highly stable on the Ni(111) surface. The CH-C clusters (shown in Figure 16(a)) are composed of the figures CH-CH-1NN and CH-C-1NN.

The ECIs of CH-CH-2NN, CH-C-2NN and C-C-2NN figures are 0.26 eV, 0.28 eV and 0.38 eV, respectively (refer to Table 6). The carbon-based 2NN figures are repulsive, whereas the 1NN figures are attractive. In the carbon-based chain configurations, the 1NN-figures have a higher frequency of occurrence than the 2NN figures (in comparison to rings/branches). Thus, we observe that the CH/C species align as carbon chains in the KMC-1NN-2NN model (as depicted in Figure 16(b)). Similarly, the final lattice state of KMC-1NN-2NN-3NN model also has CH and C species arranged in the form of straight chains (refer to Figure 16(c)). Nevertheless, the aforementioned KMC models cannot accurately capture the formation energies of long-range chains, rings and branches, since the corresponding CEs do not include long-range (longer than 3NN) or many-body contributions.

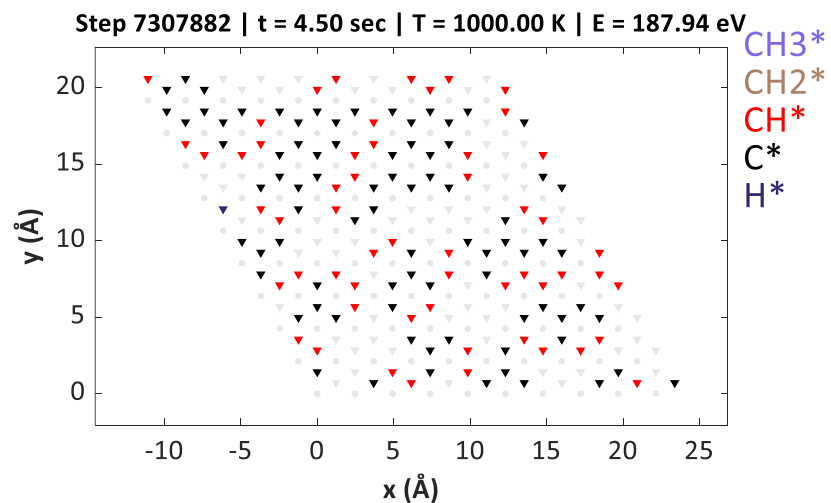
Such contributions are included in the CE of the KMC-long-range model, whose final lattice state is significantly different from those of the other KMC models. As illustrated in Figure 16(d), we find that the CH and carbon species form ring-based configurations. This is consistent with the DFT predictions (as discussed in section 4.3.1), which show that large-body C/CH ring-based structures (such as  $C_{16}$  ring and naphthalene) are thermodynamically more stable on Ni(111) than six-body chains/branches. As shown in Table 7, in the KMC long-range model, the optimised CE figures such as Carbon-three-body-ring, Carbon-four-body-square, Four-CH-semi-ring, Four-C-branch, TwoCH-oneC-ring1 and TwoC-oneCH-ring2 have ECIs -0.31 eV, -0.45 eV, -0.46 eV, -0.61 eV, -0.41 eV and -0.20 eV, respectively (indicative of substantially strong attractive interactions). These circular/branched type figures/patterns have a higher frequency of occurrence on many-body ring-based C-CH configurations. They allow us to capture the thermodynamic stability of large-body C/CH ring-based structures with better accuracy. The observed dramatic change in coke morphology (as illustrated in Figure 16(d)) could be due to the inclusion of these circular/branched type figures in the CE model of KMC-long-range.



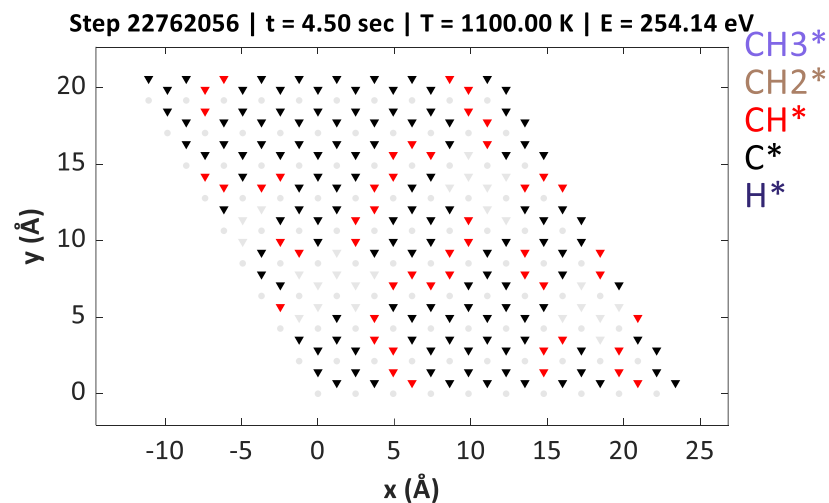
a)



b)



c)



d)

Figure 17: Lattice snapshots of the KMC-long range model upon reaching the steady state (poisoned condition) at varying temperatures. The CH<sub>4</sub> and H<sub>2</sub> pressures were maintained at 10.00 bar and 0.01 bar, respectively. a) 800 K, b) 900 K, c) 1000 K and d) 1100 K.

Based on the KMC-long-range prediction, we can conclude that the surface coke could be composed of partially hydrogenated C-CH rings, which agglomerate to form long graphene sheets upon complete poisoning of the Ni support surface. Furthermore, a few experimental studies have shown that coke has a heterogeneous composition, plausibly containing large hydrocarbons, and the morphology and thermodynamic properties of coke differ considerably from a graphitic/nickel carbide phase.<sup>168</sup> It is clear from the above discussion that the predicted morphology of the coke “terminal state” changes substantially based on the level of effective cluster interactions included in the KMC model.

#### 4.3.4 Effect of Temperature on the KMC adlayer

The final lattice snapshots (poisoned state) of the KMC-long-range model are depicted at varying temperatures (800–1100 K) in Figure 17, which shows that at lower temperatures the formation of CH/carbon rings is localised. Hence, we find mainly six-body ring configurations at specific regions, for instance, at 800 K, the rings are located at around the coordinates (2.5,15), (12.5,12.5) and (22.5,15) Å, etc. These rings are C<sub>6</sub>H<sub>y</sub> type configurations (where y varies from 1-4 in most cases) that are largely disconnected from each other. At moderate temperatures such as 900 K and 1000 K, we observe the formation of C<sub>13</sub> and C<sub>16</sub> ring-based super-clusters at various regions of the KMC lattice. On the other hand, at higher temperatures (1100 K and beyond), large islands of carbon-based rings completely cover the Ni(111) surface. The terminal points of these carbon islands are mostly populated with CH species. Based on these KMC simulations, we can conclude that Ni is susceptible to coking at extreme operating conditions, which is in good agreement with industrial observations.<sup>25</sup> The removal of these graphene/coke flakes from the Ni surface is difficult at the higher temperature regions of the steam reformer.

#### 4.4 Conclusions

The formation of coke (in the form of carbon whiskers) on the Ni catalyst surface severely hampers the productivity of MSR. These carbon whiskers can grow and accumulate on the Ni support side in the form of carbon-based rings/chains/branches. In recent years, first-principles methods such as DFT have been used to understand the stability of simple carbon-based configurations (ranging from C<sub>2</sub>-C<sub>6</sub>).<sup>157,169</sup> The DFT models developed thus far do not account for thermal, entropic and coverage effects, which are critical to understand coke formation at MSR conditions. Furthermore, these studies have focussed on a limited dataset of carbon-based configurations. A detailed understanding of the thermodynamic stability of C<sub>x</sub>H<sub>y</sub> species at steam reforming conditions is lacking in the literature.

Conventionally, mean-field MK models are employed to predict the kinetics/macroscale coverages in catalytic reactions. However, the mean-field approximations of MK models



cannot capture adsorbate correlations and lattice inhomogeneities accurately; yet it is important to systematically account for these effects in reactions such as methane cracking to properly understand the terminal state of carbon whiskers. The CE-based KMC simulations capture interactions between adsorbates or covalently bonded species with high fidelity.

In this work, DFT calculations have revealed that there is significant variation in the nature and magnitude of interaction between 1NN and 2NN C/CH pairs. At the 1NN level, the C-C, CH-C and CH-CH interactions are attractive due to overlap of p-orbitals leading to bond formation, whereas the 2NN adsorbate pairs of C/CH experience repulsive interactions. This indicates that the formation of long-range carbonaceous species on Ni(111) involves an interplay of C/CH attractions and repulsions. The many-body configurations of carbon-based species can take the form of chains, rings and branches on Ni(111). Among the long-range CH configurations, the chains and rings have better stability than branched structures. This is consistent with other works available in the literature. The correlations of C/CH species can play a crucial role in the accumulation of coke on Ni(111).

To thoroughly assess the consequences of interactions on the coke morphology, we developed MK and KMC models of the methane cracking reaction. In these simulations, the kinetics of subsequent dehydrogenations from CH<sub>4</sub> to C+4H are modelled in detail, while the formation of coke is captured at the level of thermodynamics only. Thus, C-C coupling events are not explicitly considered, but the stability of large carbon-rich islands is captured via the CE approach to a progressively higher level of accuracy. To this end, our KMC simulations incorporate the effective cluster interactions in an incremental fashion. The “zero interaction” MK and KMC models give quantitatively similar results. In the absence of interactions, the Ni(111) surface is predominantly covered with CH species. Upon inclusion of 1NN, 2NN and 3NN interactions in the KMC model, we see a substantial change in the C/CH coverages and methane cracking reaction thermodynamics. MK models predict very low coverages of CH/C species upon the inclusion of interaction terms. Since the spatial distribution of adsorbates is lost within the MK framework, the latter inaccurately predicts the average number of attractive/repulsive interactions at any time step of the simulation.

We further parameterised high-fidelity CEs using our DFT dataset, thereby enabling the calculation of the formation energies of long-range carbon-based configurations (chains, rings and branches) on Ni(111) during KMC simulations. The resulting KMC-long-range model includes the 1NN, 2NN and 3NN interactions as well as the many-body effective cluster interactions. In contrast to the lower fidelity KMC models (KMC-1NN, KMC-1NN-2NN and KMC-1NN-2NN-3NN), the KMC-long-range model predicts carbon to be the dominant species on Ni(111) at MSR conditions. The final lattice snapshot of KMC-long-range model of methane

cracking reaction clearly shows that CH/C species accumulate on Ni(111) in the form of rings. These observations are consistent with the calculated DFT energetics of large-body configurations. The accumulation of carbonaceous species seems to involve formation of C-CH ring-based structures, which might branch together at higher coverages to form graphene sheets/coke.

The DFT dataset used for CE training only comprised C, CH, CH-C configurations that occupied the three-fold hollow sites. In future efforts, the dataset can be further enriched by including carbon-based configurations that occupy top sites as well, and the KMC model can be enhanced by taking into account C-C coupling steps explicitly. These would be important to gain a thorough understanding of graphene growth (as the most stable configuration of graphene is top-fcc).<sup>144,62</sup> A multi-faceted KMC model (that includes step sites) can also be developed to capture the migration mechanism of carbon from Ni step edge to Ni terrace – this could provide a more complete picture of the Ni catalyst deactivation. The multifaceted KMC model can be compared to relevant experimental works of methane cracking available in the literature.<sup>170</sup> Furthermore, the burn-off/oxidation mechanism of the carbon-based poison from the Ni catalyst surface could be of great industrial interest (in the context of Ni catalyst regeneration). Overall, the CE parameterised KMC simulations have delivered a better understanding on the coke/graphene “terminal state” at steam reforming conditions, as they capture correlation effects with high fidelity. Our study paves the road towards future simulations which could potentially help us identify the next-generation Ni-based catalysts that are more resistant to coking.

# Chapter 5

## 5. Elucidating the role of potassium in methane steam reforming using first-principles-based Kinetic Monte Carlo Simulations

In the chemical industries, potassium is commonly employed as a promoter to reduce coke formation on the Ni catalyst surface, which has been proven to improve the productivity of the MSR reaction. Despite numerous theoretical/experimental studies, there is a lack of detailed understanding on the potassium effect at steam reforming conditions. In this chapter, we developed a first-principles-based KMC model of MSR on Ni(111) and potassium-doped Ni(111) surfaces. The KMC predictions of MSR on Ni(111) were compared to experimental rates in a systematic way. We performed KMC simulations with varying concentrations of potassium on Ni(111) to understand its effect on macroscopic coverages and MSR reaction rates. A thorough examination of the KMC process statistics was carried out to rationalise the role of potassium on MSR kinetics. Moreover, a flux analysis was conducted to identify the dominant reforming pathways on the Ni(111) and K-Ni(111) (potassium-modified) systems. These computations illustrate the beneficial effects of potassium in the MSR reaction.

### 5.1 Introduction

Developing strategies to reduce the coking propensity of Ni at steam reforming conditions is of vital importance. In the past few decades, extensive experimental and theoretical works have been conducted to address this challenge.<sup>25,155,62,171</sup> Some proposed solutions to alleviate coking and improve MSR productivity include increasing steam to methane ratio, use of promoters and doping with noble metals such as Pt, Pd and Rh.<sup>59,172-174</sup> Currently, in the industry, alkali-based promoters, such as potassium, are widely employed to improve the activity/stability of the MSR reaction. It has been reported that potassium has a beneficial effect on the overall carbon removal rate.<sup>61</sup>

Recent studies have attempted to shed light on the mechanism by which potassium promotes the carbon removal rate, thereby suppressing coke formation on the Ni surface. Borowiecki et al.<sup>53</sup> conducted an experimental study with varying loadings of potassium on the Ni/Al<sub>2</sub>O<sub>3</sub> catalyst. The study concluded that the location of potassium on Ni plays an important role in suppressing coke formation. Snoeck et al.<sup>36</sup> found that the net rate of carbon formation is reduced by adding potassium to the Ni catalyst. The authors' explanation of this beneficial effect was that the potassium increases the oxygen surface concentration, which improves the carbon removal rate. A DFT study conducted by Li et al.<sup>175</sup> found that the potassium increases the C-H cleavage barrier on Ni<sub>4</sub>/Al<sub>2</sub>O<sub>3</sub> with pre-adsorbed K compared to the pure Ni<sub>4</sub>/Al<sub>2</sub>O<sub>3</sub> system. The authors conclude that the increase in the C-H dissociation barrier helps to reduce the coke formation on Ni. Moreover, DFT studies have also been conducted to understand the effect of potassium in chemical reactions such as methanol steam reforming, WGS and methanation.<sup>176,177</sup> Despite several experimental/theoretical studies, a comprehensive

mechanistic level understanding of the role of potassium in MSR is still lacking. So far, a detailed kinetic study has not been conducted (by taking into account the surface coverage effects) to elucidate the mechanism by which potassium improves the productivity of the MSR reaction.

In this work, we employed CE-based KMC simulations to capture in detail the effect of potassium on the MSR kinetics. The MSR reaction was modelled on the pure Ni(111) and K-Ni(111) systems. The KMC simulations were performed on lattices with different loadings of potassium, which include, K-Ni(111)-0.7%, K-Ni(111)-1.4%, K-Ni(111)-2.1% and K-Ni(111)-2.8%. The pairwise lateral interactions of the MSR species were accounted using CEs on the Ni and potassium sites. The KMC simulations were used to predict the net turnover rates and macroscopic coverages of MSR species on pure Ni(111) and potassium-doped Ni(111) surfaces. The MSR turnover rates obtained from KMC on Ni(111) were compared to available experimental data (refer to Table A40 of Appendix III). The process statistics of key MSR events were systematically examined to understand the potassium promotion effect at steam reforming conditions. Furthermore, flux analysis was carried out to identify the dominant reforming pathways on the Ni(111) and K-Ni(111) systems.

## 5.2 Computational details

### 5.2.1 DFT calculations

The VASP 5.4.1 software was used to carry out spin-polarised DFT calculations. A plane-wave basis set was employed, and the kinetic energy cut-off value was set to 400 eV. The projector augmented wave (PAW) method was used to model the interactions between core and valence electrons. The electronic self-consistency convergence parameter was set to  $10^{-7}$  eV. The PBE-D3<sup>114</sup> functional was employed to approximate the exchange-correlation effects. The Ni lattice constant optimisation calculations were carried out by sampling the Brillouin zone with a  $19 \times 19 \times 1$  k-point mesh and smearing the electrons using the tetrahedron method with Blöchl corrections (value of smearing width was set to 0.05 eV). A six-layer Ni(111) slab (with the Ni atoms of the three bottom-most layers fixed to the bulk positions) was used to carry out the surface calculations. The conjugate gradient method was employed to minimise the Hellmann-Feynman forces between the mobile atoms of the Ni(111) slab. In these slab calculations, the convergence tolerance parameter for the forces was set to  $2 \times 10^{-2}$  eV/Å. The Brillouin zone was sampled with a  $5 \times 5 \times 1$  Monkhorst-Pack k-point grid and the Methfessel-Paxton method was used to carry out electron smearing (smearing width value was set to 0.1 eV).

The transition state search was performed using the dimer method.<sup>72</sup> For the vibrational calculations, the Hessian matrix was evaluated by central finite difference method (positions

of the atoms were displaced by 0.02 Å). The binding energies of adsorbates were estimated using eq. 81. In eq. 81,  $E_{tot}^{A+Ni(111)}$  represents the DFT total energy of the adsorbate-Ni(111) system,  $E_{tot}^{Ni(111)}$  is the DFT total energy of the Ni(111) slab,  $E_{tot}^{A(g)}$  indicates the DFT total energy of the adsorbate in the gas phase and  $AE^A$  is the adsorption energy of the adsorbate. The formation energies of adsorbates (represented as  $FE^A$  in eq. 82) are calculated by taking the Ni(111) slab, CH<sub>4</sub>(g), H<sub>2</sub>(g) and H<sub>2</sub>O(g) as reference species. In eq. 82, the stoichiometry between the adsorbates and gas-phase reference species is accounted for by using the real numbers  $p$ ,  $q$  and  $r$ . For example, in the case of estimation of formation energy of CHO adsorbate, the real numbers  $p$ ,  $q$  and  $r$  will take values 1.0, -2.5 and 1.0, respectively.

$$AE^A = E_{tot}^{A+Ni(111)} - E_{tot}^{Ni(111)} - E_{tot}^{A(g)} \quad \text{eq. 81}$$

$$FE^A = E_{tot}^{A+Ni(111)} - E_{tot}^{Ni(111)} - (pE_{tot}^{CH_4(g)} + qE_{tot}^{H_2(g)} + rE_{tot}^{H_2O(g)}) \quad \text{eq. 82}$$

$$ECI^{AB} = FE^{AB} - (FE^A + FE^B) \quad \text{eq. 83}$$

$$G^A = E^{DFT} + E^{ZPE} + H(T) - TS(T) \quad \text{eq. 84}$$

$$G^{FE} = G_{tot}^{A+Ni(111)} - G_{tot}^{Ni(111)} - (pG_{tot}^{CH_4(g)} + qG_{tot}^{H_2(g)} + rG_{tot}^{H_2O(g)}) \quad \text{eq. 85}$$

The pairwise adsorbate interaction values are calculated by using eq. 83. The  $ECI^{AB}$  is a quantitative measure of the nature/magnitude of interaction between adsorbates A and B on the Ni(111) surface. If the  $ECI^{AB}$  value is positive, then it is indicative of a repulsive interaction, whereas a negative  $ECI^{AB}$  value shows that the interaction between adsorbates A and B on the Ni(111) surface is attractive. For weakly interacting adsorbates, the  $ECI^{AB}$  value will be close to zero. The Gibbs free energy (will be referred to as “free energy” henceforth) of any species is obtained by using eq. 84 -  $E^{ZPE}$  represents the ZPE term,  $H(T)$  indicates the thermal energy and  $TS(T)$  constitutes the entropic contribution. The formulas of ZPE for gas-phase species and adsorbates have been provided in chapter 3 (refer to eq. 66 and eq. 67). The thermal and entropic contributions of gas-phase species/adsorbates have been obtained using the thermochemistry module of atomic simulation environment (ASE). We direct the readers to refer to section A 3.3 of Appendix III for more details on the formulas ASE employs to estimate the thermal/entropic contributions. We use eq. 85 to calculate the free energy of formation (it is estimated with reference to free energies of Ni(111) slab, CH<sub>4</sub>(g), H<sub>2</sub>(g) and H<sub>2</sub>O(g)).  $G_{tot}^{A+Ni(111)}$  represents the total free energy of the adsorbate plus Ni(111) system and  $G_{tot}^{Ni(111)}$  is the total free energy of Ni(111). The symbols  $G_{tot}^{CH_4(g)}$ ,  $G_{tot}^{H_2(g)}$  and  $G_{tot}^{H_2O(g)}$  indicate the gas-phase free energies of methane, hydrogen and water, respectively.

### 5.2.2 KMC simulations

The KMC simulations were performed using Zacros<sup>78</sup> (a graph-theoretical KMC software). A 25×25 lattice was chosen to carry out the KMC simulations. The KMC lattice convergence results are shown in Table A39 (refer to Appendix III). As shown in Table A39, the KMC predictions of the 25×25 lattice are very similar to the results of larger lattices such as 35×35 and 40×40. Thus, the 25×25 lattice is a suitable choice in terms of accuracy and computational cost. The CE methodology (which was implemented in KMC by Nielsen et al.<sup>89</sup>) was employed to capture the pairwise adsorbate interactions between the MSR species. In section 2.6 (“Methodology” chapter of this thesis), the detailed formulation of CE has been provided. In Zacros, the energetic cluster patterns are identified by solving subgraph isomorphism problems.<sup>89</sup>

Given the large number of adsorbates in the MSR reaction network, we used the following criteria to account for the most relevant adsorbate interactions: 1) the pairwise adsorbate interaction between species that are involved in a bimolecular reaction is included in the KMC simulation; 2) the lateral interactions of high-coverage species on the Ni and K sites have been captured; 3) if any adsorbate pair (usually involving a high coverage and low coverage species) appears frequently in the KMC trial simulations, then its corresponding interaction term is included in the final KMC model. The “production KMC model” of the potassium-modified Ni(111) system consists of 144 events and 78 adsorbate interaction parameters. The adsorbate diffusion events have been assumed to be quasi-equilibrated at steam reforming conditions, and the activation barrier for the diffusion of an adsorbate is considered to be around 12% of its corresponding adsorption energy on Ni(111)/K-Ni(111).<sup>109</sup> The KMC process statistics plots are examined (at regular sliding intervals) to ensure adsorbate diffusions are quasi-equilibrated throughout the KMC simulation.

### 5.2.3 Estimation of turnover rates and reaction flux in KMC

At steady-state conditions, we compute the net turnover rates of MSR by finding the slope of methane gas consumption over KMC time. Further, we divide the net turnover rate (will be referred to as “turnover rate” henceforth) by the total number of sites (refer to eq. 86). The estimated error of the predicted slope and the standard deviation of the coverage are also calculated (these are portrayed in Figure 19 of subsection 5.3.2). As shown in Figure 20, there are several pathways to form CO (end product) in the MSR reaction: 1) CHOH pathway via CHO intermediate, 2) CHOH pathway via COH intermediate, 3) CHO pathway, 4) COH pathway and 5) CO pathway. Each pathway has a unique contribution to the turnover rate of MSR. At steady-state conditions, we extract the overall (net) event frequency of each reversible elementary step,  $r_i^{overall}$  (estimated using eq. 87) from the KMC process statistics data.

$$TOF^{net} = \frac{N_{CH_4}^{molecules}}{N_{sites} \times \tau} \quad \text{eq. 86}$$

$$r_i^{overall} = \frac{N_i^{fwd-events} - N_i^{rev-events}}{N_{sites} \times \tau} \quad \text{eq. 87}$$

In eq. 86,  $N_{CH_4}^{molecules}$  is the number of CH<sub>4</sub> molecules consumed (at steady-state conditions),  $N_{sites}$  is the total number of sites of the KMC lattice and  $\tau$  represents the “KMC simulation time” (in seconds). In eq. 87, for any elementary step, the symbols  $N_i^{fwd-events}$  and  $N_i^{rev-events}$  indicate the number of occurrences of forward and reverse events, respectively (upon reaching the steady state). The value of  $\tau$  is obtained as follows:

$$\tau = t_{total} - t_{transient} \quad \text{eq. 88}$$

In eq. 88,  $t_{total}$  indicates the overall time of the simulation (in seconds) and  $t_{transient}$  represents the time spent by the simulation in transient state (in seconds). The overall event frequencies obtained from the KMC have been used to compute the contributions (%) of different MSR pathways (refer to eq. 89).

$$\text{Pathway contribution (\%)} = \frac{r_i^{overall}}{\sum_{j \in P} (r_j^{overall})} \times 100 \quad \text{eq. 89}$$

In eq. 89,  $i$  represents the unique elementary event/step of a pathway and set  $P$  contains all the “necessary events” that lead to the formation of the end product. Prats et al.<sup>178</sup> have also used a similar approach to obtain pathway contributions from the KMC simulation.

### 5.3 Results and discussions

#### 5.3.1 DFT results

The reactions of the MSR reaction network can be primarily classified into 4 categories: 1) Methane dissociation, 2) Water dissociation, 3) CH/C oxidation pathways (these include four different types) and 4) CO(g) and H<sub>2</sub>(g) formation. DFT calculations were performed and free energies were calculated for the aforementioned MSR reaction steps (at 1073 K and 10 bar) on Ni(111) and K-Ni(111). We have systematically compared the DFT predictions of this study with values available in the literature (refer to Table A32 and Table A33 of Appendix III). The transition state geometries of MSR events on K-Ni(111) are provided in Appendix III (refer to Figure A17 and Figure A18). In Figure 18(a), the free energy profiles of methane dissociation reaction steps are illustrated. It is evident from Figure 18(a) that the dissociation of methane gas to form CH<sub>3</sub> and H adsorbates (event R<sub>1</sub>) has the highest free energy barrier on Ni(111) compared to other dissociation steps. The free energy barrier of this event on K-Ni(111) is 1.70 eV, which is around 0.23 eV greater than on the Ni(111) system. The presence of potassium makes the event R<sub>1</sub> more unfavourable (this is a critical step of MSR, as shown in Figure



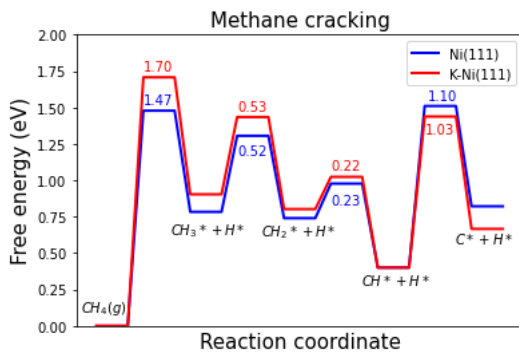
18(a)). This is in excellent agreement with the findings reported previously in the literature.<sup>17,19</sup> The free energy barriers of other CH<sub>x</sub> dissociation events are similar between the Ni(111) and K-Ni(111) surfaces. The CH dissociation step (event R<sub>4</sub>) is endothermic, having a high free energy barrier, which is in good agreement with literature studies.<sup>6,173</sup>

**Table 8. List of elementary events, activation barriers/reaction energies of the MSR reaction on Ni(111) and K-Ni(111)**

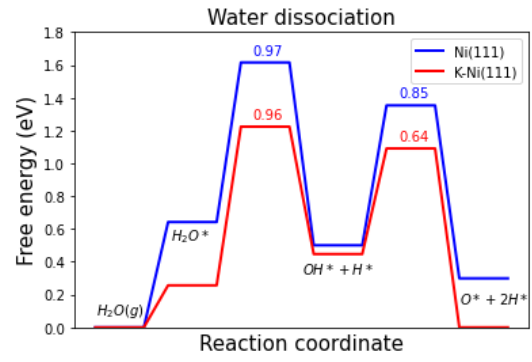
Event ID: Reaction	$E_{act}$ (eV)	$\Delta E_{rxn}^0$ (eV)	$E_{act}$ (eV)	$\Delta E_{rxn}^0$ (eV)
	Ni(111)	Ni(111)	K-Ni(111)	K-Ni(111)
R <sub>1</sub> : CH <sub>4</sub> (g) + 2* $\leftrightarrow$ CH <sub>3</sub> * + H*	0.41 (0.94)	-0.53	0.56 (0.96)	-0.40
R <sub>2</sub> : CH <sub>3</sub> * + * $\leftrightarrow$ CH <sub>2</sub> * + H*	0.66 (0.64)	0.02	0.69 (0.72)	-0.03
R <sub>3</sub> : CH <sub>2</sub> * + * $\leftrightarrow$ CH* + H*	0.26 (0.63)	-0.37	0.25 (0.67)	-0.42
R <sub>4</sub> : CH* + * $\leftrightarrow$ C* + H*	1.31 (0.84)	0.47	1.21 (0.90)	0.30
R <sub>5</sub> : 2H* $\rightarrow$ H <sub>2</sub> (g) + 2*	1.33 (0.00)	1.33	1.33 (0.00)	1.33
R <sub>6</sub> : H <sub>2</sub> O(g) + * $\leftrightarrow$ H <sub>2</sub> O*	0.00 (0.54)	-0.54	0.00 (0.87)	-0.87
R <sub>7</sub> : H <sub>2</sub> O* + * $\leftrightarrow$ OH* + H*	0.89 (1.32)	-0.43	0.79 (0.91)	-0.12
R <sub>8</sub> : OH* + * $\leftrightarrow$ O* + H*	0.98 (1.21)	-0.23	0.76 (1.24)	-0.48
R <sub>9</sub> : CH* + OH* $\leftrightarrow$ CHOH* + *	1.45 (0.80)	0.65	1.15 (0.58)	0.57
R <sub>10</sub> : CHOH* + * $\leftrightarrow$ CHO* + H*	0.75 (1.17)	-0.42	0.57 (1.15)	-0.58
R <sub>11</sub> : CHOH* + * $\leftrightarrow$ COH* + H*	0.12 (0.81)	-0.69	0.16 (0.86)	-0.70
R <sub>12</sub> : CH* + O* $\leftrightarrow$ CHO* + *	1.51 (1.05)	0.46	1.53 (1.08)	0.45
R <sub>13</sub> : C* + OH* $\leftrightarrow$ COH* + *	1.41 (1.91)	-0.50	1.01 (1.46)	-0.45
R <sub>14</sub> : CHO* + * $\leftrightarrow$ CO* + H*	0.19 (1.51)	-1.32	0.14 (1.57)	-1.43
R <sub>15</sub> : COH* + * $\leftrightarrow$ CO* + H*	0.91 (1.97)	-1.06	0.78 (2.10)	-1.32
R <sub>16</sub> : C* + O* $\leftrightarrow$ CO* + *	2.28 (3.61)	-1.33	1.61 (2.90)	-1.29
R <sub>17</sub> : CO* $\rightarrow$ CO(g) + *	2.12 (0.00)	2.12	2.46 (0.00)	2.46
R <sub>18</sub> : CO* + O* $\rightarrow$ CO <sub>2</sub> (g) + 2*	1.62 (0.36)	1.26	1.87 (0.00)	1.87

As illustrated in Figure 18(b), the presence of potassium significantly increases the stability of water on Ni(111). Zhou et al.<sup>176</sup> also make a similar observation. This is critical to reduce the build-up of CH/C species on the Ni(111) facet. We find that potassium has a negligible effect on the free energy activation barrier for the subsequent dissociation step of water (which leads to the formation of OH and H on Ni(111) – event R<sub>7</sub>). The forward free energy activation barrier of OH dissociation step (event R<sub>8</sub>) is reduced by 0.21 eV on the K-Ni(111) system. Furthermore, the thermodynamic stability of the O\* + 2H\* state is substantially higher (close to 0.3 eV) on the K-Ni(111) in comparison to Ni(111) (refer to Figure 18(b)). Thus, it is clear from the free energy analysis that the potassium promotes water dissociation on Ni(111).

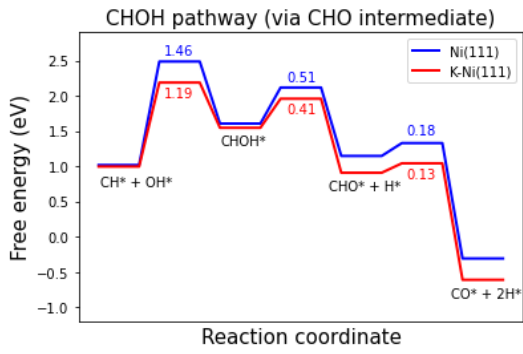
The removal of CH/C species on Ni(111) mainly happens by oxidation using OH/O species. There are several pathways for the oxidation of CH/C species on the Ni(111) facet.<sup>6,10</sup> In Figure 18, we have provided detailed free energy diagrams for each of the pathways. As shown in Figure 18(c), the “CHOH pathway via CHO” initially involves oxidation of CH species with hydroxyl, which leads to the formation of the CHOH\* intermediate (event R<sub>9</sub>). The forward free energy activation barrier of this event is substantially reduced (close to 0.27 eV) by potassium. However, the thermodynamic stability of CHOH\* intermediate remains unchanged on the K-Ni(111) system. The CHOH\* intermediate subsequently dissociates to form CHO\* (refer to event R<sub>10</sub> in Table 8). This CHO\* species further dissociates to form carbon monoxide (event R<sub>14</sub>). As illustrated in Figure 18(c), these events have slightly lower forward free energy activation barrier on the K-Ni(111) system. Alternatively, the CHOH\* intermediate can dissociate to form COH\*, which further dissociates to form CO\* (these steps are events R<sub>11</sub> and R<sub>15</sub> in Table 8, respectively). In the K-Ni(111) system, event R<sub>11</sub> has slightly higher free energy activation barrier compared to Ni(111). Whereas event R<sub>15</sub> is moderately favourable on the K-Ni(111) system than Ni(111) (as shown in Figure 18(d)). There are three other important CH/C oxidation pathways: 1) The CH\* intermediate can react with O\* to form the CHO\* intermediate (event R<sub>12</sub>), which subsequently dissociates to CO\*. For this pathway, the forward free energy activation barriers are similar between Ni(111) and K-Ni(111) (refer to Figure 18(e)). 2) The C\* species can react with hydroxyl to produce COH\* intermediate (event R<sub>13</sub>), which then undergoes subsequent dissociation to form CO\*. As shown in Figure 18(f), the forward free energy activation barrier of event R<sub>13</sub> is substantially reduced on K-Ni(111) (close to 0.30 eV). The subsequent dissociation of COH\* to CO\* also occurs more favourably on K-Ni(111). 3) The final pathway is the direct oxidation mechanism, where C\* directly reacts with O\* to form CO\* (event R<sub>16</sub>). This pathway is kinetically more favourable on the K-Ni(111) system than Ni(111) (refer to Figure 18(g)).



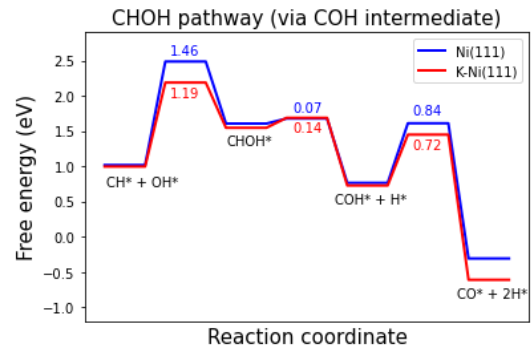
a)



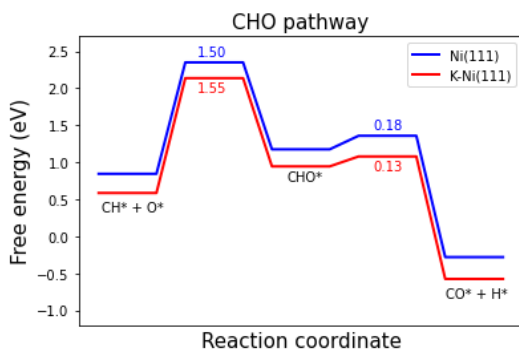
b)



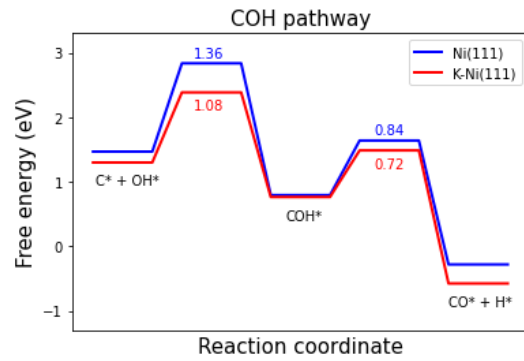
c)



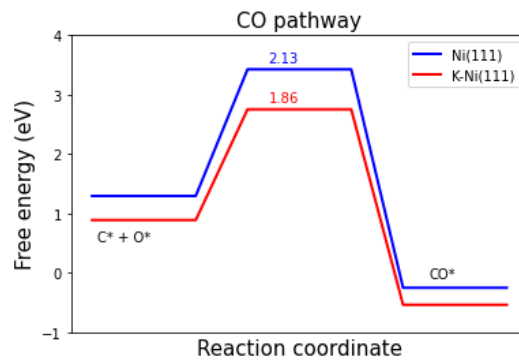
d)



e)



f)



g)

Figure 18: Free energy diagrams of MSR on Ni(111) and K-Ni(111) surfaces at 1073 K. The partial pressures of  $\text{CH}_4(\text{g})$ ,  $\text{H}_2\text{O}(\text{g})$  and  $\text{H}_2(\text{g})$  are 6.67 bar, 3.33 bar and 1 mbar, respectively.

As discussed, potassium has a strong promotional effect on the Ni(111) surface. The binding strengths of H<sub>2</sub>O/O species are increased. Furthermore, most of the CH/C oxidation pathways are more favourable on the K-Ni(111) system. Nevertheless, it is important to note that the free energy analysis does not account for the lateral interactions between adsorbates, which can substantially alter the chemistry/kinetics of the reaction. It is paramount to account for the lateral interactions between adsorbates to thoroughly understand the effect of potassium on the Ni(111) surface at steam reforming conditions. Therefore, in this study, we have developed an *ab-initio* KMC model to rationalise the role of potassium in MSR.

### 5.3.2 KMC predictions at different operating conditions

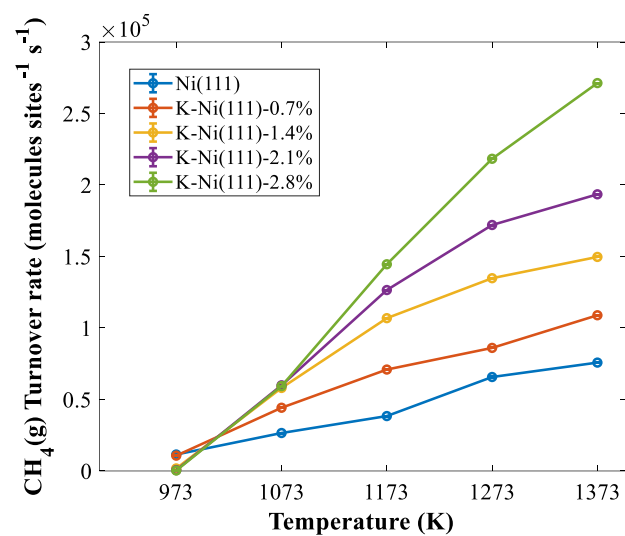
The KMC simulations of MSR on the Ni(111) and K-Ni(111) systems have been conducted by taking into account the detailed lateral interactions between adsorbates. The adsorbate interactions have been captured for the most relevant species (these include high-coverage species and species involved in bimolecular reactions). The ECI values of these adsorbate interactions are available in Appendix III (refer to Table A41). In Figure A20 of Appendix III, we depict a few schematics of the co-adsorbed geometries of MSR species on K-Ni(111). It is clear from Table A41 that the adsorbates experience significant repulsive interactions. For instance, the CH-CH, C-C and O-O interactions on Ni(111) are 0.26 eV, 0.38 eV and 0.36 eV, respectively. These interactions can substantially alter the kinetics of the MSR reaction. Furthermore, the main strategy to reduce coking is to effectively remove CH/C species from the Ni(111) surface. Thus, capturing these interactions can help us understand more clearly the removal mechanism of CH/C species. Interestingly, the ECI values of most of the MSR species in the potassium-modified Ni(111) system are very similar to Ni(111) (as shown in Table A41 Appendix III). This indicates that the potassium has a negligible impact on the lateral interactions between MSR adsorbates. Nevertheless, there are a few adsorbate interaction terms that are substantially different in the K-Ni(111) system. For example, the O-COH ECI value on Ni(111) is 0.12 eV, whereas the O-COH ECI value on K-Ni(111) is 0.31 eV. Overall, the pairwise ECI values of most MSR species on Ni(111) and K-Ni(111) are in the range of 0-0.5 eV (at the 1NN level, as shown in Table A41 of Appendix III). Therefore, lateral interactions could play a critical role in determining the favourable MSR pathways and thermodynamic stabilities of important MSR species (such as CH, C, OH and O).

As discussed previously, the KMC model has the capability to explicitly account for the lateral interactions on Ni(111) and K-Ni(111). It can give us valuable information about the detailed kinetics of MSR in the presence of potassium. In this study, we performed several KMC simulations on the Ni(111) and K-Ni(111) systems. We have treated the potassium as a site in the KMC lattice. We investigated the change in coverages/kinetics of MSR for different loadings of potassium on the Ni(111) facet. The KMC lattice configurations of Ni(111), K-

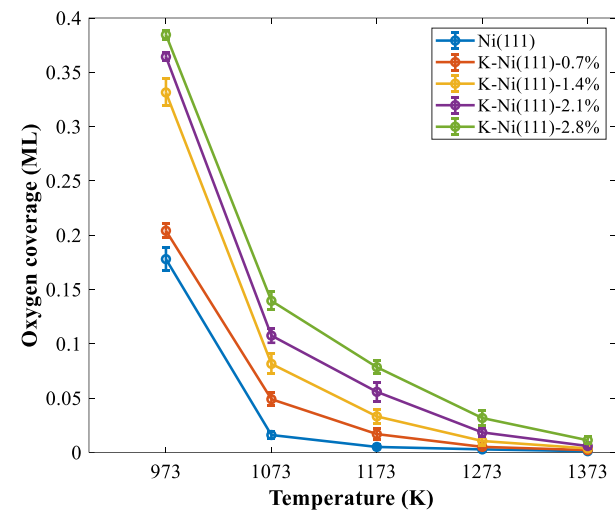
Ni(111)-0.7%, K-Ni(111)-1.4%, K-Ni(111)-2.1% and K-Ni(111)-2.8% are shown in Figure A19 of Appendix III. The Figure 19 illustrates the methane dissociation turnover rates and species coverages on the clean Ni(111) and K-Ni(111) (with different loadings) systems. As discussed earlier (in section 5.2.3), the estimated error of the slope and the standard deviation of the coverage sample are shown in Figure 19. Furthermore, we carried out simulations with five different random seeds to compute the standard error in the KMC prediction. These results are provided in Table A44 and Table A45 of Appendix III.

It is evident from Figure 19(a) that at high temperatures (1173 K and beyond), the turnover rates on the K-Ni(111) systems are much larger than the pure Ni(111) facet. For instance, at 1273 K, the turnover rate of MSR on the K-Ni(111)-2.8% is around 3 times higher than the MSR turnover rate on pure Ni(111) system. This illustrates the beneficial effects of including potassium on the Ni(111) facet. On the other hand, at 973 K (low operating temperatures), the MSR turnover rate on the K-Ni(111)-2.8% system is around 34 times lower in comparison to Ni(111) (refer to Figure 19(a)). A plausible explanation for this could be that the CH/C oxidation pathways are promoted by potassium more strongly at high temperatures compared to low temperatures. A detailed process statistics analysis can help us rationalise this observation (this is discussed in more detail in the subsequent section).

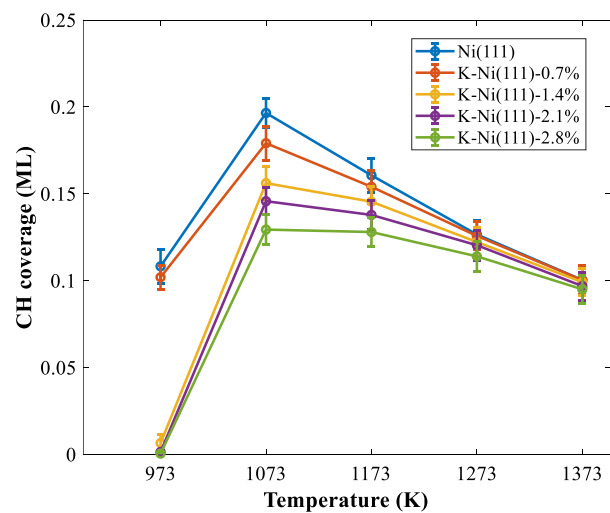
The CH, C and O species are dominant on the Ni(111) and K-Ni(111) surfaces. Thus, we show the coverage profiles of these species as a function of temperature in Figure 19 (along with error bars). The oxygen coverage profile has an interesting behaviour. At low temperatures (973 K and 1073 K), there is significant increase in the oxygen coverage on K-Ni(111) systems compared to Ni(111). For example, at 973 K, the oxygen coverage is around 0.4 ML on the K-Ni(111)-2.8% system, whereas the oxygen coverage is 0.18 ML on the pure Ni(111) system. As discussed previously, the water adsorption strength is substantially improved in the presence of potassium. Furthermore, the forward free energy activation barrier of OH dissociation (event R<sub>8</sub>) is lowered by about 0.2 eV on the K-Ni(111) surface (as shown in Figure 18(b)). Thus, there is an increase in the oxygen uptake at 973 K. On the other hand, at 973 K, potassium has a detrimental effect on the activity of the Ni catalyst at low temperatures (high oxygen coverage regime). This indicates that the presence of more O species on the potassium-modified Ni sites can potentially impede the rate of occurrence of CH/C oxidation steps (this is discussed in more detail in the subsequent section). At higher temperatures (1173 K and beyond), the oxygen coverages on the K-Ni(111) systems are similar to Ni(111) (as shown in Figure 19(b)).



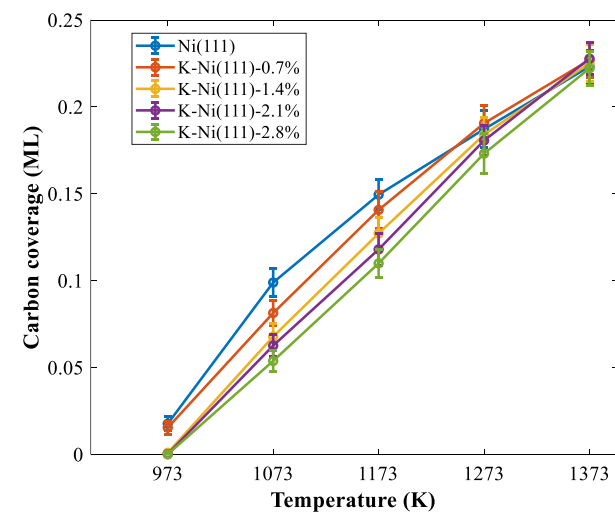
a)



b)



c)



d)

Figure 19: The turnover rate and coverages are presented with respect to temperature for the pure Ni(111) and K-Ni(111) (for different loadings) systems a)  $\text{CH}_4(\text{g})$  turnover rate, b) Oxygen coverages, c) CH coverages and d) Carbon coverages.

The CH and carbon coverage profiles are shown in Figure 19(c) and Figure 19(d), respectively. It is evident from Figure 19(c) that in the K-Ni(111) KMC models, the CH coverage is suppressed to some extent (at 973 K and 1073 K). As discussed, potassium promotes the water adsorption/OH dissociation reactions, and thus, can inhibit the formation of CH species. The CH species can act as a potential precursor to coke formation on the Ni(111) system. In chapter 4 of this thesis, we have shown that the coke terminal state is mainly composed of ring-based  $C_xH_y$  species (on Ni(111) facet) at steam reforming conditions. Thus, potassium might play a critical role in suppressing coke and thereby improve the stability of Ni. The carbon coverages are similar between Ni(111) and K-Ni(111) systems (as illustrated in Figure 19(d)). This could be mainly because the free energy barrier of the CH activation step (event  $R_4$ ) is similar between Ni(111) and K-Ni(111) systems (as shown in Figure 18(a)). Furthermore, the C-C and C-CH lateral interactions are similar on the Ni and potassium sites (refer to Table A41 of Appendix III). In the current system, we have not included the C-C coupling events that lead to coke precursors (such as  $C_2$ ,  $C_3$ ,  $C_4$  and other larger body configurations). Understanding the effect of potassium on the formation/removal of coke precursors in MSR reaction is a subject of future research efforts. Nevertheless, we have performed a preliminary DFT investigation on the  $C_2$  formation/removal steps on Ni(111) and K-Ni(111) (refer to Figure A24 of Appendix III for more details).

### 5.3.3 KMC process statistics

Careful examination of the reaction occurrence statistics (also called “process statistics”) can give us important information about the events/steps that are promoted/boosted by potassium – this can help us rationalise the observed increase in MSR turnover rate at higher temperatures. In the current scenario, we have examined the process statistics of the following steps: 1)  $CH_4$  dissociation to form  $CH_3$  and H radicals, 2) the reaction between CH and OH to form the CHOH intermediate, 3) the reaction of CH and O to generate CHO species, 4) the combination of C and OH to form the COH intermediate and 5) the formation of CO via the reaction of C and O species (the above steps are events  $R_1$ ,  $R_9$ ,  $R_{12}$ ,  $R_{13}$  and  $R_{16}$ , respectively). We specifically chose these elementary events for several reasons: firstly, the partial equilibrium ratios of all these events are close to one (refer to Table A42 of Appendix III). Thus, these events are kinetically relevant as they are not quasi-equilibrated. Secondly, the free energy analysis (as shown in Figure 18) indicates that potassium decreases the activation barriers of most of these events (such as the formation steps of CHOH/COH intermediates and the direct oxidation of C and O to form CO). Thirdly, previous MK studies have shown that these events are critical steps in the MSR reaction and significantly impact the turnover rate at steam reforming conditions.<sup>6,10</sup> The MSR reaction network, with important CH/C oxidation pathways highlighted, is illustrated in Figure 20. The overall event frequency (estimated using

eq. 87, reported in events sites<sup>-1</sup> s<sup>-1</sup>) of each MSR elementary step of the KMC Ni(111) model (at 1273 K, 10.00 bar and 2:1 H<sub>2</sub>O-CH<sub>4</sub> ratio) is also depicted.

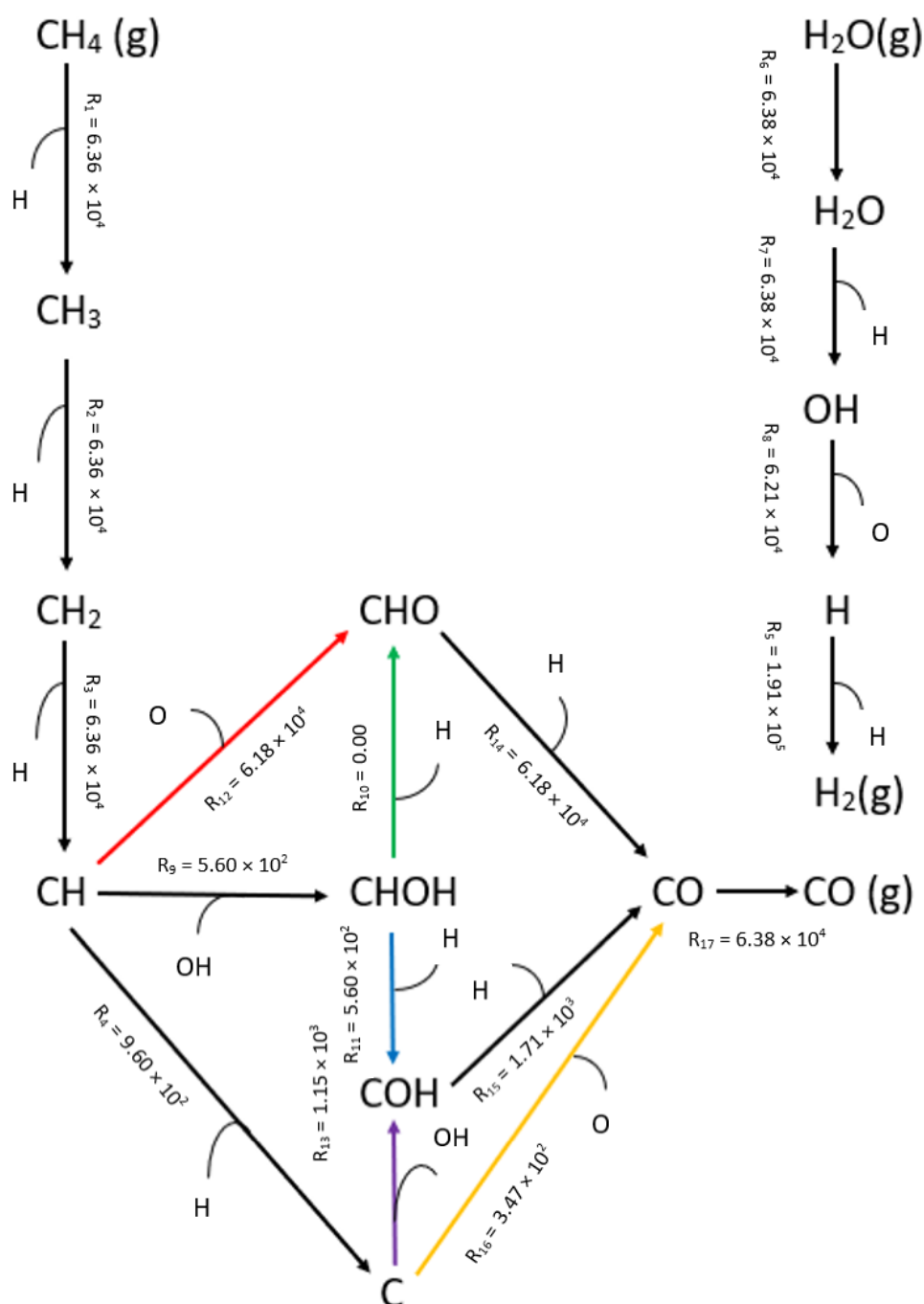
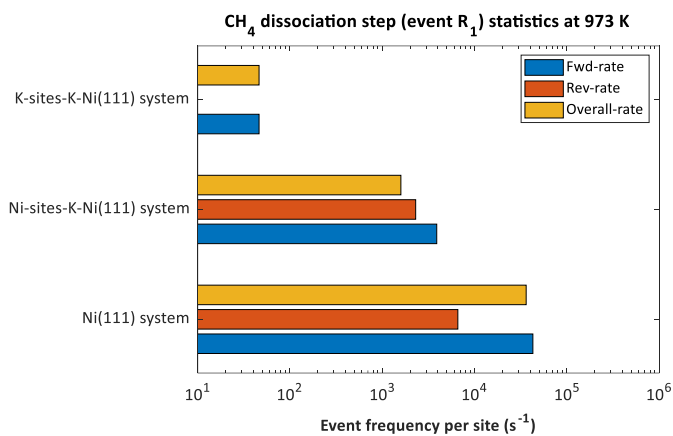


Figure 20: MSR reaction network showing several pathways to form CO: a) CHO pathway (red line), b) CHOH pathway via the CHO intermediate (green line), c) CHOH pathway via COH intermediate (blue line), d) COH pathway (purple line) and e) CO pathway (yellow line). It is important to note that these pathways have events where they merge back together – these steps are represented using black lines. Other steps/events of MSR reaction network are also indicated using black lines.

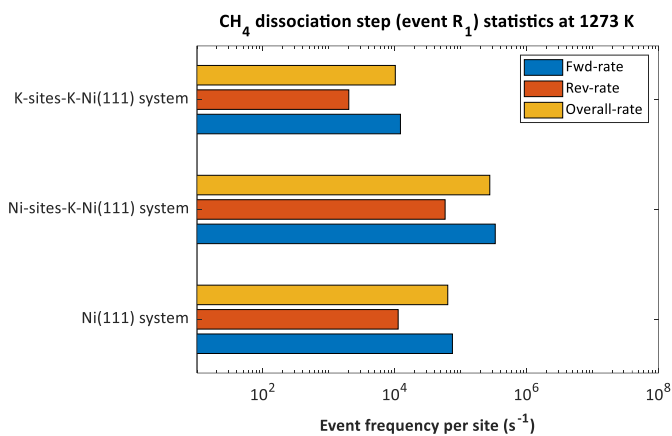


In Figure 21 and Figure 22, we have illustrated the process statistics of the events  $R_1$ ,  $R_9$ ,  $R_{12}$ ,  $R_{13}$  and  $R_{16}$  on two systems - Pure Ni(111) and K-Ni(111)-2.8%. In the K-Ni(111)-2.8% system, the MSR reaction is taking place on the Ni sites as well as the K sites. The process statistics have been shown for both of these sites in the potassium-modified Ni(111) system. The forward, reverse and overall event frequencies have been compared at two different temperatures (973 K and 1273 K). As discussed previously, at 973 K, the MSR turnover rate is close to 34 times lower on the K-Ni(111) surface than pure Ni(111). On the other hand, at 1273 K, the turnover rate of the potassium-modified Ni(111) system is around 3 times higher in comparison to pure Ni(111). Thus, the comparison of process statistics at these two temperatures is critical to clearly understand the aforementioned disparities. We direct the readers to Table A48 of Appendix III for the overall event frequencies (will be referred to as “occurrence rates” henceforth) of all MSR elementary events on Ni(111) and K-Ni(111)-2.8% (at 1273 K, 10.00 bar and 2:1 H<sub>2</sub>O-CH<sub>4</sub> ratio). It is important to note that the occurrence rates provided in Table A48 are divided by the number of sites of the corresponding site type.

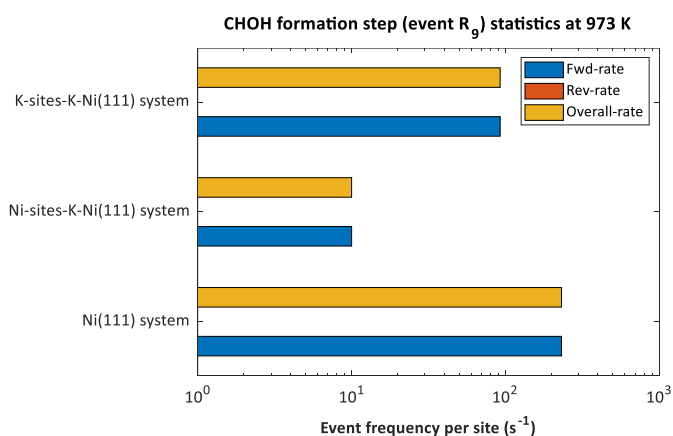
The process statistics plots of CH<sub>4</sub> dissociation step (event  $R_1$ , upon reaching the steady state) at temperatures 973 K and 1273 K are shown in Figure 21(a) and Figure 21(b), respectively. At 973 K, event  $R_1$  is not favourable on the potassium sites – this is expected as the activation barrier for this step is higher on the K-Ni(111) facet compared to Ni(111) (refer to Table 8). Furthermore, the occurrence rate of the event  $R_1$  is slightly low on the Ni sites of K-Ni(111)-2.8% compared to Ni(111) facet. This could be mainly due to coverage effects (as there is higher oxygen coverage on the K-Ni(111)-2.8% system). Similarly, the occurrence rate of event  $R_1$  on the potassium sites is substantially lower in comparison to the Ni sites at 1273 K. The process statistics plots of CHO, CHOH and COH formation steps (these are events  $R_{12}$ ,  $R_9$  and  $R_{13}$ , respectively) provide us some interesting results. At 1273 K, these events have substantially higher occurrence rates on the potassium sites of the K-Ni(111)-2.8% system. Event  $R_{12}$  occurs around 3 times faster on the potassium sites compared to the Ni(111) facet (refer to Figure 21(f)). As illustrated in Figure 21(d), the occurrence rate of event  $R_9$  is close to 28 times higher on the K sites of K-Ni(111)-2.8% than Ni(111). Moreover, the occurrence rate of event  $R_{13}$  is about 45 times faster on the potassium sites in comparison to the Ni(111) system (refer to Figure 22(b)). On the other hand, at 973 K, these events have much lower occurrence rates on the potassium sites of the K-Ni(111)-2.8% system (refer to Figure 21(c), Figure 21(e) and Figure 22(a)).



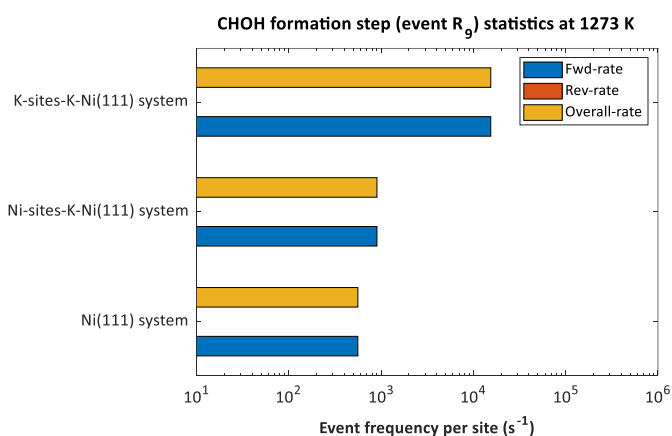
a)



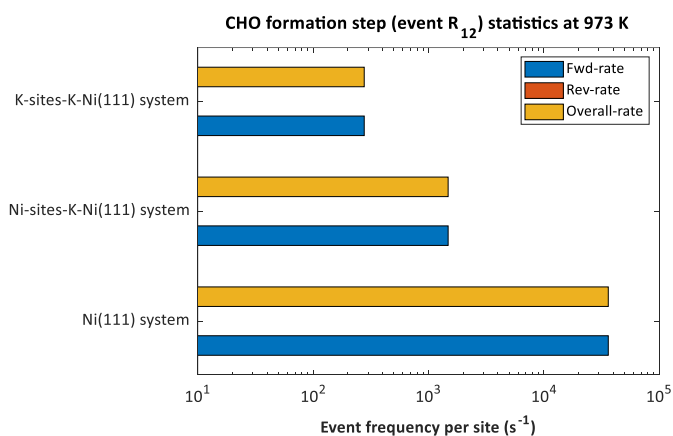
b)



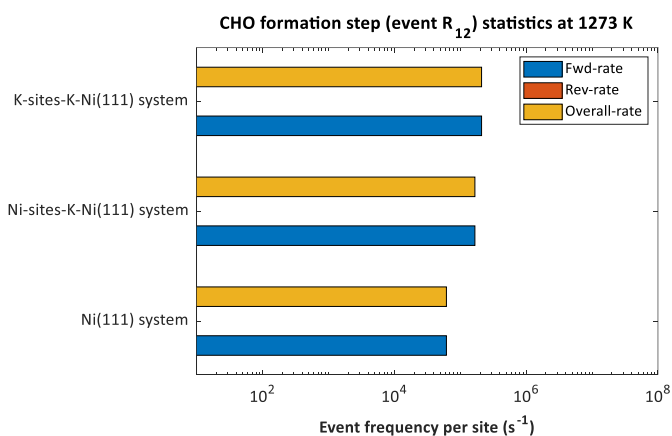
c)



d)

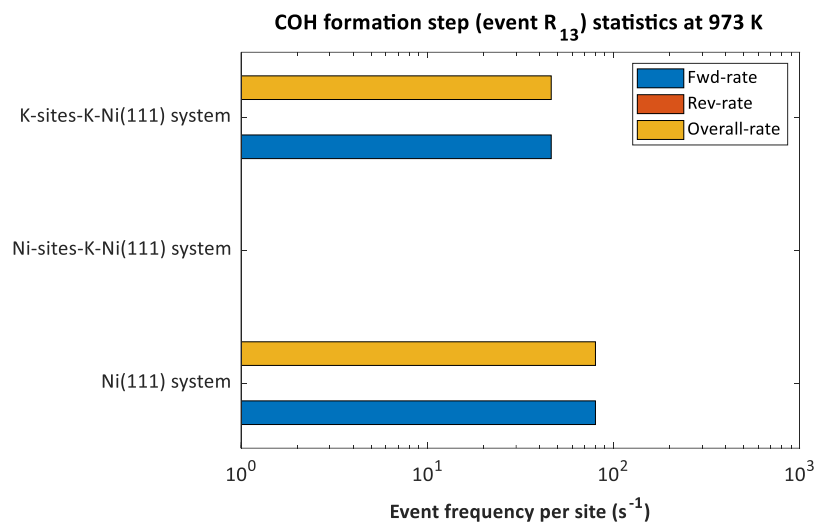


e)

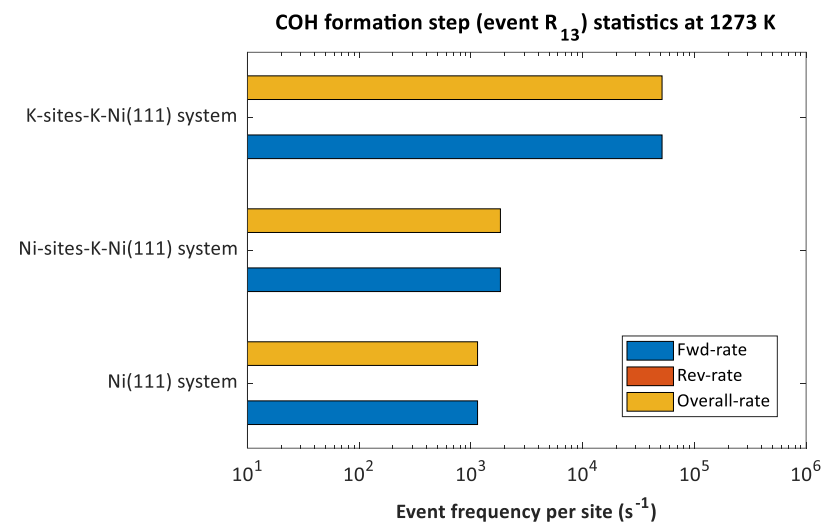


f)

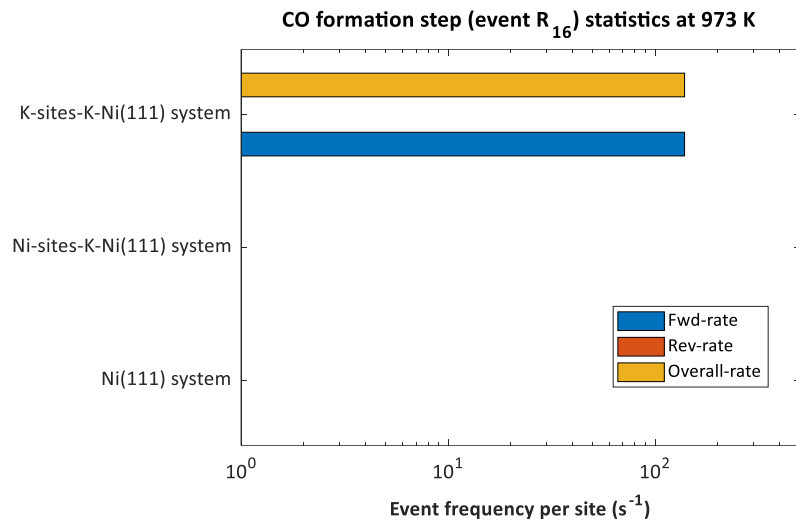
Figure 21: The event frequencies of CH<sub>4</sub> dissociation, CHOH formation and CHO formation steps are depicted. It is important to note that the event frequencies are divided with respect to the number of sites of the corresponding site type.



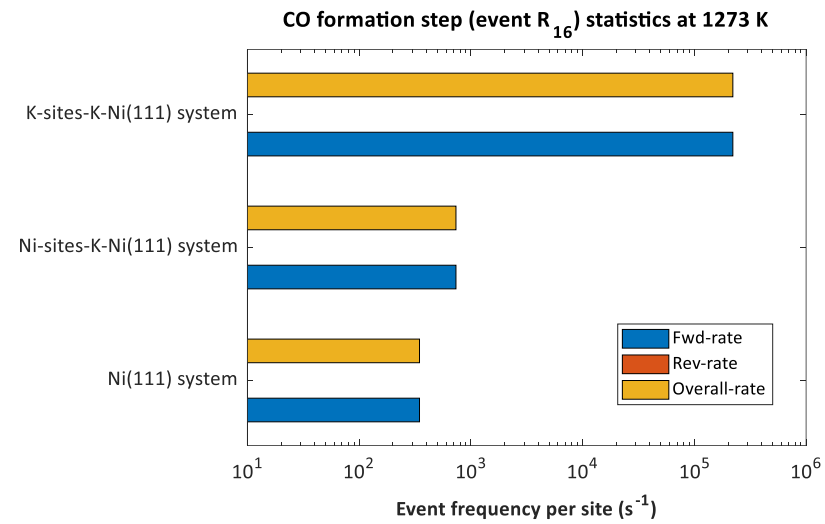
a)



b)



c)



d)

Figure 22: The event frequencies of COH formation and CO formation steps are depicted. It is important to note that the event frequencies are divided with respect to the number of sites of the corresponding site type.

It is evident from Figure 22(c) and Figure 22(d) that the potassium strongly promotes CO formation event (event  $R_{16}$ ) at both temperatures (973 K and 1273 K). Event  $R_{16}$  has a high forward activation barrier (refer to Table 8), and thus, it is not kinetically favourable at low temperatures on the Ni(111) surface (the occurrence rate on the Ni sites is zero at 973 K). On the potassium sites, event  $R_{16}$  occurs more readily as potassium reduces the forward activation barrier substantially (refer to Table 8 and the free energy diagram presented in Figure 18). As depicted in Figure 22(c), the event  $R_{16}$  takes place only on the potassium sites at 973 K. Moreover, at 1273 K, the occurrence rate of event  $R_{16}$  is around 637 times higher on the potassium sites of K-Ni(111)-2.8% compared to the pure Ni(111) system (refer to Figure 22(d)). The process statistics analysis shows that potassium has a beneficial effect by improving the rate of occurrence of CH/C oxidation events. These events play an important role in the removal of coke, and thereby, potentially increase the long-term stability of the Ni catalyst.

#### 5.3.4 KMC flux analysis

The CH/C oxidation events (as discussed above) are critical for the formation of CO in the MSR reaction. Each of these events is part of a specific reaction pathway that leads to CO formation on the Ni(111) and K-Ni(111) surfaces (as shown in Figure 20). The detailed flux analysis (estimated using eq. 89) of each of this pathway will provide us with valuable information about the dominant reforming pathway on the Ni(111) and K-Ni(111) systems at steam reforming conditions. We refer the readers to sections A 3.1 and A 3.2 of Appendix III for more information about the methodology of flux analysis. Furthermore, in Table A47 of Appendix III, we have provided the occurrence rates (divided by the total number of sites of the lattice) of all MSR elementary events on Ni(111) and K-Ni(111)-2.8%. These values are fed into the flux analysis formulation to estimate the contributions (%) of MSR pathways.

The contributions (%) of the following pathways are depicted in Figure 23: 1) CHOH pathway, 2) CHO pathway, 3) COH pathway and 4) CO pathway. It is evident from Figure 23(a) and Figure 23(c) that the CHO pathway is dominant on the pure Ni(111) surface at steam reforming conditions. This is in excellent agreement with the findings of several MK studies of MSR.<sup>6,10</sup> The flux analysis of K-Ni(111)-2.8% provides some interesting insights into the role of potassium at MSR conditions. At 973 K, we find the CHO pathway on the Ni sites (depicted as “CHO-Ni-pathway” in Figure 23(b)) to be dominant on the potassium-modified Ni(111) surface. The reforming pathways on the potassium sites have little to no contribution to the overall rate of MSR at 973 K.

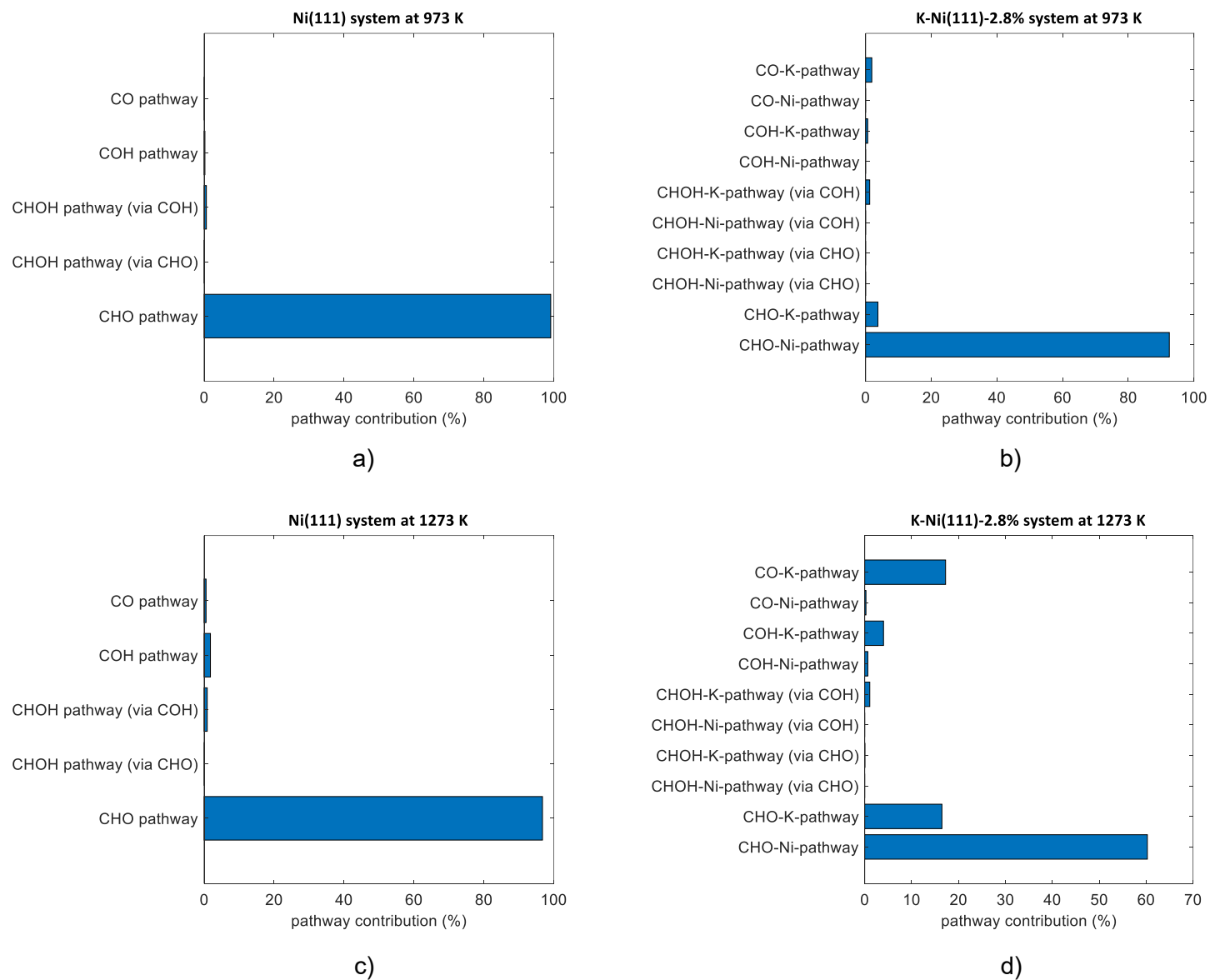


Figure 23: The MSR pathway contributions (%) of Ni(111) and K-Ni(111)-2.8% are depicted at 973 K and 1273 K.

On the other hand, at 1273 K, the CO-K-pathway and CHO-K-pathway (these are occurring on the potassium sites) contribute substantially to the net MSR turnover rate. The combined contribution of both of these pathways is around 34% (refer to Figure 23(d)). As discussed previously, the CHO formation step (event  $R_{12}$ , which is part of the CHO-K-pathway) and CO formation step (event  $R_{16}$ , belonging to the CO-K-pathway) have much higher occurrence rates on the potassium sites of K-Ni(111)-2.8% compared to the Ni(111) system (refer to Figure 21(f) and Figure 22(d)). Moreover, the COH-K-pathway has a contribution of close to 4% to the MSR turnover rate. The CHO-Ni-pathway remains to be dominant on the K-Ni(111)-2.8% system at 1273 K (the contribution is around 60%). It is important to note that the K-Ni(111)-2.8% has far fewer potassium sites than Ni sites, and thus, it is expected that CHO-Ni-pathway has the highest contribution to the net MSR rate. Nevertheless, these results clearly indicate that the potassium alters the reaction flux (pathway contributions) of MSR at high temperatures. Overall, the flux analysis reinforces the argument that potassium has a substantial effect on the MSR kinetics.

### 5.3.5 KMC lattice snapshots of K-Ni(111)

In this work, we found the oxygen coverage to improve substantially on the K-Ni(111) KMC system (at 973 K, refer to Figure 19(b)). As discussed earlier, the water binding affinity on potassium sites is very high compared to Ni(111) (refer to Figure 18(b)), and thus, the formation of oxygen is more favourable in the potassium-modified Ni(111) system. Unlike mean-field MK models, the spatial information of species is preserved in the KMC simulation. In Figure 24, we provide the final KMC lattice configurations (at 973 K, upon reaching the steady state) of the K-Ni(111) systems – K-Ni(111)-0.7%, K-Ni(111)-1.4%, K-Ni(111)-2.1% and K-Ni(111)-2.8%. It is evident from Figure 24 that the coverage of oxygen (depicted with the pink markers) is higher on the KMC lattices with higher loadings of potassium. Furthermore, we observe that the oxygen species tend to accumulate on the potassium sites with higher affinity than Ni sites (the grey triangles represent the potassium sites in the KMC lattice snapshot). These KMC lattice snapshots reveal the electronic effect induced by potassium on the Ni(111) facet. The potassium promotes the water adsorption/dissociation reactions, and thus, improves the oxygen uptake on Ni(111) at steam reforming conditions. This is in line with the observations made by other theoretical/experimental studies on the role of potassium in MSR.<sup>36,175,179,180</sup>

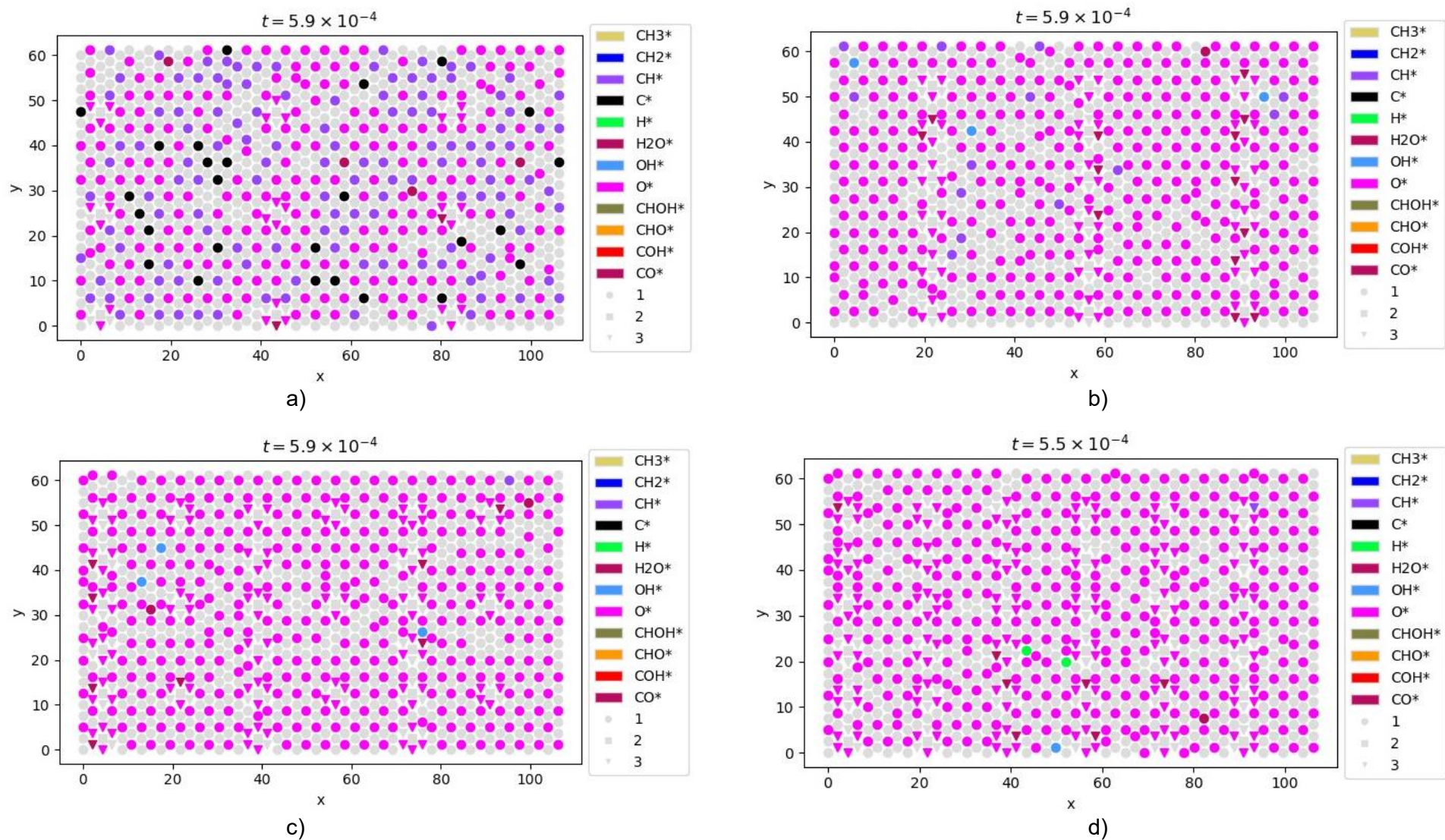


Figure 24: The final KMC lattice snapshots (upon reaching the steady state) of the K-Ni(111) systems at 973 K: a) K-Ni(111)-0.7%, b) K-Ni(111)-1.4%, c) K-Ni(111)-2.1% and d) K-Ni(111)-2.8%. The standard hexagonal lattice has been used to perform the KMC simulations. The lattice sites (Ni and K) are colour coded as grey. The colour scheme of adsorbates is shown in the KMC snapshot (The units of x and y axes are in Angstroms (Å))

Overall, the presence of potassium significantly alters the MSR kinetics at high temperatures. The net turnover rate of MSR is around 3-4 times greater on the K-Ni(111)-2.8% system at temperatures 1173-1373 K. This indicates that the potassium has a promotional effect which improves the rates of important MSR events. We analysed the KMC process statistics to understand the rate of occurrences of key MSR events on the Ni(111) and K-Ni(111)-2.8% systems. We observe that the MSR events – CHO formation (event  $R_{12}$ ), CHOH formation (event  $R_9$ ), COH formation (event  $R_{13}$ ) and CO formation (event  $R_{16}$ ) – have significantly high occurrence rates on the potassium sites of K-Ni(111)-2.8% compared to Ni(111) at 1273 K. Moreover, the flux analysis demonstrates that the CHO pathway and CO pathway on potassium sites have significantly larger contributions to the net turnover rate of MSR at high temperatures. At low temperatures (such as 973 K), the KMC snapshots reveal that the oxygen species prefer to bind more strongly to the potassium sites. These results clearly illustrate the promotional effects of potassium on Ni(111) at MSR conditions.

#### 5.4 Conclusions

In the chemical industries, potassium is widely used as a promoter to reduce coke formation and improve the productivity of MSR. A few DFT studies have shown that the presence of potassium alters the binding energy of water and the activation barriers of key MSR reaction steps/events on extended facets such as Ni(111). These theoretical works hypothesise that potassium acts as an electron donor, which can potentially improve the carbon removal rate on Ni. Nevertheless, these DFT studies do not account for thermal and entropic effects, and thus, a detailed mechanistic level understanding of the effect of potassium on MSR kinetics has remained elusive.

In this work, we developed an *ab-initio* KMC model for the MSR reaction to gain a comprehensive understanding on the role of potassium at steam reforming conditions. We performed extensive DFT calculations to compute the binding energies, activation barriers and adlayer energetics of MSR intermediates/steps on Ni(111) and K-Ni(111). In the KMC model, we captured the adsorbate-adsorbate interactions on the Ni and potassium sites by using the CE framework. The KMC simulations were carried out on the pure Ni(111) and several K-Ni(111) systems (these include K-Ni(111)-0.7%, K-Ni(111)-1.4%, K-Ni(111)-2.1% and K-Ni(111)-2.8%). The KMC model reveals that the addition of potassium on Ni(111) significantly improves the MSR net turnover rate at high temperatures. For example, at 1273 K, the MSR turnover rate is around 3 times higher on the K-Ni(111)-2.8% system in comparison to pure Ni(111). At low temperatures, the concentration of oxygen is predicted to be substantially higher on the K-Ni(111) surfaces. Furthermore, the CH coverage is suppressed, to a certain extent, on K-Ni(111) at 973 K and 1073 K. The CH species act as precursors to coke formation on the Ni catalyst surface. Thus, the potassium could potentially play an important role in



reducing coke formation on the Ni catalyst surface. These results unequivocally demonstrate the beneficial effects of potassium in the MSR reaction.

In an effort to rationalise the observed increase in MSR turnover rate in the KMC simulations, we carefully analysed the process statistics of key MSR events/steps. The process statistics plots provide us with some interesting insights into the effect of potassium at steam reforming conditions. At 1273 K, the CHO formation event (event  $R_{12}$ ) has an occurrence rate of around 3 times higher on the potassium sites of the K-Ni(111)-2.8% system compared to Ni(111). The occurrence rates of CHOH and COH formation steps (events  $R_9$  and  $R_{13}$ , respectively) are around 28 and 45 times higher on the potassium sites, respectively. Moreover, the occurrence rate of the CO formation step (event  $R_{16}$ ) is close to 637 times higher in the presence of potassium. The process statistics analysis shows that the key CH/C oxidation events are more favourable on the potassium sites at steam reforming conditions. We also performed a detailed flux analysis of the MSR reforming pathways on the Ni(111) and K-Ni(111) systems. On the Ni(111) facet, the CHO pathway is dominant at steam reforming conditions – this is in excellent agreement with the MK predictions available in the literature.<sup>6,10</sup> In the case of K-Ni(111)-2.8%, the CHO-Ni-pathway is dominant at 973 K and 1273 K. However, we find that the CHO-K-pathway and the CO-K-pathway also contribute substantially (around 34%) to the MSR turnover rate at 1273 K. Furthermore, performing degree of rate control (DORC, established by Campbell<sup>181</sup>) can provide us information about the rate-limiting/inhibiting steps of MSR. Given the stochastic variability of the KMC turnover predictions (with different random seed generators), obtaining reliable DORC values is an extremely challenging and computationally expensive task (more information is provided in Table A46 of Appendix III). It is beyond the scope of the current study to perform a thorough DORC analysis. Nevertheless, previous MK studies have shown that the rate-limiting step of MSR varies based on the operating conditions.<sup>6,10</sup> These studies have reported that the events  $R_1$ ,  $R_9$ ,  $R_{12}$  and  $R_{16}$  can be rate-limiting at MSR conditions. We have thoroughly investigated the process statistics of the aforementioned events in our KMC model.

Overall, we can conclude that the increase in MSR turnover rate in the potassium-modified Ni(111) system might be occurring due to a combination of several effects. These include the following: 1) differences in binding propensities/activation barriers of key MSR species/events on Ni and K sites, 2) lateral interactions could also impact the reaction kinetics, 3) higher rates of occurrences of important MSR steps – events  $R_9$ ,  $R_{12}$ ,  $R_{13}$  and  $R_{16}$  and 4) alterations in reforming pathway contributions (reaction flux) in the presence of potassium. In the KMC simulations, the aforementioned effects have been captured in detail at MSR conditions, and our simulations can potentially aid experimentalists in designing Ni-based catalysts that are highly stable/active for this chemistry. As part of future research efforts, the role of potassium

in C-C coupling/removal reactions can be investigated at MSR conditions. Moreover, the effect of other promising promoters such as Mo and Mn can also be studied under the CE framework of KMC.

# Chapter 6

## 6. DFT and microkinetic studies of C-C coupling reactions on the Ni(111) surface

Elucidating the growth mechanism of carbon whiskers on the Ni catalyst surface is of paramount importance to tackle the coking problem. Despite several efforts, a detailed understanding of coking kinetics on the Ni(111) surface has remained elusive. As discussed previously, the whisker carbon growth involves formation of large body carbon-based configurations ( $C_xH_y$  species) on the Ni catalyst surface. It is a formidable challenge to formulate a kinetic model that can capture the detailed steps of coke formation. In this chapter, we have developed an *ab-initio* MK model to understand the growth mechanism of carbon whiskers on Ni(111). To this end, we first performed DFT calculations to estimate the activation barriers of several C-C coupling events ( $C_2$ - $C_6$ ). Subsequently, the DFT computed data was fed into a MK model to predict the macroscopic coverages of coke precursors, favourable pathways of coking and sensitive reactions. These preliminary results/findings can motivate future works to delve further into the kinetics of large-body  $C_xH_y$  species on Ni(111).

### 6.1 Introduction

In the past few decades, there has been considerable interest in the scientific community to employ DFT calculations for delineating the coking mechanism on the Ni catalyst surface. One of the seminal DFT works in this regard, was conducted by Helveg and co-workers.<sup>58</sup> The authors employed high-resolution *in situ* transmission electron microscopy (TEM) and DFT to elucidate the growth mechanism of whisker carbon due to methane decomposition on supported Ni nanocrystals. TEM imaging reveals that the carbon nucleation process involves the formation of graphene sheets on Ni(111) at the molecular level. Furthermore, the Ni surface undergoes dynamic restructuring to create steps/defects that enable the accumulation of carbon. Based on these observations, the authors hypothesised that graphene formation involves migration of carbon atoms from Ni steps/defects to the Ni(111) surface and subsequent carbon diffusion along the Ni(111) surface. A proposed DFT model of these processes was found to explain the TEM observations satisfactorily. Subsequently, Abild-Pedersen et al.<sup>182</sup> performed detailed DFT studies to explore the favourable pathways for carbon migrations from steps/defects to the support side. These studies provide useful atomistic level insight into the coking mechanism on Ni. However, the intermediate steps/stages and plausible carbon poison precursors responsible for graphene formation on Ni(111) are not thoroughly explored, and this is critical to understand the growth of carbonaceous species on Ni(111).<sup>155</sup>

In recent years, several investigations have been conducted to expound the growth mechanism of graphene on Ni(111). Li et al.<sup>158</sup> have reported that carbon clusters/precursors (responsible for graphene growth) are mobile on the Ni catalyst surface. A few studies have investigated the thermodynamic stability of simple carbon-based clusters on Ni(111) (such as

C<sub>2</sub>, C<sub>3</sub> and C<sub>4</sub>).<sup>155,157,169</sup> Gao et al.<sup>183</sup> studied the graphene nucleation process on the Ni terrace using DFT, while Li et al.<sup>157</sup> performed DFT calculations to compute the activation barriers of C-C coupling (C<sub>2</sub>-C<sub>6</sub>) events on Ni(111). In the latter study, the authors report that it is kinetically more favourable to form branched carbon clusters than chains. Nonetheless, the aforementioned DFT studies of C-C coupling events do not account for the thermal, entropic and coverage effects. Furthermore, a comprehensive study of coking kinetics on Ni(111) is currently lacking in the literature. Thus motivated, we have developed a first-principles-based MK model for the methane cracking and C-C coupling (C<sub>2</sub>-C<sub>6</sub>) reactions. The MK model provides insights into the thermodynamic stability of carbon-based clusters, favourable pathways to coke formation and sensitivity of coking rates to methane cracking/C-C coupling elementary events at MSR conditions. The rest of this chapter is organised as follows: 1) in section 6.2, we provide details about the computational setup; 2) the results of DFT and MK studies are discussed in section 6.3 and 3) a brief summary is provided about the outcomes of the current study in section 6.4.

## 6.2 Computational details

### 6.2.1 DFT calculations

We employed the VASP software to carry out spin-polarised DFT calculations. The exchange-correlation energy was approximated by using the PBE-D3 functional. The Ni(111) surface was modelled by employing a p(4×4) six-layer slab – bottom three layers have been fixed to Ni bulk positions. The plane-wave energy cut-off value was set to 400 eV. Brillouin zone sampling was carried out using a 5×5×1 Monkhorst-Pack k-point grid. We used the PAW method to model the interactions between core and valence electrons. The convergence parameter for the electronic self-consistency loop was set to 10<sup>-7</sup> eV. In the DFT calculations, the conjugate gradient method was used to find the most stable geometry (initial states) of adsorbates on Ni(111). The adsorbate atoms and top three layers of the Ni(111) slab were relaxed until the Hellmann-Feynman forces were less than 10<sup>-2</sup> eV/Å. We carried out electron smearing by using the Methfessel-Paxton method. The dimer method<sup>72</sup> was employed to locate the transition states of methane cracking and C-C coupling events on Ni(111). We performed vibrational analysis on converged geometries using the central finite-difference method (the step size for the displacement was set to 0.02 Å). The formation energies of adsorbates were estimated using the equation below (the Ni(111) slab, CH<sub>4</sub>(g) and H<sub>2</sub>(g) are the reference states).

$$E_{FE}^{Ads} = E_{tot}^{Ads + Ni(111)} - E_{tot}^{Ni(111)} - (pE_{tot}^{CH_4(g)} + qE_{tot}^{H_2(g)}) \quad \text{eq. 90}$$

In eq. 90,  $E_{tot}^{Ni(111)}$  represents the DFT total energy of the Ni(111) slab,  $E_{tot}^{Ads + Ni(111)}$  is the DFT total energy of the adsorbate-Ni(111) system,  $E_{tot}^{CH_4(g)}$  indicates the gas-phase DFT total

energy of methane,  $E_{tot}^{H2(g)}$  refers to the gas-phase DFT total energy of hydrogen,  $E_{FE}^{Ads}$  is the formation energy of the adsorbate.  $p$  and  $q$  (real numbers) are used to stoichiometrically balance out the atoms between adsorbates and gas-phase reference species. The formula for estimating the coverage-independent forward activation barrier for a bimolecular event is given by eq. 91.

$$E_{fwd}^{act} = E_{FE}^{TS} - E_{FE}^A - E_{FE}^B \quad \text{eq. 91}$$

In the equation above,  $E_{fwd}^{act}$  represents the forward activation barrier,  $E_{FE}^{TS}$  indicates the transition state formation energy,  $E_{FE}^A$  and  $E_{FE}^B$  are the formation energies of adsorbates A and B, respectively. Campbell's DORC value ( $X_{RC,i}$ ) is estimated by using the following formula:

$$X_{RC,i} = \frac{k_i}{R} \left( \frac{\delta R}{\delta k_i} \right)_{k_j \neq i, k_i} \quad \text{eq. 92}$$

In eq. 92,  $k_i$  denotes the rate constant of an elementary event and  $R$  is the net coking rate. The rate constant of any elementary event is perturbed by 10% to determine the DORC value.

### 6.2.2 MK model

The MK model involves a system of ordinary differential equations which are solved numerically to predict turnover rates and “averaged” coverages of species (refer to section 2.7 of chapter 2 for MK formulation). The current system consists of 16 elementary events – methane cracking and C-C coupling reactions (listed in Table 9). We treated the large-body carbon-based configurations as point species in the MK model. The following assumptions have been made while developing the MK model: 1) each adsorbate can occupy only a single site in the MK model; 2) an adsorbate has the same binding energy on all catalytic sites; 3) lateral interactions between adsorbates are neglected and 4) the kinetic constants have no dependency on coverage. The MK equations have been written in MATLAB 2019b and solved numerically by invoking the ODE15s solver, which is appropriate for stiff problems. The pre-exponentials have been estimated by using the formulas provided in subsection 4.2.5 of chapter 4 (refer to eq. 77, eq. 78, eq. 79 and eq. 80).

### 6.3 Results and discussions

The coke formation process involves coupling of carbon-based clusters/species into large-body configurations that eventually totally encapsulate/poison the Ni catalyst surface. Despite numerous efforts, the detailed kinetics of coke/graphene formation has remained elusive. A major challenge with the coking process is that the C-C coupling events can generate different types of large-body structures – these include  $C_xH_y$  species in the form of rings, branches and chains. It is a formidable task to identify all the transition states of these events (as there are several plausible combinations). Furthermore, the lateral interactions between the large-body

carbon-based configurations can significantly affect the kinetics of coke/graphene formation. As a first approximation, we have developed a simple MK model (with no adsorbate interactions) to understand the nucleation process of  $C_2$ - $C_6$  species on Ni(111). We have primarily focussed on the branch/ring configurations – these structures are more likely to grow into the highly stable graphene type rings at steam reforming conditions. To the best of our knowledge, such a study is not currently available in the open literature. The rest of this section is organised as follows: 1) the DFT calculations of the methane cracking and C-C coupling reactions have been presented in section 6.3.1; 2) in section 6.3.2, we provide a thorough discussion on the MK model results at MSR conditions – these include species coverage profiles of coke precursors, identification of dominant C-C coupling pathway and sensitivity analysis of all elementary events.

### 6.3.1 DFT results

As discussed earlier, the coke nucleation on Ni(111) predominantly involves the coupling of CH/C species to form  $C_xH_y$  configurations, which can exist in the form of chains, rings and branches. We have performed DFT calculations to compute the activation barriers of these coupling events. The vibrational wavenumbers ( $cm^{-1}$ ) of the initial and transition states are shown in Table A50 and Table A51, respectively (refer to Appendix 1V). In Table 9, the activation barriers/reaction energies of methane cracking and C-C coupling reactions are shown. In the methane cracking reaction network, the CH activation step (event  $R_4$ ) has a high activation barrier (1.31 eV), which is in good agreement with DFT studies in the literature.<sup>184,169</sup> The methane dissociation event (which forms  $CH_3$  and H radicals, event  $R_1$ ) has an activation barrier of 0.41 eV. As discussed previously (refer to Table A20 of Appendix III), the forward activation barrier for event  $R_1$  changes significantly based on the DFT functional employed. Moreover, the entropic contribution for this event will be quite high, as the partition function of methane in the gas phase includes the translational/rotational modes. As shown in Table 9, the coupling of CH to form  $C_2H_2$  (event  $R_6$ ) is exothermic with a forward activation barrier of 0.81 eV. Li et al.<sup>169</sup> also find event  $R_6$  to be exothermic and report a similar forward activation barrier value. The  $C_2H_2$  species can undergo dissociation (hydrogen abstraction) to form  $C_2H$  (event  $R_7$ ) on the Ni(111) surface. Subsequently, the  $C_2H$  intermediate can dissociate to  $C_2$  (event  $R_8$ ). Both of these events are endothermic. The forward activation barriers of events  $R_7$  and  $R_8$  are 1.14 eV and 1.26 eV, respectively (refer to Table 9). The DFT study of Li et al.<sup>169</sup> also reports event  $R_7$  to be endothermic with a forward activation barrier value of 1.27 eV (this is in excellent agreement with our result). On the other hand, in the case of event  $R_8$ , the authors find the forward activation barrier is low (0.60 eV) and the reaction energy is 0.02 eV. This disparity can mainly arise due to the DFT functional. The authors have employed the RPBE functional, whereas we have used the PBE-D3 functional in our study (as discussed

previously). The  $C_2$  formation can also occur by the direct coupling of two carbon atoms (event  $R_9$ ) on the Ni(111) surface. We find this event to have an activation barrier of 1.05 eV and to be exothermic in nature. This is in reasonable agreement with the values reported in the literature (refer to Table 9). Furthermore, the  $C_2$  species is thermodynamically more stable than carbon on the Ni(111) surface. The  $C_2H_2$  and  $C_2$  species can potentially act as precursors to carbon whiskers on the Ni(111) facet. The  $C_2$  species can react with carbon to form several larger body configurations such as ( $C_3$ ,  $C_4$ ,  $C_5$  and  $C_6$  etc). The  $C_2$  coupling with carbon to form a  $C_3$  trimer (event  $R_{10}$ ) is an exothermic event. As shown in Table 9, the forward activation barriers of events  $R_9$  and  $R_{10}$  are similar. The  $C_4$  ring formation step (event  $R_{11}$ ) is kinetically more favourable than  $C_4$  branch formation (event  $R_{12}$ ) on Ni(111). Both events  $R_{11}$  and  $R_{12}$  are endothermic. Furthermore, the  $C_4$  ring has higher thermodynamic stability than  $C_4$  branch on Ni(111).

The  $C_4$  ring-based structure can further nucleate by forming  $C_5$  and  $C_6$  rings on the Ni(111) surface. The  $C_5$  ring formation event (event  $R_{13}$ ) is endothermic with a forward activation barrier of 1.10 eV. On the other hand, the  $C_6$  ring formation event (event  $R_{15}$ ) is exothermic with an activation barrier of 0.91 eV. The  $C_4$  branch-based configuration can also form other larger body branched structures (such as  $C_5$  branch and  $C_6$  branch on Ni(111)). The  $C_5$  branch formation event (event  $R_{14}$ ) has a forward activation barrier of 1.05 eV, which is similar to that of event  $R_{13}$ . However, event  $R_{14}$  is an exothermic reaction. The  $C_5$  branch to  $C_6$  branch step (event  $R_{16}$ ) has the same forward and reverse activation barrier. This event is kinetically less favourable than  $C_6$  ring formation event (refer to Table 9). Nevertheless, the  $C_6$  branch and  $C_6$  ring structures have similar thermodynamic stability on Ni(111). We have performed additional DFT calculations of C-C coupling reactions, which include higher body ring and chain-based carbon configurations (refer to Figure A25 and Figure A26 of Appendix 1V).

The C-C coupling dataset also includes “coke generation” events (refer to events  $R_{17}$  and  $R_{18}$  of Table 9). The events  $R_{17}$  and  $R_{18}$  are assumed to be fast and irreversible pseudo-desorption steps to generate “coke” that begins to poison the catalyst pores and detach the Ni nanoparticle from the support. The main idea behind including these events is to gain an understanding of the kinetics at the “initial stages” of complete deactivation. Li et al.<sup>158</sup> used a similar approach in the context of understanding carbon nanotube (CNT) growth. The authors introduced pseudo-events into the kinetic model where carbon and  $C_3$  species were incorporated into a CNT wall at the edge of the Ni nanoparticle. It is important to note that the coking process is complex, and these “fictitious events” do not capture the complete dynamics of the system. Further research is needed to unravel the end-to-end steps of the coking phenomenon.



**Table 9. Comparison of C-C coupling activation barriers/reaction energies with the literature (the numbers in parentheses are the reverse activation barriers)**

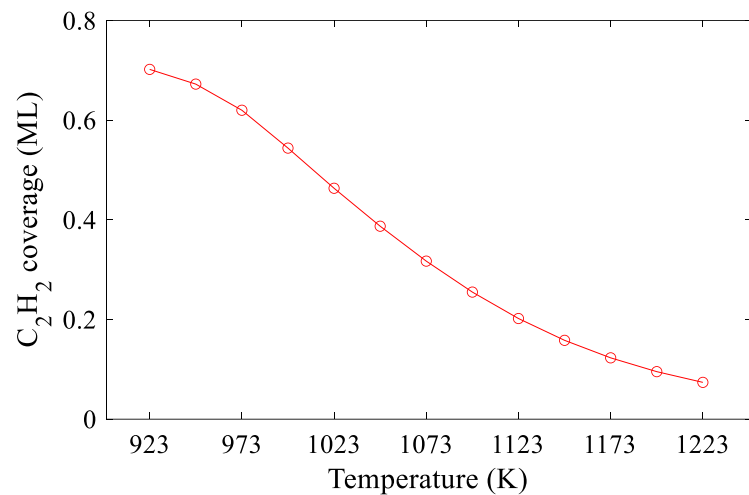
Event ID: Methane cracking events	$E_{act}$ (eV)	$\Delta E_{rxn}^0$ (eV)	$E_{act}$ (eV) Literature values
R <sub>1</sub> : CH <sub>4</sub> (g) + 2* = CH <sub>3</sub> * + H*	0.41 (0.94)	-0.53	1.29 (0.59) <sup>6</sup> , 1.05 (0.52) <sup>17</sup>
R <sub>2</sub> : CH <sub>3</sub> * + * = CH <sub>2</sub> * + H*	0.66 (0.64)	0.03	0.76 (0.13) <sup>6</sup>
R <sub>3</sub> : CH <sub>2</sub> * + * = CH* + H*	0.26 (0.63)	-0.37	0.34 (0.67) <sup>6</sup>
R <sub>4</sub> : CH* + * = C* + H*	1.31 (0.84)	0.46	1.48 (0.84) <sup>6</sup>
R <sub>5</sub> : H <sub>2</sub> (g) + 2* = 2H*	0.00 (1.33)	-1.33	0.01 (1.08) <sup>176</sup>
R <sub>6</sub> : CH* + CH* = C <sub>2</sub> H <sub>2</sub> *	0.81 (1.16)	-0.35	No value available
R <sub>7</sub> : C <sub>2</sub> H <sub>2</sub> * + * = C <sub>2</sub> H* + H*	1.14 (0.82)	0.32	1.00 (1.17) <sup>169</sup>
R <sub>8</sub> : C <sub>2</sub> H* + * = C <sub>2</sub> * + H*	1.26 (0.78)	0.48	0.60 (0.58) <sup>169</sup>
R <sub>9</sub> : C* + C* = C <sub>2</sub> *	1.05 (1.52)	-0.47	0.84 (1.48) <sup>157</sup>
R <sub>10</sub> : C <sub>2</sub> * + C* = C <sub>3</sub> *	1.16 (1.45)	-0.29	0.97 (1.29) <sup>157</sup>
R <sub>11</sub> : C <sub>3</sub> * + C* = C <sub>4ring</sub>	1.06 (0.94)	0.12	No value available
R <sub>12</sub> : C <sub>3</sub> * + C* = C <sub>4branch</sub>	1.57 (0.99)	0.58	1.16 (0.43) <sup>157</sup>
R <sub>13</sub> : C <sub>4ring</sub> + C* = C <sub>5ring</sub>	1.10 (0.90)	0.20	No value available
R <sub>14</sub> : C <sub>4branch</sub> + C* = C <sub>5branch</sub>	1.05 (1.65)	-0.60	0.23 (1.18) <sup>157</sup>
R <sub>15</sub> : C <sub>5ring</sub> + C* = C <sub>6ring</sub>	0.91 (1.14)	-0.24	0.17 (1.09) <sup>157</sup>
R <sub>16</sub> : C <sub>5branch</sub> + C* = C <sub>6branch</sub>	1.51 (1.51)	0.00	0.25 (0.75) <sup>157</sup>
R <sub>17</sub> : C <sub>6ring</sub> = Coke	0.20	Irreversible step	
R <sub>18</sub> : C <sub>6branch</sub> = Coke	0.20	Irreversible step	

Overall, the aforementioned DFT computations provide us some insight into the binding affinity and favourable pathways for the build-up of important coke precursors on the Ni(111) surface. However, these DFT calculations do not include the thermal and entropic contributions, and it is paramount to take into account these effects to gain a better understanding of coke formation mechanism at steam reforming conditions. Therefore, we have developed a MK model to predict the macroscopic coverages of coke precursors, identify the dominant carbon

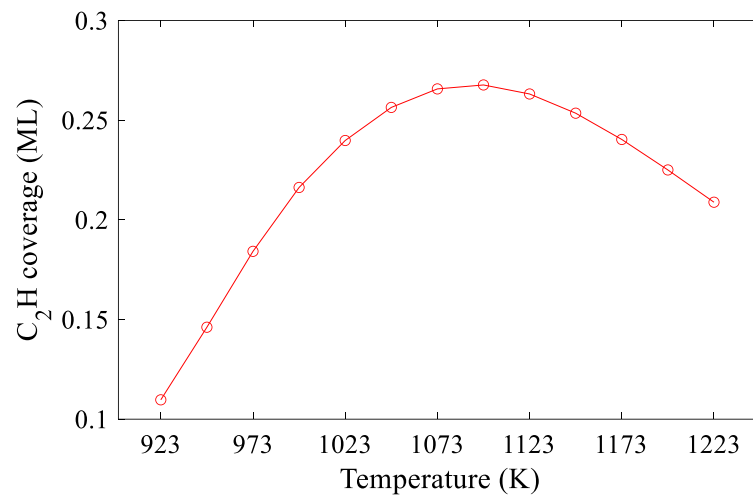
nucleation pathways and rate-limiting/inhibiting steps of the coking process (more details are provided in section 6.3.2).

### 6.3.2 MK studies

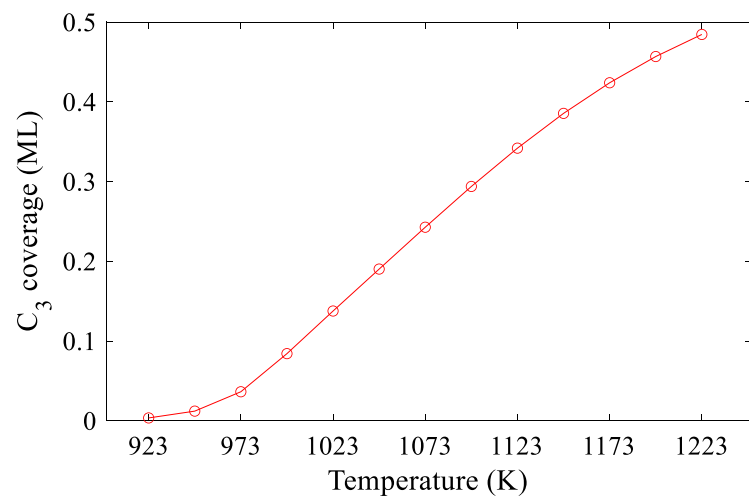
As discussed earlier, it is critical to understand the kinetics of C-C coupling reactions at MSR conditions. The MK model was employed to predict species coverages (upon reaching the steady state) at temperatures ranging from 923 K to 1223 K. The pressure of CH<sub>4</sub>(g) and H<sub>2</sub>(g) were maintained at 10 bar and 0.08 bar, respectively. In Figure 25, the macroscopic coverages of dominant species are depicted. At low temperatures (923 - 1023 K), the C<sub>2</sub>H<sub>2</sub> species is highly stable on the Ni(111) facet. The coverage of C<sub>2</sub>H<sub>2</sub> species (an important precursor of coke formation) is around 0.70 ML at 923 K. The coverage profile of C<sub>2</sub>H<sub>2</sub> exhibits a decreasing trend with respect to temperature (as shown in Figure 25(a)). There is a significant drop in C<sub>2</sub>H<sub>2</sub> coverage at temperatures 1073 K and above. As discussed earlier, the dissociation events involving the C<sub>2</sub>H<sub>x</sub> intermediates (where x ranges between 0–2) are kinetically more favourable at high temperatures (refer to Table 9) – this explains the observed decrease in C<sub>2</sub>H<sub>2</sub> coverage. The coverage of C<sub>2</sub>H species increases steadily up to 1098 K. However, it begins to decline at temperatures 1123–1223 K (refer to Figure 25(b)). The coverages of carbon and C<sub>2</sub> species are very low (less than 0.05 ML) at MSR conditions. These intermediates are short-lived as they readily undergo coupling to form larger body carbon-based configurations. As depicted in Figure 25(c), the coverage of C<sub>3</sub> species increases sharply with respect to temperature. The C<sub>3</sub> coverage is close to 0 ML at 923 K, whereas the coverage of C<sub>3</sub> species is around 0.49 ML at 1223 K. The C<sub>3</sub> species is an important precursor to form large-body carbon-based configurations on Ni(111). Suppressing the growth of C<sub>3</sub> species might be critical to reduce coke formation, and thereby, improve the long-term stability of the Ni catalyst.



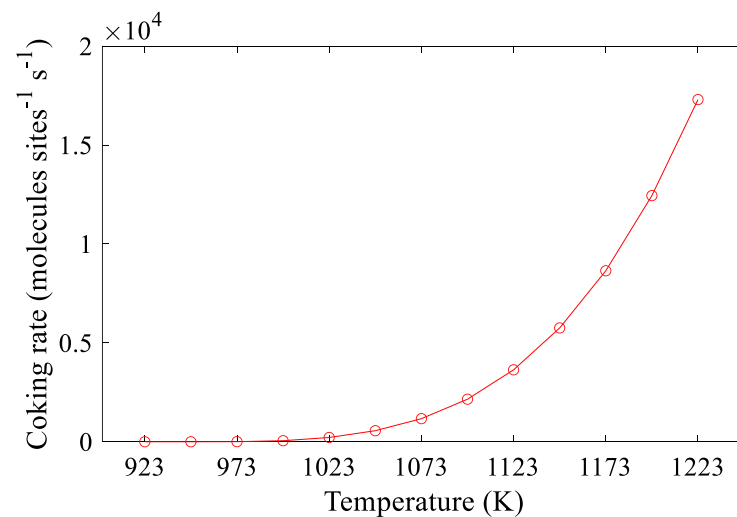
a)



b)



c)



d)

Figure 25: The coverages of dominant carbon-based species at MSR conditions: a) C<sub>2</sub>H<sub>2</sub> coverage profile with respect to temperature, b) C<sub>2</sub>H coverage profile with respect to temperature, c) C<sub>3</sub> coverage profile with respect to temperature and d) Coking rate with respect to temperature.

**Table 10. The DORC values of the methane cracking and C-C coupling events obtained by using 10% degree of perturbation.**

Event ID	923 K	973 K	1023 K	1073 K	1123 K	1173 K	1223 K
R <sub>1</sub> : CH <sub>4</sub> (g) + 2* = CH <sub>3</sub> * + H*	0.00	0.02	0.26	0.30	0.30	0.30	0.31
R <sub>2</sub> : CH <sub>3</sub> * + * = CH <sub>2</sub> * + H*	0.00	0.00	0.01	0.01	0.01	0.01	0.01
R <sub>3</sub> : CH <sub>2</sub> * + * = CH* + H*	0.00	0.00	0.00	0.00	0.00	0.00	0.00
R <sub>4</sub> : CH* + * = C* + H*	0.01	0.04	0.08	0.10	0.11	0.13	0.15
R <sub>5</sub> : H <sub>2</sub> (g) + 2* = 2H*	0.00	0.01	0.10	0.12	0.11	0.10	0.07
R <sub>6</sub> : CH* + CH* = C <sub>2</sub> H <sub>2</sub> *	0.00	0.00	0.00	0.00	0.00	0.00	0.00
R <sub>7</sub> : C <sub>2</sub> H <sub>2</sub> * + * = C <sub>2</sub> H* + H*	0.00	0.00	0.00	0.00	0.00	0.00	0.00
R <sub>8</sub> : C <sub>2</sub> H* + * = C <sub>2</sub> * + H*	0.00	0.00	0.00	0.00	0.00	0.00	0.00
R <sub>9</sub> : C* + C* = C <sub>2</sub> *	-0.01	-0.04	-0.07	-0.09	-0.10	-0.12	-0.14
R <sub>10</sub> : C <sub>2</sub> * + C* = C <sub>3</sub> *	0.00	0.01	0.03	0.01	0.00	0.00	-0.01
R <sub>11</sub> : C <sub>3</sub> * + C* = C <sub>4ring</sub>	0.00	0.00	0.00	0.00	0.00	0.00	0.00
R <sub>12</sub> : C <sub>3</sub> * + C* = C <sub>4branch</sub>	0.00	0.00	0.00	0.00	0.00	0.00	0.00
R <sub>13</sub> : C <sub>4ring</sub> + C* = C <sub>5ring</sub>	0.02	0.07	0.08	0.07	0.07	0.07	0.07
R <sub>14</sub> : C <sub>4branch</sub> + C* = C <sub>5branch</sub>	0.00	0.00	0.00	0.00	0.00	0.00	0.00
R <sub>15</sub> : C <sub>5ring</sub> + C* = C <sub>6ring</sub>	0.97	0.87	0.47	0.42	0.44	0.46	0.48
R <sub>16</sub> : C <sub>5branch</sub> + C* = C <sub>6branch</sub>	0.00	0.00	0.00	0.00	0.00	0.00	0.00

In the MK model, the coverages of large-body configurations ( $C_4$ - $C_6$ ) are low. As discussed earlier, the terminal configurations ( $C_6$  branch/ring) are part of the “coke generation” events. The  $C_6$  ring and  $C_6$  branch structures spontaneously desorb to generate coke in the system (refer to events  $R_{17}$  and  $R_{18}$ ). In Figure 25(d), the coking rates (computed by summing up the rates of events  $R_{17}$  and  $R_{18}$ ) are depicted with respect to temperature. It is evident from Figure 25(d) that the coke generation rate is very low at temperatures 923–1073 K. We observe a substantial increase in the coking rates at higher temperatures (1123–1223 K). It is well known that Ni is susceptible to coking under extreme operating conditions. Furthermore, we compared the MK predicted coking rates with experimental data (refer to Figure A28 of Appendix 1V for more details).

We performed a detailed flux analysis to identify the favourable C-C coupling pathway on the Ni(111) surface. The Methane cracking/C-C coupling reaction network and the formulation of flux analysis are presented in section A 4.1 of Appendix 1V. We found the ring formation pathway (involving events  $R_{11}$ ,  $R_{13}$  and  $R_{15}$ ) to be dominant at MSR conditions, having an average contribution of around 99.99% to the net coking rate. This indicates that the carbon has a preference to nucleate in the form of rings than branched-type structures at MSR conditions. There are also other types of nucleation events that are plausible, such as the formation of long chains, higher body rings/branches, miscellaneous structures (that are a combination of chains/branches/rings). A thorough investigation of such complicated pathways is a subject of future research studies.

We also performed the Campbell's DORC analysis (also called as the “sensitivity analysis”) to identify the rate-limiting/inhibiting steps of the coking process (refer to Table 10). It can be inferred from Table 10 that the  $C_6$  ring formation step (event  $R_{15}$ ) is strongly rate-limiting at low temperatures (923 K and 973 K). Moreover, at temperatures 1023–1223 K, the DORC value of event  $R_{15}$  lies in the range of 0.42–0.48. This implies that event  $R_{15}$  has a substantial impact on the coking rates at MSR conditions. On the other hand, the  $CH_4$  activation step (event  $R_1$ ) has little to no influence on the coking rates at low temperatures; yet, at temperatures 1023 – 1223 K, the coking rates are moderately sensitive to this event ( $R_1$ ). In the context of reducing/inhibiting coke formation, it might be critical to control the kinetics of events  $R_1$  and  $R_{15}$ .

Interestingly, we find the  $C_2$  formation step (event  $R_9$ ) to be slightly rate-inhibiting at temperatures 1123–1223 K (DORC values lie between -0.1 and -0.14). This result could be attributed to the fact that the reaction between  $C_2$  and H to form  $C_2H$  (event  $R_8$ ) is kinetically more favourable than the coupling of  $C_2$  and C to  $C_3$  (event  $R_{10}$ ) (as shown in Table 9). Thus, excess presence of  $C_2$  species could be promoting methanation. Nevertheless, in the current

MK model, we have not investigated several other coupling steps of  $C_2$  species. For instance, the  $C_2$  dimer could also undergo reactions with other carbon-based dimers/trimers to form large-body rings/branches/chains. Overall, these preliminary kinetic investigations provide important insights into the favourable pathways and rate-limiting/inhibiting steps of the coking process.

#### 6.4 Conclusions

It is imperative to gain a thorough understanding of the whisker carbon growth process to develop next-generation Ni-based catalysts that would be highly resistant to coking. The carbon whisker growth primarily involves several steps: 1) adsorption of carbon atom on the step edge of the Ni catalyst, 2) diffusion of the carbon atom from step edge to support/terrace, 3) coupling of carbon clusters on Ni(111) which leads to coke/graphene formation. Despite several theoretical/experimental studies, the coking kinetics on the Ni(111) facet is not well understood. In this chapter, we developed a first-principles-based MK model of methane cracking and C-C coupling reactions to elucidate the growth of carbon clusters on Ni(111).

The coking process on Ni(111) includes formation of large-body carbon-based clusters that exist in the form of rings, chains and branches. At first, we carried out DFT calculations to estimate the activation barriers of various coupling events on the Ni(111) facet. We found the  $C_2H_2$  formation step (event  $R_6$ ) to be exothermic. On the other hand, the dissociation steps of  $C_2H_2$  to  $C_2$  (events  $R_7$  and  $R_8$ ) are endothermic. The coupling of two carbon atoms that leads to  $C_2$  species on Ni(111) (event  $R_9$ ) is kinetically favourable at MSR conditions. Moreover, the  $C_2$  intermediate has higher thermodynamic stability than carbon. The forward activation energy and reaction energy of  $C_3$  formation step (event  $R_{10}$ ) are 1.16 eV and -0.29 eV, respectively. The event  $R_{10}$  is also favourable at high operating conditions of MSR. The  $C_3$  species can react with other carbon-based clusters to form higher body rings, branches and chains on Ni(111). In this study, we have mainly focussed on branch/ring-based configurations. We found the  $C_4$  ring formation step (event  $R_{11}$ ) to be kinetically favourable than  $C_4$  branch formation step (event  $R_{12}$ ). Both of these events ( $R_{11}$  and  $R_{12}$ ) are endothermic. The  $C_5$  branch formation step (event  $R_{14}$ ) is an exothermic reaction, whereas the  $C_5$  ring formation step (event  $R_{13}$ ) is endothermic. The forward activation barriers of events  $R_{13}$  and  $R_{14}$  are similar. We observe that the coupling of  $C_5$  ring with carbon to form  $C_6$  ring (event  $R_{15}$ ) is kinetically favourable compared to other events. The reaction energy value of event  $R_{15}$  is -0.24 eV (it is an exothermic reaction). On the other hand, the  $C_6$  branch formation step (event  $R_{16}$ ) has a substantially high forward activation barrier (1.51 eV). Thus, at extreme operating conditions of MSR, the  $C_6$  ring species could be a stable intermediate.

In this study, we developed a MK model for the methane cracking and C-C coupling reactions. We have reported the coverage profiles of important coke precursors with respect to temperature. At low temperatures, we found the  $C_2H_2$  species to have high stability on the Ni(111) surface. The coverage profile of  $C_2H_2$  species has a decreasing trend with respect to temperature. On the other hand, the coverage of  $C_2H$  species increases up to 1073 K, and then, begins to dip. We find the coverage of  $C_3$  species (an important precursor to coke formation) increases sharply with respect to temperature. In the MK model, the large-body configurations have low coverages as the terminal  $C_6$  rings/branches spontaneously desorb to generate coke in the system. It is important to note that we do not capture the complete dynamics of coking in our system. Using this simplified model, we performed flux analysis and identified that the ring formation pathway (that includes events  $R_{11}$ ,  $R_{13}$  and  $R_{15}$ ) is dominant at MSR conditions. Furthermore, the DORC results indicate that the events  $R_1$  and  $R_{15}$  substantially influence the coking rates at MSR conditions. As part of future research efforts, a vast set of DFT calculations can be performed to compute the activation barriers of C-C coupling events that involve larger body rings/branches/chains (such  $C_{10}$ ,  $C_{13}$ ,  $C_{16}$  and  $C_{30}$  species). The CE framework of KMC can be employed to account for the adsorbate-adsorbate interactions between the carbon-based species. A detailed kinetic study of the C-C coupling events can provide important clues about the coking mechanism at MSR conditions. These computations can potentially aid experimentalists in designing Ni-based catalysts that are highly resistant to coking.

# Chapter 7



## 7. Concluding remarks and future work

The idea of using of hydrogen as a clean energy source has gained immense popularity among the scientific community in the past few decades. The MSR reaction on Ni-based catalysts is an important contributor to the production of hydrogen at the industrial scale. However, the formation of coke (in the form of carbon whiskers) on the Ni catalyst surface severely hampers the productivity of MSR. The whisker carbon growth process mainly involves accumulation of carbonaceous species in the form of graphitic layers on the Ni terrace sites. Although numerous theoretical/experimental studies have been carried out, there is a lack of comprehensive understanding on the coking process at steam reforming conditions. It is of paramount importance to address the coking problem of Ni to meet the global energy demands of the 21<sup>st</sup> century. In this regard, the thesis has provided critical insights on the fundamental aspects of the coking issue in the MSR reaction.

### 7.1 Contributions of this Thesis

Developing a robust first-principles-based coking model for the MSR reaction necessitates an accurate choice of the DFT functional. In Chapter 2, the thesis explored the suitability of GGA and dispersion-inclusive functionals (such as DFT-D and vdW-DF) for the MSR graphene system. We systematically benchmarked DFT predictions with experimental data (obtained from literature) – these include binding/reaction energies of important MSR species/events and graphene (model for coke at the molecular scale). The DFT benchmark studies provide us with some important results. The GGA functionals fail to capture the van der Waals interactions between graphene and Ni(111). Moreover, the RPBE (widely employed for the MSR system) and revPBE functionals were found to have poor accuracy in predicting the binding/reaction energies of most MSR species/events. In the case of vdW-DF, the graphene binding energy prediction of optB88-vdW functional is in excellent agreement with the RPA result. The optB86b-vdW functional slightly overestimates the graphene binding energy with respect to the RPA value. The BEEF-vdW functional predicts a weak repulsive interaction between graphene and Ni(111). The vdW-DF exhibit large deviations in estimating the binding/reaction energies of important MSR species/events. The optB86b-vdW and BEEF-vdW functionals have poor predictive accuracies with respect to the experimental MSR dataset. Furthermore, the optB88-vdW functional significantly overestimates the binding energies of CO and O on Ni(111). In comparison to other vdW-DF, the optPBE-vdW functional has a low RMSD value (root-mean-square deviation – this is a quantitative measure of the overall performance of DFT functionals). The graphene binding energy prediction of optPBE-vdW functional is in reasonable agreement with RPA. Thus, the optPBE-vdW functional can be considered as an appropriate choice for studying the MSR-graphene system. Among the DFT-D functionals, the PBE-D3 and PBE-dDsC functionals provide a good estimate of the

graphene binding energy. On the other hand, we found the RPBE-D3 and revPBE-D3 functionals have a qualitative disagreement with respect to the experimental result of graphene-Ni(111). The PBE-TS functional substantially overpredicts the binding energy of graphene. We have found the RMSD value of DFT-D functionals to be significantly lower than most vdW-DF. This indicates that DFT-D functionals exhibit better overall performance in predicting the binding/reaction energies of key MSR species/events. The RPBE-D3 and revPBE-D3 functionals have lower RMSD scores (with respect to the experimental MSR dataset) compared to other DFT-D functionals. Nonetheless, these functionals do not capture the graphene-Ni(111) interaction adequately (as stated earlier). The PBE-TS functional exhibits poor accuracy in predicting the experimental binding/reaction energies data of MSR. The PBE-D3 and PBE-DdSc predictions are in reasonable agreement with the experimental MSR dataset. As stated previously, these functionals also account for the van der Waals interactions between graphene and Ni(111) with appreciable accuracy. Therefore, the PBE-D3 and PBE-DdSC functionals are suitable candidates for developing a DFT-based design of coking model for the MSR reaction. Overall, the performance of the DFT functionals is not satisfactory. The RMSD scores lie between 0.2-0.5 eV, which indicates that there is a significant scope for improvement in DFT functional accuracy. Based on the outcomes of the DFT benchmark study, we chose the PBE-D3 functional (as it is computationally cheaper than PBE-dDsC and optPBE-vdW) for our kinetic studies.

Subsequently, we developed a first-principles-based KMC model for the methane cracking reaction to understand the coking thermodynamics on Ni(111). A large dataset of DFT configurations was generated on Ni(111) – these included large-body C-C, CH-CH and C-C structures that exist in the forms of rings, branches and chains. In the KMC model, the kinetics of C-H activation steps was captured in detail, whereas the coke (which is composed of carbon-based ring/branch/chains) formation was treated at the level of thermodynamics. The CE methodology was employed to capture the short/long-range interactions and adlayer energetics of large-body carbon-based structures. We trained the CE parameters (using linear regression) to capture the energetics of the DFT dataset with high accuracy. Several KMC models were developed where the adlayer energetics were captured in an incremental fashion – KMC-without-interaction, KMC-1NN, KMC-1NN-2NN, KMC-1NN-2NN-3NN and KMC-long-range. These KMC models were systematically compared to mean-field MK models. The MK models fail to adequately capture the attractive C-C, CH-C and CH-CH correlations at steam reforming conditions. We illustrate that the coke morphology and CH/C coverages change significantly based on the level of interactions included in the KMC simulation. For instance, in the KMC-1NN model, we observe no visible ordering but there is formation of small clusters of carbon surrounded by three CH species. On the other hand, the KMC-1NN-2NN and KMC-

1NN-2NN-3NN models depict that the CH/C species align in the form of straight chains (chain-based ordering). The adlayer of KMC-long-range (which includes 1NN, 2NN, 3NN and CE fit parameters as well) is completely different from the rest of the KMC models. The KMC-long-range model predicts that coke encapsulates the Ni(111) surface in the form of C-CH ring-based structures at steam reforming conditions. At lower temperatures (such as 800 K), these C-CH rings occupy specific regions of the lattice and remain disconnected from other ring-based structures. On the other hand, at high temperatures (1100–1200 K), we find that there is complete agglomeration of C-CH rings on the Ni(111) surface. This indicates that Ni is more susceptible to coking at high temperatures, which is in excellent agreement with industrial observations.<sup>25</sup> The results of these KMC simulations can also be validated (to a certain extent) by comparisons with spectroscopic studies. Overall, the CE-based KMC simulations can potentially inspire future simulations that can help us identify next-generation Ni-based catalysts that are more resistant to coking.

Upon completion of the aforementioned study, we shifted our focus to understand the role of potassium (alkali-based promoter) in the MSR reaction. We developed KMC models of MSR on the Ni(111) and K-Ni(111) systems. The KMC simulations were performed for different loadings of potassium - K-Ni(111)-0.7%, K-Ni(111)-1.4%, K-Ni(111)-2.1% and K-Ni(111)-2.8%. At high temperatures, the net MSR turnover rate was found to be substantially higher in the K-Ni(111) systems. For instance, the MSR turnover rate of K-Ni(111)-2.8% is around 3 to 4 times higher than Ni(111) at temperatures 1173–1273 K. At low temperatures (973–1073 K), the oxygen uptake on the potassium-modified Ni(111) system is greater than Ni(111). Moreover, in the presence of potassium, the CH coverage (an important coke precursor) is reduced to a certain extent at low temperatures. These results illustrate the promotional effects of potassium at steam reforming conditions. In an attempt to rationalise the aforementioned findings, we examined the process statistics of important MSR events thoroughly. The event occurrence rate was compared systematically on the following systems: 1) Pure Ni(111) surface, 2) Ni sites of K-Ni(111)-2.8% and 3) K sites of K-Ni(111)-2.8%. At 1273 K, we observe that the CO formation step (event  $R_{16}$ ) occurrence rate was around 637 times faster on potassium sites of K-Ni(111)-2.8% compared to Ni(111). Similarly, the occurrence rates of COH formation step (event  $R_{13}$ ) and CHOH formation step (event  $R_9$ ) were found to be 45 times and 28 times faster, respectively. In comparison to the Ni(111) system, we found the CHO formation step (event  $R_{12}$ ) was about 3 times faster on K sites than Ni(111). On the other hand, the reaction occurrence rate of CH<sub>4</sub> dissociation event was substantially lower on potassium sites. The process statistics analysis unequivocally demonstrates that the key events of MSR (mainly CH/C oxidation steps) have much higher occurrence rates on potassium sites of the K-Ni(111)-2.8% system. We identified the dominant reforming pathways of MSR on Ni(111)

and K-Ni(111)-2.8% by performing a detailed flux analysis. The CHO pathway was found to be dominant on the Ni(111) surface at steam reforming conditions. This is in excellent agreement with the predictions of several MSR MK studies. On the K-Ni(111)-2.8% system, the pathway contributions (%) vary based on the operating conditions. For example, at 973 K, the CHO-Ni-pathway contributed largely to the net MSR turnover rate (around 93%). Whereas at 1273 K, the contributions of MSR pathways on the potassium sites were found to be substantial. The contributions (%) of major pathways to the net MSR turnover rate at 1273 K are as follows: 1) CHO-Ni-pathway – 60%, 2) CO-K-pathway – 17%, 3) CHO-K-pathway – 16%, and 4) COH-K-pathway – 4%. The flux analysis provides conclusive evidence that the presence of potassium has a significant impact on pathway favourability at high temperatures.

Finally, we developed a first-principles-based MK model for the methane cracking and C-C coupling reactions on Ni(111). The DFT calculations were performed to identify the transition states of carbon coupling events. We primarily focussed on the nucleation events involving branched/ring type structures as these are important precursors to graphene/coke formation. In the MK model, we included a pseudo desorption event to generate “coke” in the system. The coverage profiles of dominant species (with respect to temperature) were examined. Based on the flux analysis, we have identified the ring formation pathway to be favourable at MSR conditions. Furthermore, the sensitivity analysis reveals that the  $\text{CH}_4(\text{g})$  dissociation step (event  $\text{R}_1$ ) and  $\text{C}_6$  ring formation step (event  $\text{R}_{15}$ ) could be rate-limiting at high temperatures.

## 7.2 Opportunities for future research

As discussed previously, the thesis has examined several fundamental aspects of the coking problem in MSR. The DFT functional screening (chapter 3) reveals that the overall accuracy of GGA, DFT-D3 functionals and vdW-DF is not satisfactory. The outcomes of chapter 3 certainly motivate further research into testing other existing functionals and DFT method development. It is critical to improve the accuracy of DFT predictions to reduce the computational error in the first-principles-based design of poison resistant Ni catalysts.

The CE-based KMC model of methane cracking provides interesting insights into the coke morphology and the susceptibility of Ni to coking (refer to Chapter 5). The CE model can be further trained on larger-body configurations occupying top sites, as the top-fcc configuration is the most stable geometry of graphene on Ni(111). In the KMC simulation, the chemistry of C-C coupling events can be captured explicitly to delineate the coking mechanism. Moreover, a multifaceted KMC model can also be developed, which includes the step sites, to gain a thorough understanding of the whisker carbon growth.

In chapter 6, we performed KMC simulations to thoroughly understand the effect of the potassium (alkali-based promoter) on the MSR kinetics. The coke formation/destruction

events can also be potentially included in the MSR system. This will allow us to understand the promotional effects of potassium on the coking kinetics. Furthermore, the CE-based KMC model can be employed to thoroughly investigate the role of Ni-based bimetallic alloys (such as Ni-Au, Ni-Ag) and other promising promoters (these include Mo and Mn) in inhibiting coke formation at MSR conditions.

We developed a preliminary MK model to elucidate the coking kinetics on Ni(111) (refer to Chapter 7). Further investigations are needed to gain deeper insights into the whisker carbon growth mechanism. To this end, an extensive set of DFT calculations needs to be performed to identify the transition states of coupling events involving higher body carbon-based configurations (such as C<sub>8</sub>, C<sub>10</sub>, C<sub>13</sub> rings/branches/chains). Moreover, the lateral interactions of these carbon-based species also need to be computed using DFT. Upon generating the DFT dataset, a kinetic model can be formulated to gain a detailed understanding of the growth mechanism of carbon whiskers at steam reforming conditions.

Finally, investigations into transition metal oxide (TMO) supported/alloyed Ni catalysts are gaining prominence in the scientific community as these materials can be suitable alternative catalysts for methane reforming reactions. For instance, Ni-FeO and Ni-La<sub>2</sub>O<sub>3</sub> were found to substantially reduce the activation barrier of CH hydrogenation and carbon oxidation reactions (these are critical steps to reduce coke formation in MSR).<sup>54</sup> It is imperative to gain a detailed understanding of such strong metal-support interactions (SMSI) using DFT. A detailed DFT screening study can be performed for different material combinations to identify the suitable Ni-TMO systems for MSR. Furthermore, in a recent study, Prats and Stamatakis<sup>185</sup> report that metal nanoclusters supported on transition metal carbides (TMCs) show promising activity/stability for reforming reactions. Detailed KMC studies of the MSR reaction on different types of Ni-supported TMCs could be the next step in the discovery of novel catalysts that are resistant to coking.

## Appendix I

**Table A1. The lattice constant predictions of DFT functionals**

Functional	Ni Lattice constant prediction (Å)	Graphene Lattice constant prediction (Å)
PBE	3.522	-
RPBE	3.557	-
revPBE	3.547	-
PBE-D3	3.481	2.467
RPBE-D3	3.487	2.479
revPBE-D3	3.467	2.476
PBE-dDsC	3.502	2.467
PBE-TS	3.419	2.465
optB86b-vdW	3.493	2.466
optB88-vdW	3.514	2.465
optPBE-vdW	3.533	2.471
BEEF-vdW	3.540	2.466

Note: The experimental lattice constant value of Ni is 3.524 Å.<sup>127</sup> The experimental graphene-Ni lattice constant value is 2.464 Å.<sup>124</sup> The pure graphene DFT calculations have been carried out using a 5×5×1 k-point grid. For the PBE, RPBE and revPBE functionals, we did not calculate the pure graphene configurations, since graphene does not bind on Ni using these functionals.

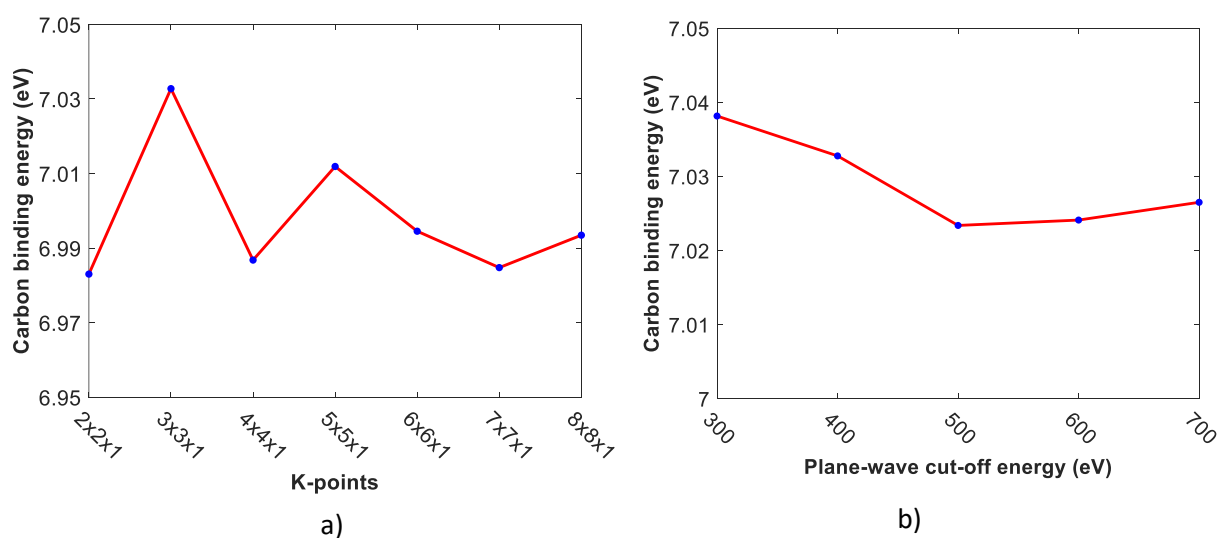
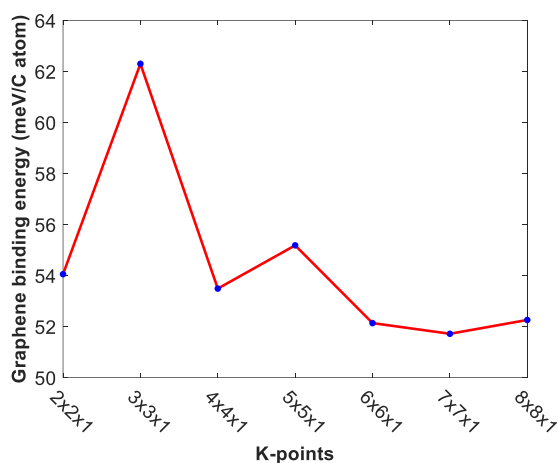
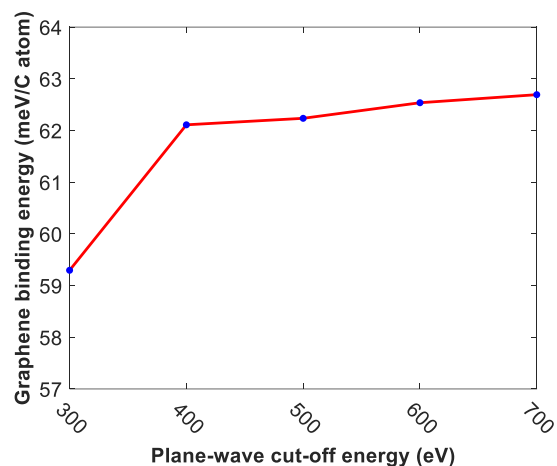


Figure A1: The convergence plots of carbon binding energy on Ni(111) using the PBE-D3 functional: (a) K-points convergence test and (b) Plane-wave cut-off energy convergence study.

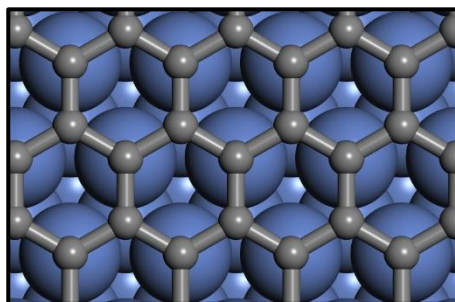


a)

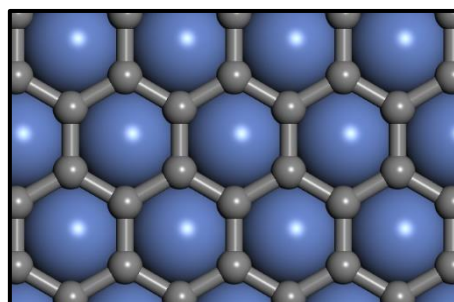


b)

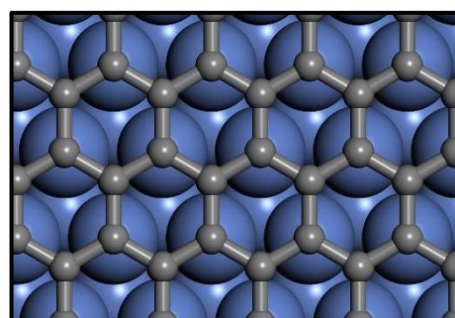
Figure A2: The convergence plots of graphene binding energy on Ni(111) using the PBE-D3 functional: (a) K-points convergence test and (b) Plane-wave cut-off energy convergence study.



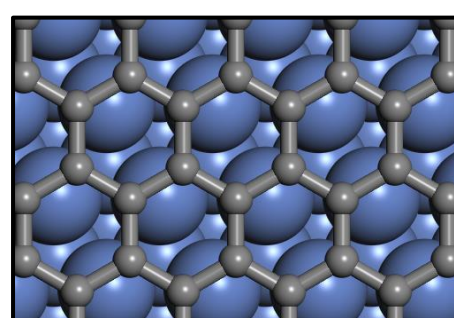
a)



b)



c)



d)

Figure A3: Graphene configurations include a) top-hcp configuration, b) fcc-hcp configuration, c) top-fcc configuration and d) bridge-top configuration.<sup>144</sup> The schematics have the following convention: The atoms in blue represent Ni and the atoms in grey are carbon.

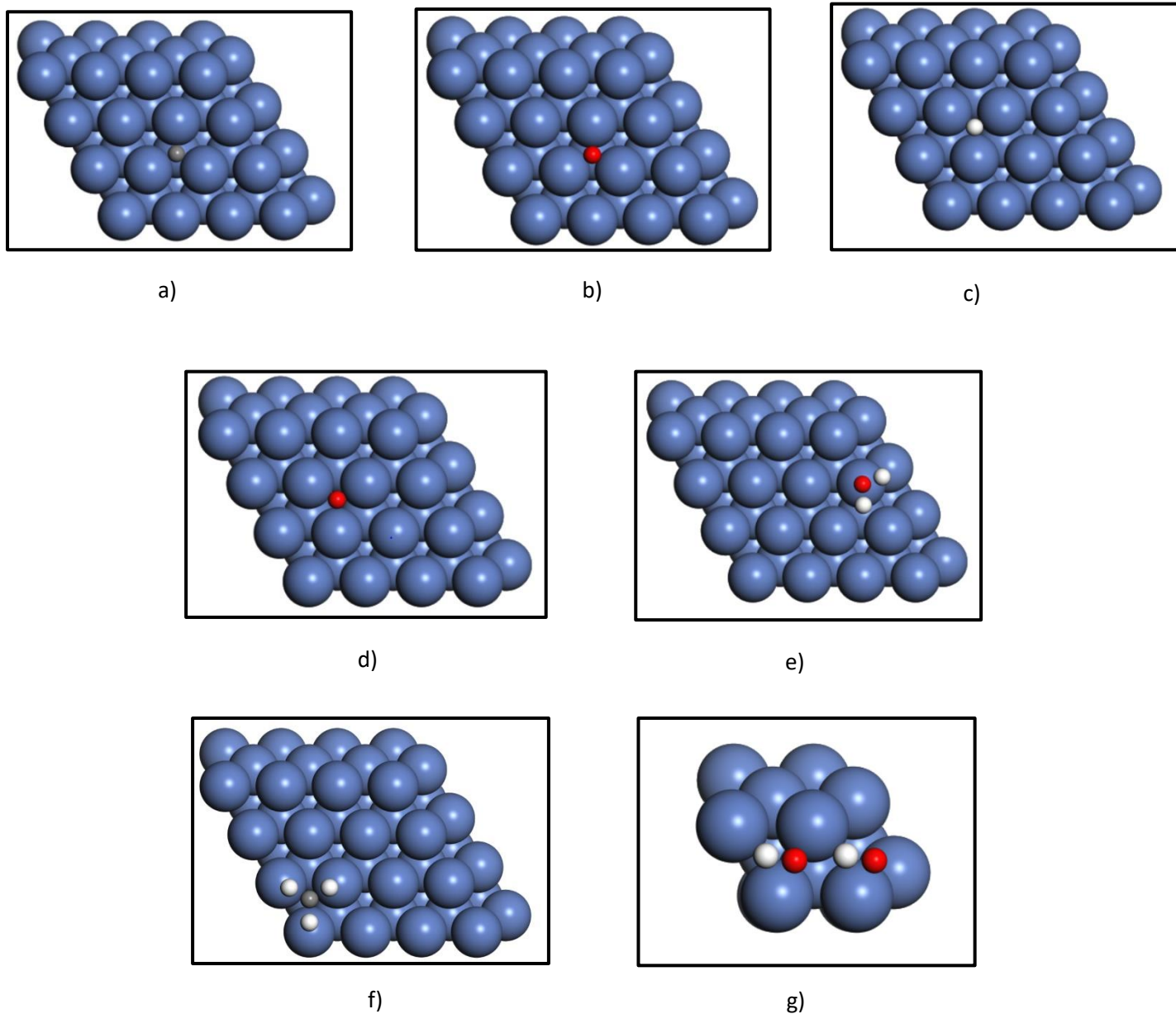


Figure A4: The preferred binding sites of MSR intermediates: a) The carbon atom occupies the hcp site. b) The CO molecule binds on the hcp site. c) The hydrogen atom is stable on the fcc site. d) The oxygen atom occupies the fcc site. e) The H<sub>2</sub>O molecule physisorbs on the top site. f) The CH<sub>3</sub> molecule binds on the fcc site. g) The two OH atoms are stable on the three-fold hollow sites. The schematics have the following convention: The atoms in blue represent Ni, the atoms in grey are carbon, the atoms in red indicate oxygen and the atoms in white are hydrogen.



**Table A2. Evaluating the performance of DFT functionals in predicting the energies of gas-phase reactions relevant to MSR, as well as graphite formation**

Method/Functional	$E_{rxn-gasph}^{MSR}$ (eV)	$E_{rxn-gasph}^{H_2O\ diss}$ (eV)	$E_{coh}^{graphite}$ (eV)	$E_{bind}^{graphite}$ (meV/C)
CCSD(T) or experiment	2.82 <sup>128,152</sup>	5.48 <sup>128,152</sup>	7.37 <sup>186</sup>	48 <sup>186</sup>
PBE	3.18	5.07	7.97	-14.04
RPBE	2.80	4.78	7.53	-36.68
revPBE	2.83	4.81	7.58	-35.75
PBE-D3	3.18	5.07	8.07	46.69
RPBE-D3	2.83	4.78	7.69	48.43
revPBE-D3	2.85	4.81	7.75	62.09
PBE-dDsC	3.18	5.07	8.22	63.03
PBE-TS	3.18	5.07	8.11	82.34
optB86b-vdW	2.81	4.92	8.07	69.91
optB88-vdW	2.68	4.89	7.98	69.56
optPBE-vdW	2.59	4.79	7.84	63.21
BEEF-vdW	2.51 ( $\pm 0.26$ )	4.70 ( $\pm 0.17$ )	7.64 ( $\pm 0.23$ )	36.68 ( $\pm 19.24$ )

Notes:  $E_{rxn-gasph}^{MSR}$  indicates the MSR reaction energy –  $CH_4(g) + H_2O(g) \rightleftharpoons CO(g) + 3H_2(g)$ ,  $E_{rxn-gasph}^{H_2O\ diss}$  represents the reaction energy of  $H_2O$  dissociation –  $2H_2O(g) \rightleftharpoons 2H_2(g) + O_2(g)$ ,  $E_{coh}^{graphite}$  and  $E_{bind}^{graphite}$  are the graphite cohesive energy and graphite interlayer binding energy, respectively.  $E_{rxn-gasph}^{MSR}$  and  $E_{rxn-gasph}^{H_2O\ diss}$  are derived from a CCSD(T) atomisation energies dataset which does not include ZPE/thermal corrections.  $E_{coh}^{graphite}$  and  $E_{bind}^{graphite}$  are obtained from experimental works reported in the literature. The graphite bulk calculations (with a supercell that contains four carbon atoms) have been performed using a k-point mesh of size  $21 \times 21 \times 7$  and a plane-wave cut-off energy value of 400 eV (refer to Figure A5(a) and Figure A5(b) for convergence plots). The lattice vectors of graphite bulk are obtained from experimental data available in the literature.<sup>186</sup>

Interestingly, all the DFT functionals have varying performance for each of the gas-phase systems. According to Table A2, the RPBE, revPBE, RPBE-D3, revPBE-D3 and optB86b-vdW functionals predict the MSR reaction energy with high accuracy. The PBE functional and its corresponding dispersion-corrected flavours (PBE-D3, PBE-dDsC and PBE-TS) overestimate

the MSR reaction energy by 0.36 eV. Whereas the vdW-DF such as optB88-vdW, optPBE-vdW and BEEF-vdW substantially underpredict the MSR reaction energy (refer to Table A2).

Most of the DFT functionals exhibit large deviations in predicting the reaction energy of H<sub>2</sub>O dissociation (as shown in Table A2). Wellendorff et al.<sup>128</sup> have also reported that the DFT functionals do not give a good description of H<sub>2</sub>O dissociation in the gas phase. The inability of DFT functionals to provide an accurate estimate of the triplet O<sub>2</sub>(g) energy is considered to be the primary reason for such a poor performance.<sup>128</sup> The RPBE and revPBE functionals predict the graphite cohesive energy with reasonable accuracy. Other DFT functionals tend to significantly overpredict the cohesive energy of graphite (refer to Table A2). The benchmark study conducted by Rêgo et al.<sup>186</sup> also concludes that the dispersion-inclusive DFT functionals overestimate graphite cohesive energy. The GGA functionals fail to capture the van der Waals interactions between consecutive layers of graphite. As shown in Table A2, these functionals predict a negative value (repulsive interaction) for the interlayer binding energy of graphite. Among the DFT-D functionals, the PBE-D3 and RPBE-D3 functionals accurately reproduce the graphite interlayer interactions. The predictions of PBE-dDsC and revPBE-D3 functionals are also in reasonable agreement with the experimental result. In contrast, the PBE-TS functional substantially overpredicts the interlayer binding energy of graphite. The vdW-DF predict the graphite interlayer interactions with acceptable accuracy (refer to Table A2).

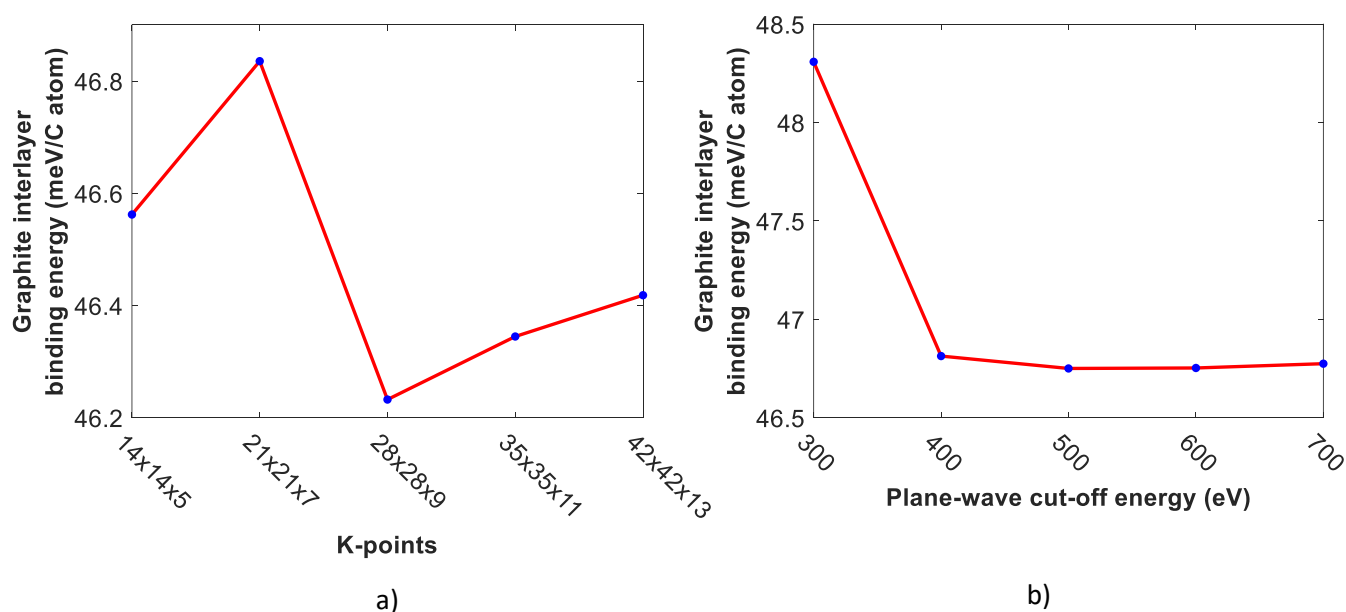


Figure A5: The convergence plots of graphite bulk system using the PBE-D3 functional: (a) K-points convergence test and (b) Plane-wave cut-off energy convergence study.

**Table A3. Comparison of DFT predictions of oxygen binding energy predictions obtained using two different approaches**

Functional	$E_{O\text{ bind}}^{method1}$ (eV)	$E_{O\text{ bind}}^{method2}$ (eV)	Deviation of $E_{method1}^{O\text{ bind}}$ from the experimental value (eV)	Deviation of $E_{method2}^{O\text{ bind}}$ from the experimental value (eV)
PBE	5.09	4.68	0.56	0.14
RPBE	4.84	4.13	0.30	-0.41
revPBE	4.87	4.20	0.34	-0.34
PBE-D3	5.17	4.75	0.63	0.22
RPBE-D3	4.97	4.27	0.44	-0.27
revPBE-D3	5.02	4.34	0.48	-0.19
PBE-dDsC	5.20	4.79	0.67	0.25
PBE-TS	5.04	4.63	0.51	0.09
optB86b-vdW	5.81	5.25	1.28	0.71
optB88-vdW	5.88	5.28	1.34	0.75
optPBE-vdW	5.76	5.06	1.23	0.53
BEEF-vdW	5.23	4.44	0.69	-0.09
Experimental value	4.53 ( $\pm 0.2$ )		-	

Note: Two methods are used to determine the  $O_2(g)$  energy: 1) The  $O_2(g)$  energy is estimated by using the following equation:  $E_{O_2\text{ gasph}}^{method1} = E_{rxn-gasph}^{H_2O\text{ diss}} + 2E_{gasph}^{H_2O} - 2E_{gasph}^{H_2}$ . The terms  $E_{rxn-gasph}^{H_2O\text{ diss}}$ ,  $E_{gasph}^{H_2O}$  and  $E_{gasph}^{H_2}$  refer to the gas-phase reaction energy of  $H_2O$  dissociation (the value is 5.48 eV; it is derived from a CCSD(T) atomisation energies dataset<sup>152</sup>),  $H_2O$  gas-phase energy and  $H_2$  gas-phase energy (both these energies are computed using DFT), respectively. The  $O_2(g)$  energy obtained from method 1 ( $E_{O_2\text{ gasph}}^{method1}$ ) is used to estimate the term  $E_{O\text{ bind}}^{method1}$  2) The  $O_2$  gas-phase energy is computed by performing a DFT calculation (the corresponding oxygen binding energy obtained under this approach is labelled as  $E_{O\text{ bind}}^{method2}$ )

As discussed previously, the DFT functionals give an inaccurate value of the energy of  $O_2$  gas-phase triplet state. In an effort to correct this error, we estimated the  $O_2$  gas-phase energy from the reaction energy of  $H_2O$  dissociation (please refer to the “Note” given below Table A3 for more details). As shown in Table A3, the oxygen binding energies ( $E_{O\text{ bind}}^{method1}$ ) obtained using this approach deviate significantly from the experimental data (refer to the third column of Table A3). In a recent study, Wellendorff et al.<sup>128</sup> have made similar observations for a few systems. A plausible explanation for this behaviour could be that the total energy of the bound state -  $O/Ni(111)$  - is also estimated poorly by the DFT functionals, and thus, the binding energy predictions of oxygen obtained using an accurate  $O_2$  gas-phase energy exhibit large deviations. On the other hand, the oxygen binding energies estimated by using the DFT

predicted  $O_2(g)$  energy ( $E_{O\text{ bind}}^{method2}$ ) have a better agreement with the experimental value (refer to the last column of Table A3). In this case, it is possible that there is a cancellation of error between the DFT energies of the bound state and the gas-phase. Hence, the DFT results of the second approach ( $E_{O\text{ bind}}^{method2}$ ) are presented in Table 3 of section 3.3.

**Table A4. The predictions of DFT functionals for MSR species (without ZPE and thermal corrections)**

DFT predictions without ZPE and thermal corrections (eV)									
Functional	CO	H <sub>2</sub> O	2×H	2×O	OH	C	CH <sub>3</sub>	CH <sub>4</sub> -diss	C-oxid
PBE	1.93	0.30	1.12	4.72	3.27	6.93	1.95	0.05	1.69
RPBE	1.54	0.10	0.79	4.17	2.90	6.46	1.51	-0.43	1.94
revPBE	1.60	0.10	0.83	4.24	2.94	6.53	1.56	-0.37	1.90
PBE-D3	2.12	0.53	1.33	4.80	3.41	7.01	2.32	0.53	1.61
RPBE-D3	1.84	0.46	1.07	4.31	3.14	6.62	2.06	0.25	1.78
revPBE-D3	1.92	0.52	1.17	4.39	3.18	6.69	2.22	0.45	1.73
PBE-dDsC	2.09	0.46	1.22	4.83	3.64	7.05	2.19	0.34	1.58
PBE-TS	2.26	0.64	1.30	4.67	3.57	7.03	2.45	0.64	1.59
optB86b-vdW	2.17	0.53	1.15	5.29	3.53	7.08	2.37	0.45	1.57
optB88-vdW	2.01	0.50	1.02	5.33	3.49	6.94	2.18	0.23	1.74
optPBE-vdW	1.88	0.45	0.92	5.11	3.37	6.79	2.05	0.08	1.82
BEEF-vdW	1.61	0.28	0.68	4.48	3.10	6.44	1.70	-0.28	2.05

Note: The computational errors of BEEF-vdW functional are not reported in Table A4

**Table A5. The ZPE corrections recorded for each of the DFT functionals**

ZPE corrections (eV)								
Functional	CO	H <sub>2</sub> O	2×H	2×O	OH	C	CH <sub>3</sub>	CH <sub>4</sub> -diss
PBE	-0.05	-0.06	-0.09	-0.06	-0.15	-0.10	-0.10	0.12
RPBE	-0.05	-0.06	-0.07	-0.06	-0.15	-0.10	-0.10	0.12
revPBE	-0.05	-0.06	-0.08	-0.06	-0.15	-0.10	-0.10	0.12
PBE-D3	-0.05	-0.06	-0.09	-0.06	-0.14	-0.10	-0.10	0.12
RPBE-D3	-0.05	-0.07	-0.07	-0.06	-0.15	-0.10	-0.09	0.13
revPBE-D3	-0.05	-0.07	-0.08	-0.06	-0.14	-0.10	-0.10	0.12
PBE-dDsC	-0.05	-0.06	-0.09	-0.06	-0.15	-0.10	-0.10	0.12
PBE-TS	-0.05	-0.06	-0.09	-0.06	-0.14	-0.10	-0.10	0.11
optB86b-vdW	-0.05	-0.07	-0.08	-0.07	-0.15	-0.10	-0.09	0.13
optB88-vdW	-0.05	-0.07	-0.08	-0.07	-0.15	-0.10	-0.09	0.13
optPBE-vdW	-0.05	-0.07	-0.07	-0.06	-0.15	-0.10	-0.10	0.13
BEEF-vdW	-0.05	-0.06	-0.07	-0.06	-0.15	-0.10	-0.10	0.12

Note: The ZPE corrections are not included for the carbon dissociation reaction (refer to Table 2 under the subsection 3.3.2 for more details).

**Table A6. The thermal corrections recorded for each of the DFT functionals**

Thermal corrections (eV)							
Functional	CO	H <sub>2</sub> O	2×O	OH	C	CH <sub>3</sub>	CH <sub>4</sub> -diss
PBE	-0.006	0.010	0.017	0.026	0.003	0.028	0.027
RPBE	-0.007	0.009	0.014	0.025	0.001	0.026	0.026
revPBE	-0.007	0.008	0.015	0.025	0.002	0.027	0.026
PBE-D3	-0.006	0.010	0.017	0.025	0.003	0.029	0.028
RPBE-D3	-0.007	0.009	0.014	0.025	0.002	0.025	0.025
revPBE-D3	-0.007	0.010	0.015	0.025	0.002	0.027	0.026
PBE-dDsC	-0.005	0.009	0.017	0.026	0.003	0.029	0.028
PBE-TS	-0.005	0.007	0.017	0.025	0.004	0.029	0.028
optB86b-vdW	-0.006	0.011	0.019	0.026	0.003	0.028	0.028
optB88-vdW	-0.006	0.011	0.019	0.026	0.003	0.027	0.027
optPBE-vdW	-0.007	0.010	0.017	0.025	0.002	0.026	0.026
BEEF-vdW	-0.008	0.009	0.015	0.025	0.001	0.026	0.025

Note: The thermal corrections are not included for the hydrogen adsorption and carbon oxidation reactions (refer to Table 2 under the subsection 3.3.2 for more details).

**Table A7. The estimated vibrational wavenumbers of hydroxyl**

Functional	Bound state wave numbers (cm <sup>-1</sup> )												Gas-phase wave numbers (cm <sup>-1</sup> )
	3247	3171	1056	940	792	776	538	428	340	254	220	136	
PBE	3247	3171	1056	940	792	776	538	428	340	254	220	136	3603
RPBE	3325	3261	1028	913	763	756	520	413	322	241	206	135	3596
revPBE	3304	3237	1038	922	772	760	524	415	324	243	209	135	3595
PBE-D3	3197	3105	1074	958	800	776	564	429	338	249	210	135	3603
RPBE-D3	3268	3185	1088	973	792	764	563	421	324	237	190	138	3595
revPBE-D3	3225	3129	1078	968	791	765	576	423	323	237	188	132	3598
PBE-dDsC	3187	3075	1068	938	824	772	602	425	339	250	211	137	3532
PBE-TS	3126	3013	1104	983	814	776	606	436	337	248	199	137	3603
optB86b-vdW	3213	3133	1061	941	789	775	561	437	344	262	223	138	3579
optB88-vdW	3273	3205	1053	929	785	778	553	437	349	260	222	139	3585
optPBE-vdW	3309	3247	1033	911	767	765	542	422	334	253	214	135	3574
BEEF-vdW	3440	3390	1023	898	762	756	540	420	332	251	207	132	3643

Note: The bound state wave numbers (mentioned above) have been calculated for two OH species adsorbed on Ni(111).

**Table A8. The estimated vibrational wavenumbers of carbon monoxide**

Functional	Bound state wave numbers (cm <sup>-1</sup> )						Gas-phase wave numbers (cm <sup>-1</sup> )
PBE	1763	344	283	282	143	143	2126
RPBE	1740	332	273	273	138	137	2103
revPBE	1745	335	277	276	141	141	2108
PBE-D3	1770	350	283	283	143	143	2126
RPBE-D3	1749	342	277	277	138	137	2103
revPBE-D3	1756	344	278	278	137	137	2108
PBE-dDsC	1766	350	284	284	145	144	2126
PBE-TS	1778	359	291	291	144	144	2126
optB86b-vdW	1762	347	283	283	143	143	2125
optB88-vdW	1757	337	279	279	142	142	2131
optPBE-vdW	1744	336	272	271	138	137	2116
BEEF-vdW	1757	333	271	271	138	138	2124

**Table A9. The estimated vibrational wavenumbers of oxygen**

Functional	Bound state wave numbers (cm <sup>-1</sup> )			Gas-phase wave numbers (cm <sup>-1</sup> )
PBE	488	393	393	1566
RPBE	470	374	373	1544
revPBE	473	378	377	1549
PBE-D3	498	389	389	1566
RPBE-D3	485	372	372	1544
revPBE-D3	495	376	376	1549
PBE-dDsC	490	393	393	1566
PBE-TS	516	381	381	1566
optB86b-vdW	502	404	404	1554
optB88-vdW	498	406	406	1535
optPBE-vdW	483	394	394	1526
BEEF-vdW	472	378	378	1551

**Table A10. The estimated vibrational wavenumbers of hydrogen**

Functional	Bound state wave numbers (cm <sup>-1</sup> )			Gas-phase wave numbers (cm <sup>-1</sup> )
PBE	1133	861	860	4307
RPBE	1103	831	830	4340
revPBE	1112	838	838	4334
PBE-D3	1150	857	857	4307
RPBE-D3	1114	810	810	4340
revPBE-D3	1136	847	846	4334
PBE-dDsC	1146	864	864	4307
PBE-TS	1198	841	840	4307
optB86b-vdW	1137	849	849	4301
optB88-vdW	1112	854	853	4349
optPBE-vdW	1101	834	834	4349
BEEF-vdW	1108	836	836	4447

**Table A11. The estimated vibrational wavenumbers of carbon**

Functional	Bound state wave numbers (cm <sup>-1</sup> )		
PBE	561	549	549
RPBE	545	534	533
revPBE	549	537	537
PBE-D3	579	540	540
RPBE-D3	574	525	525
PBE-dDsC	568	549	549
PBE-TS	612	530	530
revPBE-D3	583	525	525
optB86b-vdW	572	547	547
optB88-vdW	558	548	547
optPBE-vdW	551	539	539
BEEF-vdW	545	526	526

**Table A12. The estimated vibrational wavenumbers of water**

Functional	Bound state wave numbers (cm <sup>-1</sup> )									Gas-phase wave numbers (cm <sup>-1</sup> )		
PBE	3686	3578	1543	463	449	203	94	82	49	3831	3716	1584
RPBE	3720	3610	1569	423	413	147	87	77	58	3820	3705	1596
revPBE	3719	3608	1565	429	418	150	86	80	51	3823	3708	1594
PBE-D3	3658	3552	1536	482	480	212	107	93	27	3831	3716	1584
RPBE-D3	3645	3542	1551	519	498	187	121	90	15	3820	3703	1595
revPBE-D3	3655	3549	1550	530	515	184	139	103	25	3823	3707	1593
PBE-dDsC	3673	3566	1538	471	460	215	93	84	34	3831	3716	1584
PBE-TS	3673	3565	1538	445	440	193	86	79	15	3831	3716	1584
optB86b-vdW	3639	3530	1538	495	466	229	101	87	66	3807	3692	1584
optB88-vdW	3654	3545	1550	493	461	235	94	86	57	3807	3694	1596
optPBE-vdW	3662	3553	1559	478	446	201	91	80	58	3797	3684	1597
BEEF-vdW	3772	3661	1597	452	420	156	86	78	63	3875	3761	1624

**Table A13. The estimated vibrational wavenumbers of methane**

Functional	Gas-phase wave numbers (cm <sup>-1</sup> )								
PBE	3092	3091	3091	2975	1512	1511	1286	1286	1285
RPBE	3085	3085	3083	2969	1517	1516	1294	1294	1294
revPBE	3087	3087	3085	2971	1517	1516	1293	1293	1293
PBE-D3	3092	3091	3090	2974	1511	1510	1286	1286	1285
RPBE-D3	3071	3070	3069	2951	1512	1511	1293	1293	1292
revPBE-D3	3079	3079	3077	2960	1513	1512	1292	1291	1291
PBE-dDsC	3092	3092	3091	2976	1512	1511	1287	1287	1286
PBE-TS	3092	3091	3091	2975	1511	1511	1286	1286	1285
optB86b-vdW	3067	3066	3065	2959	1516	1515	1294	1294	1293
optB88-vdW	3072	3068	3067	2971	1535	1529	1316	1313	1310
optPBE-vdW	3063	3062	3061	2965	1529	1528	1311	1310	1310
BEEF-vdW	3104	3103	3101	2999	1550	1549	1330	1330	1329

**Table A14. The estimated vibrational wavenumbers of methyl (bound state)**

Functional	Bound state wave numbers (cm <sup>-1</sup> )											
PBE	2826	2824	2764	1292	1291	1170	479	478	402	350	219	218
RPBE	2862	2861	2799	1318	1318	1170	490	488	378	323	193	191
revPBE	2856	2855	2792	1313	1313	1169	485	484	383	329	198	197
PBE-D3	2832	2831	2766	1286	1286	1166	479	479	399	360	224	224
RPBE-D3	2862	2862	2792	1299	1299	1151	456	455	342	334	190	189
revPBE-D3	2857	2857	2785	1291	1291	1149	463	463	371	354	209	209
PBE-dDsC	2824	2822	2761	1289	1288	1172	476	475	408	357	226	225
PBE-TS	2846	2845	2783	1298	1298	1174	495	494	399	362	223	222
optB86b-vdW	2778	2777	2724	1290	1290	1176	471	471	398	354	222	222
optB88-vdW	2810	2809	2760	1318	1318	1185	474	473	387	343	208	208
optPBE-vdW	2824	2823	2773	1326	1326	1182	481	481	375	328	195	194
BEEF-vdW	2895	2893	2836	1359	1359	1195	502	501	369	327	189	187

**Table A15. The estimated vibrational wavenumbers of methyl (gas phase)**

Functional	Gas-phase wave numbers (cm <sup>-1</sup> )					
PBE	3234	3232	3054	1356	1356	524
RPBE	3226	3226	3047	1363	1363	509
revPBE	3227	3227	3048	1362	1362	513
PBE-D3	3232	3231	3052	1356	1355	525
RPBE-D3	3217	3216	3036	1363	1362	516
revPBE-D3	3220	3220	3038	1360	1360	518
PBE-dDsC	3234	3233	3055	1357	1357	525
PBE-TS	3234	3233	3054	1356	1356	525
optB86b-vdW	3212	3211	3036	1362	1361	519
optB88-vdW	3223	3221	3049	1375	1373	529
optPBE-vdW	3215	3215	3043	1376	1376	521
BEEF-vdW	3258	3258	3082	1396	1396	531



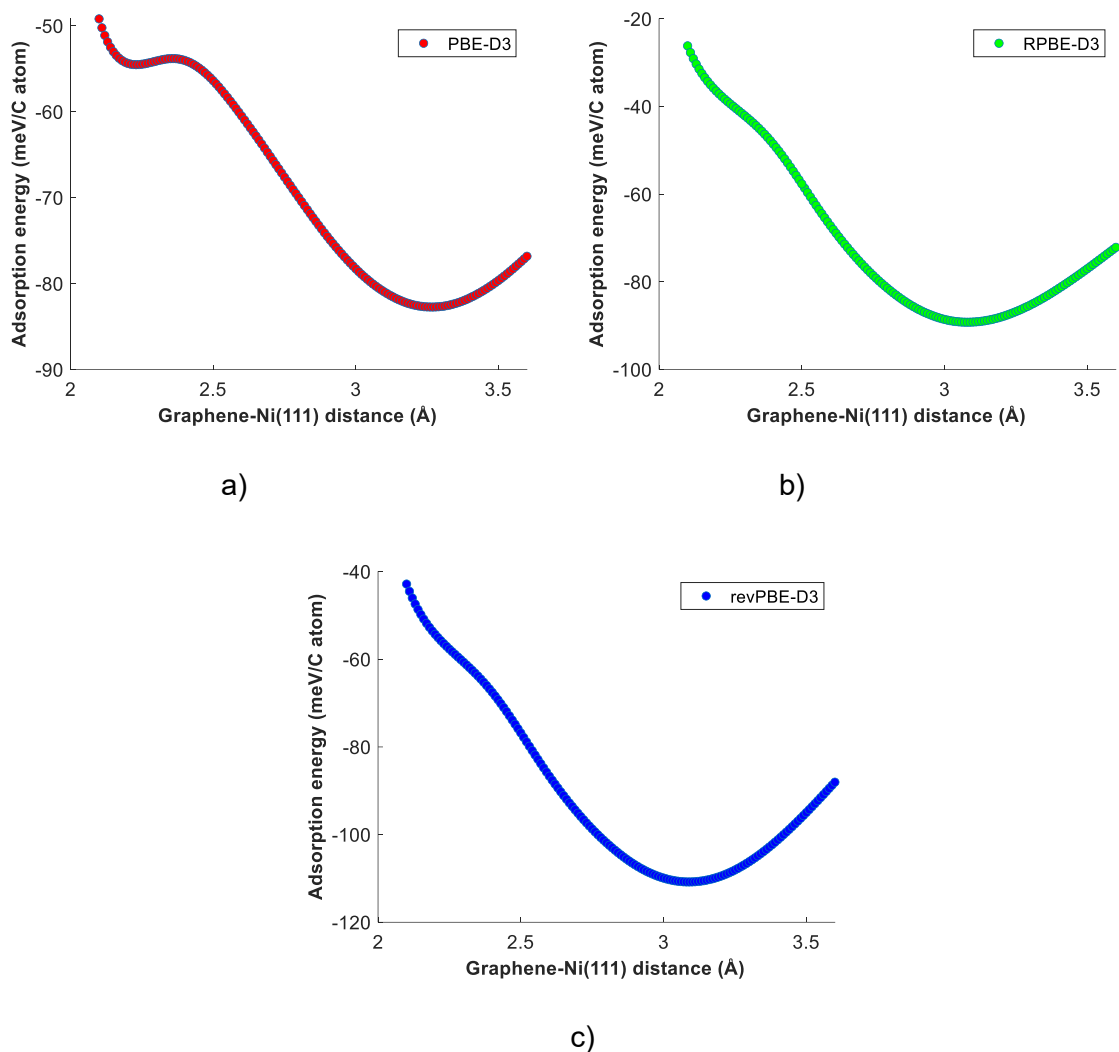


Figure A6: The potential energy profiles of graphene-Ni(111) (top-fcc geometry) using DFT-D3 functionals – (a) PBE-D3, (b) RPBE-D3 and (c) revPBE-D3 (up to the global minimum).

**Table A16. The geometric details of two distinct graphene-Ni(111) simulation setups used for the PBE-TS functional.**

Graphene-Ni(111) configuration	Ni lattice constant (Å)	Graphene lattice constant (bound on Ni(111)) (Å)	Deviation (%) from experimental Ni lattice constant (Å)	Deviation (%) from experimental graphene lattice constant (Å)
System 1	3.419	2.418	-2.97	-1.87
System 2	3.481	2.461	-1.22	-0.12

Note: The experimental lattice constants of Ni and graphene are  $3.524 \text{ Å}^{127}$  and  $2.464 \text{ Å}^{124}$ , respectively.

As shown in Table A16, we carried out DFT calculations for the PBE-TS functional using two disparate graphene-Ni(111) setups. In “System 1”, the PBE-TS optimised Ni lattice constant was used to construct the graphene-Ni(111) supercell. It can be inferred from Table A16 that the Ni lattice constant and the corresponding graphene lattice constant (bound on Ni(111)) of “System 1” are significantly lower than the experimental data. Using “System1”, we do not converge to the shallow first minimum of graphene-Ni(111) primarily because the carbon atoms experience substantial “strain” effects. The optimised graphene-Ni(111) distance of “System 1” is depicted in Figure A7(a). The PBE-D3 optimised Ni lattice constant (which is closer to the experimental value) was used in “System 2” – in this case, the carbon atoms of graphene-Ni(111) experience relatively weaker repulsive interactions. Thus, the PBE-TS calculation of “System 2” converges to the first minimum of graphene-Ni(111) (as shown in Figure A7(b)).

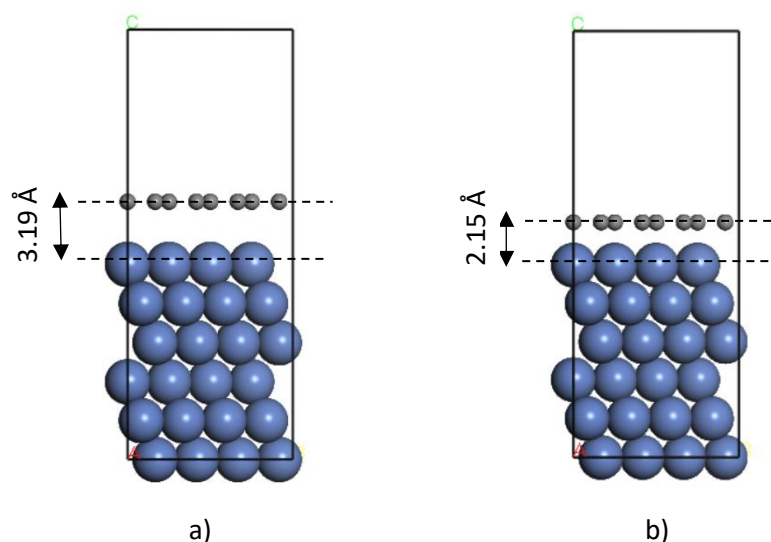


Figure A7: The graphene-Ni(111) optimised configurations obtained using the PBE-TS functional: (a) “System 1” and (b) “System 2”.

## Appendix II

**Table A17. The site preferences and the binding energies of methane cracking adsorbates**

Species	Preferred binding sites	Binding energy (eV)	Literature values (eV)
CH <sub>4</sub> <sup>*</sup>	Top	-0.26	-0.02 <sup>187</sup>
CH <sub>3</sub> <sup>*</sup>	Fcc	-2.32	-1.91 <sup>187</sup>
CH <sub>2</sub> <sup>*</sup>	Fcc	-4.33	-4.01 <sup>187</sup>
CH <sup>*</sup>	Fcc	-6.71	-6.43 <sup>187</sup>
C <sup>*</sup>	Hcp	-7.01	-6.78 <sup>187</sup>
H <sup>*</sup>	Fcc	-2.93	-2.81 <sup>187</sup>
H <sub>2</sub> <sup>*</sup>	Top	-0.49	-0.22 <sup>187</sup>

Note: Simulation details of Ref. 187: p(3x3) Ni(111) supercell, ENCUT: 400 eV, k-point mesh: 5×5×1, PBE functional.

**Table A18. The vibrational wavenumbers of converged geometries**

System	Vibrational wavenumbers (cm <sup>-1</sup> )
CH <sub>3</sub> <sup>*</sup>	2831, 2831, 2765, 1285, 1285, 1165, 480, 479, 400, 360, 225, 224
CH <sub>2</sub> <sup>*</sup>	3010, 2351, 1431, 664, 591, 532, 360, 311, 282
CH <sup>*</sup>	3031, 656, 656, 629, 418, 418
C <sup>*</sup>	580, 540, 540
H <sup>*</sup>	1150, 859, 858
H <sub>2</sub> <sup>*</sup>	2433, 1698, 925, 293, 246, 81
CH <sub>4</sub> dissociation TS	3105, 3067, 2962, 1567, 1391, 1372, 1139, 837, 725, 386, 363, 135, 91, 34, 899i
CH <sub>3</sub> dissociation TS	3008, 2514, 1851, 1369, 863, 707, 537, 451, 324, 267, 131, 850i
CH <sub>2</sub> dissociation TS	3054, 1207, 881, 677, 610, 467, 415, 360, 585i
CH dissociation TS	1858, 561, 522, 518, 128, 811i
H <sub>2</sub> dissociation TS	1905, 1691, 395, 213, 193, 532i

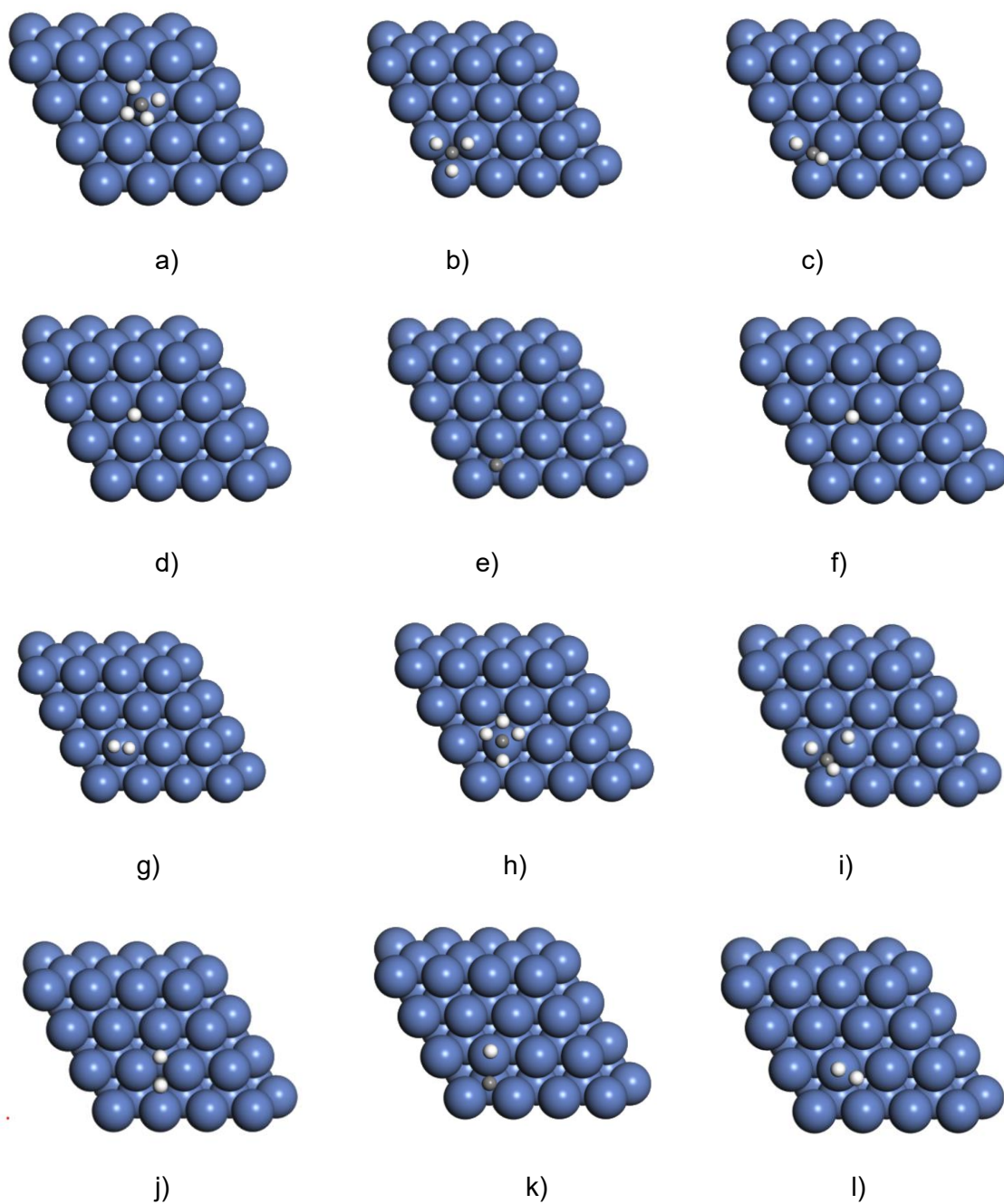


Figure A8: Top view of the initial states and transition states of the methane cracking system on Ni(111): a)  $\text{CH}_4$  physisorbed state on the top site. b)  $\text{CH}_3$  binds on the fcc site. c)  $\text{CH}_2$  adsorbs on the fcc site. d)  $\text{CH}$  binds on the fcc site. e) Carbon has a preference to bind on the hcp site. f) Hydrogen prefers to bind on the fcc site. g)  $\text{H}_2$  physisorbs on the top site. h) Transition state (TS) of methane dissociation. i) TS of  $\text{CH}_3$  dissociation. j) TS of  $\text{CH}_2$  dissociation. k) TS of  $\text{CH}$  dissociation. l) TS of  $\text{H}_2$  dissociation.

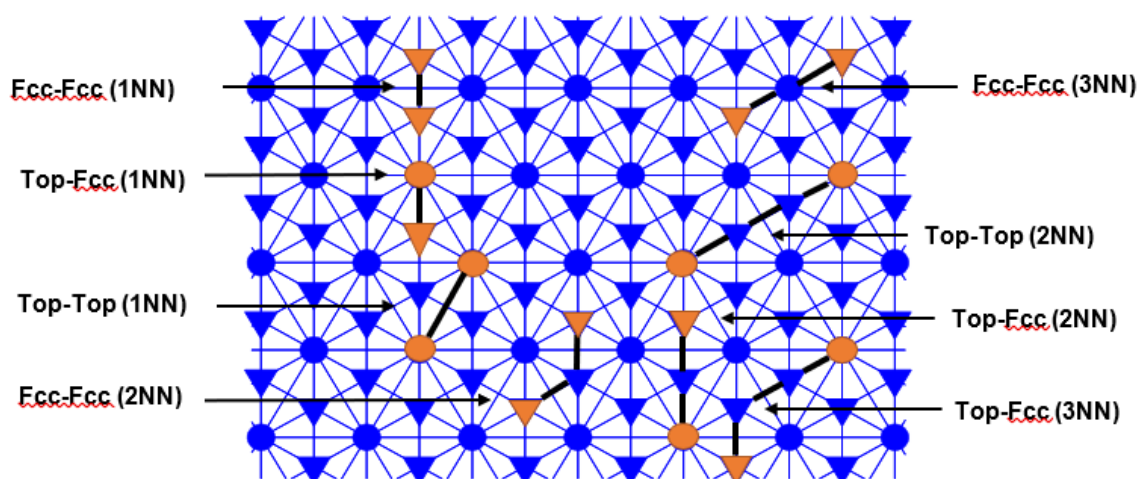


Figure A9: Schematic of the KMC lattice with all the pairwise interaction sub-patterns. The circles and triangles represent top and hollow sites, respectively. The unoccupied sites are coloured in blue, whereas the occupied sites are coloured in orange (the occupied site could be any adsorbate of the methane cracking system). Each type of interaction pattern has been given an appropriate label (as depicted above).

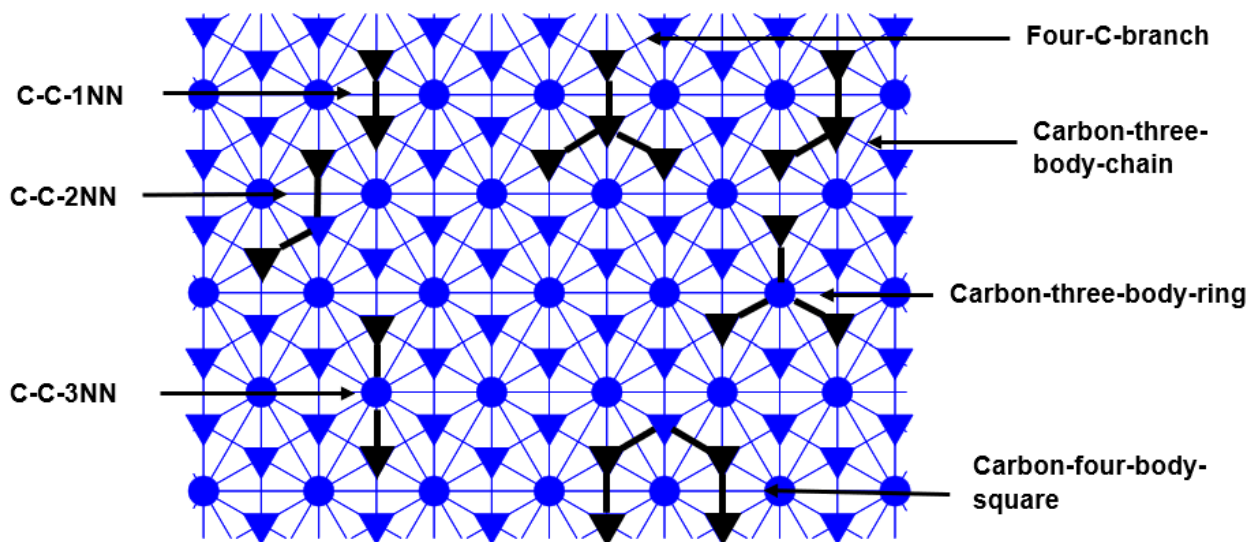


Figure A10: Schematics of interaction patterns used in the CE model for capturing long-range carbon configurations. The circles and triangles represent top and hollow sites, respectively. The unoccupied sites are coloured in blue, whereas the occupied sites by carbon are coloured in black. Each type of interaction pattern has been given an appropriate label (as shown above).

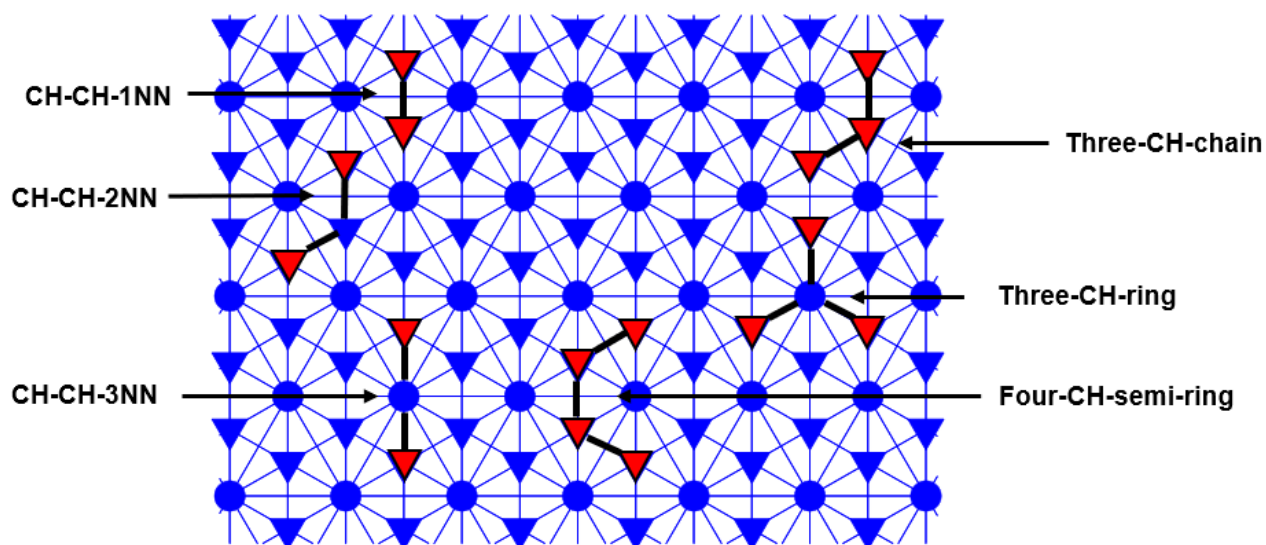


Figure A11: Schematics of interaction patterns used in the CE model for capturing long-range CH configurations. The unoccupied sites are coloured in blue, whereas the occupied sites by CH are coloured in red. Each type of interaction pattern has been given an appropriate label (as shown above).

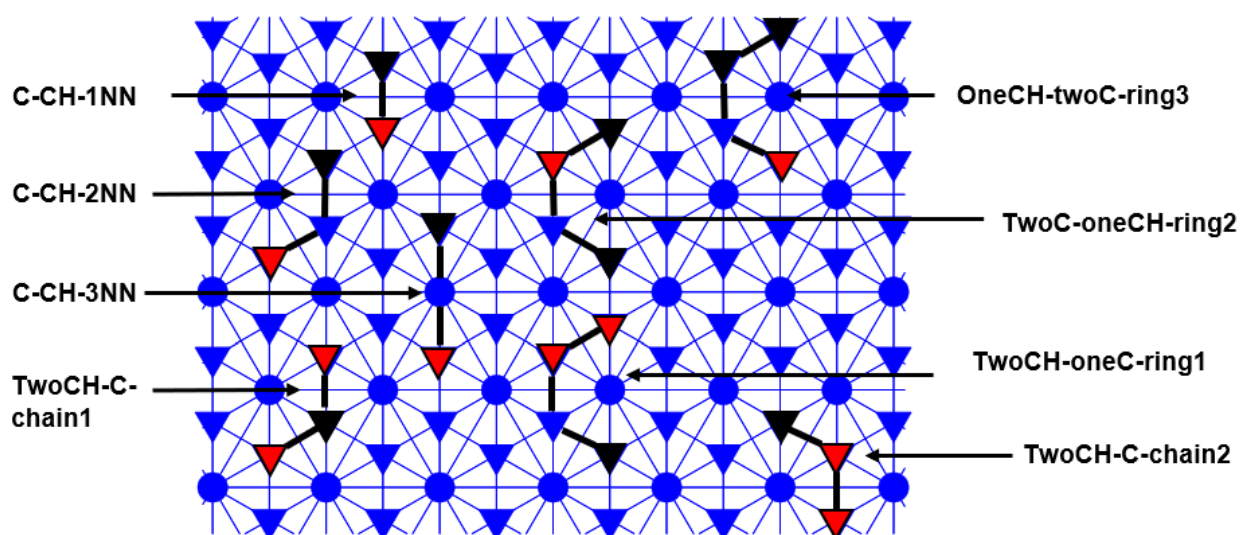


Figure A12: Schematics of interaction patterns used in the CE model for capturing long-range CH configurations and CH-C configurations. The unoccupied sites are coloured in blue, whereas the occupied sites by CH and carbon are coloured in red and black, respectively. Each type of interaction pattern has been given an appropriate label (as shown above).

**Table A19. Comparison of computed activation barriers of methane cracking reaction on Ni(111) with literature**

Reactions	Activation energy forward (eV)	Activation energy reverse (eV)	Activation energy forward (eV) (literature values)	Activation energy reverse (eV) (literature values)
CH <sub>4</sub> adsorption	0.00	0.26	0.00 <sup>133</sup>	0.02 <sup>133</sup>
CH <sub>4</sub> dissociation	0.67	0.94	1.21 <sup>188</sup> , 0.91 <sup>133</sup>	0.66 <sup>133</sup> , 0.90 <sup>133</sup>
CH <sub>3</sub> dissociation	0.66	0.64	0.87 <sup>188</sup> , 0.70 <sup>133</sup>	0.54 <sup>133</sup> , 0.63 <sup>133</sup>
CH <sub>2</sub> dissociation	0.26	0.63	0.43 <sup>188</sup> , 0.35 <sup>133</sup>	0.59 <sup>133</sup> , 0.69 <sup>133</sup>
CH dissociation	1.31	0.84	1.45 <sup>188</sup> , 1.33 <sup>133</sup>	0.80 <sup>133</sup> , 0.81 <sup>133</sup>
H <sub>2</sub> adsorption	0.00	0.49	0.00 <sup>133</sup>	0.22 <sup>133</sup>
H <sub>2</sub> dissociation	0.04	0.89	0.06 <sup>133</sup>	0.92 <sup>133</sup>
CH <sub>3</sub> diffusion	0.21	0.21	0.15 <sup>24</sup>	0.15 <sup>24</sup>
CH <sub>2</sub> diffusion	0.26	0.26	0.19 <sup>24</sup>	0.19 <sup>24</sup>
CH diffusion	0.34	0.34	0.32 <sup>24</sup>	0.32 <sup>24</sup>
C diffusion	0.32	0.32	0.31 <sup>24</sup>	0.31 <sup>24</sup>
H diffusion	0.14	0.14	0.12 <sup>24</sup>	0.12 <sup>24</sup>

Note: The activation energies reported above do not include ZPE/thermal contributions. Ref. 133 simulation details: a p(3x3) Ni(111) supercell, ENCUT: 400.00 eV, 5×5×1 Monkhorst-Pack k-point mesh and the BEEF-vdW functional have been employed. Ref. 188 simulation details: a p(3x3) Ni(111) supercell, ENCUT: 400.00 eV, 3×3×1 Monkhorst-Pack k-point mesh and the PBE functional have been employed. Ref. 24 simulation details: a p(3x3) Ni(111) supercell, ENCUT: 415.00 eV, 7×7×1 Monkhorst-Pack k-point mesh and the BEEF-vdW functional have been employed.

The first step, methane adsorption, is not included explicitly in the KMC model because methane physisorbs weakly on the Ni(111) surface and the harmonic approximation is not appropriate for weakly bound molecules. Furthermore, experimental studies have used molecular beam techniques and high-resolution electron energy loss spectroscopy (HREELS) to show that methane binds to the Ni(111) surface by the direct dissociation mechanism. Thus, in the KMC model, we have lumped the adsorption and methane dissociation steps into a single event (refer to Table 5 of Chapter 4). Similarly, we also lumped the H<sub>2</sub> adsorption and subsequent dissociation into a single step, since the H<sub>2</sub><sup>\*</sup> species is short-lived on the Ni(111) surface and dissociates spontaneously into H atoms.

As shown in Table A19, using the PBE-D3 functional, we calculate the forward activation barrier for methane dissociative adsorption to be 0.67 eV. However, many theoretical studies in the literature have reported substantially high forward activation barriers for methane dissociation (refer to Table A19). Most studies have used the GGA functionals (PBE, RPBE) for studying the methane cracking reaction network. In Table A20, we report the forward activation barriers of methane dissociative chemisorption for a range of functionals and compare their values to the experimental apparent activation energies (taken from the literature). There is a significant variation in the CH<sub>4</sub> dissociation barrier prediction among the functionals considered. We find that the PBE-D3 functional is in reasonable agreement with the experimental apparent activation energy values of methane dissociation reported in the literature (as shown in Table A20).

**Table A20. Comparison of methane dissociation activation barriers using different DFT functionals to available experimental data**

Method	Methane dissociation forward activation barrier (eV)
PBE	0.84
RPBE	1.19
revPBE	1.15
PBE-D3	0.67
RPBE-D3	0.79
revPBE-D3	0.72
optB86b-vdW	0.69
optPBE-vdW	0.91
Experiment (apparent activation barrier values)	0.54 <sup>189</sup> , 0.77 <sup>190</sup> (±0.1)

Note: The dissociation barriers reported above have been computed by considering physisorbed methane as the initial state (in the case of DFT-D3 and vdW-DF).



**Table A21. The geometry, event-multiplicity and proximity factors for each elementary event of methane cracking**

Event	Geometry factors	Event multiplicity factors	w
$\text{CH}_4(\text{g}) + \text{*}(\text{fcc}) + \text{*}(\text{top}) + \text{*}(\text{fcc}) \rightarrow \text{CH}_3\text{*}(\text{fcc}) + \text{*}(\text{top}) + \text{H*}(\text{fcc})$	3	2	1.00
$\text{CH}_3\text{*}(\text{fcc}) + \text{*}(\text{top}) + \text{H*}(\text{fcc}) \rightarrow \text{CH}_4(\text{g}) + \text{*}(\text{fcc}) + \text{*}(\text{top}) + \text{*}(\text{fcc})$	6	1	0.00
$\text{CH}_3\text{*}(\text{fcc}) + \text{*}(\text{top}) + \text{*}(\text{fcc}) \rightarrow \text{CH}_2\text{*}(\text{fcc}) + \text{*}(\text{top}) + \text{H*}(\text{fcc})$	12	1	0.50
$\text{CH}_2\text{*}(\text{fcc}) + \text{*}(\text{top}) + \text{H*}(\text{fcc}) \rightarrow \text{CH}_3\text{*}(\text{fcc}) + \text{*}(\text{top}) + \text{*}(\text{fcc})$	12	1	0.50
$\text{CH}_2\text{*}(\text{fcc}) + \text{*}(\text{fcc}) \rightarrow \text{CH*}(\text{fcc}) + \text{H*}(\text{fcc})$	3	1	0.50
$\text{CH*}(\text{fcc}) + \text{H*}(\text{fcc}) \rightarrow \text{CH}_2\text{*}(\text{fcc}) + \text{*}(\text{fcc})$	3	1	0.50
$\text{CH*}(\text{fcc}) + \text{*}(\text{top}) + \text{*}(\text{fcc}) \rightarrow \text{C*}(\text{fcc}) + \text{*}(\text{top}) + \text{H*}(\text{fcc})$	6	1	0.50
$\text{C*}(\text{fcc}) + \text{*}(\text{top}) + \text{H*}(\text{fcc}) \rightarrow \text{CH*}(\text{fcc}) + \text{*}(\text{top}) + \text{*}(\text{fcc})$	6	1	0.50
$\text{*}(\text{fcc}) + \text{H}_2(\text{g}) + \text{*}(\text{fcc}) \rightarrow \text{H*}(\text{fcc}) + \text{*}(\text{top}) + \text{H*}(\text{fcc})$	3	2	0.50
$\text{H*}(\text{fcc}) + \text{*}(\text{top}) + \text{H*}(\text{fcc}) \rightarrow \text{*}(\text{fcc}) + \text{H}_2(\text{g}) + \text{*}(\text{fcc})$	3	2	0.50

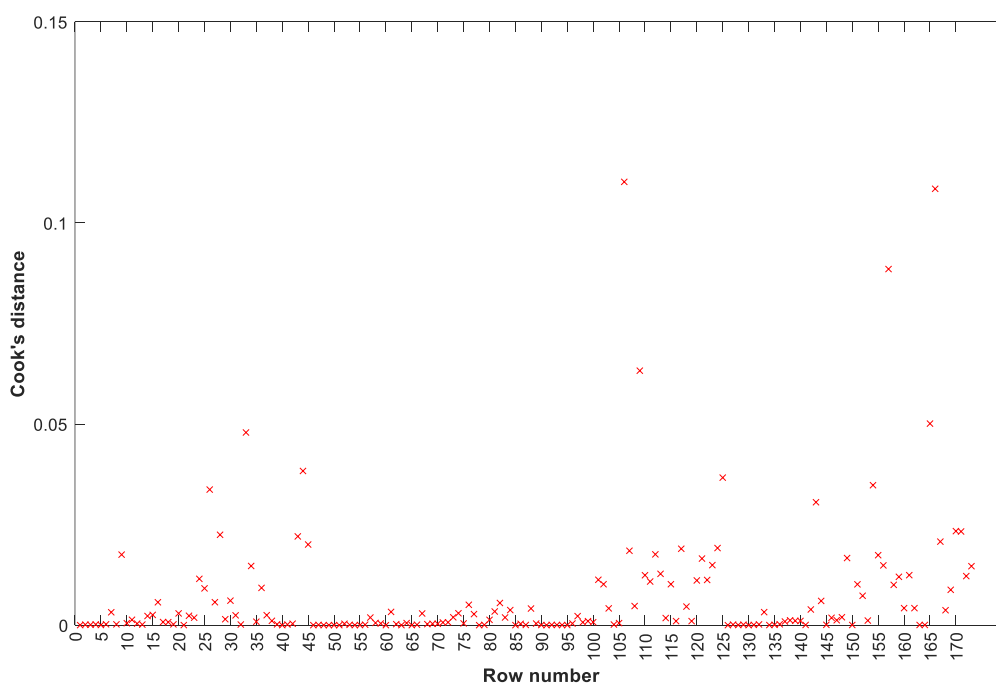


**Figure A13: Cook's distances for the DFT parameterised CE model**

**Table A22. Effective cluster interaction (ECI) values of pairwise sub-patterns**

Co-adsorbed system	ECI-1NN (eV)	ECI-2NN (eV)	ECI-3NN (eV)
C-CH <sub>3</sub>	5.000	0.337	0.171
C-CH <sub>2</sub>	5.000	0.270	0.099
CH-C	-0.494	0.275	0.104
C-C	-0.471	0.375	0.242
C-H	0.653	0.129	0.018
CH-CH <sub>3</sub>	5.000	0.312	0.223
CH-CH <sub>2</sub>	5.000	0.197	0.109
CH-CH	-0.355	0.261	0.113
CH-H	0.543	0.063	0.002
CH <sub>2</sub> -CH <sub>3</sub>	5.000	0.356	0.287
CH <sub>2</sub> -CH <sub>2</sub>	-0.366	0.161	0.125
CH <sub>2</sub> -H	5.000	0.065	0.014
H-CH <sub>3</sub>	0.534	0.089	0.055
H-H	0.268	0.004	-0.017
CH <sub>3</sub> -CH <sub>3</sub>	5.000	5.000	5.000

Note: The corresponding graph-pattern for every pairwise interaction parameter is depicted in Figure A9.

**Table A23. Effective cluster interaction (ECI) values of the CE parameterised KMC model (referred to as “KMC-long-range”)**

Co-adsorbed system	ECI-1NN (eV)	ECI-2NN (eV)	ECI-3NN (eV)
C-CH <sub>3</sub>	5.000	0.270	0.104
C-CH <sub>2</sub>	5.000	0.203	0.032
CH-C	-0.471	0.171	0.096
C-C	-0.458	0.343	0.219
C-H	0.586	0.062	-0.050
CH-CH <sub>3</sub>	5.000	0.276	0.187
CH-CH <sub>2</sub>	5.000	0.162	0.007
CH-CH	-0.314	0.208	0.006
CH-H	0.508	0.027	-0.034
CH <sub>2</sub> -CH <sub>3</sub>	5.000	0.355	0.286
CH <sub>2</sub> -CH <sub>2</sub>	-0.365	0.161	0.125
CH <sub>2</sub> -H	5.000	0.065	0.014
H-CH <sub>3</sub>	0.534	0.089	0.055
H-H	0.268	0.004	-0.016
CH <sub>3</sub> -CH <sub>3</sub>	5.000	5.000	5.000
<b>ECI parameters of C/CH species (eV)</b>			
Carbon-one-body	2.320		
CH-one-body	1.162		
Carbon-three-body-chain	-0.146		
Carbon-three-body-ring	-0.313		
Carbon-four-body-square	-0.447		
Four-C-branch	-0.611		
Three-CH-chain	0.411		
Three-CH-ring	-0.065		
Four-CH-semi-ring	-0.463		
TwoCH-C-chain1	0.170		
TwoCH-C-chain2	0.227		
TwoCH-oneC-ring1	-0.414		
TwoC-oneCH-ring2	-0.196		
OneCH-twoC-ring3	-0.076		

Note: The corresponding graph pattern of CE-fit parameters are illustrated in Figure A10, Figure A11 and Figure A12.

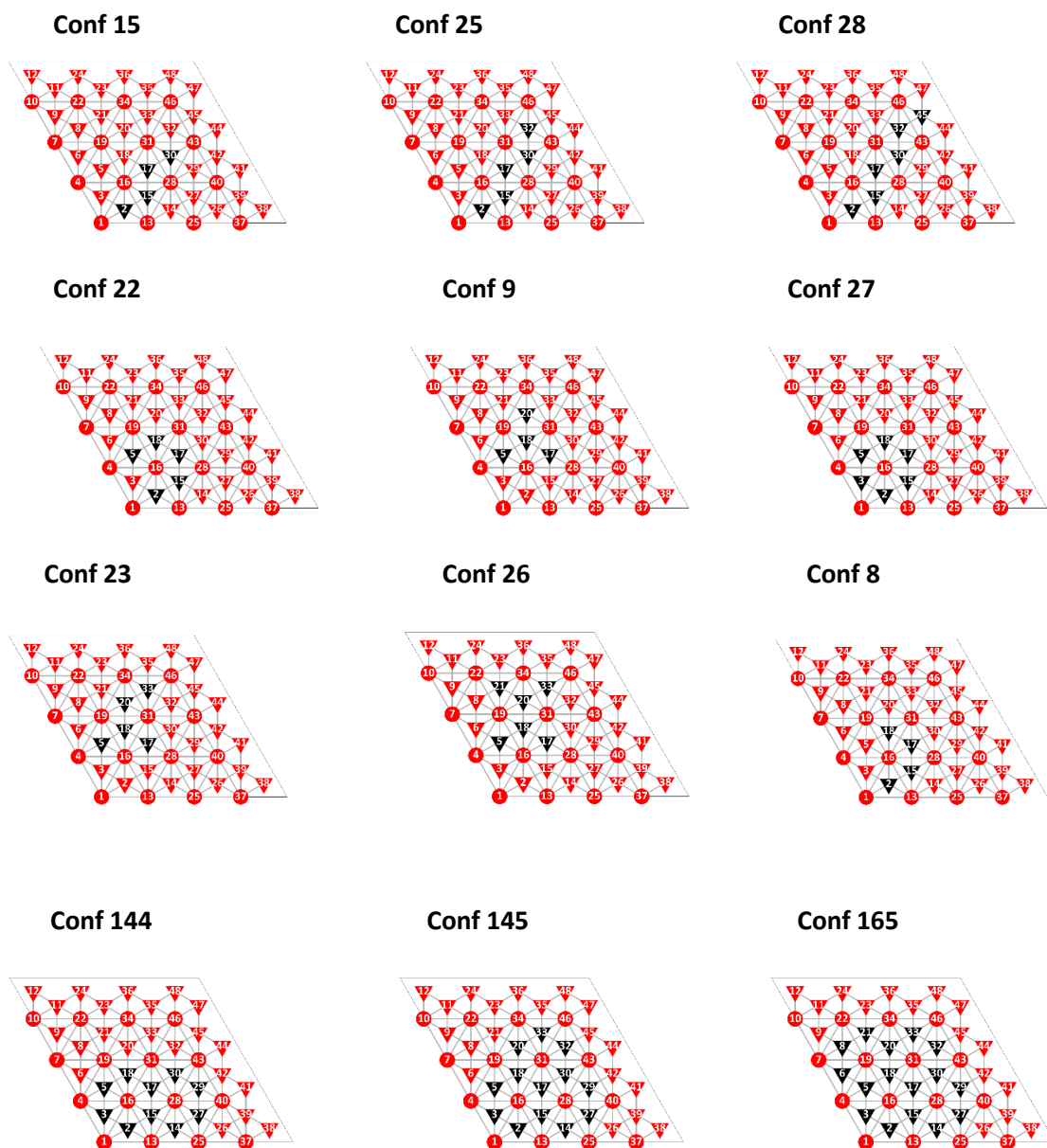


Figure A14: Schematics of a few representative/important carbon configurations of the DFT dataset (which was used for CE training with a 4x4 KMC lattice). The top and hollow sites are represented by circles and triangles, respectively. The sites coloured in red are unoccupied, whereas the sites coloured in black are occupied by carbon.

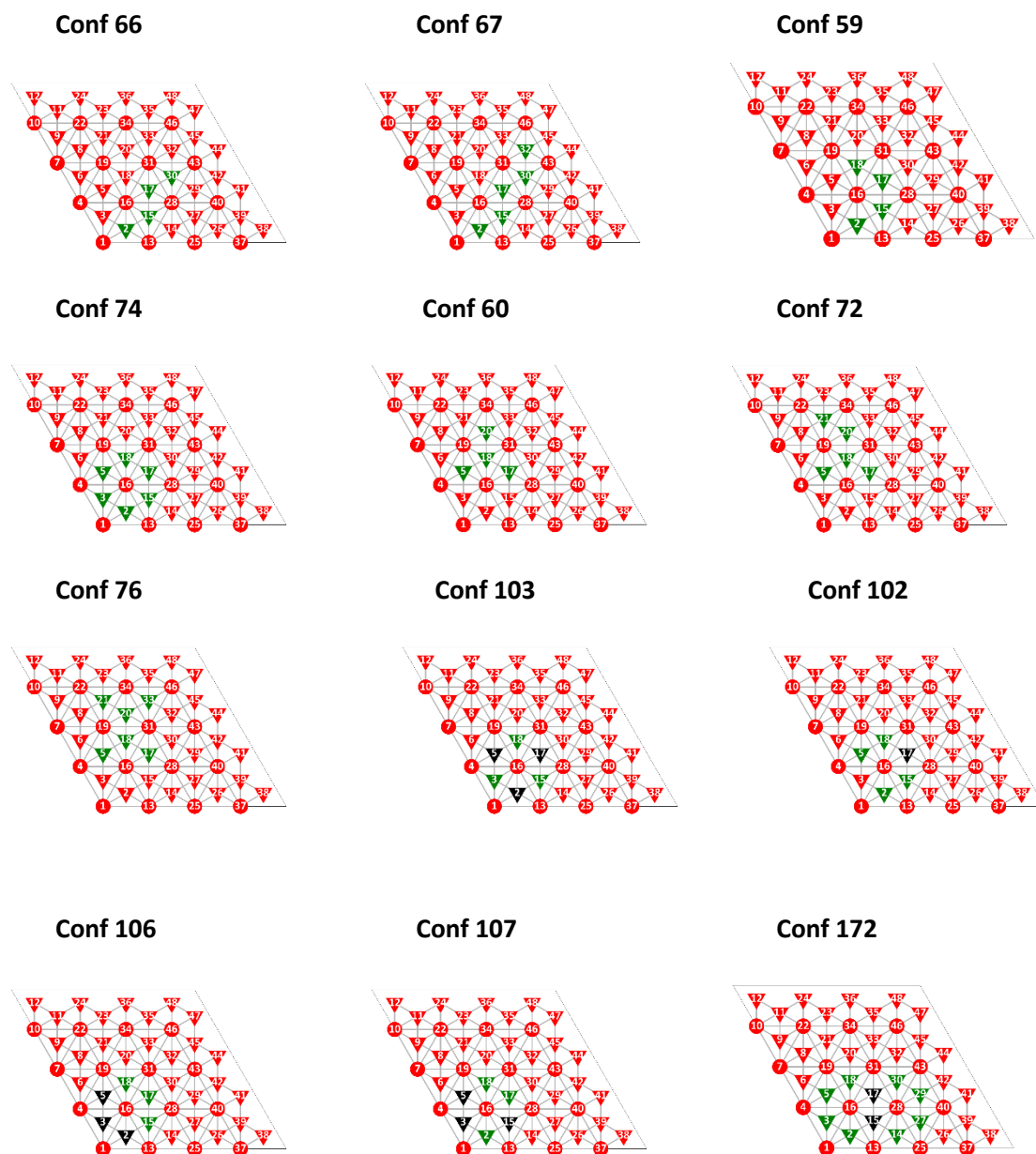


Figure A15: Schematics of a few representative/important CH and C-CH configurations of the DFT dataset (which was used for CE training with a  $4 \times 4$  KMC lattice). The top and hollow sites are represented by circles and triangles, respectively. The sites coloured in red are unoccupied, whereas the sites coloured in green and black are occupied by CH and carbon, respectively.

**Table A24. Results of the KMC lattice convergence test performed using KMC-1NN model at 800 K, 10.00 bar CH<sub>4</sub> (g) and 0.01 bar H<sub>2</sub> (g)**

KMC lattice size	CH coverage (ML)	Carbon coverage (ML)
5x5	1.25	0.50
10x10	1.35	0.59
20x20	1.41	0.57
30x30	1.41	0.59

**Table A25. Free energy and kinetic data of methane cracking reaction steps at 800 K, 10.00 bar CH<sub>4</sub> (g) and 0.01 H<sub>2</sub> (g)**

Reaction	$\Delta G_{fwd}^{act}$ (eV)	$\Delta G_{rev}^{act}$ (eV)	$\Delta G_{rxn}^{energy}$ (eV)	$k_{fwd}$ (s <sup>-1</sup> )	$k_{rev}$ (s <sup>-1</sup> )	$K_{eq}$ (s <sup>-1</sup> )
CH <sub>4</sub> direct dissociation	1.11	0.73	0.38	$1.69 \times 10^6$	$4.19 \times 10^8$	$4.04 \times 10^{-3}$
CH <sub>3</sub> dissociation	0.51	0.56	-0.05	$1.02 \times 10^{10}$	$4.94 \times 10^9$	2.07
CH <sub>2</sub> dissociation	0.20	0.57	-0.37	$9.15 \times 10^{11}$	$4.27 \times 10^9$	$2.14 \times 10^2$
CH dissociation	1.12	0.71	0.41	$1.46 \times 10^6$	$5.60 \times 10^8$	$2.61 \times 10^{-3}$
H <sub>2</sub> associative desorption	0.91	0.98	-0.07	$3.08 \times 10^7$	$1.12 \times 10^7$	2.76

**Table A26. Free energy and kinetic data of methane cracking reaction steps at 900 K, 10.00 bar CH<sub>4</sub> (g) and 0.01 H<sub>2</sub> (g)**

Reaction	$\Delta G_{fwd}^{act}$ (eV)	$\Delta G_{rev}^{act}$ (eV)	$\Delta G_{rxn}^{energy}$ (eV)	$k_{fwd}$ (s <sup>-1</sup> )	$k_{rev}$ (s <sup>-1</sup> )	$K_{eq}$ (s <sup>-1</sup> )
CH <sub>4</sub> direct dissociation	1.20	0.71	0.49	$3.57 \times 10^6$	$1.98 \times 10^9$	$1.80 \times 10^{-3}$
CH <sub>3</sub> dissociation	0.52	0.57	-0.05	$2.29 \times 10^{10}$	$1.20 \times 10^{10}$	1.91
CH <sub>2</sub> dissociation	0.22	0.57	-0.35	$1.10 \times 10^{12}$	$1.20 \times 10^{10}$	$9.12 \times 10^1$
CH dissociation	1.12	0.70	0.42	$1.00 \times 10^7$	$2.25 \times 10^9$	$4.45 \times 10^{-3}$
H <sub>2</sub> associative desorption	0.87	1.11	-0.24	$2.52 \times 10^8$	$1.14 \times 10^7$	$2.21 \times 10^1$

**Table A27. Free energy and kinetic data of methane cracking reaction steps at 1000 K, 10.00 bar CH<sub>4</sub> (g) and 0.01 H<sub>2</sub> (g)**

Reaction	$\Delta G_{fwd}^{act}$ (eV)	$\Delta G_{rev}^{act}$ (eV)	$\Delta G_{rxn}^{energy}$ (eV)	$k_{fwd}$ (s <sup>-1</sup> )	$k_{rev}$ (s <sup>-1</sup> )	$K_{eq}$ (s <sup>-1</sup> )
CH <sub>4</sub> direct dissociation	1.29	0.69	0.60	$6.56 \times 10^6$	$6.93 \times 10^9$	$9.46 \times 10^{-4}$
CH <sub>3</sub> dissociation	0.52	0.57	-0.05	$4.98 \times 10^{10}$	$2.79 \times 10^{10}$	1.79
CH <sub>2</sub> dissociation	0.23	0.57	-0.34	$1.44 \times 10^{12}$	$2.79 \times 10^{10}$	$5.17 \times 10^1$
CH dissociation	1.11	0.70	0.41	$5.30 \times 10^7$	$6.17 \times 10^9$	$8.58 \times 10^{-3}$
H <sub>2</sub> associative desorption	0.84	1.25	-0.41	$1.22 \times 10^9$	$1.04 \times 10^7$	$1.17 \times 10^2$

**Table A28. Free energy and kinetic data of methane cracking reaction steps at 1100 K, 10.00 bar CH<sub>4</sub> (g) and 0.01 H<sub>2</sub> (g)**

Reaction	$\Delta G_{fwd}^{act}$ (eV)	$\Delta G_{rev}^{act}$ (eV)	$\Delta G_{rxn}^{energy}$ (eV)	$k_{fwd}$ (s <sup>-1</sup> )	$k_{rev}$ (s <sup>-1</sup> )	$K_{eq}$ (s <sup>-1</sup> )
CH <sub>4</sub> direct dissociation	1.38	0.67	0.71	$1.09 \times 10^7$	$1.95 \times 10^{10}$	$5.58 \times 10^{-4}$
CH <sub>3</sub> dissociation	0.52	0.57	-0.05	$9.49 \times 10^{10}$	$5.60 \times 10^{10}$	1.69
CH <sub>2</sub> dissociation	0.24	0.58	-0.34	$1.82 \times 10^{12}$	$5.04 \times 10^{10}$	$3.61 \times 10^1$
CH dissociation	1.11	0.69	0.42	$1.88 \times 10^8$	$1.58 \times 10^{10}$	$1.19 \times 10^{-2}$
H <sub>2</sub> associative desorption	0.81	1.39	-0.58	$4.45 \times 10^9$	$9.80 \times 10^6$	$4.54 \times 10^2$

**Table A29. Free energy and kinetic data of methane cracking reaction steps at 1200 K, 10.00 bar CH<sub>4</sub> (g) and 0.01 H<sub>2</sub> (g)**

Reaction	$\Delta G_{fwd}^{act}$ (eV)	$\Delta G_{rev}^{act}$ (eV)	$\Delta G_{rxn}^{energy}$ (eV)	$k_{fwd}$ (s <sup>-1</sup> )	$k_{rev}$ (s <sup>-1</sup> )	$K_{eq}$ (s <sup>-1</sup> )
CH <sub>4</sub> direct dissociation	1.47	0.65	0.82	$1.67 \times 10^7$	$4.65 \times 10^{10}$	$3.60 \times 10^{-4}$
CH <sub>3</sub> dissociation	0.52	0.57	-0.05	$1.64 \times 10^{11}$	$1.01 \times 10^{11}$	1.62
CH <sub>2</sub> dissociation	0.25	0.58	-0.33	$2.23 \times 10^{12}$	$9.15 \times 10^{10}$	$2.43 \times 10^1$
CH dissociation	1.11	0.69	0.42	$5.44 \times 10^8$	$3.16 \times 10^{10}$	$1.72 \times 10^{-2}$
H <sub>2</sub> associative desorption	0.78	1.53	-0.75	$1.32 \times 10^{10}$	$9.37 \times 10^6$	$1.41 \times 10^3$

**Table A30: The replica runs of KMC-1NN system at 1000 K, 10.00 bar CH<sub>4</sub>(g) and 0.01 H<sub>2</sub>(g)**

KMC runs	CH coverage (ML)	Carbon coverage (ML)
Random seed 1	1.0581	0.8819
Random seed 2	1.0603	0.8797
Random seed 3	1.0305	0.9095
Random seed 4	0.9879	0.9521
Random seed 5	1.0593	0.8807
Average values	1.0392 (±0.0313)	0.9008 (±0.0313)

**Note:** The value provided in the parenthesis is the KMC population standard deviation (also called as the “KMC standard error”)

**Table A31. The replica runs of KMC-long-range system at 1000 K, 10.00 bar CH<sub>4</sub>(g) and 0.01 H<sub>2</sub>(g)**

KMC runs	CH coverage (ML)	Carbon coverage (ML)
Random seed 1	0.5595	0.8217
Random seed 2	0.5583	0.8802
Random seed 3	0.5748	0.7632
Random seed 4	0.5566	0.9056
Random seed 5	0.5100	0.7961
Average values	0.5518 (±0.0084)	0.8333 (±0.0589)

**Note:** The value provided in the parenthesis is the KMC standard error.

As shown in Table A30 and Table A31, the standard errors of the KMC-1NN and KMC-long-range models are very low.



## Appendix III

**Table A32. The adsorption energies of MSR species on Ni(111) and K-Ni(111)**

Species	Preferred binding site – Ni(111)	Preferred binding site – K-Ni(111)	Binding energies Ni(111) (eV)	Binding energies K-Ni(111) (eV)	Literature values – Ni(111)	Literature values – K-Ni(111)
CH <sub>3</sub> *	fcc	fcc	-2.32	-2.19	-1.89	-1.59
CH <sub>2</sub> *	fcc	fcc	-4.33	-4.25	-4.03	-3.90
CH*	fcc	fcc	-6.58	-6.55	-6.41	-6.38
C*	hcp	hcp	-7.01	-7.13	-6.89	-7.06
H*	fcc	hcp	-2.93	-2.93	-2.80	-2.81
H <sub>2</sub> O*	top	top	-0.53	-0.87	-0.27	-0.68
OH*	fcc	bridge	-3.61	-3.64	-3.27	-3.24
O*	fcc	fcc	-5.81	-6.07	-5.39	-5.65
CHOH*	fcc	fcc	-3.42	-3.49	-3.88	-4.00
CHO*	hcp	hcp	-2.55	-2.79	-2.27	-2.49
COH*	hcp	hcp	-4.65	-4.73	-4.39	-4.44
CO*	hcp	hcp	-2.12	-2.46	-1.93	-2.35

Note: The literature values (reported above) have been obtained from the work of Zhou and Liu.<sup>176</sup> The authors used the following computational setup: 1) p(3×3) unit cell, 2) PBE functional, 3) 4×4×1 Monkhorst-Pack k-point grid and 4) Kinetic energy cut-off value – 385 eV.

**Table A33. Comparison of MSR activation barriers with literature values**

Event ID: Reaction	$E_{act}$ (eV) Ni(111)	$E_{act}$ (eV) K-Ni(111)	Ni(111) literature values (eV)	K- Ni(111) literature values (eV)
R <sub>1</sub> : CH <sub>4</sub> (g) + 2* $\leftrightarrow$ CH <sub>3</sub> * + H*	0.41 (0.94)	0.56 (0.96)	1.29 (0.59) <sup>6</sup> , 1.05 (0.52) <sup>17</sup>	1.26 <sup>17</sup>
R <sub>2</sub> : CH <sub>3</sub> * + * $\leftrightarrow$ CH <sub>2</sub> * + H*	0.66 (0.64)	0.69 (0.72)	0.76 (0.64) <sup>6</sup>	Not available
R <sub>3</sub> : CH <sub>2</sub> * + * $\leftrightarrow$ CH* + H*	0.26 (0.63)	0.25 (0.67)	0.34 (0.67) <sup>6</sup>	Not available
R <sub>4</sub> : CH* + * $\leftrightarrow$ C* + H*	1.31 (0.84)	1.21 (0.90)	1.48 (0.84) <sup>6</sup>	Not available
R <sub>5</sub> : 2H* $\rightarrow$ H <sub>2</sub> (g) + 2*	1.33 (0.00)	1.33 (0.00)	1.08 (0.01) <sup>176</sup>	1.10 (0.00) <sup>176</sup>
R <sub>6</sub> : H <sub>2</sub> O(g) + * $\leftrightarrow$ H <sub>2</sub> O*	0.00 (0.54)	0.00 (0.87)	0.00 (0.27) <sup>176</sup> , 0.00 (0.02) <sup>6</sup>	0.00 (0.68) <sup>176</sup>
R <sub>7</sub> : H <sub>2</sub> O* + * $\leftrightarrow$ OH* + H*	0.89 (1.32)	0.79 (0.91)	0.86 (1.27) <sup>176</sup> , 0.97 (1.06) <sup>6</sup>	0.81 (0.80) <sup>176</sup>
R <sub>8</sub> : OH* + * $\leftrightarrow$ O* + H*	0.98 (1.21)	0.76 (1.24)	0.98 (1.17) <sup>176</sup> , 0.99 (1.22) <sup>6</sup>	0.70 (1.21) <sup>176</sup>
R <sub>9</sub> : CH* + OH* $\leftrightarrow$ CHOH* + *	1.45 (0.80)	1.15 (0.58)	1.45 (0.72) <sup>176</sup> , 1.27 (0.77) <sup>6</sup>	1.17 (0.61) <sup>176</sup>
R <sub>10</sub> : CHOH* + * $\leftrightarrow$ CHO* + H*	0.75 (1.17)	0.57 (1.15)	0.71 (1.14) <sup>176</sup> , 0.82 (1.31) <sup>6</sup>	0.58 (1.05) <sup>176</sup>
R <sub>11</sub> : CHOH* + * $\leftrightarrow$ COH* + H*	0.12 (0.81)	0.16 (0.86)	0.10 (0.83) <sup>176</sup> , 0.13 (0.87) <sup>6</sup>	0.22 (0.89) <sup>176</sup>
R <sub>12</sub> : CH* + O* $\leftrightarrow$ CHO* + *	1.51 (1.05)	1.53 (1.08)	1.54 (1.04) <sup>176</sup> , 1.56 (1.32) <sup>6</sup>	1.52 (0.94) <sup>176</sup>
R <sub>13</sub> : C* + OH* $\leftrightarrow$ COH* + *	1.41 (1.91)	1.01 (1.46)	1.06 (1.49) <sup>176</sup> , 1.30 (2.18) <sup>6</sup>	1.06 (1.49) <sup>176</sup>
R <sub>14</sub> : CHO* + * $\leftrightarrow$ CO* + H*	0.19 (1.51)	0.14 (1.57)	0.05 (1.61) <sup>176</sup> , 0.24 (1.36) <sup>6</sup>	0.05 (1.61) <sup>176</sup>
R <sub>15</sub> : COH* + * $\leftrightarrow$ CO* + H*	0.91 (1.97)	0.78 (2.10)	0.72 (2.09) <sup>176</sup> , 1.02 (1.90) <sup>6</sup>	0.72 (2.09) <sup>176</sup>
R <sub>16</sub> : C* + O* $\leftrightarrow$ CO* + *	2.28 (3.61)	1.61 (2.90)	1.60 (2.88) <sup>176</sup> , 2.15 (3.67) <sup>6</sup>	1.55 (2.85) <sup>176</sup>
R <sub>17</sub> : CO* $\rightarrow$ CO(g) + *	2.12 (0.00)	2.46 (0.00)	1.90 (0.00) <sup>176</sup> , 1.53 (0.00) <sup>6</sup>	2.35 (0.00) <sup>176</sup>
R <sub>18</sub> : CO* + O* $\rightarrow$ CO <sub>2</sub> (g) + 2*	1.62 (0.36)	1.87 (0.00)	1.57 (0.60) <sup>176</sup> , 1.54 (1.22) <sup>6</sup>	1.61 (0.50) <sup>176</sup>

Note: The values shown in parenthesis are the reverse activation barriers. The computational setup of Blaylock et al.<sup>6</sup> is as follows: 1) p(2×2) periodic cell, 2) RPBE functional, 3) 6×6×1 Monkhorst-Pack k-point grid and 4) Plane wave energy cut-off value – 340 eV. Bengaard et al.<sup>17</sup> employed a p(2x2) unit cell, RPBE functional, Chadi-Cohen k-point set and kinetic energy cut-off value of 340 eV. The computational details of Zhou and Liu<sup>176</sup> work have been provided as a “Note” under Table A32.

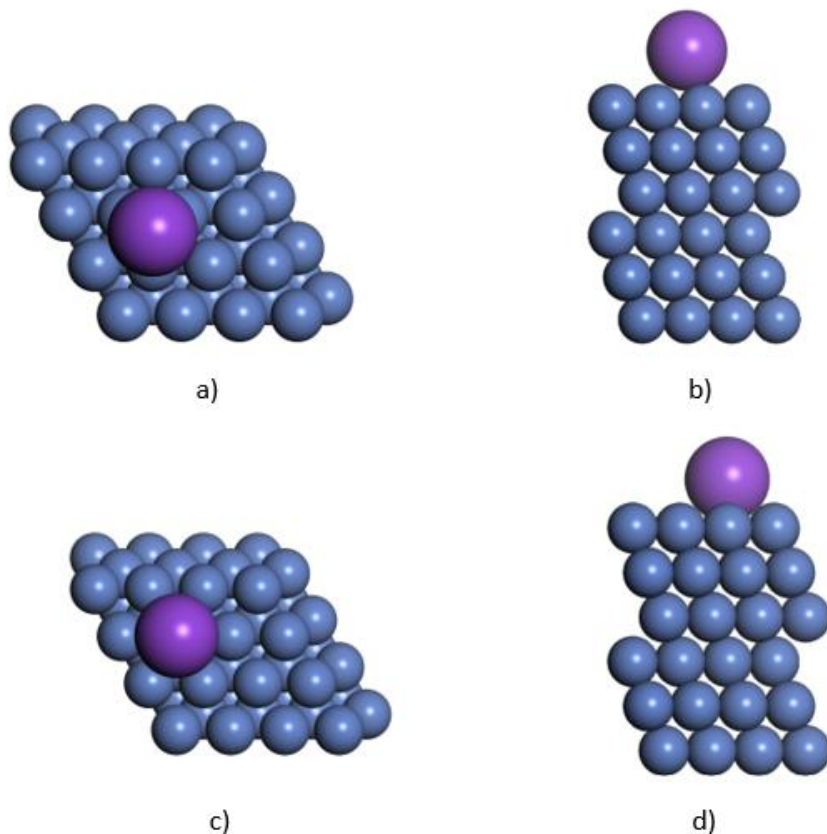


Figure A16: The DFT schematics of potassium-modified Ni(111) systems: a) System 1 - Potassium deposited on Ni(111) (top view), b) System 1 - Potassium deposited on Ni(111) (side view), c) System 2 - Potassium as a substitutional alloy (top view) and d) System 2 - Potassium as a substitutional alloy (side view).

**Table A34. The formation energies of the two different potassium-modified Ni(111) systems**

System name	Total DFT energy (eV)	Ni bulk DFT energy (eV)	Potassium gas-phase DFT energy (eV)	Formation energy (eV)
System 1	-548.30	-573.07	-0.08	24.85
System 2	-541.43	-567.10	-0.08	25.74

Note: The Ni bulk DFT energy is -5.97 eV/atom. There are 96 Ni atoms in system 1, the total Ni bulk energy is estimated as  $\text{Ni}_{\text{bulk}}^{\text{system } 1} = 96 \times -5.97 = -573.07$ . Whereas system 2 consists of 95 Ni atoms, the total Ni bulk energy is calculated as  $\text{Ni}_{\text{bulk}}^{\text{system } 2} = 95 \times -5.97 = -567.10$ .

The potassium can adsorb/bind at several locations on the Ni catalyst surface. We have compared the stabilities of potassium in two different systems: System 1 - Potassium deposited on the Ni(111) facet and System 2 - Potassium as a substitutional alloy. In Figure A16, the DFT configurations of these two systems (top and side views) are illustrated. The formation energies of these two systems have been estimated with reference to Ni bulk and potassium gas-phase energies (by accounting for the stoichiometry). It is evident from Table A34 that the formation energy of system 1 (Potassium deposited on Ni(111)) is lower than system 2 (Potassium as a substitutional alloy). This indicates that the potassium has higher stability in system 1. Therefore, in the current study, we have used system 1 as a model to understand the potassium effect on MSR kinetics.

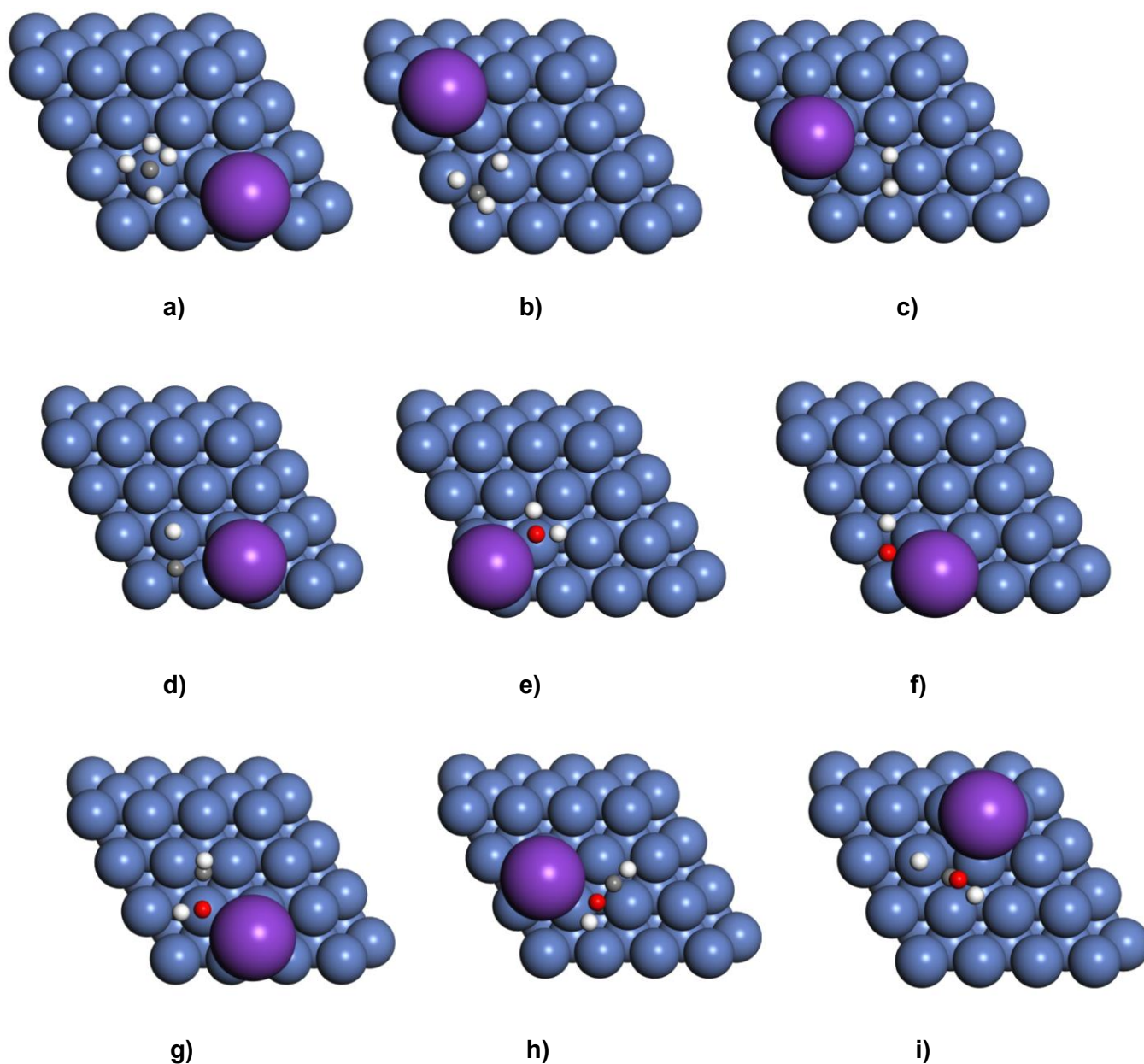


Figure A17: The transition states of MSR elementary events on the K-Ni(111) system: a)  $\text{CH}_4$  dissociation, b)  $\text{CH}_3$  dissociation, c)  $\text{CH}_2$  dissociation, d)  $\text{CH}$  dissociation, e)  $\text{H}_2\text{O}$  dissociation, f)  $\text{OH}$  dissociation, g)  $\text{CHOH}$  formation, h)  $\text{CHOH}$  dissociation to form  $\text{CHO}$  and i)  $\text{CHOH}$  dissociation to form  $\text{COH}$ . The schematics have the following colour convention: 1) blue atoms – Ni, 2) Grey atoms – carbon, 3) White atoms – hydrogen, 4) Red atoms – oxygen.

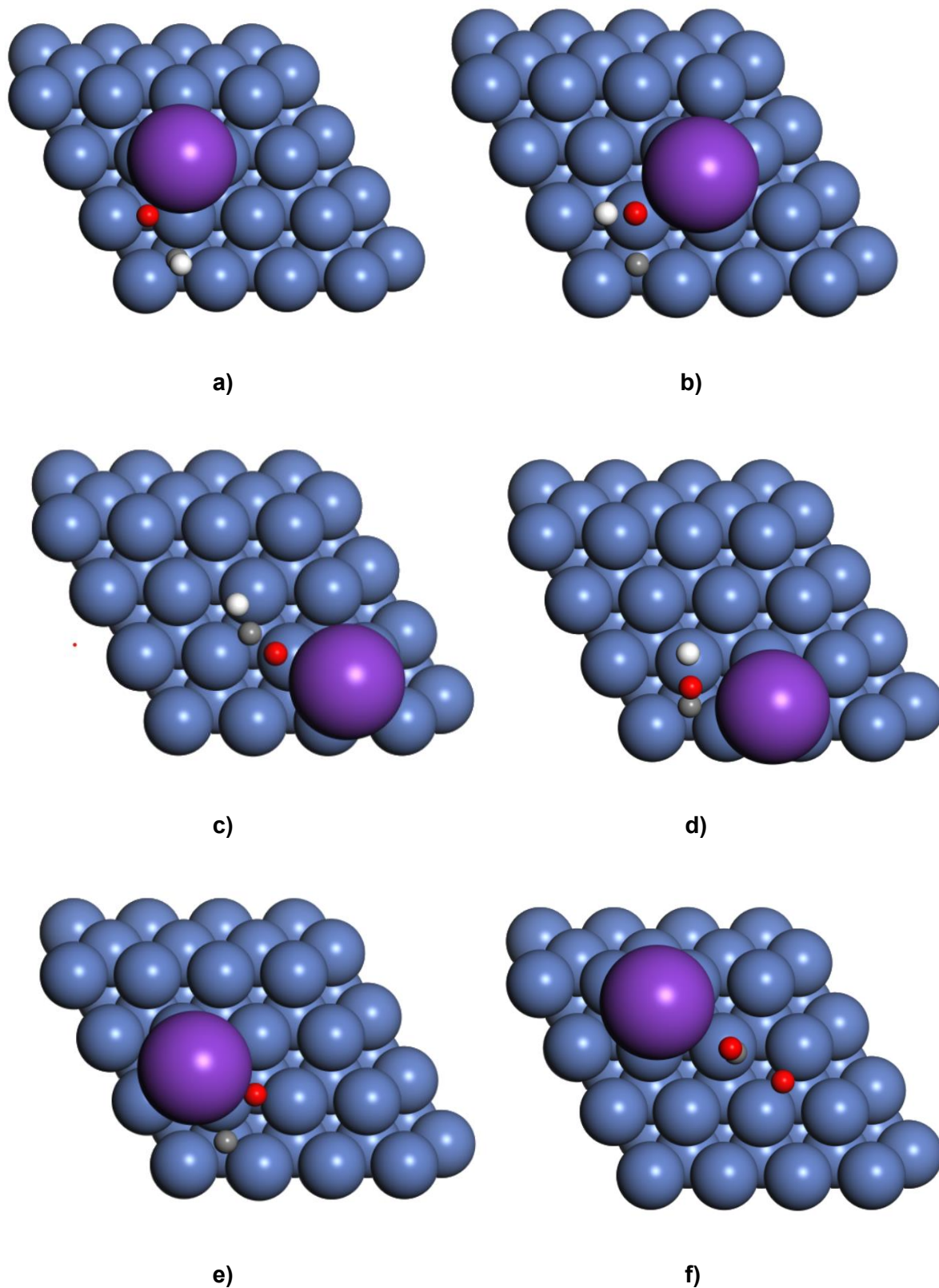


Figure A18: Pictorial representation of MSR transition states on the K-Ni(111) surface: a) CHO formation, b) COH formation, c) CHO dissociation, d) COH dissociation, e) CO formation and f) CO oxidation to CO<sub>2</sub> (g). The schematics have the following colour convention: 1) blue atoms – Ni, 2) Grey atoms – carbon, 3) White atoms – hydrogen, 4) Red atoms – oxygen.

**Table A35. The vibrational wavenumbers of Initial states on Ni(111)**

System	Vibrational wavenumbers (cm <sup>-1</sup> )
CH <sub>3</sub> *	2829.82, 2827.38, 2762.97, 1283.70, 1283.58, 1164.88, 479.00, 478.52, 399.65, 360.89, 224.68, 224.37
CH <sub>2</sub> *	3011.95, 2345.88, 1432.71, 663.32, 591.08, 532.50, 360.08, 310.92, 281.66
CH*	3034.74, 653.72, 653.31, 629.43, 418.55, 418.40
C*	578.52, 541.49, 541.48
H*	1153.17, 865.69, 864.85
H <sub>2</sub> O*	3650.49, 3545.34, 1537.00, 493.15, 481.94, 210.73, 116.24, 90.89, 41.28
OH*	3705.76, 481.28, 480.56, 411.52, 263.77, 263.22
O*	498.55, 389.71, 389.70
CHOH*	3526.63, 2142.43, 1562.24, 1216.68, 1108.95, 660.46, 453.32, 395.98, 291.25, 286.65, 116.80, 104.46
CHO*	2907.28, 1277.83, 1163.23, 621.57, 487.55, 324.75, 252.05, 164.28, 148.66
COH*	3589.47, 1272.10, 1087.30, 445.46, 416.20, 398.87, 153.83, 150.35, 65.96
CO*	1769.07, 350.80, 284.52, 284.30, 143.49, 143.20

**Table A36. The vibrational wavenumbers of Transition states on Ni(111)**

System	Vibrational wavenumbers (cm <sup>-1</sup> )
Event R <sub>1</sub>	3106.68, 3067.01, 2961.02, 1557.96, 1389.54, 1370.72, 1137.45, 841.12, 724.05, 387.74, 377.13, 135.77, 92.29, 38.37, 894.84i
Event R <sub>2</sub>	3009.96, 2516.37, 1852.78, 1368.65, 862.75, 708.71, 537.77, 448.48, 324.80, 267.90, 128.46, 858.09i
Event R <sub>3</sub>	3057.10, 1211.03, 889.96, 675.15, 609.68, 465.91, 414.12, 360.79, 562.25i
Event R <sub>4</sub>	1860.65, 561.77, 523.53, 517.73, 123.78, 812.22i
Event R <sub>7</sub>	3622.61, 810.48, 752.21, 671.10, 423.32, 394.36, 136.18, 100.36, 820.40i
Event R <sub>8</sub>	1077.62, 468.15, 455.31, 290.31, 276.94, 1194.70i
Event R <sub>9</sub>	3611.34, 3055.65, 943.39, 806.06, 593.95, 534.24, 524.69, 429.26, 406.25, 243.63, 92.07, 274.67i
Event R <sub>10</sub>	2876.95, 1270.01, 1183.08, 1026.83, 684.26, 554.19, 438.43, 285.49, 240.05, 153.39, 49.72, 1247.13i
Event R <sub>11</sub>	3582.18, 2012.75, 1236.01, 1141.19, 553.68, 439.59, 403.02, 322.86, 227.73, 207.78, 123.58, 633.01i
Event R <sub>12</sub>	3066.32, 914.10, 675.62, 573.85, 477.81, 417.07, 356.11, 181.75, 502.73i
Event R <sub>13</sub>	3635.34, 756.91, 574.97, 526.04, 450.30, 408.20, 376.07, 60.84, 229.24i
Event R <sub>14</sub>	2442.53, 1395.54, 1049.96, 527.08, 327.88, 273.13, 166.85, 139.32, 312.21i
Event R <sub>15</sub>	1466.36, 1171.89, 496.29, 437.51, 346.31, 314.56, 187.83, 104.21, 1524.23i
Event R <sub>16</sub>	558.67, 510.05, 417.28, 346.94, 83.72, 534.24i
Event R <sub>18</sub>	1917.23, 574.92, 395.21, 392.37, 339.64, 252.86, 73.10, 45.11, 433.84i



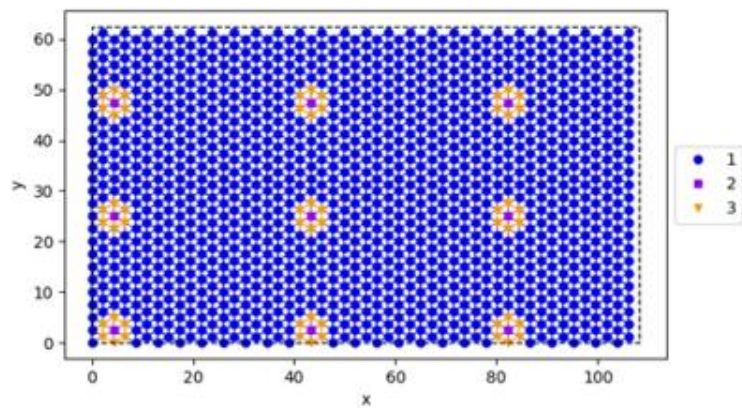
**Table A37. The vibrational wavenumbers of Initial states on K-Ni(111)**

System	Vibrational wavenumbers (cm <sup>-1</sup> )
CH <sub>3</sub> *	2825.86, 2823.92, 2757.49, 1291.88, 1291.17, 1144.04, 493.45, 489.02, 399.33, 346.13, 215.92, 214.91
CH <sub>2</sub> *	2977.52, 2365.15, 1420.11, 666.30, 568.93, 513.81, 377.97, 310.70, 285.28
CH*	2977.92, 668.00, 633.05, 624.37, 425.29, 414.45
C*	572.07, 529.92, 514.27
H*	1147.49, 852.41, 825.15
H <sub>2</sub> O*	3519.68, 3479.24, 1577.90, 484.15, 365.12, 243.25, 139.36, 127.12, 18.84
OH*	3593.07, 697.35, 549.92, 337.70, 202.50, 195.87
O*	473.34, 373.72, 351.32
CHOH*	3421.81, 2396.93, 1432.90, 1189.80, 957.35, 676.13, 504.84, 443.63, 327.73, 269.82, 145.53, 89.60
CHO*	2867.76, 1216.03, 1177.22, 590.33, 485.77, 289.29, 269.76, 197.47, 159.32
COH*	3595.05, 1174.53, 1069.70, 474.06, 442.53, 395.13, 184.38, 168.82, 89.77
CO*	1628.71, 373.93, 345.54, 337.69, 185.64, 153.38

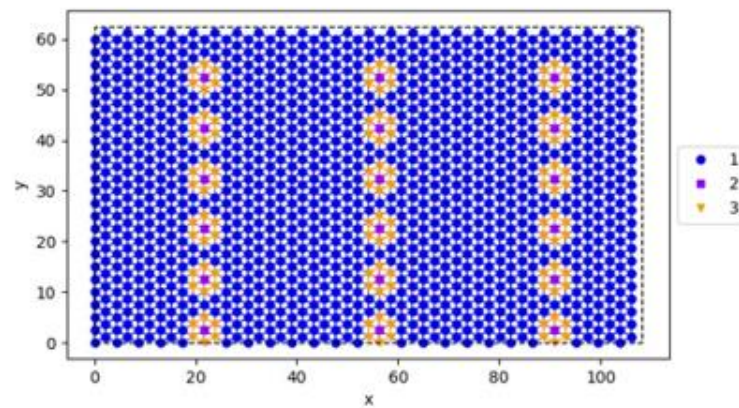


**Table A38. The vibrational wavenumbers of Transition states of MSR reaction on K-Ni(111)**

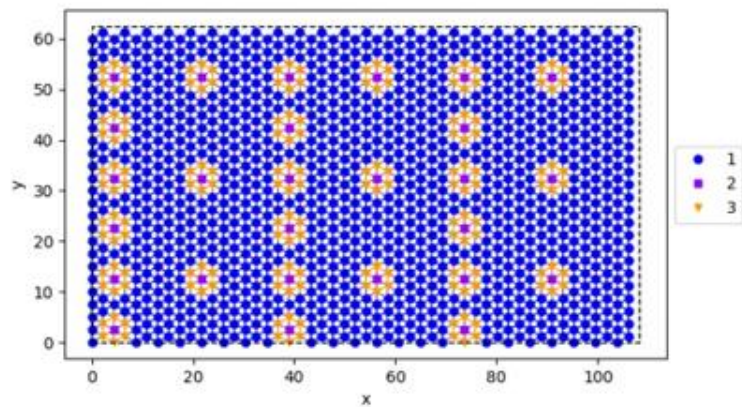
System	Vibrational wavenumbers (cm <sup>-1</sup> )
Event R <sub>1</sub>	3080.09, 3046.63, 2948.71, 1587.58, 1391.36, 1375.08, 1109.89, 832.58, 715.94, 377.33, 336.20, 136.82, 108.66, 94.15, 940.91i
Event R <sub>2</sub>	2991.41, 2508.20, 1784.59, 1372.26, 852.78, 717.45, 532.42, 453.22, 320.80, 247.95, 114.08, 918.96i
Event R <sub>3</sub>	3031.84, 1211.51, 891.76, 669.08, 605.30, 484.13, 409.81, 360.38, 543.24i
Event R <sub>4</sub>	1829.99, 544.63, 513.93, 484.07, 168.36, 807.37i
Event R <sub>7</sub>	3619.40, 866.37, 820.51, 593.52, 380.91, 269.38, 225.53, 154.22, 998.75i
Event R <sub>8</sub>	1072.28, 512.07, 424.29, 267.48, 248.09, 1197.89i
Event R <sub>9</sub>	3621.51, 3025.16, 994.68, 842.29, 561.19, 524.56, 504.42, 437.46, 290.74, 198.26, 153.33, 278.12i
Event R <sub>10</sub>	2880.13, 1211.68, 1166.09, 994.56, 690.75, 587.57, 485.21, 300.90, 271.27, 183.55, 93.70, 1325.01i
Event R <sub>11</sub>	3553.58, 1985.75, 1209.85, 1046.26, 551.88, 462.75, 420.85, 376.80, 265.85, 203.19, 155.87, 663.03i
Event R <sub>12</sub>	3036.61, 910.25, 659.99, 571.38, 443.79, 402.58, 317.42, 228.97, 442.94i
Event R <sub>13</sub>	3670.28, 747.49, 590.06, 528.74, 442.86, 408.28, 267.77, 199.16, 168.96i
Event R <sub>14</sub>	2535.83, 1315.44, 1089.83, 498.53, 343.09, 257.66, 175.32, 142.37, 339.16i
Event R <sub>15</sub>	1358.88, 1145.91, 545.87, 453.98, 374.29, 364.51, 196.94, 153.45, 1554.67i
Event R <sub>16</sub>	557.96, 473.74, 434.08, 328.45, 296.60, 422.93i
Event R <sub>18</sub>	1815.58, 548.99, 406.33, 374.96, 346.85, 280.61, 93.62, 51.07, 401.66i



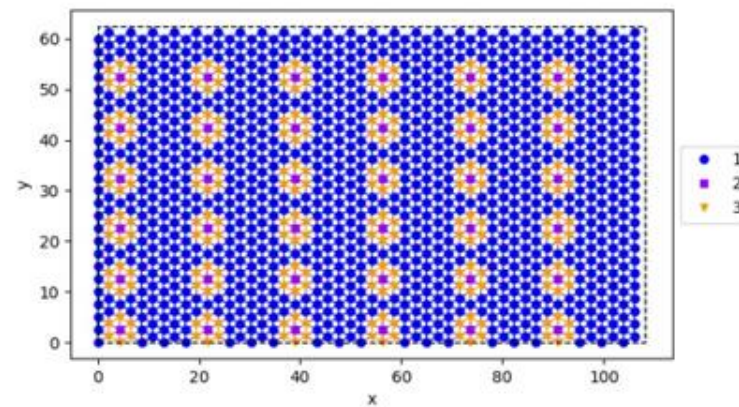
a)



b)



c)



d)

Figure A19: The KMC lattice snapshots of the K-Ni(111) systems with varying potassium loadings: a) K-Ni(111)-0.7%, b) K-Ni(111)-1.4%, c) K-Ni(111)-2.1% and d) K-Ni(111)-2.8%. The KMC lattice has been colour coded as follows: 1) Circular Sites in blue represent Ni, 2) Purple square sites indicate potassium (inactive) and 3) Potassium-modified sites are the orange-coloured triangles. The MSR reaction is occurring on the Ni and potassium-modified sites.

**Table A39. KMC lattice convergence test of the Ni(111) system at 1073 K, 10.00 bar CH<sub>4</sub> (g) and 0.01 bar H<sub>2</sub> (g) (H<sub>2</sub>O-CH<sub>4</sub> ratio is maintained at 2:1)**

KMC lattice size	CH coverage (ML)	Carbon coverage (ML)	Turnover rate (molecules sites <sup>-1</sup> s <sup>-1</sup> )
25x25	0.20	0.10	2.65 × 10 <sup>4</sup>
30x30	0.19	0.09	3.21 × 10 <sup>4</sup>
35x35	0.19	0.10	2.87 × 10 <sup>4</sup>
40x40	0.20	0.10	2.54 × 10 <sup>4</sup>

**Table A40. Comparison between KMC predictions and experimental results at 873 K**

CH <sub>4</sub> (g) pressure (bar)	H <sub>2</sub> O (g) pressure (bar)	KMC predicted rates (mol g <sup>-1</sup> s <sup>-1</sup> )	Experimental rates (mol g <sup>-1</sup> s <sup>-1</sup> )
1.4	1.0	0.017	20.000
1.6	1.0	0.019	23.000
2	2.0	0.063	34.000
2.5	2.0	0.047	39.000
3	3.0	0.071	50.000
3.5	3.0	0.117	63.000

Note: The experimental rates have been obtained from the work of Wei and Iglesia.<sup>14</sup> Appropriate unit conversions have been made to the KMC predicted rates in order to make a reliable comparison to the experimental data.

As shown in Table A40, the KMC predicted rates on Ni(111) are around 500-1000 times slower than the experimental rates. This is an expected outcome as the experimental work of Wei and Iglesia<sup>14</sup> has been carried out on Ni/MgO catalyst. The KMC model developed in this study does not take into account the undercoordinated surfaces of Ni (step edge and flat). Furthermore, the effect of metal support interaction is also neglected in the KMC simulation. Thus, we find a substantial disparity in the KMC and experimental rates. In the literature, the MSR rates predicted using MK models (on the Ni(111) facet) also report a similar disagreement with experimental results.<sup>6</sup> As part of future studies, a multifaceted KMC model can be developed for MSR on Ni to obtain better agreement with experimental rates.

**Table A41. Effective cluster interaction (ECI) values of pairwise sub-patterns on Ni(111) and K-Ni(111)**

Co-adsorbed system	ECI value Ni(111)	ECI value K-Ni(111)
CH-CH <sub>3</sub>	0.31	0.31
CH-CH <sub>2</sub>	0.20	0.19
CH-CH	0.26	0.21
CH-C	0.28	0.31
CH-O	0.27	0.29
CH-OH	0.29	0.16
CH-H	0.06	0.07
CH-CHO	0.18	0.12
CH-COH	0.16	0.19
CH-CO	0.14	0.15
CH-H <sub>2</sub> O	0.02	0.01
C-CH <sub>3</sub>	0.34	0.31
C-CH <sub>2</sub>	0.27	0.26
C-C	0.38	0.46
C-OH	0.32	0.24
C-O	0.34	0.41
C-H	0.13	0.13
C-CHO	0.20	0.29
C-COH	0.21	0.27
C-H <sub>2</sub> O	0.06	-0.006
C-CO	0.25	0.25
H-CH <sub>3</sub>	0.08	0.09
H-CH <sub>2</sub>	0.07	0.06
H-OH	0.10	0.04
H-O	0.12	0.11
H-H	0.003	-0.009
H-CO	0.03	0.01
H-CHO	0.01	-0.01
H-COH	0.06	0.03
O-CH <sub>3</sub>	5.00	5.00
O-CH <sub>2</sub>	0.23	0.25
O-COH	0.12	0.31
O-CO	0.33	0.28
O-O	0.36	0.41
O-OH	0.23	0.21
O-CHO	0.22	5.00
C-CHOH	0.19	0.19
CH-CHOH	0.17	0.01
O-CHOH	0.26	0.23

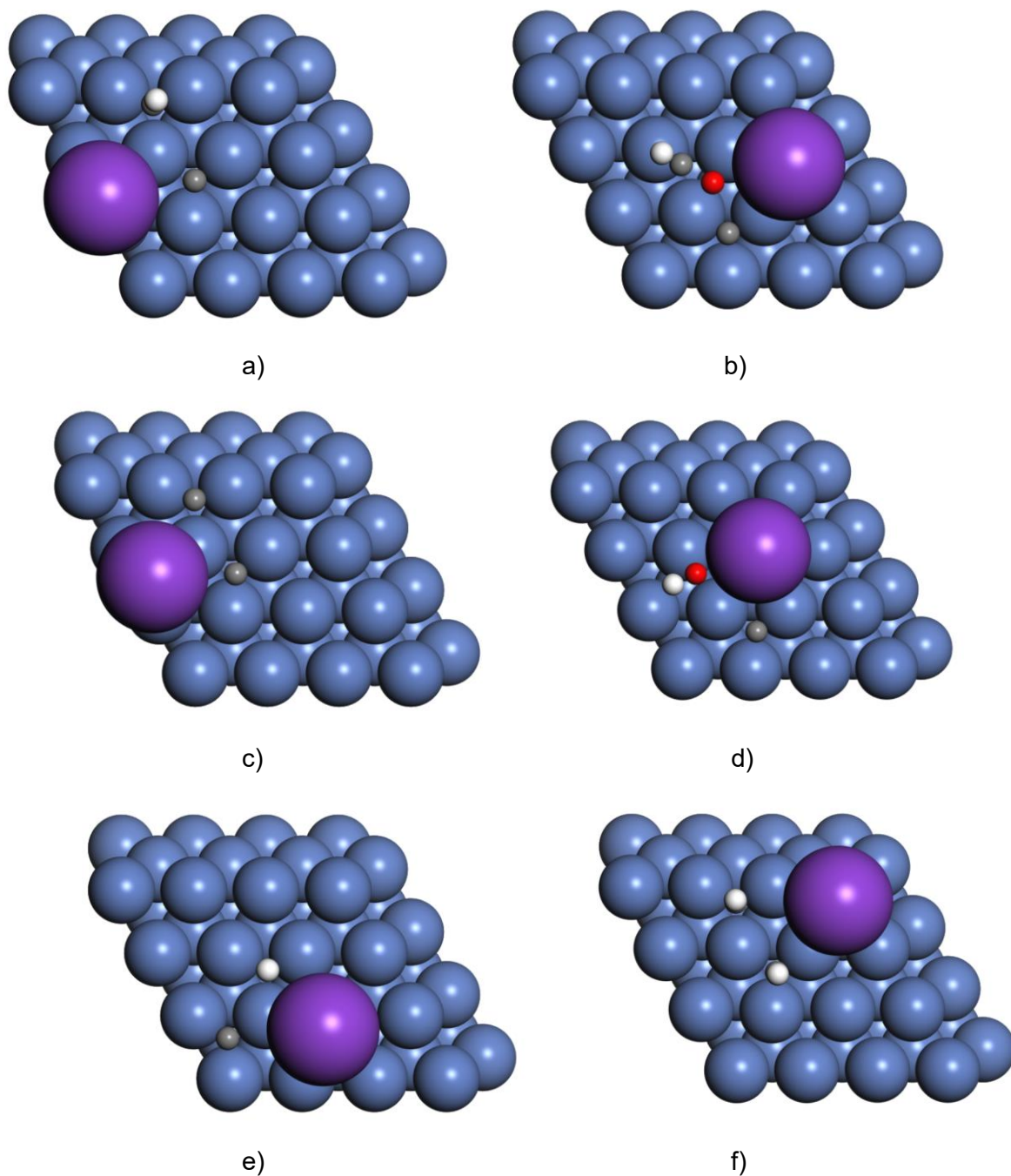


Figure A20: The DFT configurations of co-adsorbed (pairwise) species on the K-Ni(111) system: a) C-CH pair, b) C-CHO pair, c) C-C pair, d) C-OH pair, e) C-H pair and f) CH-CH pair. The schematics have the following colour convention: 1) blue atoms – Ni, 2) Purple atoms – K, 3) Grey atoms – carbon, 4) White atoms – hydrogen, 5) Red atoms – oxygen.

**Table A42. The partial equilibrium (PE) ratios of MSR events on the Ni(111) and K-Ni(111)-2.8% systems at 1273 K and 10.00 bar (H<sub>2</sub>O-CH<sub>4</sub> ratio is maintained at 2:1)**

Event ID: elementary step	PE ratio – pure Ni(111)	PE ratio – Ni sites K-Ni(111)-2.8%	PE ratio – K sites K-Ni(111)-2.8%
R <sub>1</sub> : CH <sub>4</sub> (g) + 2* ↔ CH <sub>3</sub> * + H*	0.87	0.85	0.86
R <sub>2</sub> : CH <sub>3</sub> * + * ↔ CH <sub>2</sub> * + H*	0.56	0.60	0.56
R <sub>3</sub> : CH <sub>2</sub> * + * ↔ CH* + H*	0.50	0.50	0.50
R <sub>4</sub> : CH* + * ↔ C* + H*	0.50	0.50	0.50
R <sub>5</sub> : 2H* → H <sub>2</sub> (g) + 2*	1.00	1.00	1.00
R <sub>6</sub> : H <sub>2</sub> O(g) + * ↔ H <sub>2</sub> O*	0.50	0.50	0.50
R <sub>7</sub> : H <sub>2</sub> O* + * ↔ OH* + H*	0.92	0.91	0.63
R <sub>8</sub> : OH* + * ↔ O* + H*	0.59	0.53	0.53
R <sub>9</sub> : CH* + OH* ↔ CHOH* + *	1.00	1.00	1.00
R <sub>10</sub> : CHOH* + * ↔ CHO* + H*	Not defined	Not defined	1.00
R <sub>11</sub> : CHOH* + * ↔ COH* + H*	0.96	0.84	0.90
R <sub>12</sub> : CH* + O* ↔ CHO* + *	1.00	1.00	1.00
R <sub>13</sub> : C* + OH* ↔ COH* + *	1.00	1.00	1.00
R <sub>14</sub> : CHO* + * ↔ CO* + H*	1.00	1.00	1.00
R <sub>15</sub> : COH* + * ↔ CO* + H*	1.00	1.00	1.00
R <sub>16</sub> : C* + O* ↔ CO* + *	1.00	1.00	1.00
R <sub>17</sub> : CO* → CO(g) + *	1.00	1.00	1.00
R <sub>18</sub> : CO* + O* → CO <sub>2</sub> (g) + 2*	1.00	1.00	1.00

**Table A43. The forward/reverse pre-exponential values of MSR events on the K-Ni(111)-2.8% system at 1273 K and 10.00 bar (H<sub>2</sub>O-CH<sub>4</sub> ratio is maintained at 2:1)**

Event ID: elementary step	Pre-exp fwd (s <sup>-1</sup> )	Pre-exp rev (s <sup>-1</sup> )	Pre-exp fwd (s <sup>-1</sup> )	Pre-exp rev (s <sup>-1</sup> )
	Ni sites	Ni sites	K sites	K sites
	K- Ni(111)	K- Ni(111)	K- Ni(111)	K- Ni(111)
R <sub>1</sub> : CH <sub>4</sub> (g) + 2* ↔ CH <sub>3</sub> * + H*	2.60 × 10 <sup>8</sup>	3.57 × 10 <sup>14</sup>	1.09 × 10 <sup>8</sup>	1.28 × 10 <sup>14</sup>
R <sub>2</sub> : CH <sub>3</sub> * + * ↔ CH <sub>2</sub> * + H*	9.22 × 10 <sup>13</sup>	5.00 × 10 <sup>13</sup>	1.11 × 10 <sup>14</sup>	5.92 × 10 <sup>13</sup>
R <sub>3</sub> : CH <sub>2</sub> * + * ↔ CH* + H*	2.73 × 10 <sup>13</sup>	4.07 × 10 <sup>13</sup>	2.66 × 10 <sup>13</sup>	3.62 × 10 <sup>13</sup>
R <sub>4</sub> : CH* + * ↔ C* + H*	1.67 × 10 <sup>14</sup>	1.22 × 10 <sup>14</sup>	1.35 × 10 <sup>14</sup>	8.81 × 10 <sup>13</sup>
R <sub>5</sub> : 2H* → H <sub>2</sub> (g) + 2*	5.14 × 10 <sup>15</sup>	0.00	4.44 × 10 <sup>15</sup>	0.00
R <sub>6</sub> : H <sub>2</sub> O(g) + * ↔ H <sub>2</sub> O*	1.94 × 10 <sup>8</sup>	4.85 × 10 <sup>13</sup>	1.94 × 10 <sup>9</sup>	2.92 × 10 <sup>14</sup>
R <sub>7</sub> : H <sub>2</sub> O* + * ↔ OH* + H*	7.37 × 10 <sup>12</sup>	2.09 × 10 <sup>14</sup>	2.75 × 10 <sup>12</sup>	8.86 × 10 <sup>13</sup>
R <sub>8</sub> : OH* + * ↔ O* + H*	7.21 × 10 <sup>13</sup>	1.16 × 10 <sup>14</sup>	6.34 × 10 <sup>13</sup>	1.05 × 10 <sup>14</sup>
R <sub>9</sub> : CH* + OH* ↔ CHOH* + *	1.91 × 10 <sup>13</sup>	9.76 × 10 <sup>12</sup>	1.40 × 10 <sup>13</sup>	1.22 × 10 <sup>13</sup>
R <sub>10</sub> : CHOH* + * ↔ CHO* + H*	2.38 × 10 <sup>14</sup>	1.91 × 10 <sup>14</sup>	9.94 × 10 <sup>13</sup>	6.68 × 10 <sup>13</sup>
R <sub>11</sub> : CHOH* + * ↔ COH* + H*	3.51 × 10 <sup>13</sup>	7.15 × 10 <sup>12</sup>	2.67 × 10 <sup>13</sup>	7.80 × 10 <sup>12</sup>
R <sub>12</sub> : CH* + O* ↔ CHO* + *	2.29 × 10 <sup>13</sup>	5.84 × 10 <sup>12</sup>	1.88 × 10 <sup>13</sup>	6.64 × 10 <sup>12</sup>
R <sub>13</sub> : C* + OH* ↔ COH* + *	3.64 × 10 <sup>13</sup>	5.16 × 10 <sup>12</sup>	1.03 × 10 <sup>13</sup>	4.02 × 10 <sup>12</sup>
R <sub>14</sub> : CHO* + * ↔ CO* + H*	2.28 × 10 <sup>13</sup>	5.80 × 10 <sup>12</sup>	2.39 × 10 <sup>13</sup>	1.01 × 10 <sup>13</sup>
R <sub>15</sub> : COH* + * ↔ CO* + H*	3.72 × 10 <sup>13</sup>	3.73 × 10 <sup>13</sup>	3.48 × 10 <sup>13</sup>	3.38 × 10 <sup>13</sup>
R <sub>16</sub> : C* + O* ↔ CO* + *	1.15 × 10 <sup>14</sup>	1.02 × 10 <sup>13</sup>	2.66 × 10 <sup>13</sup>	6.07 × 10 <sup>12</sup>
R <sub>17</sub> : CO* → CO(g) + *	2.07 × 10 <sup>16</sup>	0.00	4.00 × 10 <sup>16</sup>	0.00
R <sub>18</sub> : CO* + O* → CO <sub>2</sub> (g) + 2*	4.72 × 10 <sup>13</sup>	0.00	5.19 × 10 <sup>13</sup>	0.00

### A 3.1 Flux analysis for a typical reaction

The flux analysis for a generic reaction network. The symbol  $r$  (in Figure A21) is the net occurrence rate of an elementary step.

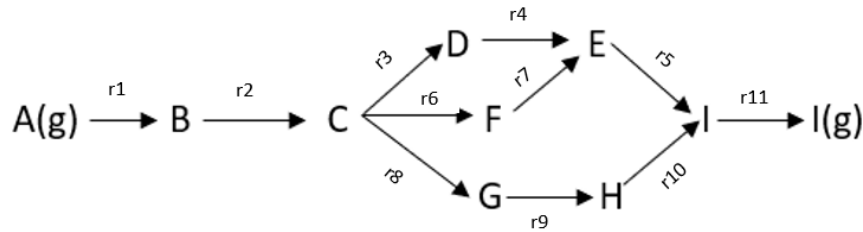


Figure A21: The reaction network for the formation product  $I(g)$  from  $A(g)$ . The above reaction has been used as a generic example to explain the flux analysis method.

Upon reaching the steady state, the rate of coverage change of all intermediate species is zero.  $\theta$  represents the fractional coverage of species (it is normalised with respect to the total number of sites).

$$\frac{d\theta_B}{dt} = r_1 - r_2 = 0 \quad \text{eqA. 1}$$

$$\frac{d\theta_C}{dt} = r_3 + r_6 + r_8 - r_2 = 0 \quad \text{eqA. 2}$$

$$\frac{d\theta_D}{dt} = r_4 - r_3 = 0 \quad \text{eqA. 3}$$

$$\frac{d\theta_E}{dt} = r_5 - r_4 - r_7 = 0 \quad \text{eqA. 4}$$

$$\frac{d\theta_F}{dt} = r_7 - r_6 = 0 \quad \text{eqA. 5}$$

$$\frac{d\theta_G}{dt} = r_9 - r_8 = 0 \quad \text{eqA. 6}$$

$$\frac{d\theta_H}{dt} = r_{10} - r_9 = 0 \quad \text{eqA. 7}$$

$$\frac{d\theta_I}{dt} = r_{11} - r_5 - r_{10} = 0 \quad \text{eqA. 8}$$

The following equations are derived from the above conditions:

$$r_1 = r_2 \quad \text{eqA. 9}$$

$$r_2 = r_3 + r_6 + r_8 \quad \text{eqA. 10}$$

$$r_3 = r_4 \quad \text{eqA. 11}$$

$$r_2 = r_3 + r_6 + r_8 \quad \text{eqA. 12}$$



$$r_3 = r_4 \quad \text{eqA. 13}$$

$$r_5 = r_4 + r_7 \quad \text{eqA. 14}$$

$$r_6 = r_7 \quad \text{eqA. 15}$$

$$r_8 = r_9 \quad \text{eqA. 16}$$

$$r_9 = r_{10} \quad \text{eqA. 17}$$

$$r_{11} = r_5 + r_{10} \quad \text{eqA. 18}$$

In the current reaction network, there are three pathways to form the species I (which are shown below):



Figure A22: Pictorial representation of the different pathways of a generic reaction network.

The overall flux to form species I is given by the following relationship:

$$r_{total} = r_{11} = r_5 + r_{10} \quad \text{eqA. 19}$$

The flux contribution of pathway 1 to the overall rate to form species I is estimated as follows:

$$r_3 = r_4 = r_{pathway1} \quad \text{eqA. 20}$$

$$Flux_{pathway1} (\%) = \frac{r_{pathway1} \times 100}{r_{total}} = \frac{r_3 \times 100}{r_5 + r_{10}} = \frac{r_4 \times 100}{r_5 + r_{10}} \quad \text{eqA. 21}$$

The flux contribution of pathway 2 to the overall rate to form species I is computed as follows:

$$r_6 = r_7 = r_{pathway2} \quad \text{eqA. 22}$$

$$Flux_{pathway2} (\%) = \frac{r_{pathway2} \times 100}{r_{total}} = \frac{r_6 \times 100}{r_5 + r_{10}} = \frac{r_7 \times 100}{r_5 + r_{10}} \quad \text{eqA. 23}$$

The flux contribution of pathway 3 to the overall rate to form species I is calculated as follows:

$$r_8 = r_9 = r_{10} = r_{pathway3} \quad \text{eqA. 24}$$

$$Flux_{pathway3} (\%) = \frac{r_{pathway3} \times 100}{r_{total}} = \frac{r_8 \times 100}{r_5 + r_{10}} = \frac{r_9 \times 100}{r_5 + r_{10}} = \frac{r_{10} \times 100}{r_5 + r_{10}} \quad \text{eqA. 25}$$

### A 3.2 Flux analysis of MSR reaction on Ni(111)

In Chapter 5, the flow diagram and event IDs of MSR have been depicted in Figure 20 and Table 8, respectively. At steady-state conditions, the rate of coverage change of all MSR intermediates is zero. The symbol  $r$  (in equations below) indicates the overall occurrence rate of an elementary event. The suffix of symbol  $r$  has been numbered based on the event ID of MSR steps (as shown in Table 8 of Chapter 5). The diffusion events are assumed to be quasi-equilibrated. Thus, the net occurrence rates of all diffusions are zero.  $\theta$  represents the fractional coverage of species (it is normalised with respect to total number of sites of the KMC lattice).

$$\frac{d\theta_{fcc}}{dt} = -2r_1 - r_2 - r_3 - r_4 + 2r_5 - r_6 - r_7 - r_8 + r_9 - r_{10} - r_{11} + r_{12} + r_{13} \quad \text{eqA. 26}$$

$$- r_{14} - r_{15} + r_{16} + r_{17} + 2r_{18} = 0$$

$$\frac{d\theta_{CH3}}{dt} = r_1 - r_2 = 0 \quad \text{eqA. 27}$$

$$\frac{d\theta_{CH2}}{dt} = r_2 - r_3 = 0 \quad \text{eqA. 28}$$

$$\frac{d\theta_{CH}}{dt} = r_3 - r_4 - r_9 - r_{12} = 0 \quad \text{eqA. 29}$$

$$\frac{d\theta_C}{dt} = r_4 - r_{13} - r_{16} = 0 \quad \text{eqA. 30}$$

$$\frac{d\theta_H}{dt} = r_1 + r_2 + r_3 + r_4 - 2r_5 + r_7 + r_8 + r_{10} + r_{11} + r_{14} + r_{15} = 0 \quad \text{eqA. 31}$$

$$\frac{d\theta_{H2O}}{dt} = r_6 - r_7 = 0 \quad \text{eqA. 32}$$

$$\frac{d\theta_{OH}}{dt} = r_7 - r_8 - r_9 - r_{13} = 0 \quad \text{eqA. 33}$$

$$\frac{d\theta_O}{dt} = r_8 - r_{12} - r_{16} - r_{18} = 0 \quad \text{eqA. 34}$$

$$\frac{d\theta_{CHOH}}{dt} = r_9 - r_{10} - r_{11} = 0 \quad \text{eqA. 35}$$

$$\frac{d\theta_{CHO}}{dt} = r_{10} + r_{12} - r_{14} = 0 \quad \text{eqA. 36}$$

$$\frac{d\theta_{COH}}{dt} = r_{11} + r_{13} - r_{15} = 0 \quad \text{eqA. 37}$$

$$\frac{d\theta_{CO}}{dt} = r_{14} + r_{15} + r_{16} - r_{17} - r_{18} = 0 \quad \text{eqA. 38}$$

From the above differential equations, the following relationships exist at steady state:

$$r_1 = r_2 \quad \text{eqA. 39}$$

$$r_2 = r_3 \quad \text{eqA. 40}$$

$$r_3 = r_4 + r_9 + r_{12} \quad \text{eqA. 41}$$

$$r_4 = r_{13} + r_{16} \quad \text{eqA. 42}$$

$$r_6 = r_7 \quad \text{eqA. 43}$$

$$r_7 = r_8 + r_9 + r_{13} \quad \text{eqA. 44}$$

$$r_8 = r_{12} + r_{16} + r_{18} \quad \text{eqA. 45}$$

$$r_9 = r_{10} + r_{11} \quad \text{eqA. 46}$$

$$r_{14} = r_{10} + r_{12} \quad \text{eqA. 47}$$

$$r_{15} = r_{11} + r_{13} \quad \text{eqA. 48}$$

$$r_{14} + r_{15} + r_{16} = r_{17} + r_{18} \quad \text{eqA. 49}$$

Upon reaching the steady state in KMC simulations, we check if the above relationships are satisfied using the event frequencies obtained from the KMC process statistics data. Using the aforementioned relationships, we can derive the following:

$$r_1 = r_3 = r_4 + r_9 + r_{12} \quad \text{eqA. 50}$$

$$r_1 = r_4 + r_{10} + r_{11} + r_{12} \quad \text{eqA. 51}$$

$$r_1 = r_4 + r_{14} + r_{11} \quad \text{eqA. 52}$$

$$r_1 = r_{13} + r_{16} + r_{14} + r_{11} \quad \text{eqA. 53}$$

$$r_1 = r_{14} + r_{15} + r_{16} \quad \text{eqA. 54}$$

$$r_1 = r_{14} + r_{15} + r_{16} = r_{COspec}^{prod} \quad \text{eqA. 55}$$

The overall flux to form CO species ( $r_{COspec}^{prod}$ ) on the Ni(111) surface, which is the main intermediate of all the MSR pathways, is given by eqA. 55.

There are totally five MSR pathways – the routes are shown in Figure A23.

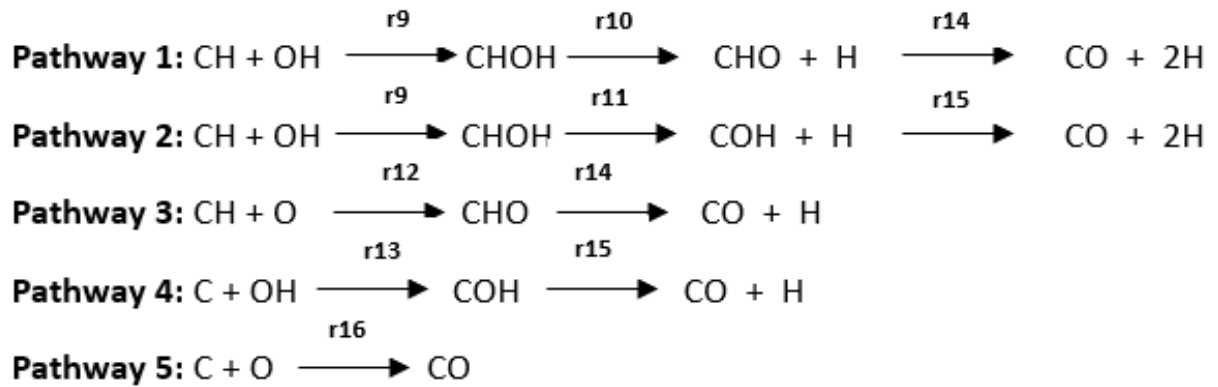


Figure A23: Pictorial representation of the different MSR pathways: Pathway 1 – CHOH pathway via CHO intermediate, Pathway 2 - CHOH pathway via COH intermediate, Pathway 3 - CHO pathway, Pathway 4 – COH pathway, 5) Pathway 5 – CO pathway.

The flux contributions of the different MSR pathways (depicted in Figure A23) are estimated using the equations below.

$$Flux_{\text{pathway1}} (\%) = \frac{r_{\text{pathway1}} \times 100}{r_{\text{COspec}}^{\text{prod}}} = \frac{r_{10} \times 100}{r_{14} + r_{15} + r_{16}} \quad \text{eqA. 56}$$

$$Flux_{\text{pathway2}} (\%) = \frac{r_{\text{pathway2}} \times 100}{r_{\text{COspec}}^{\text{prod}}} = \frac{r_{11} \times 100}{r_{14} + r_{15} + r_{16}} \quad \text{eqA. 57}$$

$$Flux_{\text{pathway3}} (\%) = \frac{r_{\text{pathway3}} \times 100}{r_{\text{COspec}}^{\text{prod}}} = \frac{r_{12} \times 100}{r_{14} + r_{15} + r_{16}} \quad \text{eqA. 58}$$

$$Flux_{\text{pathway4}} (\%) = \frac{r_{\text{pathway4}} \times 100}{r_{\text{COspec}}^{\text{prod}}} = \frac{r_{13} \times 100}{r_{14} + r_{15} + r_{16}} \quad \text{eqA. 59}$$

$$Flux_{\text{pathway5}} (\%) = \frac{r_{\text{pathway5}} \times 100}{r_{\text{COspec}}^{\text{prod}}} = \frac{r_{16} \times 100}{r_{14} + r_{15} + r_{16}} \quad \text{eqA. 60}$$

For the K-Ni(111)-2.8% system, we follow a similar procedure to obtain the pathway contributions (%).

### A 3.3 Calculation of thermal/entropic contributions and free energies

We have used the ASE thermochemistry module to estimate the thermal, entropic and free energies of gas-phase molecules/adsorbates. The ASE thermochemistry module uses the equations of the textbook “Essentials of Computational Chemistry” (Chapter 10) by C.J Cramer. The thermal energy of gas-phase species is computed using eqA. 61.

$$H_{gas} = \frac{N_{trans}}{2} k_B T + \frac{N_{rot}}{2} k_B T + \sum_k^{3N-N_{trans}-N_{rot}} \frac{h v_k}{\exp\left(\frac{h v_k}{k_B T}\right) - 1} + k_B T \quad \text{eqA. 61}$$

In eqA. 61,  $N_{trans}$  indicates the number of translational modes,  $N_{rot}$  is the number of rotational modes,  $v_k$  represents the vibrational frequency of any  $k^{\text{th}}$  mode and  $T$  is the temperature. For any gas-phase species,  $N_{trans}$  takes the value 3. In the case of monoatomic gas-phase species,  $N_{rot}$  value is 0. The  $N_{rot}$  values for linear and non-linear gas-phase molecules are 2 and 3, respectively.

The total entropic contribution of gas-phase species is calculated by using eqA. 62. The translational component of the entropic contribution is provided by eqA. 63.

$$S_{gas} = S_{trans} + S_{rot} + S_{vib} + S_{elec} - k_B \log_e \frac{P}{P^o} \quad \text{eqA. 62}$$

$$S_{trans} = k_B \left( \log_e \left( \frac{(2\pi m k_B T)^{\frac{3}{2}}}{h^3} \frac{k_B T}{P^o} \right) + \frac{5}{2} \right) \quad \text{eqA. 63}$$

In eqA. 62 and eqA. 63,  $P^o$  is the standard pressure (in bar) and  $m$  is the mass of the molecule. In the case of a monoatomic gas, the rotational component of the entropy is zero. The rotational components of the entropies of linear and non-linear molecules are computed using eqA. 64 and eqA. 65, respectively.

$$S_{rot} = k_B \left( \log_e \left( \frac{8\pi^2 I k_B T}{\sigma h^2} \right) + 1 \right) \quad \text{eqA. 64}$$

$$S_{rot} = k_B \left( \log_e \left( \frac{\sqrt{\pi I_A I_B I_C}}{\sigma} \left( \frac{8\pi^2 k_B T}{h^2} \right)^{\frac{3}{2}} \right) + \frac{3}{2} \right) \quad \text{eqA. 65}$$

$$S_{vib} = k_B \sum_i^{DOF_{vib}} \left( \frac{h v_i}{k_B T \left( \exp\left(\frac{h v_i}{k_B T}\right) - 1 \right)} - \log_e \left( 1 - \exp\left(-\frac{h v_i}{k_B T}\right) \right) \right) \quad \text{eqA. 66}$$

$$S_{elec} = k_B \log_e (2S_{spin} + 1) \quad \text{eqA. 67}$$

In eqA. 64 and eqA. 65, the symbols  $I$  and  $\sigma$  indicate the moment of inertia and symmetry factor, respectively. The vibrational component of the entropy is given by eqA. 66. For ground state with higher spin multiplicity, the electronic component of the entropy ( $S_{elec}$ ) is estimated. We use eqA. 67 to compute  $S_{elec}$ , where  $S_{spin}$  indicates the spin multiplicity. For instance, for a doublet, the value of  $S_{spin}$  is 0.5. On the other hand, in the case of a triplet,  $S_{spin}$  takes the value 1.

The harmonic approximation is employed to estimate the thermal/entropic contributions of species adsorbed on the Ni(111) surface. The frustrated translations/rotations of adsorbates are treated as vibrations. The thermal contribution of an adsorbate with  $N$  atoms is given by eqA. 68 (the “PV” term is negligible in this case). We use eqA. 69 to calculate the entropic contribution of an adsorbate.

$$H_{adsorbate} = \sum_k^{3N} \frac{h v_k}{\exp\left(\frac{h v_k}{k_B T}\right) - 1} \quad \text{eqA. 68}$$

$$S_{adsorbate} = k_B \sum_i^{3N} \left( \frac{h v_i}{k_B T \left( \exp\left(\frac{h v_i}{k_B T}\right) - 1 \right)} - \log_e \left( 1 - \exp\left(-\frac{h v_i}{k_B T}\right) \right) \right) \quad \text{eqA. 69}$$

**Table A44. KMC replicas of the Ni(111) system at 1273 K and 10.00 bar (H<sub>2</sub>O-CH<sub>4</sub> ratio is maintained at 2:1)**

KMC runs	CH coverage (ML)	Carbon coverage (ML)	Turnover rate (molecules sites <sup>-1</sup> s <sup>-1</sup> )
Random seed 1	0.1266	0.1872	-6.57 × 10 <sup>4</sup>
Random seed 2	0.1266	0.1877	-6.38 × 10 <sup>4</sup>
Random seed 3	0.1257	0.1837	-6.97 × 10 <sup>4</sup>
Random seed 4	0.1263	0.1878	-6.22 × 10 <sup>4</sup>
Random seed 5	0.1262	0.1873	-6.27 × 10 <sup>4</sup>
Average values	0.1263 (±0.0004)	0.1867 (±0.0017)	-6.48 × 10 <sup>4</sup> (±3.02 × 10 <sup>3</sup> )

**Note:** The value provided in the parenthesis is the KMC population standard deviation (also called as the “KMC standard error”).

**Table A45. KMC replicas of the K-Ni(111)-2.8% system at 1273 K and 10.00 bar (H<sub>2</sub>O-CH<sub>4</sub> ratio is maintained at 2:1)**

KMC runs	CH coverage (ML)	Carbon coverage (ML)	Turnover rate (molecules sites <sup>-1</sup> s <sup>-1</sup> )
Random seed 1	0.1280	0.1731	-2.18 × 10 <sup>5</sup>
Random seed 2	0.1144	0.1687	-2.38 × 10 <sup>5</sup>
Random seed 3	0.1129	0.1687	-2.36 × 10 <sup>5</sup>
Random seed 4	0.1125	0.1687	-2.29 × 10 <sup>5</sup>
Random seed 5	0.1151	0.1719	-2.21 × 10 <sup>5</sup>
Average values	0.1166 (±0.0065)	0.1702 (±0.0021)	-2.29 × 10 <sup>5</sup> (±8.79 × 10 <sup>3</sup> )

**Note:** The value provided in the parenthesis is the KMC standard error.

The KMC predictions with different random seed generators are shown for the Ni(111) and K-Ni(111)-2.8% systems in Table A44 and Table A45, respectively. The population average and standard deviation of coverage/turnover rate values have been estimated. As shown in Table A44 and Table A45, the stochastic variability in KMC coverage predictions is minimal/negligible. On the other hand, the turnover rate values change substantially for the different KMC replicas. The KMC turnover rate standard errors for the Ni(111) and K-Ni(111)-2.8% models are 3.02e+03 and 8.79e+03, respectively. Nevertheless, these deviations (around 3-5% of the average turnover rate value) are well within the limits to make reliable comparisons. It is evident from Table A44 and Table A45 that the average turnover rate of K-Ni(111)-2.8% is around 3.5 times (close to 250%) larger than the average turnover rate of Ni(111). Thus, the KMC standard errors do not have any impact on the conclusions/claims made in Chapter 5.

**Table A46. The DORC result variability in KMC simulations of MSR on the K-Ni(111)-2.8% system**

KMC runs	Turnover rate – actual (molecules sites <sup>-1</sup> s <sup>-1</sup> )	Turnover rate – R <sub>12</sub> sensitivity (molecules sites <sup>-1</sup> s <sup>-1</sup> )
Random seed 1	-2.18 × 10 <sup>5</sup>	-2.33 × 10 <sup>5</sup>
Random seed 2	-2.38 × 10 <sup>5</sup>	-2.24 × 10 <sup>5</sup>
Random seed 3	-2.36 × 10 <sup>5</sup>	-2.35 × 10 <sup>5</sup>
Random seed 4	-2.29 × 10 <sup>5</sup>	-2.39 × 10 <sup>5</sup>
Random seed 5	-2.21 × 10 <sup>5</sup>	-2.41 × 10 <sup>5</sup>
Average values	-2.29 × 10 <sup>5</sup> (±8.79 × 10 <sup>3</sup> )	-2.34 × 10 <sup>5</sup> (±6.37 × 10 <sup>3</sup> )
X <sub>RC,R<sub>12</sub></sub>	0.25 (±0.49)	

The DORC analysis (established by Campbell) is a useful approach to identify the rate-determining step of any reaction network. The DORC value for any event *i* is computed as follows:

$$X_{RC,i} = \frac{k_i}{R} \left( \frac{\delta R}{\delta k_i} \right)_{k_j \neq i, K_i} \quad \text{eqA. 70}$$

In the above equation, *k<sub>i</sub>* represents the rate constant of event *i*, *K<sub>i</sub>* indicates the equilibrium constant of event *i* and *R* is the MSR turnover rate. Usually, the rate constant of the desired event is perturbed by around 5-10% and the change in turnover rate is recorded. If *X<sub>RC,i</sub>* value is around -1, then event *i* is rate-inhibiting. On the other hand, a *X<sub>RC,i</sub>* value closer to 1 indicates that event *i* is the rate-limiting step. If *X<sub>RC,i</sub>* is around 0, then event *i* has no impact on the turnover rate.

In the current KMC model, we find that there is a degree of variability in the turnover rate prediction. This mainly arises due to the inherent stochastic nature of KMC. As shown in Table A46, for different random seeds, the variability in turnover rate prediction of the K-Ni(111)-2.8% KMC model is as high as 20%. We performed the sensitivity analysis for event R<sub>12</sub> by perturbing its rate constant by 10%. The KMC turnover rate predictions for different random seeds are shown in the last column of Table A46. We found the average values of the turnover rates and estimated the DORC value using eqA. 70. Furthermore, we employed error



propagation to quantify the variability in DORC value. As shown in Table A46, the error estimate of DORC is 0.49 – this is not an acceptable range. Therefore, it is not feasible to obtain reliable DORC values from the current KMC system. In the literature, there are very few studies that report DORC values using KMC models. Although Liu et al.<sup>49</sup> and Lozano-Reis et al.<sup>24</sup> have computed DORC values with KMC, the authors have not provided information about the number of replica runs and the degree of perturbation. Furthermore, the error estimate in DORC prediction has not been reported.

Some recommendations to reduce the error in DORC prediction using KMC include – 1) The rate constant perturbation value must be finalised by performing several trial simulations, 2) The number of KMC replica runs must be fixed. 3) The replica simulations should be carried out for longer timescales to reduce the KMC standard error. The aforementioned procedure must be performed for all the desirable events. Since this is a computationally intensive task, it is beyond the scope of the current study to estimate DORC.

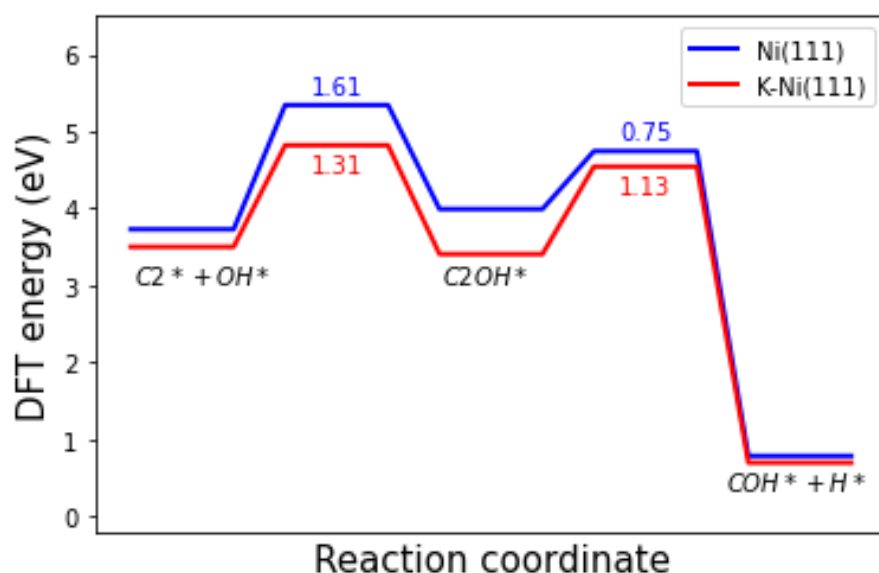


Figure A24: The potential energy diagram of the  $C_2OH$  mechanism on Ni(111) and K-Ni(111)

In Figure A24, we show the removal mechanism of  $C_2$  precursor on the Ni(111) and K-Ni(111) facets. It is interesting to observe that  $C_2$  reacts with OH species to form the  $C_2OH$  intermediate. Subsequently, the  $C_2OH$  intermediate undergoes dissociation to form COH species on the Ni(111) and K-Ni(111) surfaces. In comparison to Ni(111), we find that it is kinetically favourable to form the  $C_2OH$  intermediate on K-Ni(111) (as illustrated in Figure A24). Furthermore, the  $C_2OH$  intermediate has higher thermodynamic stability on K-Ni(111) than Ni(111). The above result is a “first approximation” for the coke removal mechanism. Detailed DFT investigations are needed to find other pathways of coke removal. These studies can potentially aid in the design of Ni catalysts that are resistant to coking.

**Table A47. The overall event frequencies of MSR steps on Ni(111) and K-Ni(111)-2.8% at 1273 K, 10.00 bar and H<sub>2</sub>O-CH<sub>4</sub> ratio maintained at 2:1.**

Event ID: elementary step	Ni(111)	K-Ni(111)-2.8%	K-Ni(111)-2.8%	K-Ni(111)-2.8%
	$\frac{N_{\text{tot-events}}}{N_{\text{total sites}} \times \tau}$	$\frac{N_{\text{Ni-events}}}{N_{\text{total sites}} \times \tau}$	$\frac{N_{\text{K-events}}}{N_{\text{total sites}} \times \tau}$	$\frac{N_{\text{tot-events}}}{N_{\text{total sites}} \times \tau}$
R <sub>1</sub> : CH <sub>4</sub> (g) + 2* ↔ CH <sub>3</sub> * + H*	6.36 × 10 <sup>4</sup>	2.27 × 10 <sup>5</sup>	1.81 × 10 <sup>3</sup>	2.29 × 10 <sup>5</sup>
R <sub>2</sub> : CH <sub>3</sub> * + * ↔ CH <sub>2</sub> * + H*	6.36 × 10 <sup>4</sup>	2.27 × 10 <sup>5</sup>	1.98 × 10 <sup>3</sup>	2.29 × 10 <sup>5</sup>
R <sub>3</sub> : CH <sub>2</sub> * + * ↔ CH* + H*	6.36 × 10 <sup>4</sup>	2.74 × 10 <sup>5</sup>	-4.47 × 10 <sup>4</sup>	2.29 × 10 <sup>5</sup>
R <sub>4</sub> : CH* + * ↔ C* + H*	9.60 × 10 <sup>2</sup>	1.23 × 10 <sup>5</sup>	-7.19 × 10 <sup>4</sup>	5.07 × 10 <sup>4</sup>
R <sub>5</sub> : 2H* → H <sub>2</sub> (g) + 2*	1.91 × 10 <sup>5</sup>	6.67 × 10 <sup>5</sup>	2.23 × 10 <sup>4</sup>	6.89 × 10 <sup>5</sup>
R <sub>6</sub> : H <sub>2</sub> O(g) + * ↔ H <sub>2</sub> O*	6.38 × 10 <sup>4</sup>	1.22 × 10 <sup>5</sup>	1.10 × 10 <sup>5</sup>	2.32 × 10 <sup>5</sup>
R <sub>7</sub> : H <sub>2</sub> O* + * ↔ OH* + H*	6.38 × 10 <sup>4</sup>	1.28 × 10 <sup>5</sup>	1.03 × 10 <sup>5</sup>	2.31 × 10 <sup>5</sup>
R <sub>8</sub> : OH* + * ↔ O* + H*	6.21 × 10 <sup>4</sup>	1.26 × 10 <sup>5</sup>	9.12 × 10 <sup>4</sup>	2.17 × 10 <sup>5</sup>
R <sub>9</sub> : CH* + OH* ↔ CHOH* + *	5.60 × 10 <sup>2</sup>	7.41 × 10 <sup>2</sup>	2.75 × 10 <sup>3</sup>	3.49 × 10 <sup>3</sup>
R <sub>10</sub> : CHOH* + * ↔ CHO* + H*	0.00	0.00	54.9	54.9
R <sub>11</sub> : CHOH* + * ↔ COH* + H*	5.60 × 10 <sup>2</sup>	9.61 × 10 <sup>2</sup>	2.47 × 10 <sup>3</sup>	3.43 × 10 <sup>3</sup>
R <sub>12</sub> : CH* + O* ↔ CHO* + *	6.18 × 10 <sup>4</sup>	1.37 × 10 <sup>5</sup>	3.75 × 10 <sup>4</sup>	1.75 × 10 <sup>5</sup>
R <sub>13</sub> : C* + OH* ↔ COH* + *	1.15 × 10 <sup>3</sup>	1.51 × 10 <sup>3</sup>	9.14 × 10 <sup>3</sup>	1.07 × 10 <sup>4</sup>
R <sub>14</sub> : CHO* + * ↔ CO* + H*	6.18 × 10 <sup>4</sup>	1.35 × 10 <sup>5</sup>	3.98 × 10 <sup>4</sup>	1.75 × 10 <sup>5</sup>
R <sub>15</sub> : COH* + * ↔ CO* + H*	1.71 × 10 <sup>3</sup>	6.95 × 10 <sup>3</sup>	7.14 × 10 <sup>3</sup>	1.41 × 10 <sup>4</sup>
R <sub>16</sub> : C* + O* ↔ CO* + *	3.47 × 10 <sup>2</sup>	6.04 × 10 <sup>2</sup>	3.93 × 10 <sup>4</sup>	3.99 × 10 <sup>4</sup>
R <sub>17</sub> : CO* → CO(g) + *	6.38 × 10 <sup>4</sup>	1.52 × 10 <sup>5</sup>	7.42 × 10 <sup>4</sup>	2.27 × 10 <sup>5</sup>
R <sub>18</sub> : CO* + O* → CO <sub>2</sub> (g) + 2*	80.00	4.39 × 10 <sup>2</sup>	1.89 × 10 <sup>3</sup>	2.33 × 10 <sup>3</sup>

**Table A48. The overall event frequencies of MSR steps on Ni(111) and K-Ni(111)-2.8% (divided by the number of sites of the corresponding site type) at 1273 K, 10.00 bar and H<sub>2</sub>O-CH<sub>4</sub> ratio maintained at 2:1.**

Event ID: elementary step	Ni(111)	K-Ni(111)-2.8%	K-Ni(111)-2.8%
	$\frac{N_{\text{Ni-events}}}{N_{\text{Ni-sites}} \times \tau}$	$\frac{N_{\text{Ni-events}}}{N_{\text{Ni-sites}} \times \tau}$	$\frac{N_{\text{K-events}}}{N_{\text{K-sites}} \times \tau}$
R <sub>1</sub> : CH <sub>4</sub> (g) + 2* ↔ CH <sub>3</sub> * + H*	6.36 × 10 <sup>4</sup>	2.76 × 10 <sup>5</sup>	1.02 × 10 <sup>4</sup>
R <sub>2</sub> : CH <sub>3</sub> * + * ↔ CH <sub>2</sub> * + H*	6.36 × 10 <sup>4</sup>	2.76 × 10 <sup>5</sup>	1.11 × 10 <sup>4</sup>
R <sub>3</sub> : CH <sub>2</sub> * + * ↔ CH* + H*	6.36 × 10 <sup>4</sup>	3.33 × 10 <sup>5</sup>	-2.51 × 10 <sup>5</sup>
R <sub>4</sub> : CH* + * ↔ C* + H*	9.60 × 10 <sup>2</sup>	1.49 × 10 <sup>5</sup>	-4.04 × 10 <sup>5</sup>
R <sub>5</sub> : 2H* → H <sub>2</sub> (g) + 2*	1.91 × 10 <sup>5</sup>	8.11 × 10 <sup>5</sup>	1.25 × 10 <sup>5</sup>
R <sub>6</sub> : H <sub>2</sub> O(g) + * ↔ H <sub>2</sub> O*	6.38 × 10 <sup>4</sup>	1.48 × 10 <sup>5</sup>	6.17 × 10 <sup>5</sup>
R <sub>7</sub> : H <sub>2</sub> O* + * ↔ OH* + H*	6.38 × 10 <sup>4</sup>	1.56 × 10 <sup>5</sup>	5.80 × 10 <sup>5</sup>
R <sub>8</sub> : OH* + * ↔ O* + H*	6.21 × 10 <sup>4</sup>	1.54 × 10 <sup>5</sup>	5.13 × 10 <sup>5</sup>
R <sub>9</sub> : CH* + OH* ↔ CHOH* + *	5.60 × 10 <sup>2</sup>	9.02 × 10 <sup>2</sup>	1.54 × 10 <sup>4</sup>
R <sub>10</sub> : CHOH* + * ↔ CHO* + H*	0.00	0.00	3.09 × 10 <sup>2</sup>
R <sub>11</sub> : CHOH* + * ↔ COH* + H*	5.60 × 10 <sup>2</sup>	1.17 × 10 <sup>3</sup>	1.39 × 10 <sup>4</sup>
R <sub>12</sub> : CH* + O* ↔ CHO* + *	6.18 × 10 <sup>4</sup>	1.67 × 10 <sup>5</sup>	2.11 × 10 <sup>5</sup>
R <sub>13</sub> : C* + OH* ↔ COH* + *	1.15 × 10 <sup>3</sup>	1.84 × 10 <sup>3</sup>	5.14 × 10 <sup>4</sup>
R <sub>14</sub> : CHO* + * ↔ CO* + H*	6.18 × 10 <sup>4</sup>	1.65 × 10 <sup>5</sup>	2.23 × 10 <sup>5</sup>
R <sub>15</sub> : COH* + * ↔ CO* + H*	1.71 × 10 <sup>3</sup>	8.45 × 10 <sup>3</sup>	4.01 × 10 <sup>4</sup>
R <sub>16</sub> : C* + O* ↔ CO* + *	3.47 × 10 <sup>2</sup>	7.35 × 10 <sup>2</sup>	2.21 × 10 <sup>5</sup>
R <sub>17</sub> : CO* → CO(g) + *	6.38 × 10 <sup>4</sup>	1.86 × 10 <sup>5</sup>	4.17 × 10 <sup>5</sup>
R <sub>18</sub> : CO* + O* → CO <sub>2</sub> (g) + 2*	80.00	5.34 × 10 <sup>2</sup>	1.06 × 10 <sup>4</sup>

## Appendix 1V

**Table A49. The formation energies (eV) of CH<sub>x</sub> and C<sub>x</sub>H<sub>y</sub> species on Ni(111)**

Species	Formation energy (eV)
CH <sub>3</sub> <sup>*</sup>	0.13
CH <sub>2</sub> <sup>*</sup>	0.83
CH <sup>*</sup>	1.13
C <sup>*</sup>	2.25
H <sup>*</sup>	-0.67
C <sub>2</sub> H <sub>2</sub> <sup>*</sup>	1.90
C <sub>2</sub> H <sup>*</sup>	2.89
C <sub>2</sub> <sup>*</sup>	4.04
C <sub>3</sub> <sup>*</sup>	6.00
C <sub>4ring</sub> <sup>*</sup>	8.38
C <sub>5ring</sub> <sup>*</sup>	10.84
C <sub>6ring</sub> <sup>*</sup>	12.85
C <sub>4branch</sub> <sup>*</sup>	8.83
C <sub>5branch</sub> <sup>*</sup>	10.49
C <sub>6branch</sub> <sup>*</sup>	12.73

**Table A50. The vibrational wavenumbers of initial states**

System	Vibrational wavenumbers (cm <sup>-1</sup> )
CH <sub>3</sub> *	2830.80, 2830.35, 2765.35, 1285.50, 1285.21, 1165.14, 479.61, 479.20, 400.02, 360.04, 224.63, 224.04
CH <sub>2</sub> *	3009.83, 2351.06, 1431.41, 663.80, 590.88, 532.43, 360.15, 310.70, 282.07
CH*	3031.00, 656.49, 655.91, 629.34, 418.43, 418.14
C*	579.57, 540.45, 540.45
H*	1150.49, 859.07, 858.27
C <sub>2</sub> H <sub>2</sub> *	3027.59, 3013.34, 1209.13, 1049.62, 848.31, 811.55, 698.64, 476.33, 441.63, 300.47, 272.89, 266.23
C <sub>2</sub> H*	3075.17, 1341.09, 867.52, 700.79, 486.19, 421.69, 395.86, 319.00, 224.11
C <sub>2</sub> *	1410.88, 498.03, 441.07, 355.20, 346.76, 331.42
C <sub>3</sub> *	1496.96, 1142.00, 480.87, 469.23, 430.87, 386.03, 349.35, 255.02, 165.31
C <sub>4ring</sub> *	1379.02, 1286.76, 934.73, 525.08, 492.97, 440.33, 398.89, 379.29, 361.13, 344.84, 257.83, 171.76
C <sub>5ring</sub> *	1332.60, 1320.78, 1046.08, 903.61, 584.70, 503.14, 470.33, 446.91, 397.95, 388.64, 370.72, 351.52, 333.15, 223.21, 129.96
C <sub>6ring</sub> *	1166.79, 1165.27, 1165.25, 972.75, 972.75, 893.61, 741.88, 547.85, 547.84, 433.08, 424.30, 424.29, 391.81, 391.79, 377.45, 236.90, 236.89, 192.63
C <sub>4branch</sub> *	1041.92, 1041.91, 985.48, 520.65, 511.77, 511.77, 447.83, 447.82, 444.99, 302.76, 289.45, 289.45
C <sub>5branch</sub> *	1421.41, 1133.15, 1051.81, 860.22, 581.95, 524.83, 510.80, 480.65, 469.27, 444.80, 381.90, 369.05, 327.99, 266.04, 244.10
C <sub>6branch</sub> *	1119.86, 1104.68, 1102.15, 1097.64, 774.38, 638.52, 540.40, 513.27, 509.80, 506.67, 494.23, 475.56, 436.74, 393.96, 380.38, 331.75, 283.92, 271.11

**Table A51. The vibrational wavenumbers of transition states**

Event ID: elementary step	Vibrational wavenumbers (cm <sup>-1</sup> )
R <sub>1</sub> : CH <sub>4</sub> (g) + 2* = CH <sub>3</sub> * + H*	3105.25, 3067.22, 2962.35, 1566.86, 1390.55, 1371.81, 1138.80, 837.03, 725.34, 386.47, 363.21, 134.98, 91.16, 34.37, 898.83i
R <sub>2</sub> : CH <sub>3</sub> * + * = CH <sub>2</sub> * + H*	3008.28, 2514.45, 1851.07, 1369.35, 863.10, 706.56, 536.77, 451.14, 323.89, 266.87, 131.18, 850.24i
R <sub>3</sub> : CH <sub>2</sub> * + * = CH* + H*	3054.45, 1207.13, 880.83, 676.57, 609.92, 466.83, 414.54, 360.17, 585.20i
R <sub>4</sub> : CH* + * = C* + H*	1858.43, 561.04, 522.37, 517.84, 128.04, 811.49i
R <sub>6</sub> : CH* + CH* = C <sub>2</sub> H <sub>2</sub> *	3054.31, 3045.92, 888.31, 836.40, 675.44, 665.96, 594.81, 587.56, 449.24, 443.09, 233.76, 453.22i
R <sub>7</sub> : C <sub>2</sub> H <sub>2</sub> * + * = C <sub>2</sub> H* + H*	3079.93, 1523.39, 1356.40, 884.79, 690.55, 523.41, 430.19, 389.81, 323.31, 264.15, 220.82, 1014.03i
R <sub>8</sub> : C <sub>2</sub> H* + * = C <sub>2</sub> * + H*	1393.89, 1234.60, 570.71, 452.46, 397.13, 357.48, 333.07, 313.82, 868.29i
R <sub>9</sub> : C* + C* = C <sub>2</sub> *	569.09, 545.80, 539.49, 488.30, 361.02, 435.96i
R <sub>10</sub> : C <sub>2</sub> * + C* = C <sub>3</sub> *	1327.00, 547.43, 521.96, 456.39, 432.39, 363.59, 353.53, 297.70, 455.68i
R <sub>11</sub> : C <sub>3</sub> * + C* = C <sub>4ring</sub>	1490.01, 1131.41, 539.16, 508.66, 484.21, 473.89, 424.22, 379.41, 332.13, 271.28, 158.72, 462.73i
R <sub>12</sub> : C <sub>3</sub> * + C* = C <sub>4branch</sub>	1272.40, 1044.56, 575.89, 555.98, 504.77, 495.80, 432.06, 391.35, 324.90, 288.54, 110.82, 444.04i
R <sub>13</sub> : C <sub>4ring</sub> + C* = C <sub>5ring</sub>	1386.58, 1273.35, 947.35, 549.15, 537.71, 510.33, 503.03, 435.87, 397.22, 386.20, 367.90, 314.52, 256.12, 184.24, 425.75i
R <sub>14</sub> : C <sub>4branch</sub> + C* = C <sub>5branch</sub>	1059.78, 987.86, 946.14, 554.09, 531.96, 513.76, 508.71, 502.76, 461.50, 453.14, 442.79, 322.19, 302.03, 272.36, 425.46i
R <sub>15</sub> : C <sub>5ring</sub> + C* = C <sub>6ring</sub>	1448.29, 1261.76, 1097.77, 860.17, 579.62, 573.88, 527.93, 481.14, 459.56, 428.92, 400.86, 396.69, 385.80, 382.58, 287.29, 223.21, 157.00, 488.40i
R <sub>16</sub> : C <sub>5branch</sub> + C* = C <sub>6branch</sub>	1306.23, 1143.17, 1087.81, 835.10, 637.44, 577.81, 527.24, 519.21, 504.09, 481.71, 465.33, 419.61, 398.29, 345.24, 339.39, 240.46, 165.36, 400.83i

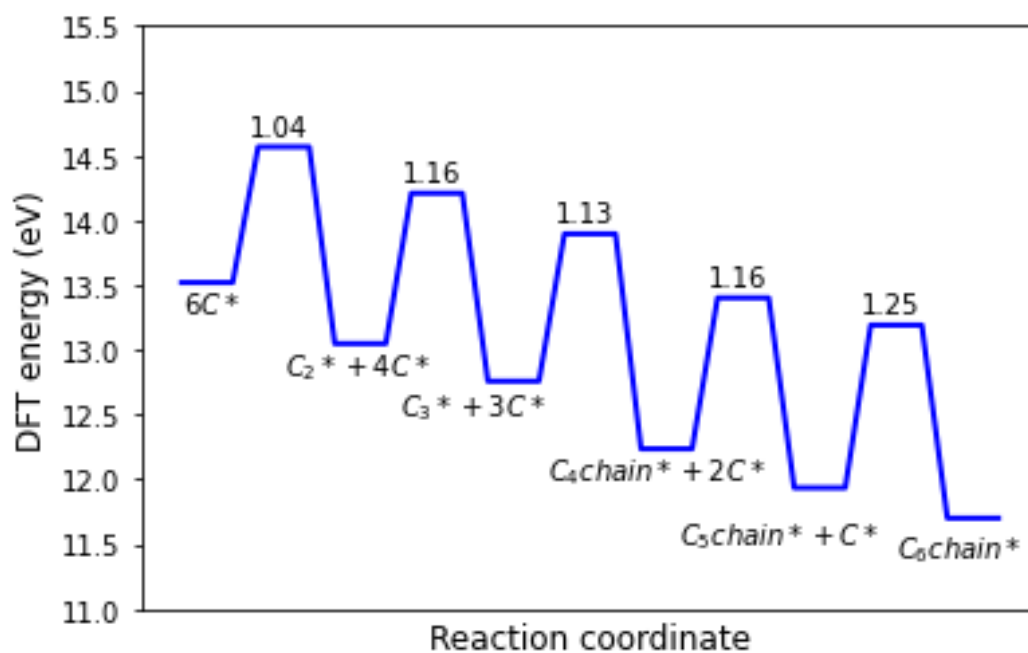


Figure A25: The C-C coupling events to form C<sub>6</sub> chain on the Ni(111) facet.

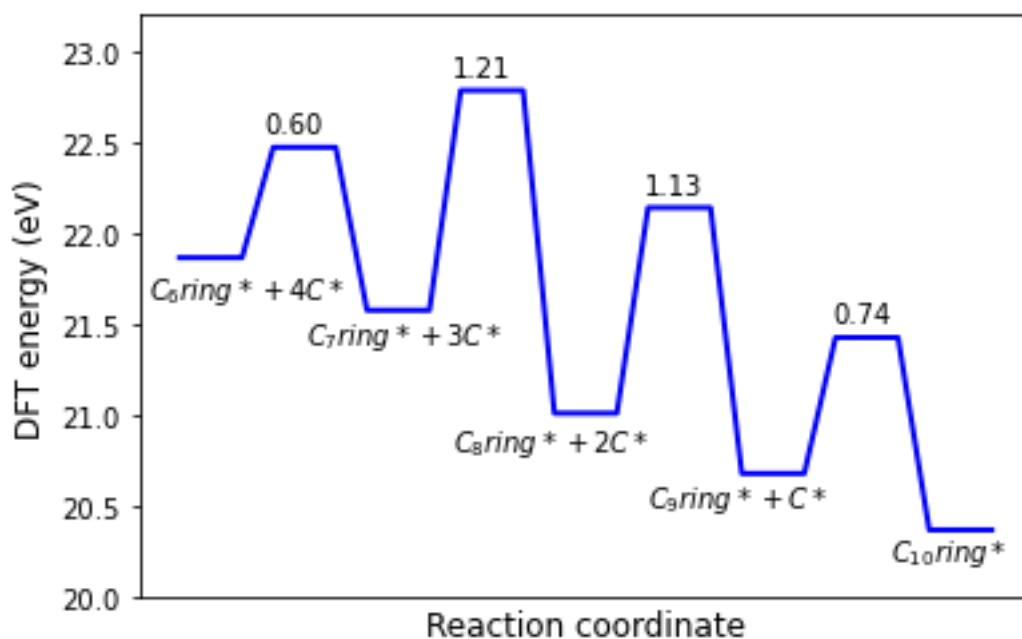


Figure A26: The C-C coupling events to form C<sub>10</sub> ring on the Ni(111) surface.

#### A 4.1 Flux analysis of methane cracking and C-C coupling reactions

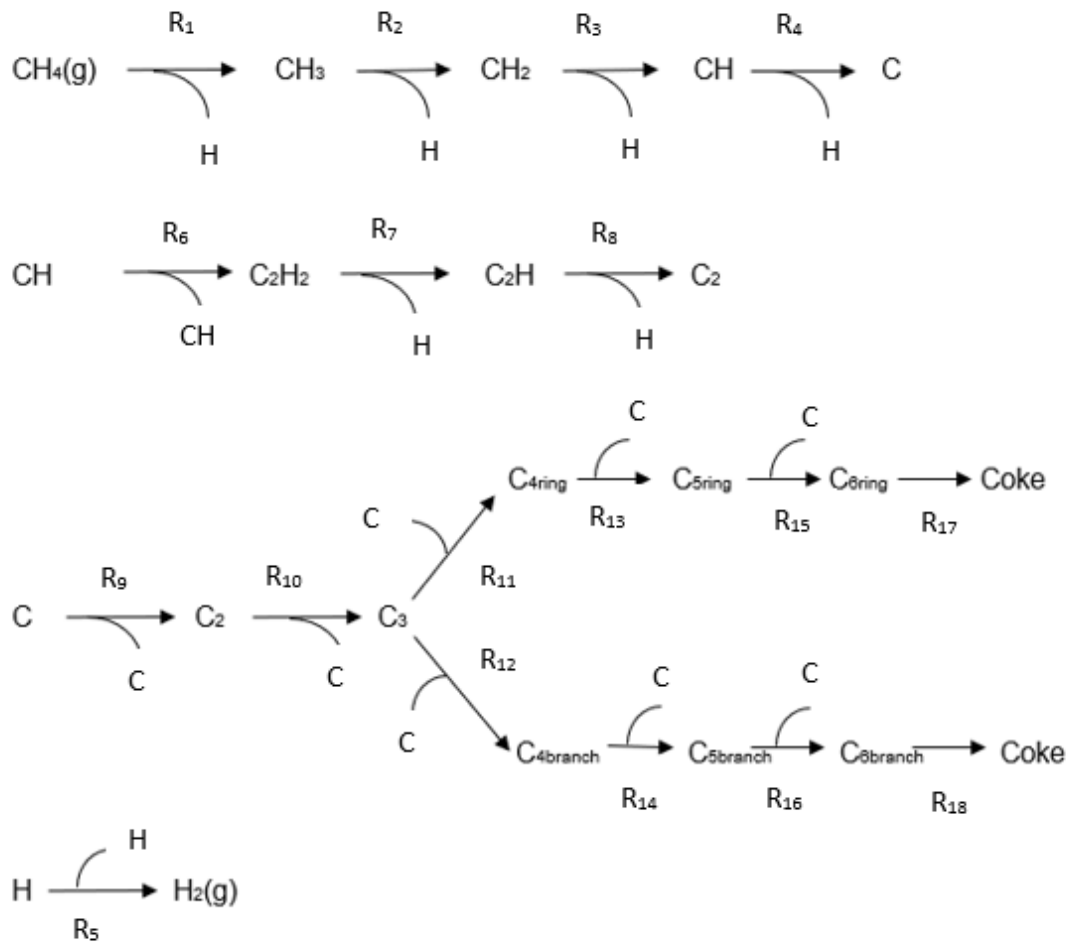


Figure A27: Pictorial representation of methane cracking and C-C coupling reaction network.

At steady-state conditions, the rate of change of intermediate species will be zero.

$$\frac{d\theta_{CH_3}}{dt} = R_1 - R_2 = 0 \quad \text{eqA. 71}$$

$$\frac{d\theta_{CH_2}}{dt} = R_2 - R_3 = 0 \quad \text{eqA. 72}$$

$$\frac{d\theta_{CH}}{dt} = R_3 - R_4 - 2R_6 = 0 \quad \text{eqA. 73}$$

$$\frac{d\theta_C}{dt} = R_4 - 2R_9 - R_{10} - R_{11} - R_{12} - R_{13} - R_{14} - R_{15} - R_{16} = 0 \quad \text{eqA. 74}$$

$$\frac{d\theta_H}{dt} = R_1 + R_2 + R_3 + R_4 + 2R_5 + R_7 + R_8 = 0 \quad \text{eqA. 75}$$

$$\frac{d\theta_{C_2H_2}}{dt} = R_6 - R_7 = 0 \quad \text{eqA. 76}$$



$$\frac{d\theta_{C_2H}}{dt} = R_7 - R_8 = 0 \quad \text{eqA. 77}$$

$$\frac{d\theta_{C_2}}{dt} = R_8 + R_9 - R_{10} = 0 \quad \text{eqA. 78}$$

$$\frac{d\theta_{C_3}}{dt} = R_{10} - R_{11} - R_{12} = 0 \quad \text{eqA. 79}$$

$$\frac{d\theta_{C_{4ring}}}{dt} = R_{11} - R_{13} = 0 \quad \text{eqA. 80}$$

$$\frac{d\theta_{C_{5ring}}}{dt} = R_{13} - R_{15} = 0 \quad \text{eqA. 81}$$

$$\frac{d\theta_{C_{6ring}}}{dt} = R_{15} - R_{17} = 0 \quad \text{eqA. 82}$$

$$\frac{d\theta_{C_{4branch}}}{dt} = R_{12} - R_{14} = 0 \quad \text{eqA. 83}$$

$$\frac{d\theta_{C_{5branch}}}{dt} = R_{14} - R_{16} = 0 \quad \text{eqA. 84}$$

$$\frac{d\theta_{C_{6branch}}}{dt} = R_{16} - R_{18} = 0 \quad \text{eqA. 85}$$

$$\begin{aligned} \frac{d\theta_{fcc}}{dt} = & -2R_1 - R_2 - R_3 - R_4 - 2R_5 + R_6 - R_7 - R_8 + R_9 + R_{10} \\ & + R_{11} + R_{12} + R_{13} + R_{14} + R_{15} + R_{16} + R_{17} + R_{18} = 0 \end{aligned} \quad \text{eqA. 86}$$

From the above equations, the following relationships exist at the steady state:

$$R_1 = R_2 \quad \text{eqA. 87}$$

$$R_2 = R_3 \quad \text{eqA. 88}$$

$$R_3 = R_4 + 2R_6 \quad \text{eqA. 89}$$

$$R_6 = R_7 \quad \text{eqA. 90}$$

$$R_7 = R_8 \quad \text{eqA. 91}$$

$$R_8 + R_9 = R_{10} \quad \text{eqA. 92}$$

$$R_{10} = R_{11} + R_{12} \quad \text{eqA. 93}$$

$$R_{11} = R_{13} \quad \text{eqA. 94}$$

$$R_{13} = R_{15} \quad \text{eqA. 95}$$

$$R_{15} = R_{17} \quad \text{eqA. 96}$$

$$R_{12} = R_{14} \quad \text{eqA. 97}$$

$$R_{14} = R_{16} \quad \text{eqA. 98}$$

$$R_{16} = R_{18} \quad \text{eqA. 99}$$

From the aforementioned relationships, the following can be derived:

$$R_1 = R_4 + 2R_6 \quad \text{eqA. 100}$$

$$R_4 = 2R_9 + R_{10} + 3(R_{17} + R_{18}) \quad \text{eqA. 101}$$

$$R_1 = 2R_9 + R_{10} + 3(R_{17} + R_{18}) + 2R_6 \quad \text{eqA. 102}$$

$$R_{10} = R_9 + R_6 \quad \text{eqA. 103}$$

$$R_1 = 3R_{10} + 3(R_{17} + R_{18}) \quad \text{eqA. 104}$$

$$R_{10} = R_{17} + R_{18} \quad \text{eqA. 105}$$

$$R_1 = 6(R_{17} + R_{18}) \quad \text{eqA. 106}$$

$$R_{cons}^{CH_4} = R_1 = 6(R_{17} + R_{18}) = 6 R_{prod}^{coke} \quad \text{eqA. 107}$$

It is evident from eqA. 107 that the rate of CH<sub>4</sub> consumption ( $R_{cons}^{CH_4}$ ) is six times the rate of coke production ( $R_{prod}^{coke}$ ) – this balances the stoichiometry as coke production involves the desorption of C<sub>6</sub> ring-based structures (which includes six carbon atoms). As shown in Figure A27, there are two pathways to coking: 1) C<sub>6</sub> ring pathway and 2) C<sub>6</sub> branch pathway.

The flux contribution of C<sub>6</sub> ring pathway (%) is estimated as follows:

$$R_{11} = R_{13} = R_{15} = R_{17} = R_{\text{ring-pathway}} \quad \text{eqA. 108}$$

$$\begin{aligned} \text{Flux}_{C_6\text{ring-pathway}} (\%) &= \frac{R_{\text{ring-pathway}} \times 100}{R_{prod}^{coke}} = \frac{R_{11} \times 100}{R_{17} + R_{18}} = \frac{R_{13} \times 100}{R_{17} + R_{18}} \\ &= \frac{R_{15} \times 100}{R_{17} + R_{18}} = \frac{R_{17} \times 100}{R_{17} + R_{18}} \end{aligned} \quad \text{eqA. 109}$$

The flux contribution of C<sub>6</sub> branch pathway (%) is estimated as follows:

$$R_{12} = R_{14} = R_{16} = R_{18} = R_{\text{branch-pathway}} \quad \text{eqA. 110}$$

$$\begin{aligned} \text{Flux}_{\text{C6branch-pathway}} (\%) &= \frac{R_{\text{branch-pathway}} \times 100}{R_{\text{prod}}^{\text{coke}}} = \frac{R_{12} \times 100}{R_{17} + R_{18}} \\ &= \frac{R_{14} \times 100}{R_{17} + R_{18}} = \frac{R_{16} \times 100}{R_{17} + R_{18}} = \frac{R_{18} \times 100}{R_{17} + R_{18}} \end{aligned} \quad \text{eqA. 111}$$

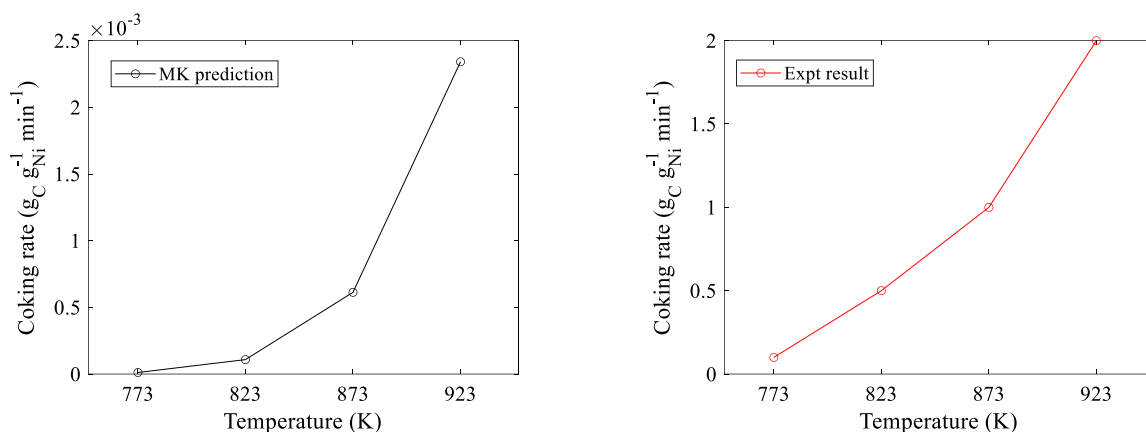


Figure A28: Comparison of MK predicted coking rates with experimental rates (taken from the literature<sup>158,170</sup>).

As shown in Figure A28, we systematically compared the MK predictions with available experimental data (appropriate unit conversions have been made). The MK predicted coking rates are close to 1000 times slower than the experimental rates. This is an expected outcome as the MK model does not capture the end-to-end dynamics of the coking process. Furthermore, the metal support interactions are not taken into account in the MK model.

## References

1. R. Ramachandran and R. K. Menon, An overview of industrial uses of hydrogen, *International Journal of Hydrogen Energy*, 1998, **23**, 593-598.
2. A. E. Farrell, D. W. Keith and J. J. Corbett, A strategy for introducing hydrogen into transportation, *Energy policy*, 2003, **31**, 1357-1367.
3. B. D. Solomon and A. Banerjee, A global survey of hydrogen energy research, development and policy, *Energy policy*, 2006, **34**, 781-792.
4. H. M. Wang, D. W. Blaylock, A. H. Dam, S. E. Liland, K. R. Rout, Y. A. Zhu, W. H. Green, A. Holmen and D. Chen, Steam methane reforming on a Ni-based bimetallic catalyst: density functional theory and experimental studies of the catalytic consequence of surface alloying of Ni with Ag, *Catalysis Science & Technology*, 2017, **7**, 1713-1725.
5. L. Dehimi, Y. Benguerba, M. Virginie and H. Hijazi, Microkinetic modelling of methane dry reforming over Ni/Al<sub>2</sub>O<sub>3</sub> catalyst, *International Journal of Hydrogen Energy*, 2017, **42**, 18930-18940.
6. D. W. Blaylock, T. Ogura, W. H. Green and G. J. O. Beran, Computational Investigation of Thermochemistry and Kinetics of Steam Methane Reforming on Ni(111) under Realistic Conditions, *Journal of Physical Chemistry C*, 2009, **113**, 4898-4908.
7. N. Salhi, A. Boulahouache, C. Petit, A. Kiennemann and C. Rabia, Steam reforming of methane to syngas over NiAl<sub>2</sub>O<sub>4</sub> spinel catalysts, *International Journal of Hydrogen Energy*, 2011, **36**, 11433-11439.
8. M. N. Pedernera, J. Pina and D. O. Borio, Kinetic evaluation of carbon formation in a membrane reactor for methane reforming, *Chemical Engineering Journal*, 2007, **134**, 138-144.
9. D. Chen, R. Lodeng, H. Svendsen and A. Holmen, Hierarchical Multiscale Modeling of Methane Steam Reforming Reactions, *Industrial & Engineering Chemistry Research*, 2011, **50**, 2600-2612.
10. D. W. Blaylock, Y.-A. Zhu and W. H. Green, Computational investigation of the thermochemistry and kinetics of steam methane reforming over a multi-faceted nickel catalyst, *Topics in Catalysis*, 2011, **54**, 828-844.
11. W. An, X. C. Zeng and C. H. Turner, First-principles study of methane dehydrogenation on a bimetallic Cu/Ni(111) surface, *Journal of Chemical Physics*, 2009, **131**.
12. B. Abdullah, N. A. A. Ghani and D. V. N. Vo, Recent advances in dry reforming of methane over Ni-based catalysts, *Journal of Cleaner Production*, 2017, **162**, 170-185.
13. J. Xu and G. F. Froment, Methane Steam Reforming, Methanation and Water-Gas Shift .1. Intrinsic Kinetics, *AIChE journal*, 1989, **35**, 88-96.
14. J. Wei and E. Iglesia, Isotopic and kinetic assessment of the mechanism of reactions of CH<sub>4</sub> with CO<sub>2</sub> or H<sub>2</sub>O to form synthesis gas and carbon on nickel catalysts, *Journal of Catalysis*, 2004, **224**, 370-383.
15. L. M. Aparicio, Transient isotopic studies and microkinetic modeling of methane reforming over nickel catalysts, *Journal of Catalysis*, 1997, **165**, 262-274.
16. D. Chen, R. Lødeng, A. Anundskås, O. Olsvik and A. Holmen, Deactivation during carbon dioxide reforming of methane over Ni catalyst: microkinetic analysis, *Chemical Engineering Science*, 2001, **56**, 1371-1379.
17. H. S. Bengaard, J. K. Norskov, J. Sehested, B. S. Clausen, L. P. Nielsen, A. M. Molenbroek and J. R. Rostrup-Nielsen, Steam reforming and graphite formation on Ni catalysts, *Journal of Catalysis*, 2002, **209**, 365-384.
18. G. Jones, J. G. Jakobsen, S. S. Shim, J. Kleis, M. P. Andersson, J. Rossmeisl, F. Abild-Pedersen, T. Bligaard, S. Helveg, B. Hinnemann, J. R. Rostrup-Nielsen, I. Chorkendorff, J. Sehested and J. K. Norskov, First principles calculations and experimental insight into methane steam reforming over transition metal catalysts, *Journal of Catalysis*, 2008, **259**, 147-160.

19. O. Mohan, S. Shambhawi, A. A. Lapkin and S. H. Mushrif, Investigating methane dry reforming on Ni and B promoted Ni surfaces: DFT assisted microkinetic analysis and addressing the coking problem, *Catalysis Science & Technology*, 2020, 6628-6643.
20. O. Mohan, S. Shambhawi, R. Xu, A. A. Lapkin and S. H. Mushrif, Investigating CO<sub>2</sub> Methanation on Ni and Ru: DFT Assisted Microkinetic Analysis, *ChemCatChem*, 2021, **13**, 2420-2433.
21. D. J. Liu, F. Zahariev, M. S. Gordon and J. W. Evans, Predictive Beyond-Mean-Field Rate Equations for Multisite Lattice-Gas Models of Catalytic Surface Reactions: CO Oxidation on Pd(100), *Journal of Physical Chemistry C*, 2016, **120**, 28639-28653.
22. M. Pineda and M. Stamatakis, Beyond mean-field approximations for accurate and computationally efficient models of on-lattice chemical kinetics, *Journal of Chemical Physics*, 2017, **147**.
23. K. Reuter and M. Scheffler, First-principles kinetic Monte Carlo simulations for heterogeneous catalysis: Application to the CO oxidation at RuO<sub>2</sub>(110), *Physical Review B*, 2006, **73**, 045433.
24. P. Lozano-Reis, H. Prats, P. Gamallo, F. Illas and R. Sayos, Multiscale Study of the Mechanism of Catalytic CO<sub>2</sub> Hydrogenation: Role of the Ni(111) Facets, *ACS Catalysis*, 2020, **10**, 8077-8089.
25. J. Sehested, Four challenges for nickel steam-reforming catalysts, *Catalysis Today*, 2006, **111**, 103-110.
26. J. Xu and M. Saeys, Improving the coking resistance of Ni-based catalysts by promotion with subsurface boron, *Journal of Catalysis*, 2006, **242**, 217-226.
27. M. C. Zonneville, J. J. C. Geerlings and R. A. Vansanten, Conversion of Surface Carbide to Subsurface Carbon on Cobalt (0001) - a Theoretical-Study, *Surface Science*, 1990, **240**, 253-262.
28. R. W. Joyner, G. R. Darling and J. B. Pendry, Stability of Bulk and Surface Carbide Layers and Their Relation to the Fischer-Tropsch Hydrocarbon Synthesis, *Surface Science*, 1988, **205**, 513-522.
29. N. A. K. Aramouni, J. G. Touma, B. Abu Tarboush, J. Zeaiter and M. N. Ahmad, Catalyst design for dry reforming of methane: Analysis review, *Renewable & Sustainable Energy Reviews*, 2018, **82**, 2570-2585.
30. J. W. Snoeck, G. F. Froment and M. Fowles, Kinetic study of the carbon filament formation by methane cracking on a nickel catalyst, *Journal of Catalysis*, 1997, **169**, 250-262.
31. S. Helveg, J. Sehested and J. R. Rostrup-Nielsen, Whisker carbon in perspective, *Catalysis Today*, 2011, **178**, 42-46.
32. M. Perez-Cabero, E. Romeo, C. Royo, A. Monzon, A. Guerrero-Ruiz and I. Rodriguez-Ramos, Growing mechanism of CNTs: a kinetic approach, *Journal of Catalysis*, 2004, **224**, 197-205.
33. S. C. Tsang, J. B. Claridge and M. L. H. Green, Recent Advances in the Conversion of Methane to Synthesis Gas, *Catalysis Today*, 1995, **23**, 3-15.
34. H. Nakano, S. Kawakami, T. Fujitani and J. Nakamura, Carbon deposition by disproportionation of CO on a Ni(977) surface, *Surface Science*, 2000, **454**, 295-299.
35. J. R. Nielsen and D. L. Trimm, Mechanisms of Carbon Formation on Nickel-Containing Catalysts, *Journal of Catalysis*, 1977, **48**, 155-165.
36. J. W. Snoeck, G. F. Froment and M. Fowles, Steam/CO<sub>2</sub> reforming of methane. Carbon formation and gasification on catalysts with various potassium contents, *Industrial & Engineering Chemistry Research*, 2002, **41**, 3548-3556.
37. J. Guo, H. Lou and X. M. Zheng, The deposition of coke from methane on a Ni/MgAl<sub>2</sub>O<sub>4</sub> catalyst, *Carbon*, 2007, **45**, 1314-1321.
38. A. Amin, W. Epling and E. Croiset, Reaction and Deactivation Rates of Methane Catalytic Cracking over Nickel, *Industrial & Engineering Chemistry Research*, 2011, **50**, 12460-12470.
39. I. Alstrup and M. T. Tavares, Kinetics of Carbon Formation from CH<sub>4</sub>+H<sub>2</sub> on Silica-Supported Nickel and Ni-Cu Catalysts, *Journal of Catalysis*, 1993, **139**, 513-524.

40. M. Borghei, R. Karimzadeh, A. Rashidi and N. Izadi, Kinetics of methane decomposition to CO<sub>x</sub>-free hydrogen and carbon nanofiber over Ni-Cu/MgO catalyst, *International Journal of Hydrogen Energy*, 2010, **35**, 9479-9488.
41. P. van Helden, J. A. van den Berg, M. A. Petersen, W. J. van Rensburg, I. M. Ciobica and J. van de Loosdrecht, Computational investigation of the kinetics and mechanism of the initial steps of the Fischer-Tropsch synthesis on cobalt, *Faraday Discussions*, 2017, **197**, 117-151.
42. B. Zijlstra, R. J. P. Broos, W. Chen, G. L. Bezemer, I. A. W. Filot and E. J. M. Hensen, The Vital Role of Step-Edge Sites for Both CO Activation and Chain Growth on Cobalt Fischer-Tropsch Catalysts Revealed through First-Principles-Based Microkinetic Modeling Including Lateral Interactions, *ACS Catalysis*, 2020, **10**, 9376-9400.
43. M. Stamatakis, Kinetic modelling of heterogeneous catalytic systems, *Journal of Physics-Condensed Matter*, 2015, **27**.
44. C. Wu, D. J. Schmidt, C. Wolverton and W. F. Schneider, Accurate coverage-dependence incorporated into first-principles kinetic models: Catalytic NO oxidation on Pt (111), *Journal of Catalysis*, 2012, **286**, 88-94.
45. A. Goswami, H. Y. Ma and W. F. Schneider, Consequences of adsorbate-adsorbate interactions for apparent kinetics of surface catalytic reactions, *Journal of Catalysis*, 2022, **405**, 410-418.
46. M. Andersen, C. Panosetti and K. Reuter, A Practical Guide to Surface Kinetic Monte Carlo Simulations, *Frontiers in Chemistry*, 2019, **7**.
47. M. Neurock and E. W. Hansen, First-principles-based molecular simulation of heterogeneous catalytic surface chemistry, *Computers & Chemical Engineering*, 1998, **22**, S1045-S1060.
48. S. Piccinin and M. Stamatakis, CO Oxidation on Pd(111): A First-Principles-Based Kinetic Monte Carlo Study, *ACS Catalysis*, 2014, **4**, 2143-2152.
49. J. Y. Liu, L. Tan, L. L. Huang, Q. Wang and Y. C. Liu, Kinetic Monte Carlo Modeling for the NO-CO Reaction Mechanism on Rh(100) and Rh(111), *Langmuir*, 2020, **36**, 3127-3140.
50. B. W. J. Chen, M. Stamatakis and M. Mavrikakis, Kinetic Isolation between Turnovers on Au-18 Nanoclusters: Formic Acid Decomposition One Molecule at a Time, *ACS Catalysis*, 2019, **9**, 9446-9457.
51. S. Matera, H. Meskine and K. Reuter, Adlayer inhomogeneity without lateral interactions: Rationalizing correlation effects in CO oxidation at RuO<sub>2</sub>(110) with first-principles kinetic Monte Carlo, *Journal of Chemical Physics*, 2011, **134**.
52. M. Stamatakis, Y. Chen and D. G. Vlachos, First-Principles-Based Kinetic Monte Carlo Simulation of the Structure Sensitivity of the Water-Gas Shift Reaction on Platinum Surfaces, *Journal of Physical Chemistry C*, 2011, **115**, 24750-24762.
53. T. Borowiecki, A. Denis, M. Rawski, A. Golebiowski, K. Stolecki, J. Dmytrzyk and A. Kotarba, Studies of potassium-promoted nickel catalysts for methane steam reforming: Effect of surface potassium location, *Applied Surface Science*, 2014, **300**, 191-200.
54. K. Hassan-Legault, O. Mohan and S. H. Mushrif, Molecular insights into the activity and stability of popular methane reforming catalysts using quantum mechanical tools, *Current Opinion in Chemical Engineering*, 2019, **26**, 38-45.
55. F. Abild-Pedersen, O. Lytken, J. Engbæk, G. Nielsen, I. Chorkendorff and J. K. Nørskov, Methane activation on Ni(111):: Effects of poisons and step defects, *Surface Science*, 2005, **590**, 127-137.
56. O. Mohan, Q. T. Trinh, A. Banerjee and S. H. Mushrif, Predicting CO<sub>2</sub> adsorption and reactivity on transition metal surfaces using popular density functional theory methods, *Molecular Simulation*, 2019, **45**, 1163-1172.
57. M. S. Tameh, A. K. Dearden and C. Huang, Accuracy of Density Functional Theory for Predicting Kinetics of Methanol Synthesis from CO and CO<sub>2</sub> Hydrogenation on Copper, *The Journal of Physical Chemistry C*, 2018, **122**, 17942-17953.

58. S. Helveg, C. Lopez-Cartes, J. Sehested, P. L. Hansen, B. S. Clausen, J. R. Rostrup-Nielsen, F. Abild-Pedersen and J. K. Nørskov, Atomic-scale imaging of carbon nanofibre growth, *Nature*, 2004, **427**, 426-429.
59. V. K. Jaiswar, S. Katheria, G. Deo and D. Kunzru, Effect of Pt doping on activity and stability of Ni/MgAl<sub>2</sub>O<sub>4</sub> catalyst for steam reforming of methane at ambient and high pressure condition, *International Journal of Hydrogen Energy*, 2017, **42**, 18968-18976.
60. M. Wang, Z. Fu and Z. Yang, Tuning the Performance of Ni-Based Catalyst by Doping Coinage Metal on Steam Reforming of Methane and Carbon-Tolerance, *Fuel Cells*, 2014, **14**, 251-258.
61. M. Carlsson, Carbon Formation in Steam Reforming and Effect of Potassium Promotion Potassium dopants prevent carbon formation and aid catalyst recovery, *Johnson Matthey Technology Review*, 2015, **59**, 313-318.
62. S. S. Yadavalli, G. Jones and M. Stamatakis, DFT benchmark studies on representative species and poisons of methane steam reforming on Ni(111), *Physical Chemistry Chemical Physics*, 2021, **23**, 15601-15612.
63. D. S. Sholl and J. A. Steckel, *Density functional theory: a practical introduction*, John Wiley & Sons, 2011.
64. P. Janthon, S. J. Luo, S. M. Kozlov, F. Vines, J. Limtrakul, D. G. Truhlar and F. Illas, Bulk Properties of Transition Metals: A Challenge for the Design of Universal Density Functionals, *Journal of Chemical Theory and Computation*, 2014, **10**, 3832-3839.
65. A. Szabo and N. S. Ostlund, *Modern Quantum chemistry: Introduction to advanced Electronic Structure Theory*, 1989.
66. K. Burke, *The ABC of DFT*, 2007.
67. C. Cesari, M. Bortoluzzi, F. Forti, L. Gubbels, C. Femoni, M. C. Iapalucci and S. Zacchini, 2-D Molecular Alloy Ru-M (M = Cu, Ag, and Au) Carbonyl Clusters: Synthesis, Molecular Structure, Catalysis, and Computational Studies, *Inorganic Chemistry*, 2022.
68. R. M. Martin, *Electronic Structure: Basic Theory and Practical Methods*, 2004.
69. J. Klimes and A. Michaelides, Perspective: Advances and challenges in treating van der Waals dispersion forces in density functional theory, *Journal of Chemical Physics*, 2012, **137**, 120901.
70. S. Gautier, S. N. Steinmann, C. Michel, P. Fleurat-Lessard and P. Sautet, Molecular adsorption at Pt(111). How accurate are DFT functionals?, *Physical Chemistry Chemical Physics*, 2015, **17**, 28921-28930.
71. P. Kratzer and J. Neugebauer, The Basics of Electronic Structure Theory for Periodic Systems, *Frontiers in Chemistry*, 2019, **7**, 106.
72. G. Henkelman and H. Jonsson, A dimer method for finding saddle points on high dimensional potential surfaces using only first derivatives, *Journal of Chemical Physics*, 1999, **111**, 7010-7022.
73. G. Henkelman and H. Jónsson, Improved tangent estimate in the nudged elastic band method for finding minimum energy paths and saddle points, *Journal of Chemical Physics*, 2000, **113**, 9978-9985.
74. G. Henkelman, B. P. Uberuaga and H. Jónsson, A climbing image nudged elastic band method for finding saddle points and minimum energy paths, *Journal of Chemical Physics*, 2000, **113**, 9901-9904.
75. J. A. G. Torres, P. C. Jennings, M. H. Hansen, J. R. Boes and T. Bligaard, Low-Scaling Algorithm for Nudged Elastic Band Calculations Using a Surrogate Machine Learning Model, *Physical review letters*, 2019, **122**.
76. D. G. Truhlar, W. L. Hase and J. T. Hynes, Current Status of Transition-State Theory, *Journal of Physical Chemistry*, 1983, **87**, 2664-2682.
77. J. K. Nørskov, F. Studt, F. Abild-Pedersen and T. Bligaard, *Fundamental Concepts in Heterogeneous Catalysis*, 2014.

78. M. Stamatakis and D. G. Vlachos, A graph-theoretical kinetic Monte Carlo framework for on-lattice chemical kinetics, *The Journal of Chemical Physics* 2011, **134**(21), 214115.
79. A. P. J. Jansen, *An Introduction to Kinetic Monte Carlo simulations of surface reactions*, 2012.
80. R. Réocreux, C. Michel, P. Fleurat-Lessard, P. Sautet and S. N. Steinmann, Evaluating Thermal Corrections for Adsorption Processes at the Metal/Gas Interface, *Journal of Physical Chemistry C*, 2019, **123**, 28828-28835.
81. L. H. Sprowl, C. T. Campbell and L. Arnadóttir, Hindered Translator and Hindered Rotor Models for Adsorbates: Partition Functions and Entropies (vol 120, pg 9719, 2016), *Journal of Physical Chemistry C*, 2017, **121**, 9655-9655.
82. M. Stamatakis and D. G. Vlachos, Unraveling the Complexity of Catalytic Reactions via Kinetic Monte Carlo Simulation: Current Status and Frontiers, *ACS Catalysis*, 2012, **2**, 2648-2663.
83. K. G. Papanikolaou and M. Stamatakis, *Toward the accurate modeling of the kinetics of surface reactions using the kinetic Monte Carlo method* 2020.
84. D. T. Gillespie, A general method for numerically simulating the stochastic time evolution of coupled chemical reactions, *Journal of computational physics*, 1976, **22**, 403-434
85. D. T. Gillespie, Approximate accelerated stochastic simulation of chemically reacting systems, *Journal of Chemical Physics*, 2001, **115**, 1716-1733.
86. A. P. J. Jansen, Monte-Carlo Simulations of Chemical-Reactions on a Surface with Time-Dependent Reaction-Rate Constants, *Computer Physics Communications*, 1995, **86**, 1-12.
87. M. J. Hoffmann, S. Matera and K. Reuter, kmos: A lattice kinetic Monte Carlo framework, *Computer Physics Communications*, 2014, **185**, 2138-2150.
88. B. Hammer and J. K. Nørskov, Theoretical Surface Science and Catalysis — Calculations and Concepts, *In Advances in Catalysis* 2000, **45** 71-129
89. J. Nielsen, M. d'Avezac, J. Hetherington and M. Stamatakis, Parallel kinetic Monte Carlo simulation framework incorporating accurate models of adsorbate lateral interactions, *Journal of Chemical Physics*, 2013, **139**, 224706.
90. H. R. Tang, A. Van der Ven and B. L. Trout, Lateral interactions between oxygen atoms adsorbed on platinum (111) by first principles, *Molecular Physics*, 2004, **102**, 273-279.
91. Y. Zhang, V. Blum and K. Reuter, Accuracy of first-principles lateral interactions: Oxygen at Pd (100). , *Physical Review B*, 2007, **75**, 235406.
92. R. Drautz, R. Singer and M. Fahnle, Cluster expansion technique: An efficient tool to search for ground-state configurations of adatoms on plane surfaces, *Physical Review B*, 2003, **67**, 035418.
93. H. R. Tang, A. Van der Ven and B. L. Trout, Phase diagram of oxygen adsorbed on platinum (111) by first-principles investigation, *Physical Review B*, 2004, **70**, 045420.
94. C. Stampfl, Predicting surface phase transitions from ab initio based statistical mechanics and thermodynamics, *Phase Transitions*, 2007, **80**, 311-332.
95. K. Frey, D. J. Schmidt, C. Wolverton and W. F. Schneider, Implications of coverage-dependent O adsorption for catalytic NO oxidation on the late transition metals, *Catal. Sci. Technol.*, 2014, **4**, 4356-4365.
96. A. Bajpai, K. Frey and W. F. Schneider, Binary Approach to Ternary Cluster Expansions: NO-O-Vacancy System on Pt(111), *Journal of Physical Chemistry C*, 2017, **121**, 7344-7354.
97. D. J. Schmidt, W. Chen, C. Wolverton and W. F. Schneider, Performance of Cluster Expansions of Coverage-Dependent Adsorption of Atomic Oxygen on Pt(111), *Journal of Chemical Theory and Computation*, 2012, **8**, 264-273.
98. S. D. Miller and J. R. Kitchin, Uncertainty and figure selection for DFT based cluster expansions for oxygen adsorption on Au and Pt (111) surfaces, *Molecular Simulation*, 2009, **35**, 920-927.
99. C. Kim, Y. Lee and B. U. Park, Cook's distance in local polynomial regression, *Statistics & Probability Letters*, 2001, **54**, 33-40.



100. A. H. Motagamwala and J. A. Dumesic, Microkinetic Modeling: A Tool for Rational Catalyst Design, *Chemical Reviews*, 2021, **121**, 1049-1076.
101. M. Jorgensen and H. Gronbeck, First-Principles Microkinetic Modeling of Methane Oxidation over Pd(100) and Pd(111), *ACS Catalysis*, 2016, **6**, 6730-6738.
102. M. Stamatakis and D. G. Vlachos, Equivalence of on-lattice stochastic chemical kinetics with the well-mixed chemical master equation in the limit of fast diffusion, *Computers & Chemical Engineering*, 2011, **35**, 2602-2610.
103. M. Andersen, C. P. Plaisance and K. Reuter, Assessment of mean-field microkinetic models for CO methanation on stepped metal surfaces using accelerated kinetic Monte Carlo, *Journal of Chemical Physics*, 2017, **147**.
104. L. C. Grabow, A. A. Gokhale, S. T. Evans, J. A. Dumesic and M. Mavrikakis, Mechanism of the water gas shift reaction on Pt: First principles, experiments, and microkinetic modeling, *Journal of Physical Chemistry C*, 2008, **112**, 4608-4617.
105. T. G. Gambu, R. K. Abrahams and E. van Steen, Micro-Kinetic Modelling of CO-TPD from Fe(100) Incorporating Lateral Interactions, *Catalysts*, 2019, **9**, 310.
106. A. Bajpai, K. Frey and W. F. Schneider, Comparison of Coverage-Dependent Binding Energy Models for Mean-Field Microkinetic Rate Predictions, *Langmuir*, 2020, **36**, 465-474.
107. T. Bligaard, J. K. Norskov, S. Dahl, J. Matthiesen, C. H. Christensen and J. Sehested, The Bronsted-Evans-Polanyi relation and the volcano curve in heterogeneous catalysis, *Journal of Catalysis*, 2004, **224**, 206-217.
108. M. G. Evans and M. Polanyi, Inertia and driving force of chemical reactions., *Transactions of the Faraday Society*, 1938, **34**, 0011-0023.
109. A. U. Nilekar, J. Greeley and M. Mavrikakis, A simple rule of thumb for diffusion on transition-metal surfaces, *Angewandte Chemie-International Edition*, 2006, **45**, 7046-7049.
110. A. Chatterjee and D. G. Vlachos, An overview of spatial microscopic and accelerated kinetic Monte Carlo methods, *Journal of Computer-Aided Materials Design*, 2007, **14**, 253-308.
111. S. Ravipati, M. D'Avezac, J. Nielsen, J. Hetherington and M. Stamatakis, A Caching Scheme To Accelerate Kinetic Monte Carlo Simulations of Catalytic Reactions, *Journal of Physical Chemistry A*, 2020, **124**, 7140-7154.
112. M. J. Hoffmann and T. Bligaard, A Lattice Kinetic Monte Carlo Solver for First-Principles Microkinetic Trend Studies, *Journal of Chemical Theory and Computation*, 2018, **14**, 1583-1593.
113. F. Mittendorfer, A. Garhofer, J. Redinger, J. Klimes, J. Harl and G. Kresse, Graphene on Ni(111): Strong interaction and weak adsorption, *Physical Review B*, 2011, **84**, 201401.
114. S. Grimme, J. Antony, S. Ehrlich and H. Krieg, A consistent and accurate ab initio parametrization of density functional dispersion correction (DFT-D) for the 94 elements H-Pu, *Journal of Chemical Physics*, 2010, **132**.
115. A. Tkatchenko and M. Scheffler, Accurate Molecular Van Der Waals Interactions from Ground-State Electron Density and Free-Atom Reference Data, *Physical review letters*, 2009, **102**, 073005.
116. S. N. Steinmann and C. Corminboeuf, A generalized-gradient approximation exchange hole model for dispersion coefficients, *Journal of Chemical Physics*, 2011, **134**.
117. S. N. Steinmann and C. Corminboeuf, Comprehensive Benchmarking of a Density-Dependent Dispersion Correction, *J Chem Theory Comput*, 2011, **7**, 3567-3577.
118. F. Ortmann, F. Bechstedt and W. G. Schmidt, Semiempirical van der Waals correction to the density functional description of solids and molecular structures, *Physical Review B*, 2006, **73**, 205101.
119. M. Dion, H. Rydberg, E. Schroder, D. C. Langreth and B. I. Lundqvist, Van der Waals density functional for general geometries, *Physical review letters*, 2004, **92**, 246401.
120. J. Klimes, D. R. Bowler and A. Michaelides, Chemical accuracy for the van der Waals density functional, *Journal of Physics-Condensed Matter*, 2010, **22**, 022201.

121. J. Klimes, D. R. Bowler and A. Michaelides, Van der Waals density functionals applied to solids, *Physical Review B*, 2011, **83**, 195131.
122. J. Wellendorff, K. T. Lundgaard, A. Mogelhoff, V. Petzold, D. D. Landis, J. K. Nørskov, T. Bligaard and K. W. Jacobsen, Density functionals for surface science: Exchange-correlation model development with Bayesian error estimation, *Physical Review B*, 2012, **85**, 235149.
123. X. Li, J. Feng, E. G. Wang, S. Meng, J. Klimes and A. Michaelides, Influence of water on the electronic structure of metal-supported graphene: Insights from van der Waals density functional theory, *Physical Review B*, 2012, **85**, 085425.
124. P. Janthon, F. Vines, S. M. Kozlov, J. Limtrakul and F. Illas, Theoretical assessment of graphene-metal contacts, *Journal of Chemical Physics*, 2013, **138**.
125. H. Munoz-Galan, F. Vines, J. Gebhardt, A. Gorling and F. Illas, The contact of graphene with Ni(111) surface: description by modern dispersive forces approaches, *Theoretical Chemistry Accounts*, 2016, **135**, 1-9.
126. L. Zhu, C. Liu, X. Wen, Y.-W. Li and H. Jiao, Molecular or dissociative adsorption of water on clean and oxygen pre-covered Ni(111) surfaces, *Catalysis Science & Technology*, 2019, **9**, 199-212.
127. F. Goltl, E. A. Murray, S. A. Tacey, S. Rangarajan and M. Mavrikakis, Comparing the performance of density functionals in describing the adsorption of atoms and small molecules on Ni(111), *Surface Science*, 2020, **700**, 121675.
128. J. Wellendorff, T. L. Silbaugh, D. Garcia-Pintos, J. K. Nørskov, T. Bligaard, F. Studt and C. T. Campbell, A benchmark database for adsorption bond energies to transition metal surfaces and comparison to selected DFT functionals, *Surface Science*, 2015, **640**, 36-44.
129. M. K. Rana, H. S. Koh, J. Hwang and D. J. Siegel, Comparing van der Waals Density Functionals for CO<sub>2</sub> Adsorption in Metal Organic Frameworks, *Journal of Physical Chemistry C*, 2012, **116**, 16957-16968.
130. J. P. Perdew, K. Burke and M. Ernzerhof, Generalized gradient approximation made simple (vol 77, pg 3865, 1996), *Physical review letters*, 1997, **78**, 1396-1396.
131. B. Hammer, L. B. Hansen and J. K. Nørskov, Improved adsorption energetics within density-functional theory using revised Perdew-Burke-Ernzerhof functionals, *Physical Review B*, 1999, **59**, 7413-7421.
132. Y. K. Zhang and W. T. Yang, Comment on "Generalized gradient approximation made simple", *Physical review letters*, 1998, **80**, 890-890.
133. Y. A. Zhu, D. Chen, X. G. Zhou and W. K. Yuan, DFT studies of dry reforming of methane on Ni catalyst, *Catalysis Today*, 2009, **148**, 260-267.
134. J. D. Li, E. Croiset and L. Ricardez-Sandoval, Effect of carbon on the Ni catalyzed methane cracking reaction: A DFT study, *Applied Surface Science*, 2014, **311**, 435-442.
135. R. Reocreux, C. Michel, P. Fleurat-Lessard, P. Sautet and S. N. Steinmann, Evaluating Thermal Corrections for Adsorption Processes at the Metal/Gas Interface, *Journal of Physical Chemistry C*, 2019, **123**, 28828-28835.
136. J. C. Shelton, H. R. Patil and J. M. Blakely, Equilibrium Segregation of Carbon to a Nickel (111) Surface - Surface Phase-Transition, *Surface Science*, 1974, **43**, 493-520.
137. L. X. Benedict, N. G. Chopra, M. L. Cohen, A. Zettl, S. G. Louie and V. H. Crespi, Microscopic determination of the interlayer binding energy in graphite, *Chemical Physics Letters*, 1998, **286**, 490-496.
138. R. Zacharia, H. Ulbricht and T. Hertel, Interlayer cohesive energy of graphite from thermal desorption of polyaromatic hydrocarbons, *Physical Review B*, 2004, **69**, 155406.
139. J. Harl and G. Kresse, Accurate Bulk Properties from Approximate Many-Body Techniques, *Physical review letters*, 2009, **103**, 056401.
140. S. Shepard and M. Smeu, First principles study of graphene on metals with the SCAN and SCAN+rVV10 functionals, *Journal of Chemical Physics*, 2019, **150**.

141. T. Olsen, J. Yan, J. J. Mortensen and K. S. Thygesen, Dispersive and Covalent Interactions between Graphene and Metal Surfaces from the Random Phase Approximation, *Physical review letters*, 2011, **107**, 156401.
142. Y. Gamo, A. Nagashima, M. Wakabayashi, M. Terai and C. Oshima, Atomic structure of monolayer graphite formed on Ni(111), *Surface Science*, 1997, **374**, 61-64.
143. F. Bianchini, L. L. Patera, M. Peressi, C. Africh and G. Comelli, Atomic Scale Identification of Coexisting Graphene Structures on Ni(111), *Journal of Physical Chemistry Letters*, 2014, **5**, 467-473.
144. W. Zhao, S. M. Kozlov, O. Hofert, K. Gotterbarm, M. P. A. Lorenz, F. Vines, C. Papp, A. Gorling and H. P. Steinruck, Graphene on Ni(111): Coexistence of Different Surface Structures, *Journal of Physical Chemistry Letters*, 2011, **2**, 759-764.
145. J. T. Stuckless, N. Alsarraf, C. Wartnaby and D. A. King, Calorimetric Heats of Adsorption for Co on Nickel Single-Crystal Surfaces, *Journal of Chemical Physics*, 1993, **99**, 2202-2212.
146. W. Zhao, S. J. Carey, Z. T. Mao and C. T. Campbell, Adsorbed Hydroxyl and Water on Ni(111): Heats of Formation by Calorimetry, *ACS Catalysis*, 2018, **8**, 1485-1489.
147. J. Lapujoulade and K. S. Neil, Chemisorption of Hydrogen on (111) Plane of Nickel, *Journal of Chemical Physics*, 1972, **57**, 3535.
148. J. T. Stuckless, C. E. Wartnaby, N. AlSarraf, S. J. B. DixonWarren, M. Kovar and D. A. King, Oxygen chemisorption and oxide film growth on Ni{100}, {110}, and {111}: Sticking probabilities and microcalorimetric adsorption heats, *Journal of Chemical Physics*, 1997, **106**, 2012-2030.
149. S. J. Carey, W. Zhao, A. Frehner, C. T. Campbell and B. Jackson, Energetics of Adsorbed Methyl and Methyl Iodide on Ni(111) by Calorimetry: Comparison to Pt(111) and Implications for Catalysis, *ACS Catalysis*, 2017, **7**, 1286-1294.
150. F. P. Netzer and T. E. Madey, The Structure of Co on Ni(111), *Journal of Chemical Physics*, 1982, **76**, 710-715.
151. A. Takeuchi and H. Wise, Thermodynamic Properties of Surface Carbon on Metals .1. Nickel, *Journal of Physical Chemistry* 1983, **87**, 5372-5376.
152. R. Haunschild and W. Kloppe, New accurate reference energies for the G2/97 test set, *Journal of Chemical Physics*, 2012, **136**.
153. T. L. Silbaugh and C. T. Campbell, Energies of Formation Reactions Measured for Adsorbates on Late Transition Metal Surfaces, *Journal of Physical Chemistry C*, 2016, **120**, 25161-25172.
154. A. J. R. Hensley, K. Ghale, C. Rieg, T. Dang, E. Anderst, F. Studt, C. T. Campbell, J. S. McEwen and Y. Xu, DFT-Based Method for More Accurate Adsorption Energies: An Adaptive Sum of Energies from RPBE and vdW Density Functionals, *Journal of Physical Chemistry C*, 2017, **121**, 4937-4945.
155. S. G. Wang, X. Y. Liao, D. B. Cao, Y. W. Li, J. G. Wang and H. J. Jiao, Formation of carbon species on Ni(111): Structure and stability, *Journal of Physical Chemistry C*, 2007, **111**, 10894-10903.
156. D. J. Cheng, G. Barcaro, J. C. Charlier, M. Hou and A. Fortunelli, Homogeneous Nucleation of Graphitic Nanostructures from Carbon Chains on Ni(111), *Journal of Physical Chemistry C*, 2011, **115**, 10537-10543.
157. J. D. Li, E. Croiset and L. Ricardez-Sandoval, Carbon clusters on the Ni(111) surface: a density functional theory study, *Physical Chemistry Chemical Physics*, 2014, **16**, 2954-2961.
158. J. D. Li, E. Croiset and L. Ricardez-Sandoval, Carbon nanotube growth: First-principles-based kinetic Monte Carlo model, *Journal of Catalysis*, 2015, **326**, 15-25.
159. B. W. J. Chen, L. Xu and M. Mavrikakis, Computational Methods in Heterogeneous Catalysis, *Chemical Reviews*, 2021, **121**, 1007-1048.
160. F. Hess, P. P. T. Krause, S. F. Rohrlack, J. P. Hofmann, A. Farkas and H. Over, One-dimensional confinement in heterogeneous catalysis: Trapped oxygen on RuO<sub>2</sub>(110) model catalysts, *Surface Science*, 2012, **606**, L69-L73.

161. S. Hofmann, R. Sharma, C. Ducati, G. Du, C. Mattevi, C. Cepek, M. Cantoro, S. Pisana, A. Parvez, F. Cervantes-Sodi, A. C. Ferrari, R. Dunin-Borkowski, S. Lizzit, L. Petaccia, A. Goldoni and J. Robertson, In situ observations of catalyst dynamics during surface-bound carbon nanotube nucleation, *Nano letters*, 2007, **7**, 602-608.
162. M. Lin, J. P. Y. Tan, C. Boothroyd, K. P. Loh, E. S. Tok and Y. L. Foo, Dynamical observation of bamboo-like carbon nanotube growth, *Nano letters*, 2007, **7**, 2234-2238.
163. M. Pineda and M. Stamatakis, Kinetic Monte Carlo simulations for heterogeneous catalysis: Fundamentals, current status, and challenges, *Journal of Chemical Physics*, 2022, **156**.
164. S. Ravipati, G. D. Savva, I. A. Christidi, R. Guichard, J. Nielsen, R. Reocreux and M. Stamatakis, Coupling the time-warp algorithm with the graph-theoretical kinetic Monte Carlo framework for distributed simulations of heterogeneous catalysts, *Computer Physics Communications*, 2022, **270**, 108148.
165. K. G. Papanikolaou, M. T. Darby and M. Stamatakis, Engineering the Surface Architecture of Highly Dilute Alloys: An ab Initio Monte Carlo Approach, *ACS Catalysis*, 2020, **10**, 1224-1236.
166. S. S. Yadavalli, G. Jones and M. Stamatakis, *Journal*, 2022, DOI: 10.17172/NOMAD/2023.04.12-2.
167. J. R. Rostrup-Nielsen, J. Sehested and J. K. Nørskov, Hydrogen and synthesis gas by steam- and CO<sub>2</sub> reforming, *Advances in Catalysis*, Vol 47, 2002, **47**, 65-139.
168. A. M. Amin, E. Croiset and W. Epling, Review of methane catalytic cracking for hydrogen production, *International Journal of Hydrogen Energy*, 2011, **36**, 2904-2935.
169. J. D. Li, E. Croiset and L. Ricardez-Sandoval, Theoretical investigation of the methane cracking reaction pathways on Ni (111) surface, *Chemical Physics Letters*, 2015, **639**, 205-210.
170. A. M. Amin, E. Croiset, C. Constantinou and W. Epling, Methane cracking using Ni supported on porous and non-porous alumina catalysts, *International Journal of Hydrogen Energy*, 2012, **37**, 9038-9048.
171. S. Mahamulkar, K. H. Yin, P. K. Agrawal, R. J. Davis, C. W. Jones, A. Malek and H. Shibata, Formation and Oxidation/Gasification of Carbonaceous Deposits: A Review, *Industrial & Engineering Chemistry Research*, 2016, **55**, 9760-9818.
172. E. Meloni, M. Martino and V. Palma, A Short Review on Ni Based Catalysts and Related Engineering Issues for Methane Steam Reforming, *Catalysts*, 2020, **10**, 352.
173. S. S. Maluf and E. M. Assaf, Ni catalysts with Mo promoter for methane steam reforming, *Fuel*, 2009, **88**, 1547-1553.
174. X. D. Feng, J. Feng and W. Y. Li, Insight into MgO promoter with low concentration for the carbon-deposition resistance of Ni-based catalysts in the CO<sub>2</sub> reforming of CH<sub>4</sub>, *Chinese Journal of Catalysis*, 2018, **39**, 88-98.
175. M. R. Li, Z. Lu and G. C. Wang, The effect of potassium on steam-methane reforming on the Ni-4/Al<sub>2</sub>O<sub>3</sub> surface: a DFT study, *Catalysis Science & Technology*, 2017, **7**, 3613-3625.
176. M. X. Zhou and B. Liu, DFT Investigation on the Competition of the Water-Gas Shift Reaction Versus Methanation on Clean and Potassium-Modified Nickel(111) Surfaces, *ChemCatChem*, 2015, **7**, 3928-3935.
177. Y. X. Wang, H. L. Zhang, P. An, H. S. Wu and J. F. Jia, Effect of Potassium on Methanol Steam Reforming on the Cu(111) and Cu(110) Surfaces: A DFT Study, *The Journal of Physical Chemistry C*, 2021, **125**, 20905-20918.
178. H. Prats, S. Posada-Pérez, J. A. Rodríguez, R. Sayós and F. Illas, Kinetic Monte Carlo Simulations Unveil Synergic Effects at Work on Bifunctional Catalysts, *ACS Catalysis*, 2019, **9**, 9117-9126.
179. I. Alstrup, B. S. Clausen, C. Olsen, R. H. H. Smits and J. R. Rostrup-Nielsen, Promotion of steam reforming catalysts, *Studies in surface science and catalysis*, 1998, **119**, 5-14.
180. T. Borowiecki, A. Golebiowski, J. Ryczkowski and B. Stasinska, The influence of promoters on the coking rate of nickel catalysts in the steam reforming of hydrocarbons, *Natural Gas Conversion V*, 1998, **119**, 711-716.

181. C. Stegelmann, A. Andreasen and C. T. Campbell, Degree of Rate Control: How Much the Energies of Intermediates and Transition States Control Rates, *Journal of the American Chemical Society*, 2009, **131**, 13563-13563.
182. F. Abild-Pedersen, J. K. Nørskov, J. R. Rostrup-Nielsen, J. Sehested and S. Helveg, Mechanisms for catalytic carbon nanofiber growth studied by ab initio density functional theory calculations, *Physical Review B*, 2006, **73**, 115419.
183. J. F. Gao, J. Yip, J. J. Zhao, B. I. Yakobson and F. Ding, Graphene Nucleation on Transition Metal Surface: Structure Transformation and Role of the Metal Step Edge, *Journal of the American Chemical Society*, 2011, **133**, 5009-5015.
184. J. D. Li, E. Croiset and L. Ricardez-Sandoval, Methane dissociation on Ni (100), Ni (111), and Ni (553): a comparative density functional theory study, *Journal of Molecular Catalysis A: Chemical*, 2012, **365**, 103-114.
185. H. Prats and M. Stamatakis, Stability and reactivity of metal nanoclusters supported on transition metal carbides, *Nanoscale Advances*, 2023, **5**, 3214-3224.
186. C. R. C. Rego, L. N. Oliveira, P. Tereshchuk and J. L. F. Da Silva, Comparative study of van der Waals corrections to the bulk properties of graphite, *Journal of Physics: Condensed Matter*, 2015, **27**, 415502.
187. C. Fan, Y. A. Zhu, M. L. Yang, Z. J. Sui, X. G. Zhou and D. Chen, Density Functional Theory-Assisted Microkinetic Analysis of Methane Dry Reforming on Ni Catalyst, *Industrial & Engineering Chemistry Research*, 2015, **54**, 5901-5913.
188. J. T. Niu, Y. L. Wang, Y. Y. Qi, A. H. Dam, H. M. Wang, Y. A. Zhu, A. Holmen, J. Y. Ran and D. Chen, New mechanism insights into methane steam reforming on Pt/Ni from DFT and experimental kinetic study, *Fuel*, 2020, **266**, 117143.
189. T. P. Beebe, D. W. Goodman, B. D. Kay and J. T. Yates, Kinetics of the Activated Dissociative Adsorption of Methane on the Low Index Planes of Nickel Single-Crystal Surfaces, *The Journal of chemical physics*, 1987, **87**, 2305-2315.
190. R. C. Egeberg, S. Ullmann, I. Alstrup, C. B. Mullins and I. Chorkendoff, Dissociation of CH<sub>4</sub> on Ni(111) and Ru(0001), *Surface Science*, 2002, **497**, 183-193.